NASA-TM-84614 19830020905

# NASA Technical Memorandum 84614

# Wind-Tunnel Investigation of Aerodynamic Loading on a 0.237-Scale Model of a Remotely Piloted Research Vehicle With a Thick, High-Aspect-Ratio Supercritical Wing

Thomas A. Byrdsong and Cuyler W. Brooks, Jr.

JUNE 1983

**25**

25th Anniversary
1958-1983

NASA

# Wind-Tunnel Investigation of Aerodynamic Loading on a 0.237-Scale Model of a Remotely Piloted Research Vehicle With a Thick, High-Aspect-Ratio Supercritical Wing

Thomas A. Byrdsong and Cuyler W. Brooks, Jr.
*Langley Research Center*
*Hampton, Virginia*

## SUMMARY

Wind-tunnel measurements were made of the wing-surface static-pressure distributions on a 0.237-scale model of a remotely piloted research vehicle equipped with a thick, high-aspect-ratio supercritical wing. Data are presented for two model configurations (with and without a ventral pod) at Mach numbers from 0.70 to 0.92 at angles of attack from -4° to 8°. Large variations of wing-surface local pressure distributions were developed; however, the characteristic supercritical-wing pressure distribution occurred near the design condition of 0.80 Mach number and 2° angle of attack. The significant variations of the local pressure distributions indicated pronounced shock-wave movements that were highly sensitive to angle of attack and Mach number. The effect of the vertical pod varied with test conditions; however at the higher Mach numbers, the effects on wing flow characteristics were significant at semispan stations as far outboard as 0.815. There were large variations of the wing loading in the range of test conditions, both model configurations exhibited a well-defined peak value of normal-force coefficient at the cruise angle of attack (2°) and Mach number (0.80).

## INTRODUCTION

The Drones for Aerodynamic and Structural Testing (DAST) project (ref. 1) is a NASA flight program which uses a modified Firebee II target drone vehicle (ref. 2) as a test-bed aircraft for testing aeroelastic research wings (ARW). In the integrated design of the second wing (ARW-2), the structural integrity of the wing depends on the successful operation of multiple-function active control systems. The ARW-2 design includes active controls for maneuver load alleviation, gust load alleviation, relaxed static stability, and flutter suppression.

This vehicle will be flight tested with simultaneous operation of the active control systems. The successful conduct of this flight-test program depends to a considerable degree on prior prediction of the performance, flightworthiness, and stability and control characteristics of the research vehicle. Wind-tunnel investigations are used to predict these characteristics. In addition, the wind-tunnel data are used to provide an estimate of vehicle flight characteristics for a computer simulation program. The simulation program is used in the planning of specific flight-research missions and as an aid in the prediction of structural loadings at critical points in the flight envelope.

A wind-tunnel investigation of wing static-pressure distributions was conducted for a 0.237-scale model of the DAST ARW-2 flight-test vehicle. The research wing (ARW-2), which has a high aspect ratio with thick supercritical airfoil sections, was designed to cruise at a Mach number near 0.80. Two configurations of the model were tested. The configurations differed only by the presence or absence of a ventral pod to house the instrumentation for the flight vehicle. The purposes of this investigation were to determine the wing-surface static-pressure distributions at the design flight condition and to indicate trends of the wing performance at off-design conditions. Experimental results were obtained at Mach numbers from about 0.70 to 0.92, angles of attack from about -4° to 8°, and a Reynolds number of $16.5 \times 10^6$ per meter. Plots of the data show the basic pressure distributions at five semispan stations, the effect of angle of attack and Mach number on the pressure distributions, and

additional selected aerodynamic characteristics derived from the pressure distributions. Corresponding force-balance data of this study are contained in reference 3. A compilation of all wing-surface static-pressure measurements is presented in a "Supplement to NASA TM-84614," which is available upon request. A request form is included at the back of this report. Request for the supplement should be addressed to:

> NASA Scientific and Technical Information Facility
> P.O. Box 8757
> Baltimore/Washington International Airport, MD 21240

## SYMBOLS

All dimensional values are given in SI Units; however, measurements and calculations were made in U.S. Customary Units.

$b$      reference wing span, 137.16 cm

$C_L$      lift coefficient, $\text{Lift}/q_\infty S$

$C_N$      normal-force coefficient, $\displaystyle\int_0^1 \int_0^1 (c_{p,\ell} - c_{p,u}) \, d(x/c) \, d[y/(b/2)]$

$c_p$      sectional pressure coefficient, $(p - p_\infty)/q_\infty$ ($C_p$ in computer-generated figures)

$c_{p,\text{sonic}}$      sectional pressure coefficient at sonic conditions ($C_{p,\text{sonic}}$ in computer-generated figures)

$c$      local streamwise chord, cm

$c_{av}$      average chord, $S/b$, cm

$c_m$      wing-section pitching-moment coefficient about quarter-chord point, $\displaystyle\int_0^1 (c_{p,\ell} - c_{p,u})(0.25 - x/c) \, d(x/c)$

$c_n$      wing-section normal-force coefficient, $\displaystyle\int_0^1 (c_{p,\ell} - c_{p,u}) \, d(x/c)$

$c_{p,\ell}$      pressure coefficient on wing lower surface

$c_{p,u}$      pressure coefficient on wing upper surface

$\bar{c}$      wing mean aerodynamic chord, cm

$\bar{c}_t$      horizontal-tail mean aerodynamic chord, cm

$M$      free-stream Mach number

| m | wing-surface streamwise local slope |
|---|---|
| $p$ | local static pressure, Pa |
| $p_\infty$ | free-stream static pressure, Pa |
| $q_\infty$ | free-stream dynamic pressure, Pa |
| $R$ | radius |
| $S$ | area of basic wing panels including fuselage intercept, $m^2$ |
| $t$ | wing local thickness, cm |
| $x$ | longitudinal distance, cm |
| $y$ | spanwise distance from plane of symmetry, cm |
| $z$ | airfoil section vertical coordinate, cm |
| $z_c$ | vertical distance to section camber line measured from section chord line |
| $\alpha$ | angle of attack, deg |
| $\alpha_n$ | angle of attack expressed to nearest integer, deg |
| $\varepsilon$ | angle of twist of local airfoil section, deg |

Subscript:

| max | maximum value |
|---|---|

Abbreviations:

| M.S. | model station, m |
|---|---|
| W.L. | water line, m |

## APPARATUS AND PROCEDURE

### MODEL DESCRIPTION

The wind-tunnel investigation was conducted using a 0.237-scale model of the test-bed aircraft, a modified Firebee II target drone (ref. 2), equipped with a thick, high-aspect-ratio supercritical wing. The general arrangement of the basic wind-tunnel model (configuration A) is shown in figure 1, and the model planform with selected geometric data is shown in figure 2.

The supercritical wing was constructed of stainless steel and was mounted in a high-wing position, so that its reference plane coincided with water line -0.013 m (incidence angle of 0°). The spanwise distribution of twist is shown in figure 3, and the maximum thickness-to-chord ratio for the wing is shown in figure 4. The reference wing (wing planform excluding the trailing-edge extension) had an aspect ratio of 10.3, a taper ratio of 0.40, a quarter-chord sweep angle of 27°, and a

dihedral angle of 0°. The area of the reference wing planform, including the fuselage intercept, was 0.183 m$^2$, the mean geometric chord of the reference wing panel was 14.13 cm, and the span was 1.37 m. Nondimensional wing airfoil coordinates at the wing-fuselage junction, the wing-planform break, and the wing tip are presented in table I of reference 3. A comparison of the airfoil shape, thickness, camber line shape, and surface slopes at semispan stations 0.259, 0.630, and 0.963 are shown in figure 5. A streamwise surface discontinuity (crease) on the wing surface is shown in figure 2. The crease is located at the planform break and is the result of the change of airfoil thickness distribution along the span.

The left wing panel of the model was instrumented with 135 static-pressure orifices. Fifteen orifices were located on the wing upper surface, and 12 orifices were located on the lower wing surfaces at each of 5 semispan stations. The spanwise and chordwise locations of the orifices are shown in figure 6. Pressure orifices that were rendered inactive due to tube leakage or blockage are indicated by an asterisk (fig. 6(b)).

The model fuselage was constructed of fiberglass skin, aluminum bulkheads, and a rectangular steel beam 1.282 m in length (from M.S. = 0.433 to M.S. = 1.715) to provide for a large degree of structural rigidity. Except for the keel and parachute-riser housing, surface projections and protuberances on the aircraft fuselage were not simulated on the model. The model was not equipped with flow-through air ducts; however, the abrupt change in fuselage area at the inlet duct and inlet plow on the flight vehicle (ref. 4) was modified to provide a smooth contour in place of the inlet for attached flow conditions. A sketch showing a side view of the air inlet-duct and the revised contour is shown in figure 7. The exit-duct area was covered by a flat surface having a rectangular clearance hole that provided access to the fuselage cavity for the model support system. Cross-sectional views of the model fuselage geometry are presented in figure 8.

Two configurations of the wind-tunnel model were used for this study. The configurations, designated configuration A and configuration B, differed only by the addition of a ventral pod (fig. 9) to the model. Figure 1 is a sketch of configuration A, and figure 10 shows photographs of configuration B.

TEST FACILITY

The investigation was conducted in the Langley 8-Foot Transonic Pressure Tunnel. This facility is a continuous-flow, single-return, slotted-throat tunnel having controls that allow for the independent variation of Mach number, density, temperature, and dewpoint. The test section is square in cross section with the upper and lower walls axially slotted (each wall having an open ratio of approximately 0.06) to permit changing the test-section Mach number continuously through the transonic speed range. The stagnation pressures in the tunnel can be varied from a minimum value of approximately 0.25 atm at all test Mach numbers to a maximum value of approximately 1.5 atm at transonic Mach numbers and to approximately 2.0 atm at Mach numbers of 0.40 or less (1 atm = 101.3 kPa). A more detailed description of the tunnel may be found in reference 5.

BOUNDARY-LAYER TRANSITION STRIPS

Boundary-layer transition strips were placed on all model components for this investigation as indicated in figure 11. All transition strips were 0.3 cm wide and

4

were made of carborundum grit embedded in a plastic adhesive. The size and location of each strip were determined by the techniques of references 6 and 7 and from experiences gained by using transition strips on similar wind-tunnel models (ref. 8). The model surface forward of the strips was kept smooth to maintain laminar flow.

## MEASUREMENTS AND TEST CONDITIONS

Wing-surface static-pressure measurements presented herein were taken over a Mach number range from approximately 0.70 to 0.92 for angles of attack that varied from approximately -4° to 8° at a Reynolds number of about $16.5 \times 10^6$ per meter and at a sideslip angle of 0° for undeflected control surfaces. The model angle of attack was measured by means of a $\pm 10g$ linear servo accelerometer that was housed within the fuselage cavity and aligned with the longitudinal reference axis $(1g = 9.8 \text{ m/sec}^2)$. The investigation was conducted at a stagnation temperature of 322 K and at a dew point low enough to avoid significant condensation effects (see ref. 9).

## ACCURACIES AND CORRECTIONS

The angle of attack of the model was corrected for flow angularity in the tunnel test section. No corrections have been applied to the data for sting interference effects or for the effects of either solid wake blockage or lift interference due to wall effects. The estimated accuracy of Mach number was 0.003. It is believed that angle of attack and angle of sideslip are accurate to $\pm 0.1°$.

## PRESENTATION OF RESULTS

Wing-surface static-pressure measurements were obtained during a wind-tunnel investigation of the model for its static stability and control characteristics. The basic force and moment data and selected stability and control characteristics are presented in reference 3. The wing local static-pressure measurements were reduced to coefficient form, and computer plots of the local-pressure coefficients were generated to show chordwise pressure distributions at five semispan stations. The chordwise pressure distributions were then fitted with a smooth curve generated by a cubic-spline computer program based on the method of reference 10. The sonic pressure coefficient is included in the figures to indicate regions where the flow was supercritical. The section normal-force and pitching-moment coefficients were computed by numeric integration of the fitted curves of the chordwise pressure distributions.

The panel normal-force coefficient was computed by numeric integration of a fitted curve through the five spanwise section normal-force coefficients that were weighted to account for wing taper. In this computation, the section normal-force coefficient was assumed to vary parabolically over the wing center section. The parabola was assumed to have a vertical axis of symmetry at the fuselage centerline and to match the coefficient value and slope at the first inboard data station. To extend the curve for integration of the panel normal-force coefficient from the last outboard data station to the wing tip, a section normal-force coefficient of zero was assumed at the wing tip, and this value was treated as a sixth point in the cubic-spline fitting and subsequent integration.

5

The results of this investigation are presented in the following figures:

## CHORDWISE PRESSURE DISTRIBUTIONS

### Basic Data

The basic chordwise pressure distributions are presented for pressure orifices located at five semispan stations over a range of Mach numbers from 0.70 to 0.92, and over a range of angle of attack from -4° to 8°. Although considerably more pressure data were obtained for model configuration A than for model configuration B, results are only presented where comparable test conditions exist for the two configurations. The data show an evolvement of the characteristic local-pressure distribution for supercritical airfoils which is fairly well defined in the results for Mach numbers from 0.80 to 0.86 at angles of attack of 2° and 4°. The salient features of these pressure distributions are the nearly constant supercritical pressures of the wing upper surface from about 5 percent to 55 or 60 percent of the wing local chord (for $y/(b/2)$ = 0.44, 0.63, and 0.82) and relatively high lower-surface pressures in the region of the wing cusp (aft loading). In addition, of considerable importance is the relatively steep adverse pressure gradient resulting from a shock wave on the wing upper surface. This pressure gradient contributes to a substantial wave-drag increment and possible flow separation caused by interaction of the shock wave and boundary layer. An indication of the character of the flow in the vicinity of the cruise condition (M = 0.80;  $\alpha$ = 2°) is shown in figures 14 and 15 by fluorescent-oil

flow visualization photographs. The photographs show conditions of the flow on the upper and lower surfaces of the right wing panel for angles of attack of 1.5°, 1.9°, and 2.4° at a Mach number of 0.80. It should be noted that the pressure data presented in figures 12 and 13 were obtained from the left wing panel, whereas the flow visualization results presented in figures 14 and 15 were obtained from the right wing panel. A comparison of these data at comparable test conditions indicates an expected similarity between the pressure data and visual indications (photographic) of the severity and location of the adverse pressure gradient along the span. The primary shock wave is indicated in figures 12(c) and 13(c) for an angle of attack of 1.9° by the substantial adverse (steep) pressure gradient at the downstream end of the characteristic pressure plateau of supercritical-airfoil sections (i.e., $x/c = 0.60$ and $y/(b/2) = 0.44$). The effect of this wave is shown in the flow visualization results (figs. 14(b) and 15(b)) by the accumulated oil (narrow light area) that extends along the wing span on the upper surface. A similar accumulation of oil on the inboard wing panel (upper surface), forward of the transition strip and extending from the vicinity of the wing leading edge and fuselage junction to about the 15-percent semispan station, is probably attributable to a laminar bubble. Also evident are several wedges of turbulent flow upstream of the transition strip. This transition is attributed to foreign particles that became attached to or embedded in the wing surface subsequent to the model preparation for this phase of the test program. In summary, the data show that large variations of wing-surface pressure distributions occurred with angle of attack and Mach number; however, characteristic pressure distributions were developed for Mach number and angle of attack ($M = 0.80$; $\alpha_n = 2°$), where the results of reference 3 indicate near-optimum efficiency for both model configurations.

## Effect of Ventral Pod

The effect of ventral pod addition on the wing local-pressure distributions is indicated by comparison of the results of figures 12 and 13. These effects varied with test conditions and resulted in significant changes in the pressure coefficient for upper and lower surfaces and for outboard and inboard sections of the wing. For the lower Mach numbers (0.70 to 0.80), the pod generally produced an additional flow acceleration in the region of the inboard lower wing surface. This additional flow acceleration resulted in somewhat lower values of pressure coefficient. When supercritical flow existed on the inboard lower surface (i.e., at negative angles of attack), the addition of the pod increased the chordwise extent of supercritical flow and the strength of the shock wave, thereby producing a decrease in the pressure coefficient up to 0.50 (i.e., $x/c = 0.30$, $y/(b/2) = 0.259$, $\alpha = -4°$, and $M = 0.70$). The changes in the pressure coefficient for the upper surface and for the outboard lower surface at these conditions were minimal. At the higher Mach numbers (0.86 and above), the effects of the pod are shown in the pressure coefficients for most of the wing span for both the upper and lower surfaces. At these Mach numbers and moderate angles of attack, the data for the wing lower surface exhibit a small chordwise region of supersonic flow that extends across most of the span. The addition of the pod resulted in an increase in the local supersonic Mach number and a rearward expansion of the supersonic bubble with corresponding changes in the pressure coefficients (up to 0.52 at $x/c = 0.60$, $y/(b/2) = 0.444$, and $\alpha = 2°$). This effect is shown to some degree at all spanwise stations except the most outboard one. The pressure coefficients on the wing upper surface also exhibit large regions of supersonic flow. However, the addition of the pod had little effect on the pressure distributions except for conditions where flow separation or incipient flow separation existed on the upper surface. Under these conditions, the addition of the pod resulted in a forward movement of the upper-surface shock wave with associated

increases in the pressure coefficients for the affected regions. The more significant upper-surface shock-wave movements occurred at span stations out to 0.815 for the test conditions investigated. In summary, the major effects of adding the pod at the higher Mach numbers were to strengthen and displace rearward the shock wave on the wing lower surface and to displace forward the shock wave on the wing upper surface at conditions of incipient flow separation. At Mach numbers below 0.80, the significant effects were limited to the inboard surface, but at Mach numbers of 0.86 and above, major effects occurred along the wing span out to station 0.815.

## Effect of Angle of Attack

The effects of angle of attack on the wing-surface pressure distributions are presented in figures 16 and 17 for model configurations A and B, respectively. These data are composite plots of the fitted curves through the experimental local pressures presented in figures 12 and 13. Separate composite plots of the pressure distributions are shown for the upper and lower surfaces, respectively. The values of angle of attack indicated in the key to figures 16 and 17 are the actual values expressed to the nearest integer $\alpha_n$. The data (figs. 16 and 17) show an expected and pronounced effect of angle of attack on the surface pressure distributions. The lower-surface pressure distributions in the vicinity of the cusp were relatively insensitive to angle of attack, but significant changes occurred for the pressures on the wing upper surface, where supersonic flow was developed at most test conditions. These data indicate chordwise displacement of the shock-wave location with variations of angle of attack when the local flow velocities were supercritical. The data for Mach numbers from 0.75 to 0.84 indicate an initial shock-wave displacement in the downstream direction, followed by a reversed shock-wave displacement in the upstream direction as angle of attack was progressively increased. The downstream shock-wave displacement resulted from the rearward expansion of the supersonic region, and the reversed upstream shock-wave displacement was associated with flow separation at the wing trailing edge. The condition at which a reversal in the direction of shock-wave movement occurred corresponds to the initial development of wing stall, as indicated in the force-data results of reference 3. In general, the data of figures 16 and 17 indicate an expected and pronounced effect of angle of attack on the local-pressure distributions. Reversed shock-wave movement on the wing upper surface was associated with the initiation of wing stall. Similar effects of angle of attack have been reported for other investigations, some of which are references 11 through 13.

## Effect of Mach Number

The effect of Mach number on the wing-surface pressure distributions are presented in figures 18 and 19 for model configurations A and B, respectively. These data are composite plots of the curves fitted through the experimental local pressure in figures 12 and 13. Separate composite plots of the pressure distributions are shown for the upper and lower wing surfaces. The data show large variations of the wing local-pressure distributions with Mach number over the range of angle of attack tested. An example of the more interesting variation is indicated in the pressure distributions for an angle of attack of 2° (fig. 18(d)), where extensive upper-surface pressure plateaus were developed along the wing span at most of the test Mach numbers. For an angle of attack of 2°, these data show that the maximum negative pressure plateau was developed at the wing design Mach number (fig. 18(d)) and that there was a large influence of Mach number on the plateau pressure level and on the extent of the upper-surface supersonic region. The position of the shock wave that terminated the supersonic region generally moved downstream with increasing Mach.

number, but the movement was not regular and, in some instances, was in the opposite direction as Mach number was increased. (See upper-surface pressures in fig. 18(d); y/(b/2) = 0.444.) For the lower-surface pressures, the largest effect of Mach number occurred at conditions where shock waves were present. At Mach numbers above 0.90, separated flow conditions are indicated for the pressures on the lower surface near the wing trailing edge for a portion of the angle-of-attack range. In summary, the data of figures 18 and 19 indicate that there were significant Mach number effects on the wing-surface pressure distributions. The salient feature of these effects was the pronounced sensitivity of shock-wave location to Mach number.

WING-SECTION AERODYNAMIC CHARACTERISTICS

Section Normal-Force Coefficient

Variations of the wing-section normal-force coefficient with angle of attack are presented in figure 20 for model configurations A and B. The data show that the variations of the normal-force coefficient were essentially linear at Mach numbers from 0.70 to 0.80 and nonlinear at Mach numbers above 0.80. This nonlinearity reflects substantial changes in the local-pressure distributions on the wing upper and lower surfaces due primarily to the effects of shock-wave movement or flow separation near the trailing edge or both. A transition of the normal-force coefficient from linear to nonlinear variations is indicated in the results for the cruise Mach number of 0.80 (fig. 20(c)). The data show a significantly reduced normal-force-curve slope at angles of attack above the cruise angle of attack (2°) for all spanwise stations. For these conditions (fig. 17(c)), the local-pressure distributions indicate possible flow separation at the most inboard and outboard stations. This separation accounts for the relative upstream shock-wave location and for the reversed (downstream) shock-wave movement at stations 0.444 and 0.630 as angle of attack was increased. These effects of angle of attack are enhanced considerably at the higher Mach numbers, where the data exhibit large nonlinearities.

An effect of the ventral pod on the section normal-force coefficients is also indicated in the results of figure 20. These data show that, for most test conditions, the effect of the pod was translated to a reduction of the normal-force coefficient. This effect was small at the lower Mach numbers (M < 0.84) and significantly larger at the higher Mach numbers of 0.90 and 0.92. The relatively small reduction of the normal-force coefficient at the lower Mach numbers was generally more pronounced at the three inboard stations and was due primarily to changes in the local pressures on the wing lower surface (figs. 12 and 13). The reduction of normal-force coefficients varied considerably along the wing span at the larger Mach numbers of 0.90 and 0.92 and was attributed to very large changes in the local-pressure coefficients (above 0.50) on both the upper and lower surfaces. In contrast, the results also indicate occasions when the effect of the pod resulted in an increase of the section normal-force coefficient. Several examples of this condition are shown in the results for a Mach number of 0.86 (fig. 20(e); i.e., $\alpha$ = -4°, 6°, and 8°). An examination of the corresponding local-pressure distributions (figs. 12 and 13) shows that there was a larger effect of the pod on the wing upper-surface pressures than there was on the lower-surface pressures. Although the overall change in the upper and lower local-pressure coefficients was generally very small at each spanwise station, in most instances it was the integrated effect of the small distributed change and the local peak pressure coefficients ($\Delta c_{p,u}$ = 0.30) on the wing upper surface that provided for the more positive values of section normal-force coefficients. In general, the data of figure 20 indicate that there were significant nonlinear variations of section normal-force coefficient with angle of attack. The

nonlinearity, which became significant at Mach numbers above 0.80, was attributed to shock-wave movement and flow separation. The addition of the ventral pod generally resulted in a large reduction of the section normal-force coefficients at Mach numbers above 0.86.

## Section Pitching-Moment Coefficient

Variations of wing-section pitching-moment coefficient with angle of attack are presented in figure 21 for model configurations A and B. The variations were nonlinear and generally small at Mach numbers of 0.75 and below, and they became significantly larger as Mach number was increased. Relatively large negative pitching-moment coefficients existed at each semispan station in the range of test Mach numbers. The negative pitching moment is attributed to the aft-loading characteristic of supercritical airfoil sections, which is, in part, the result of the camber near the airfoil trailing edge (fig. 5). The data of figure 21 also indicate an effect of the ventral pod on the section pitching-moment coefficient. The effect was generally negligible at the lower Mach numbers from 0.70 to 0.80. When Mach number was increased to the higher values, the presence of the ventral pod generally resulted in a marked positive shift. At the intermediate Mach number of 0.84, the data for the inboard stations indicate that there was a small shift in the section pitching-moment coefficient. With increasing Mach number, the effect became significantly larger, and the area of greatest impact moved progressively outboard on the wing. As with the section normal-force coefficient, the effect of the pod on the pitching-moment coefficient was primarily caused by the influence of the pod on the wing lower-surface pressures at Mach numbers up to 0.86 and on both the upper- and lower-surface pressures at Mach numbers above 0.86. (See section entitled "Effect of Ventral Pod.") The noteworthy aspects of the data of figure 21 are the nonlinear variations of section pitching-moment coefficient with angle of attack that became significant at the higher Mach numbers, and the ventral-pod effects that resulted in a large positive shift in the pitching-moment coefficient at Mach numbers above 0.86.

## WING-PANEL LOADING CHARACTERISTICS

Variations of wing-panel loading with angle of attack are presented in figure 22 for model configurations A and B at Mach numbers from 0.70 to 0.92. These data were obtained from the wing-section normal-force coefficients of figure 20 and were weighted to account for wing-planform taper. Characteristic wing-panel loadings are shown for the range of angle of attack at the lower Mach numbers (0.70 ≤ M ≤ 0.80). At Mach numbers above 0.80, a general depression was developed in the loading for the mid semispan region. This effect, which occurred at most of the test angles of attack, is attributed to movement of a relatively strong shock wave on the wing upper surface, as noted. (See section entitled "Section Normal-Force Coefficient.")

Variations of the wing-panel loading with Mach number are presented in figure 23 for model configurations A and B at angles of attack from -4° to 4°. These data are cross plots of the results presented in figure 22. An effect of Mach number is clearly indicated at most of the test conditions. This effect, which is very similar to the effect of angle of attack, is also indicated as a depression in the panel loading at each test angle of attack. The Mach number at which the depression in the loading was initially developed decreased as angle of attack was increased. The smallest loadings were generally obtained at Mach numbers of 0.90 and 0.92, which are well above the design Mach number of 0.80.

10

Variations of the integrated-panel normal-force coefficients with Mach number are presented in figure 24 for model configurations A and B. These data were obtained by integrating the weighted section normal-force coefficient (fig. 22) across the span for each angle of attack. The data (fig. 24) show that the effect of Mach number on the panel normal-force coefficient varied with test conditions. For most test conditions, there was a reduction in panel normal-force coefficient at a given angle of attack as Mach number was increased above 0.80. At an angle of attack of 2°, a well-defined peak value of the normal-force coefficient is indicated at the design Mach number of 0.80.

A comparison of the wing-panel normal-force coefficient and the balance-measured normal-force coefficient is presented in figure 25 for both model configurations. The wing-panel normal-force coefficient was obtained from figure 24, and the balance-measured normal-force coefficient was obtained from the force-data results of the wind-tunnel test program (ref. 3). The pressure and force data were obtained simultaneously during the wind-tunnel test. The data of figure 25 show that the variations of the normal-force coefficients were comparable for the force and pressure data for model configurations A and B. The integrated pressure data were slightly larger than the force data except at a Mach number of 0.90, where the two sets of data tend to agree at the higher angles of attack. The indicated difference between these data is attributed to the assumptions used for the chordwise and spanwise integrations that generated the panel normal-force coefficient and to the existence of fuselage and horizontal-tail loads included in the force data. A nominal difference in pressure data of about 0.1 or less is indicated for most test conditions. The agreement between these data is considered good.

CONCLUSIONS

A wind-tunnel investigation has been conducted to determine the wing-surface local pressure distributions of a rigid 0.237-scale force model of a remotely piloted research vehicle with a thick, high-aspect-ratio supercritical wing. Data are presented for two model configurations (with and without a ventral pod) at Mach numbers from 0.70 to 0.92 at angles of attack from -4° to 8°. The results of this investigation indicated the following:

1. Large variations of wing-surface pressure distributions were developed in the range of test conditions. The characteristic supercritical wing pressure distribution occurred, as expected, near the design condition of Mach 0.80 and 2° angle of attack.

2. The significant variation of wing-surface pressure distributions indicated pronounced shock-wave movements that were highly sensitive to angle of attack and Mach number.

3. The effect of the ventral pod on the wing flow characteristics varied with test conditions. At Mach numbers below 0.80, significant effects were limited to the inboard lower surface, and at Mach numbers of 0.86 and above, major effects occurred along the wing span out to station 0.815.

4. At the higher Mach numbers, the primary effects of the pod were to strengthen and displace rearward the shock wave on the wing lower surface, and to displace forward the shock wave on the wing upper surface at conditions of incipient flow separation.

11

5. There were significant nonlinear variations of the section normal-force and pitching-moment coefficients at the higher Mach numbers. The addition of the ventral pod generally resulted in a reduction of the section normal-force coefficient at all Mach numbers tested, and in a large positive shift in the section pitching-moment coefficient at Mach numbers above 0.86.

6. There were large variations of wing loading in the range of test conditions; however, at the cruise angle of attack (2°) these configurations exhibited a well-defined peak value of panel normal-force coefficient at the design Mach number (0.80).

7. A comparison of the normal-force coefficients derived from pressure-data and force-data measurements indicates good agreement.


Langley Research Center
National Aeronautics and Space Administration
Hampton, VA 23665
March 29, 1983

REFERENCES

1. Murrow, H. N.; and Eckstrom, C. V.: Drones for Aerodynamic and Structural Testing (DAST) - A Status Report. J. of Aircr., vol. 16, no. 8, Aug. 1979, pp. 521-526.

2. Eckstrom, Clinton V.; and Peele, Ellwood L.: Flight Assessment of a Large Supersonic Drone Aircraft for Research Use. NASA TM X-3259, 1975.

3. Byrdsong, Thomas A.; and Brooks, Cuyler W., Jr.: Wind-Tunnel Investigation of Longitudinal and Lateral-Directional Stability and Control Characteristics of a 0.237-Scale Model of a Remotely Piloted Research Vehicle With a Thick, High-Aspect-Ratio Supercritical Wing. NASA TM-81790, 1980.

4. Byrdsong, Thomas A.: Flight Measurements of Lifting Pressures for a Thin Low-Aspect-Ratio Wing at Subsonic, Transonic, and Low Supersonic Speeds. NASA TM X-3405, 1977.

5. Schaefer, William T., Jr.: Characteristics of Major Active Wind Tunnels at the Langley Research Center. NASA TM X-1130, 1965.

6. Braslow, Albert L.; and Knox, Eugene C.: Simplified Method for Determination of Critical Height of Distributed Roughness Particles for Boundary-Layer Transition at Mach Numbers From 0 to 5. NACA TN 4363, 1958.

7. Blackwell, James A., Jr.: Preliminary Study of Effects of Reynolds Number and Boundary-Layer Transition Location on Shock-Induced Separation. NASA TN D-5003, 1969.

8. Bartlett, Dennis W.: Wind-Tunnel Investigation of Several High-Aspect-Ratio Supercritical Wing Configurations on a Wide-Body-Type Fuselage. NASA TM X-71996, 1977.

9. Jordan, Frank L., Jr.: Investigation at Near-Sonic Speed of Some Effects of Humidity on the Longitudinal Aerodynamic Characteristics of An NASA Supercritical-Wing Research Airplane Model. NASA TM X-2618, 1972.

10. Akima, Horoshi: A New Method of Interpolation and Smooth Curve Fitting Based on Local Procedures. J. Assoc. Comput. Mach., vol. 17, no. 4, Oct. 1970, pp. 589-602.

11. Roos, Frederick W.: Some Features of the Unsteady Pressure Field in Transonic Airfoil Buffeting. AIAA Paper 79-0351, Jan. 1979.

12. Montoya, Lawrence C.; and Banner, Richard D.: F-8 Supercritical Wing Flight Pressure, Boundary-Layer, and Wake Measurements and Comparisons With Wind-Tunnel Data. NASA TM X-3544, 1977.

13. Hurley, Francis X.; Spaid, Frank W.; Roos, Frederick W.; Stivers, Louis S., Jr.; and Bandettini, Angelo: Detailed Transonic Flow Field Measurements About a Supercritical Airfoil Section. NASA TM X-3244, 1975.

Parachute-riser housing

20.27

34.72

137.16

19.67

204.07

Keel
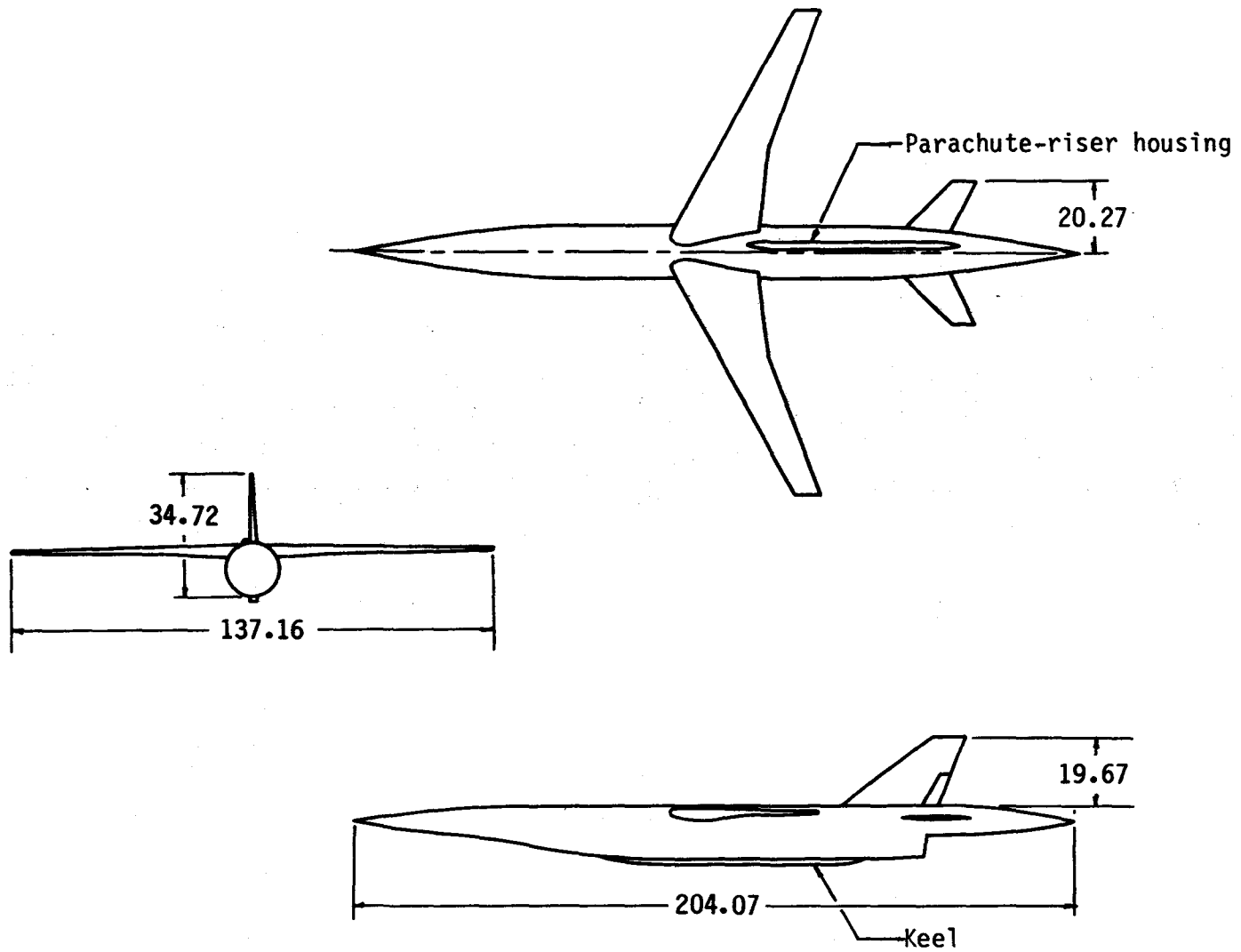
Figure 1.- Basic wind-tunnel model (configuration A).
(Dimensions are in centimeters.)
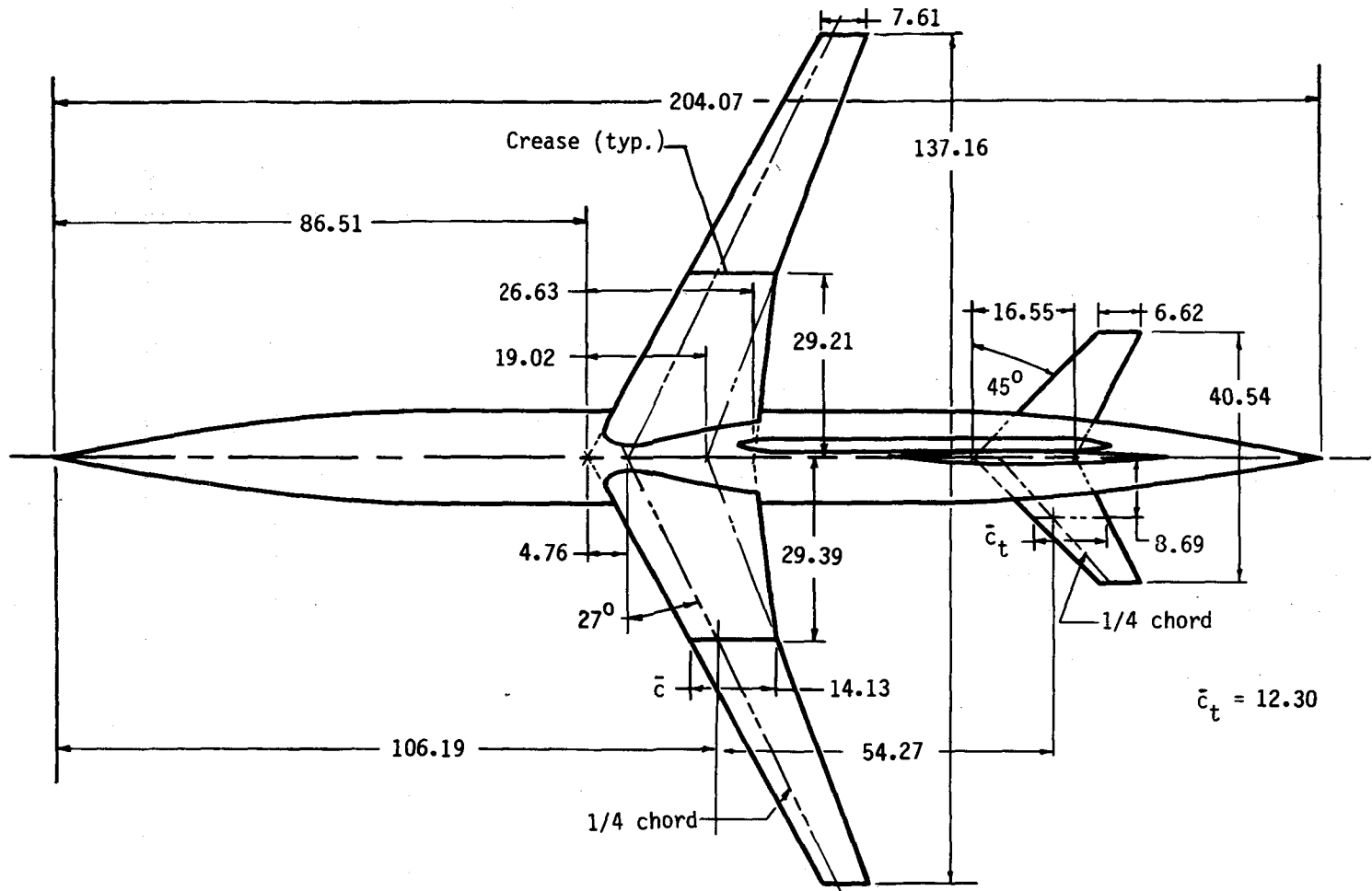
Figure 2.- Planform of wind-tunnel model. (Dimensions are in centimeters unless otherwise noted.)
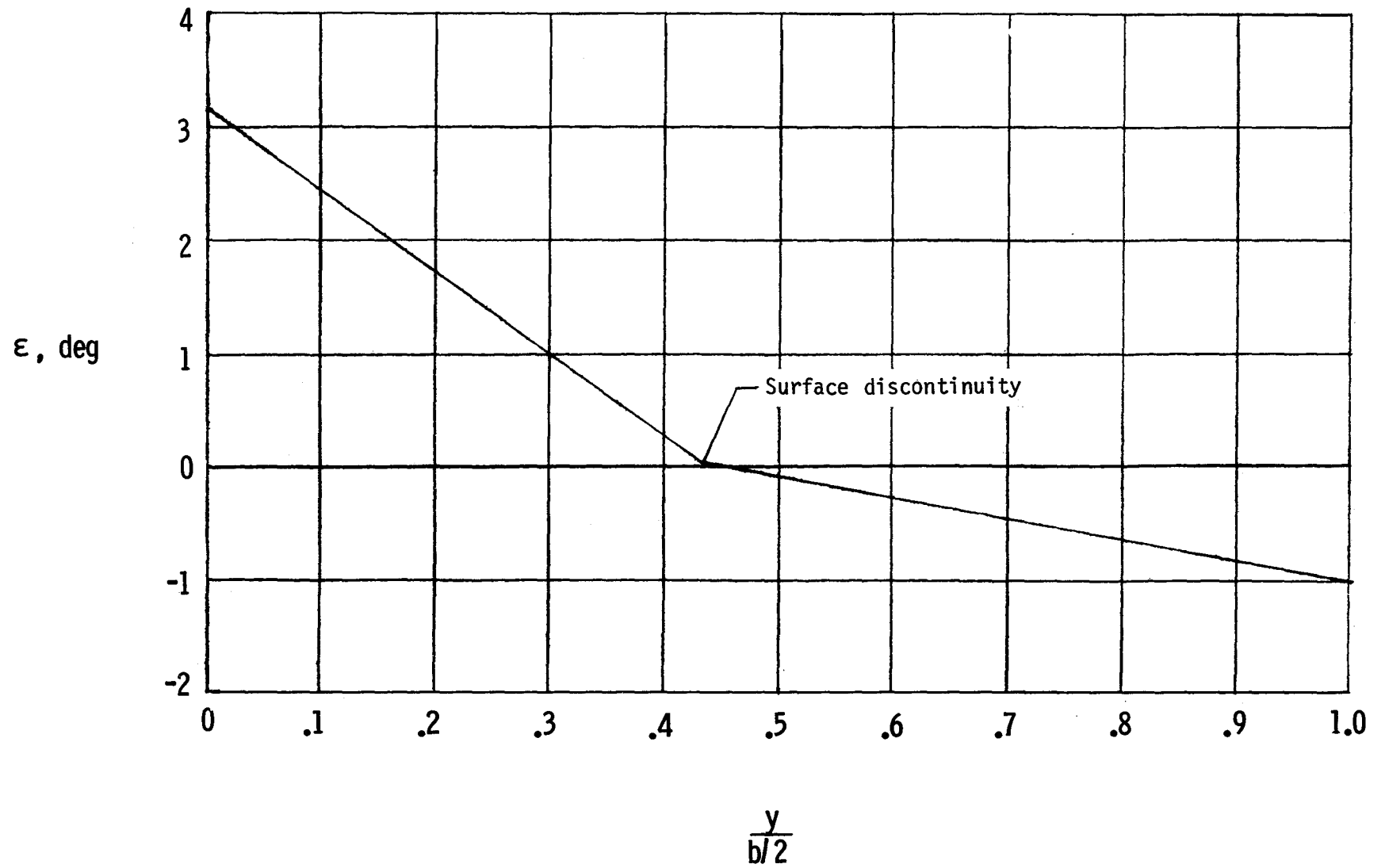
Figure 3.- Wing-section twist distribution relative to wing-section chord.
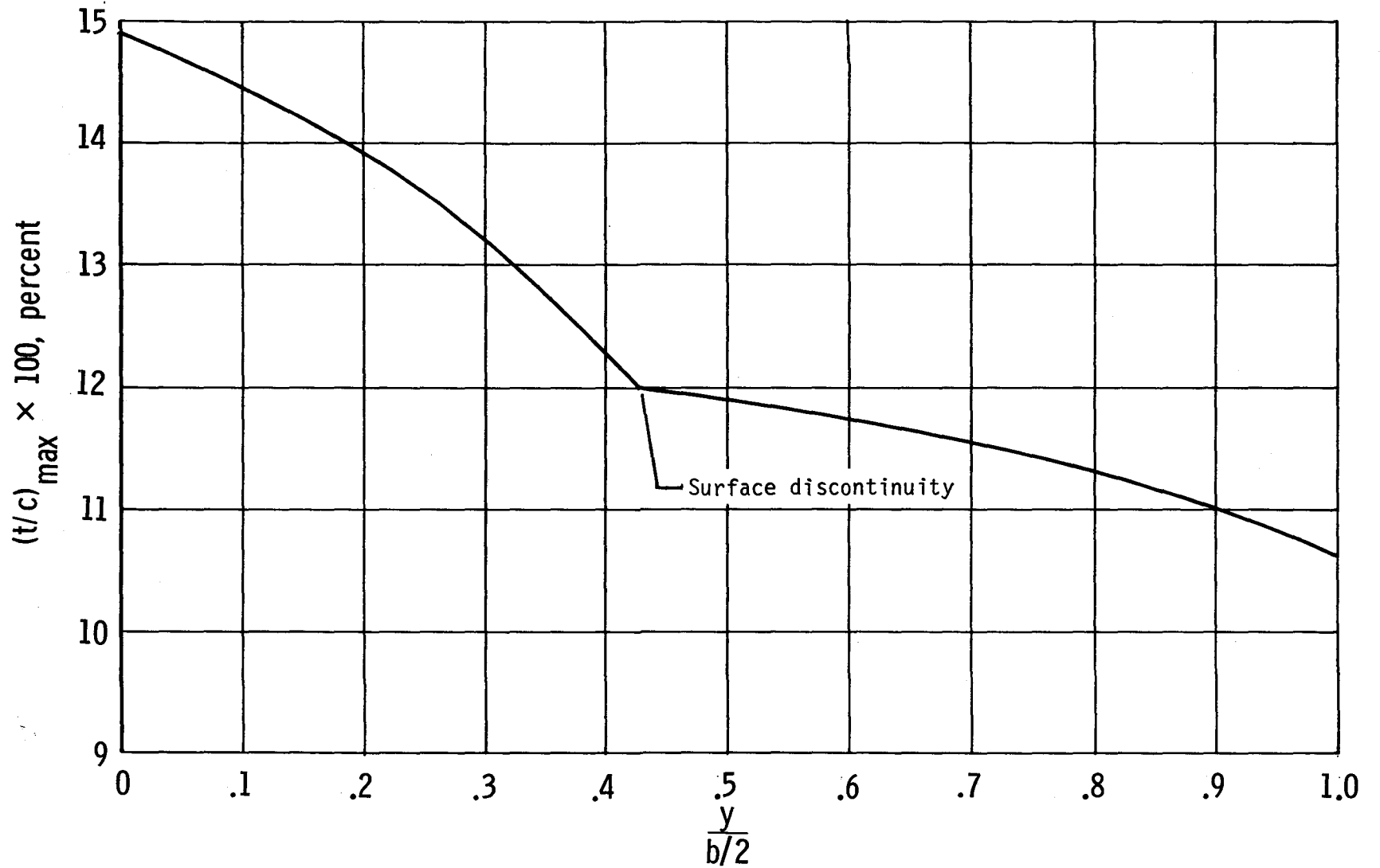
Figure 4.- Wing-section maximum thickness distribution.
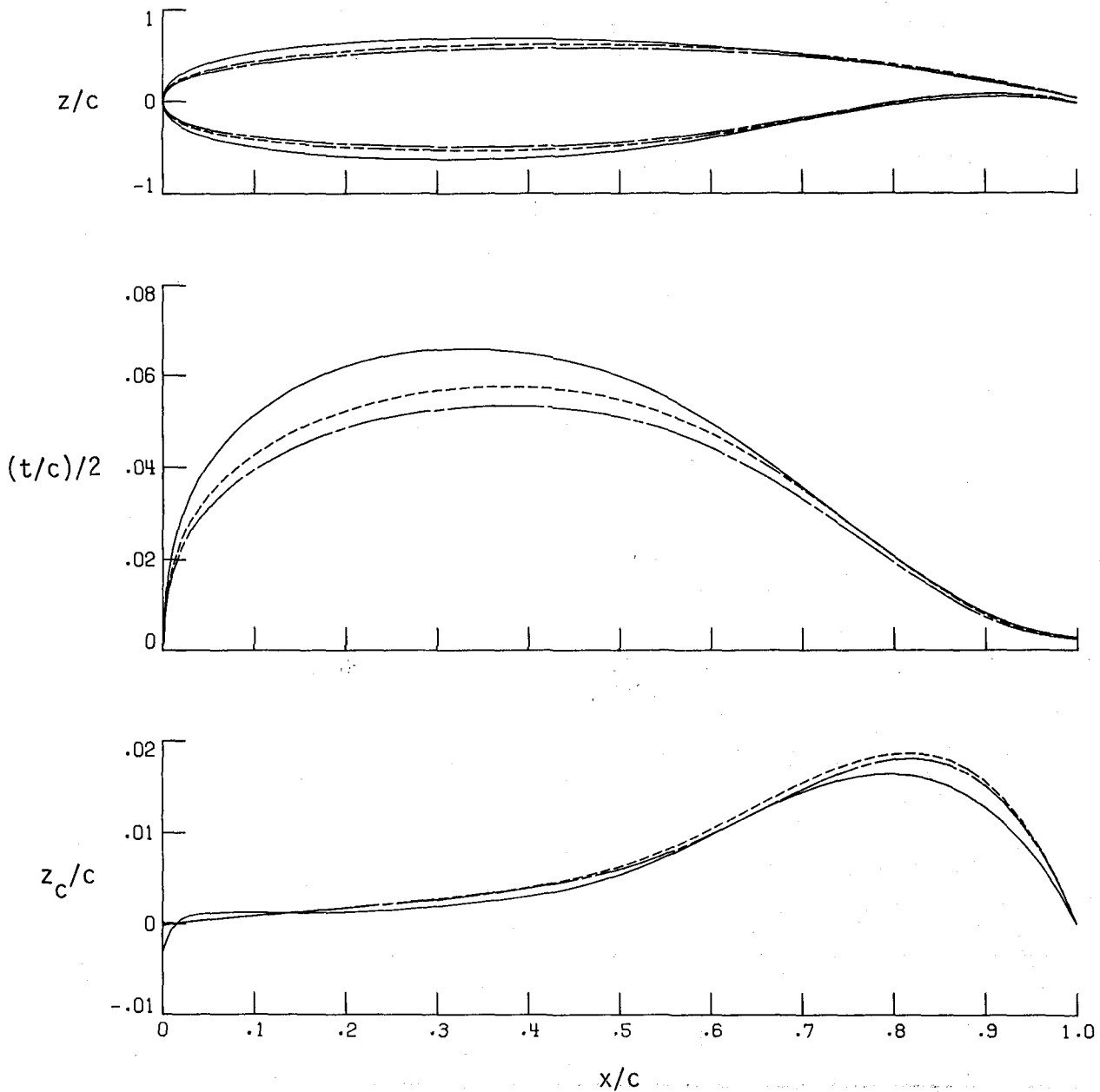
Figure 5.- Comparison of selected airfoil properties at three semispan stations with twist removed.
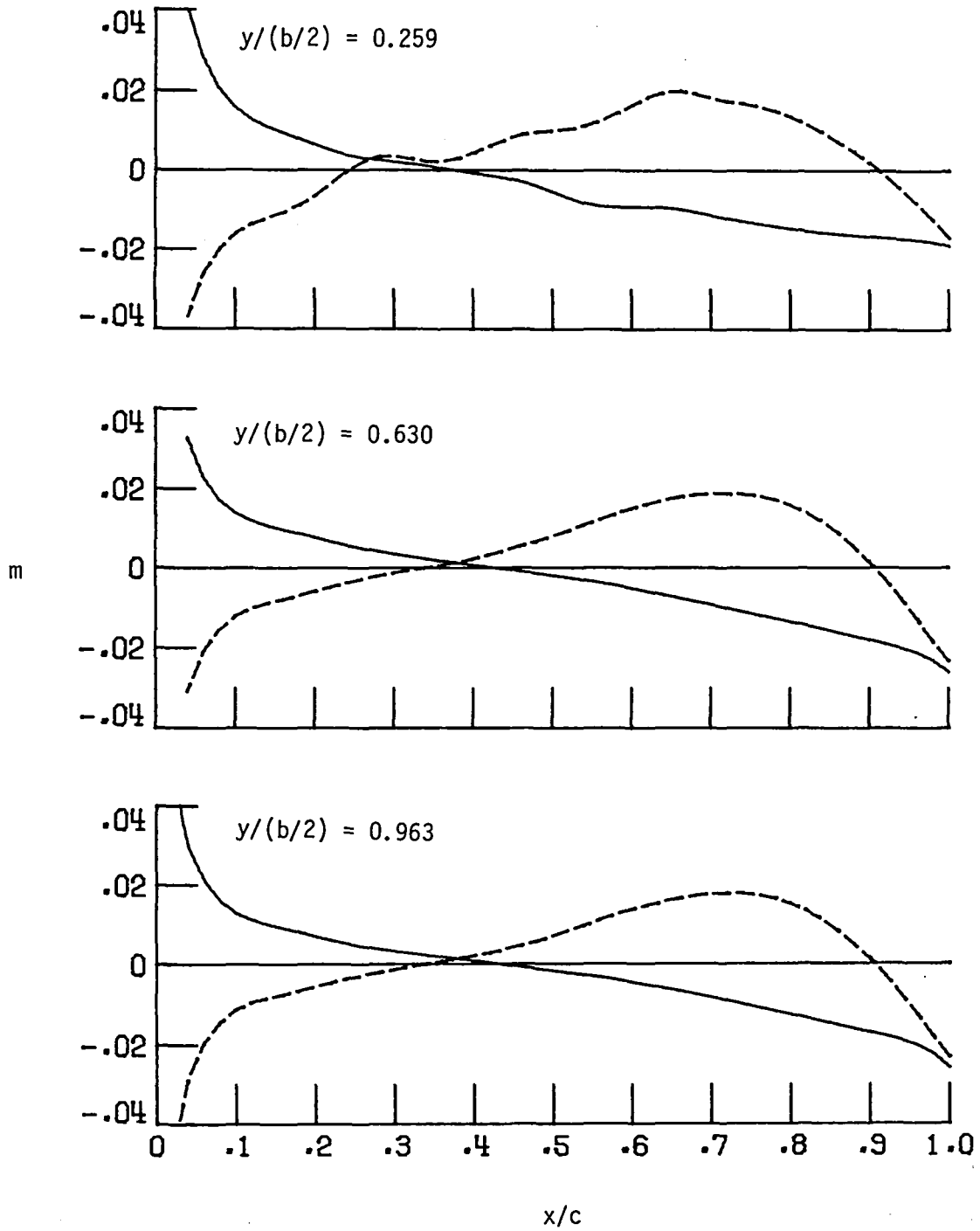
Figure 5.- Concluded.

| y, cm | 17.78 | 30.48 | 43.18 | 55.88 | 66.04 |
|---|---|---|---|---|---|
| y/(b/2) | 0.259 | 0.444 | 0.630 | 0.815 | 0.963 |
| c, cm | 16.09 | 13.97 | 11.85 | 9.74 | 8.04 |

28°48'

26.67

Fuselage

7.62

17.78

30.48

43.18

55.88

66.04

68.58
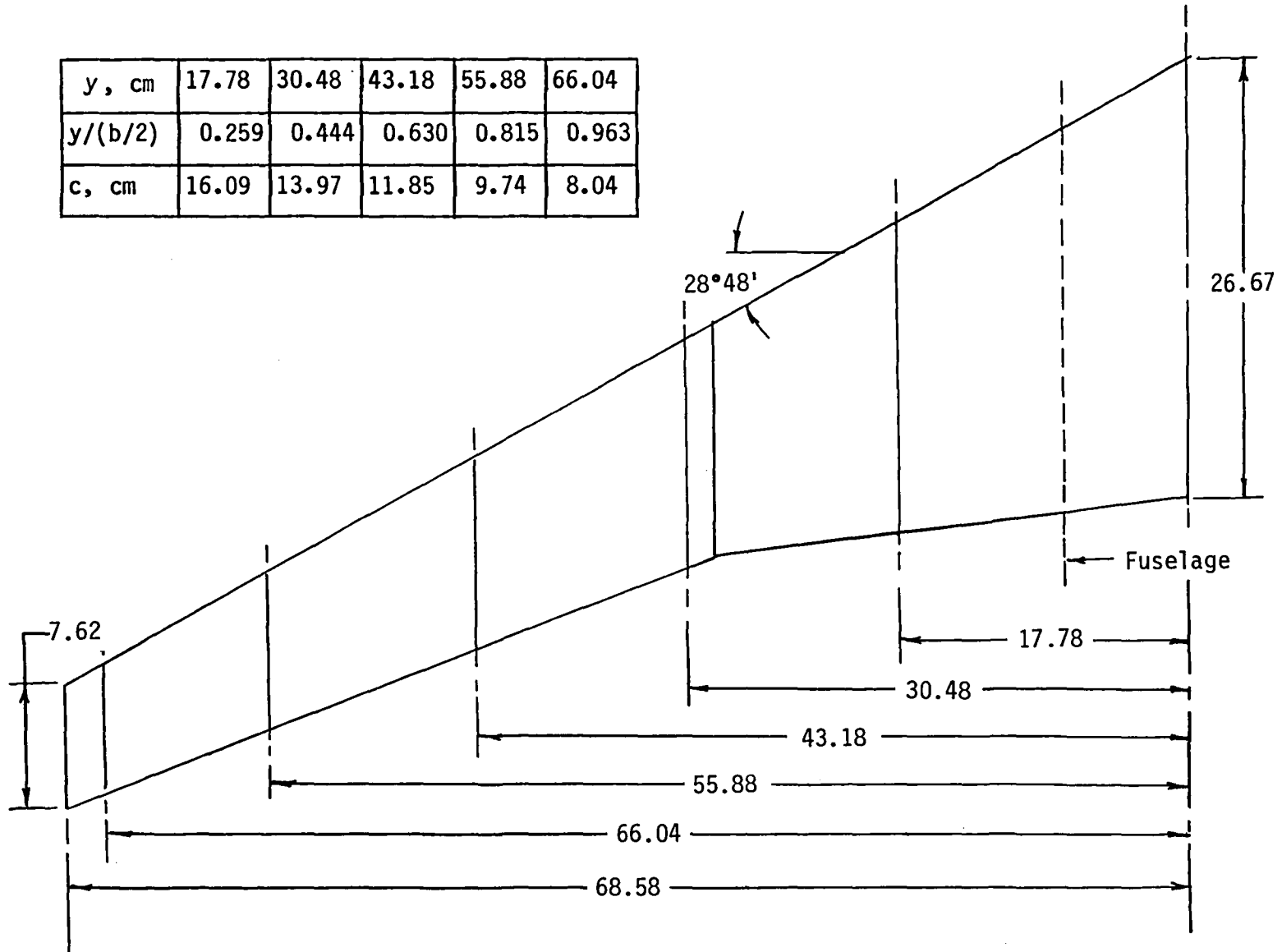
(a) Orifice spanwise locations.

Figure 6.- Location of pressure orifices on left wing panel. (Dimensions
are in centimeters unless otherwise noted.)

| Wing orifice location x/c at semispan station y/(b/2) of - | | | | |
|---|---|---|---|---|
| 0.259 | 0.444 | 0.630 | 0.815 | 0.963 |
| Left wing upper surface | | | | |
| 0.025 | 0.025 | 0.025 | 0.025 | 0.025 |
| .075 | .075 | .075 | .075 | .075 |
| .125* | .125 | .125 | .125 | .125 |
| .20 | .20 | .20 | .20 | .20 |
| .30 | .30 | .30 | .30 | .30 |
| .40 | .40 | .40 | .40 | .40 |
| .45 | .45 | .45 | .45 | .45 |
| .50 | .50 | .50 | .50 | .50 |
| .55 | .55 | .55 | .55 | .55 |
| .60 | .60 | .60 | .60 | .60 |
| .65 | .65 | .65 | .65 | .65 |
| .70 | .70 | .70 | .70 | .70 |
| .80 | .80 | .80 | .80 | .80 |
| .90 | .90 | .90* | .90 | .90 |
| 1.00* | 1.00* | 1.00* | 1.00* | 1.00* |
| Left wing lower surface | | | | |
| 0.025 | 0.025 | 0.025 | 0.025 | 0.025 |
| .075 | .075 | .075 | .075* | .075* |
| .125 | .125 | .125 | .125 | .125 |
| .20 | .20 | .20 | .20 | .20 |
| .30 | .30 | .30 | .30 | .30 |
| .40 | .40 | .40 | .40 | .40 |
| .50 | .50 | .50 | .50 | .50 |
| .60 | .60 | .60 | .60 | .60 |
| .70 | .70 | .70 | .70 | .70 |
| .80 | .80* | .80* | .80 | .80 |
| .90 | .90 | .90* | .90 | .90* |
| .975 | .975 | .975* | .975 | .975* |

*Inactive pressure orifices.

(b) Orifice chordwise locations.

Figure 6.- Concluded.

M.S. 0.33                                                  M.S. 0.94

Model contour

Inlet duct

Inlet plow

Keel
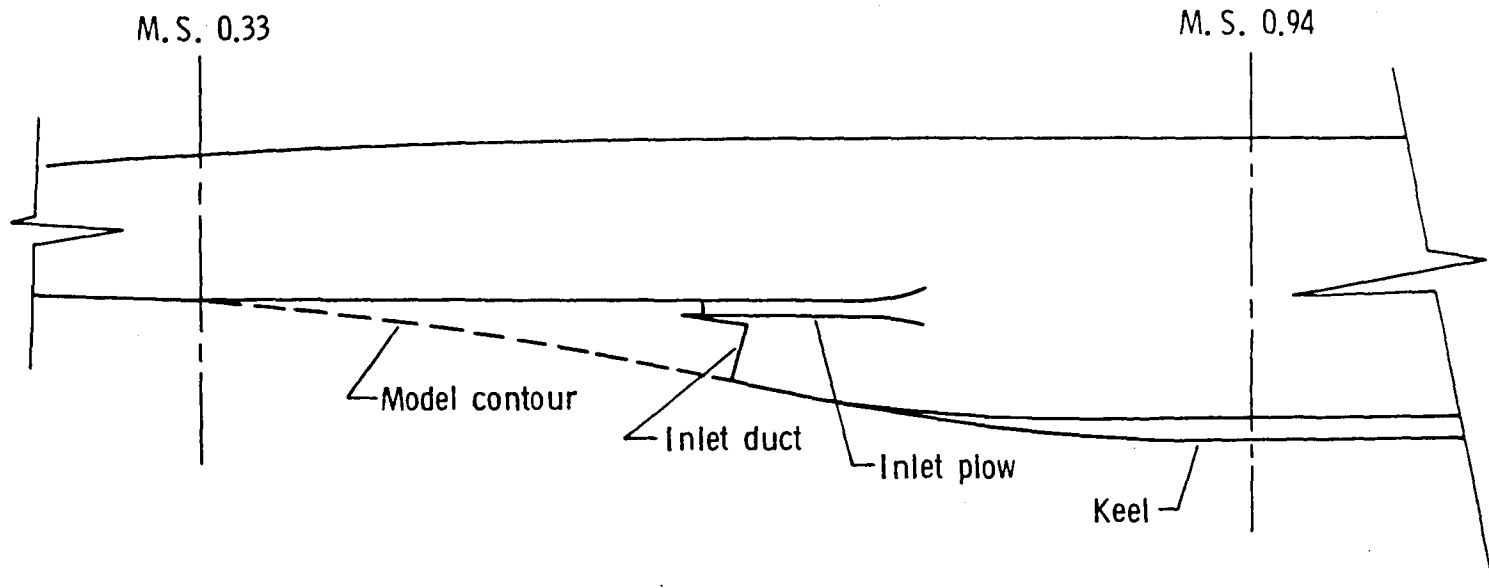
Figure 7.- Engine air-inlet elevation.
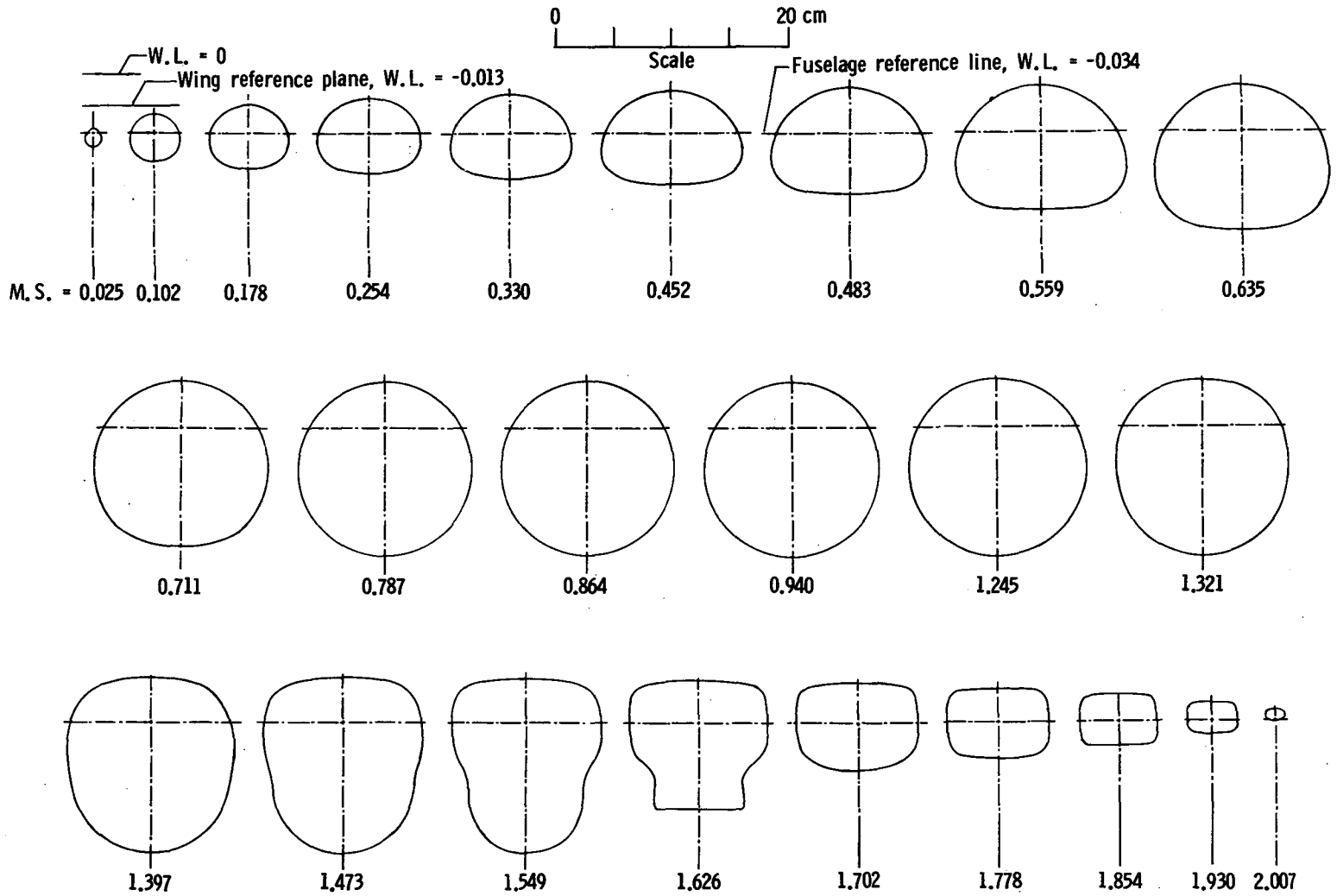
Figure 8.- Cross-sectional views of fuselage geometry.

R = 7.53

R = 1.81

R = 1.81

6.90

8.79

SECTION A-A

A

A

R = 8.43

R = 8.43

M. S.
69.23

M. S.
90.90

M. S.
110.76

M. S.
124.61

R = 4.39

R = 4.93

R = .60

.73
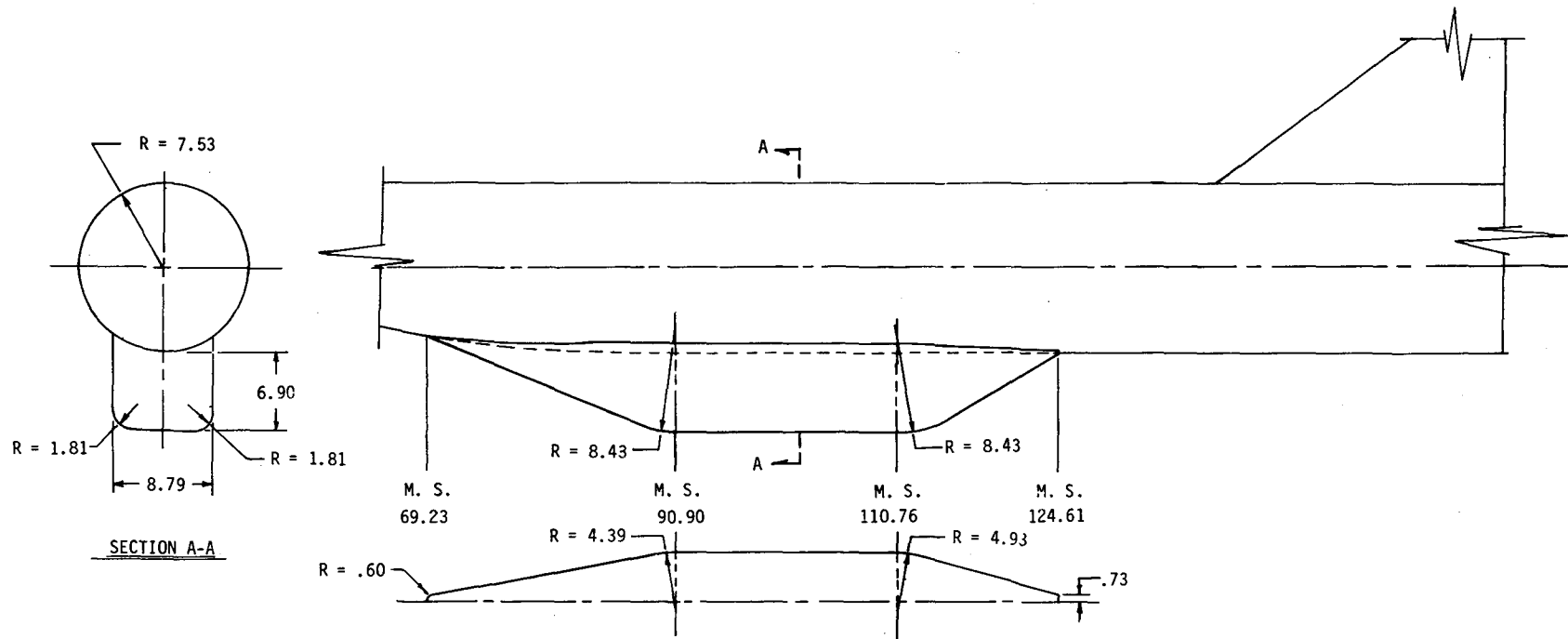
Figure 9.- Sketch of pod design for model configuration B.  (Dimensions are in centimeters.)
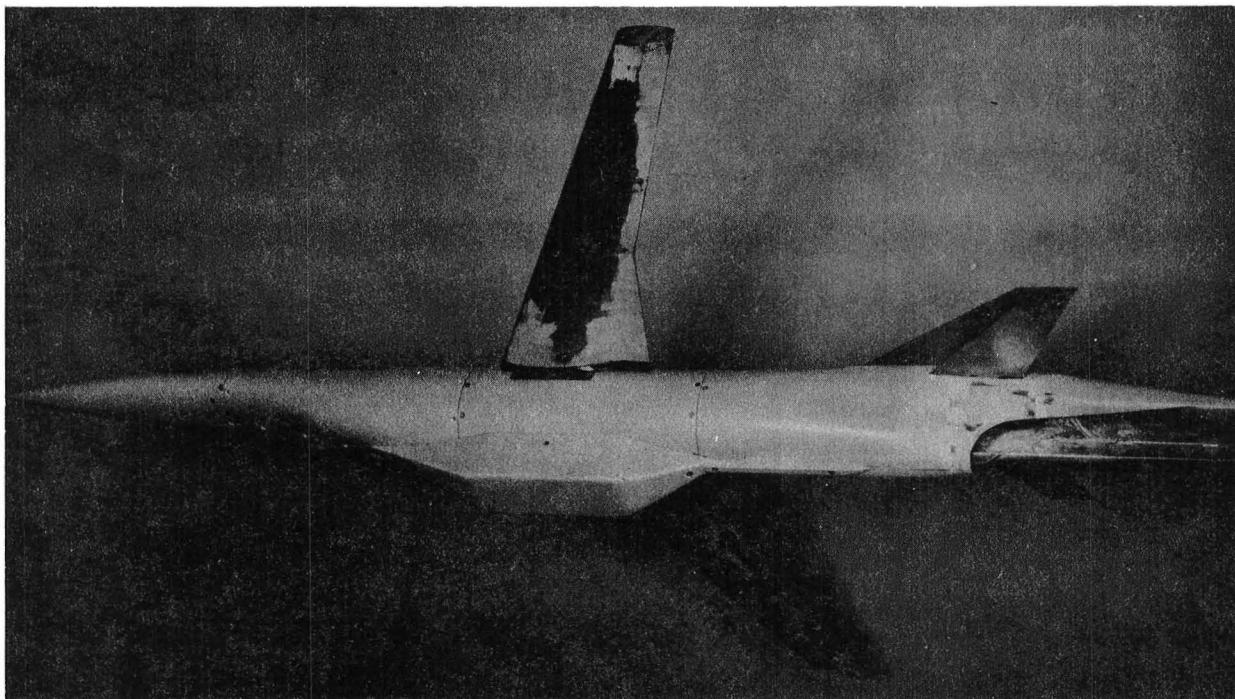
L-77-7242
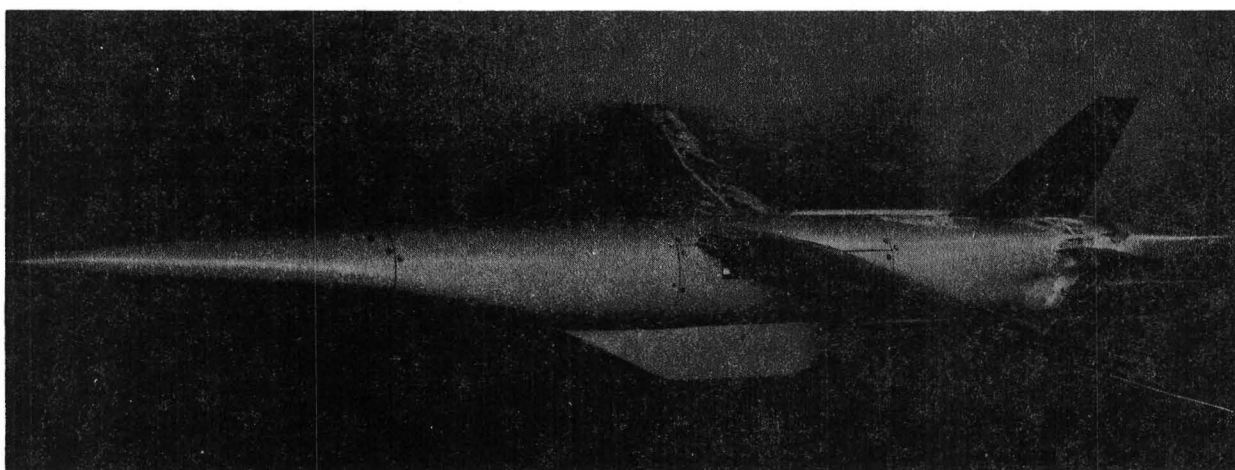


L-77-7241

Figure 10.- Photographs of model configuration B.
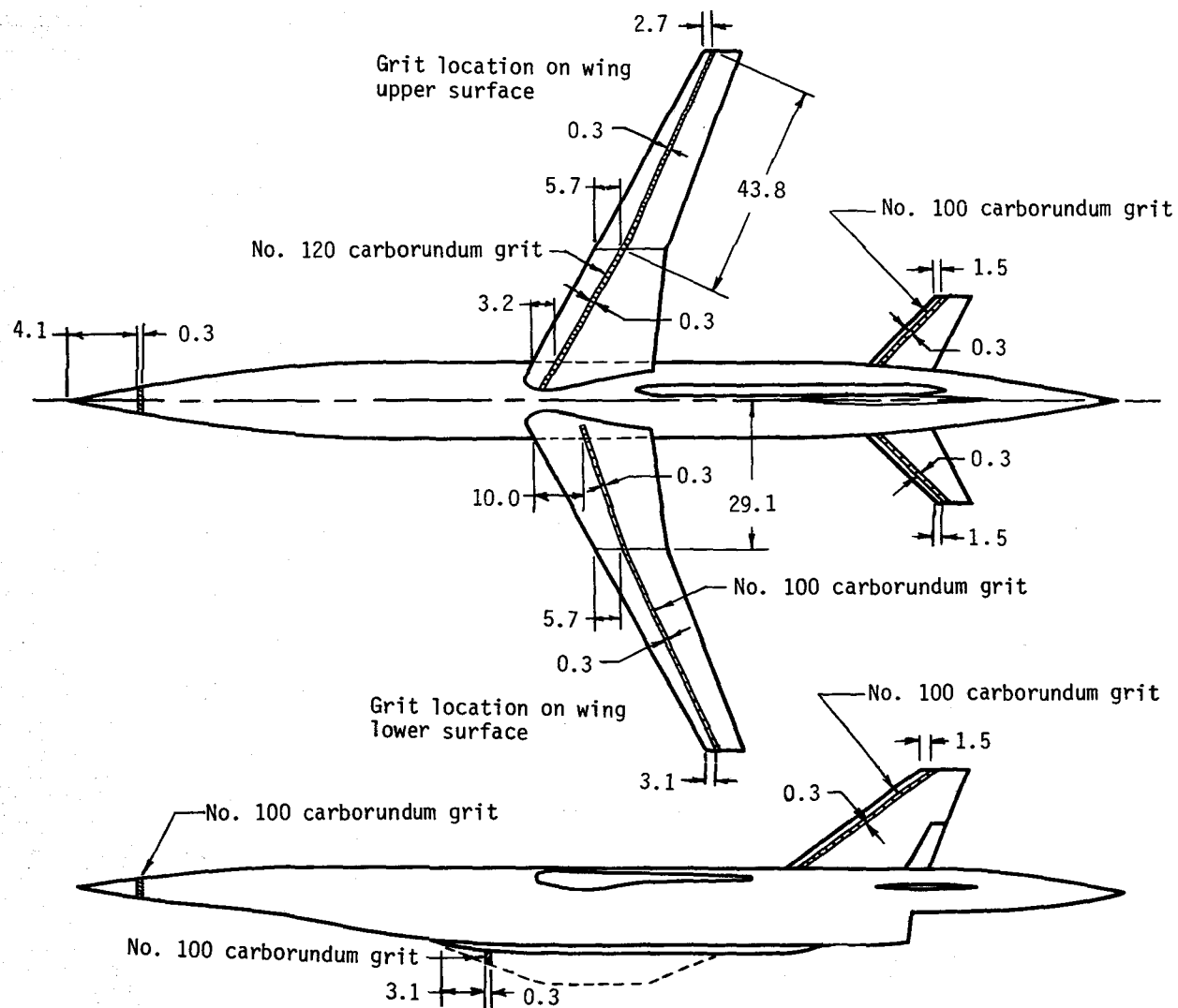
Figure 11.- Model carborundum grit size and location. (Dimensions are in centimeters.)

$$\alpha = -4.1^{o}$$
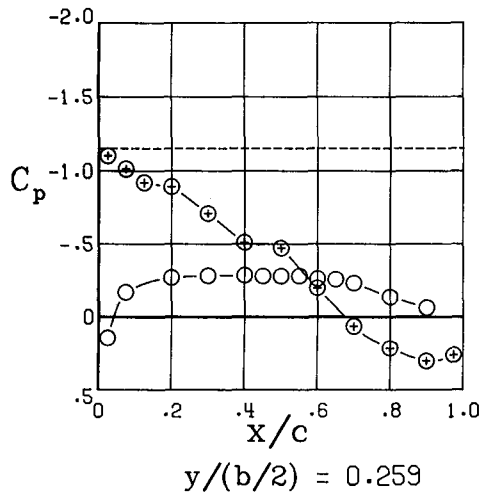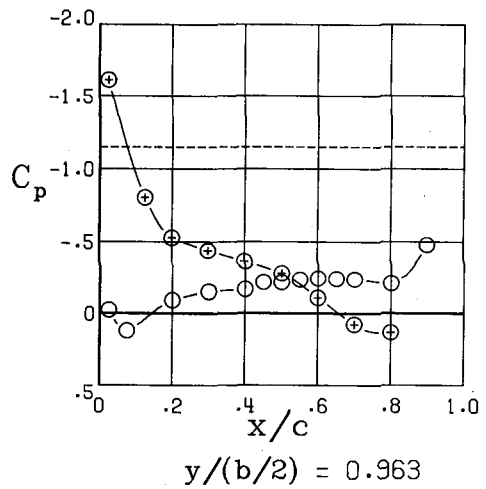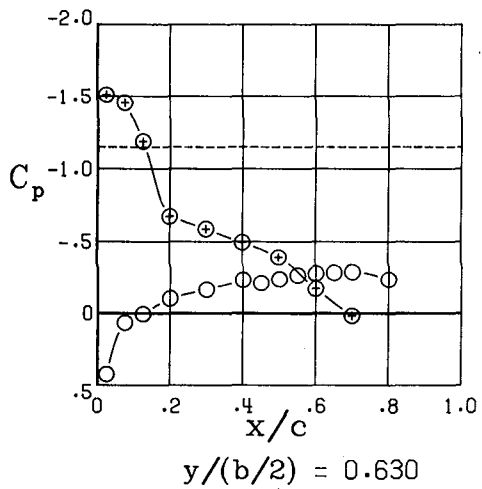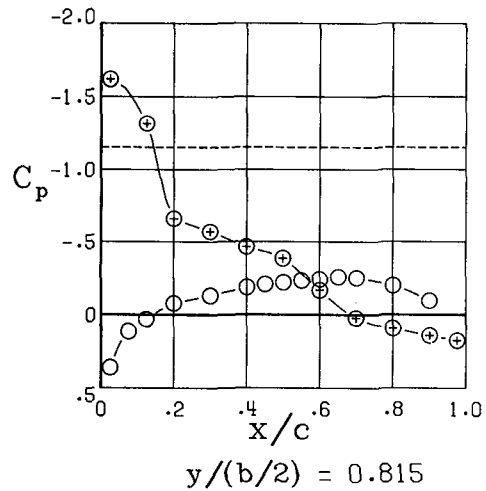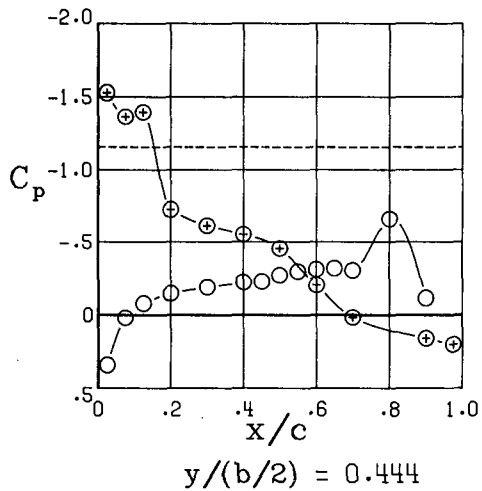
(a)  M = 0.70.

Figure 12.- Wing pressure distributions for model configuration A.
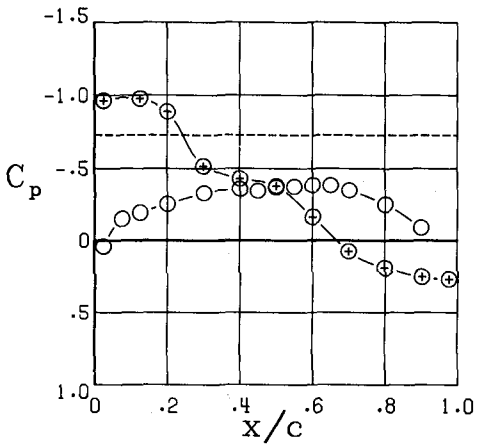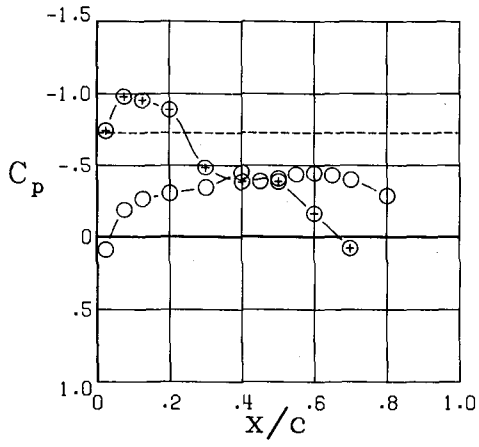
$$y/(b/2) = 0.259$$
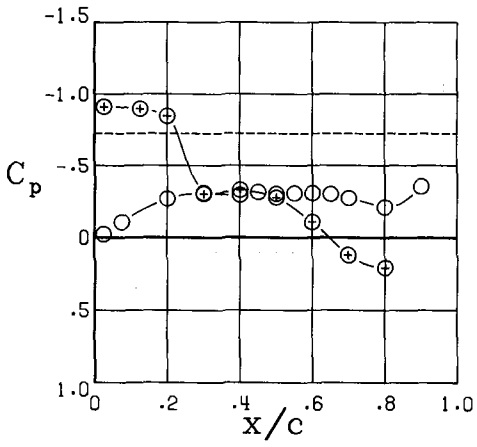
○ Upper surface
⊕ Lower surface
------ $C_{p,sonic}$

$$y/(b/2) = 0.444$$

$$y/(b/2) = 0.815$$

$$y/(b/2) = 0.630$$

$$y/(b/2) = 0.963$$
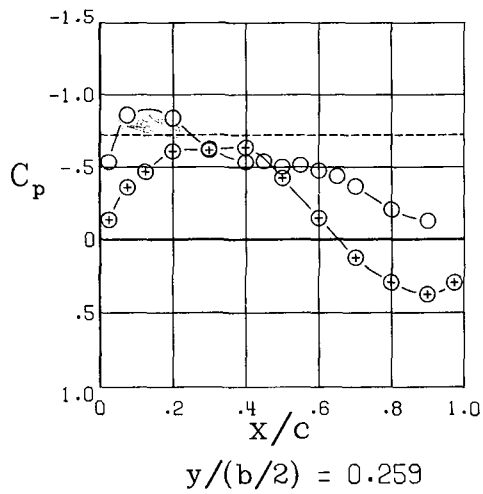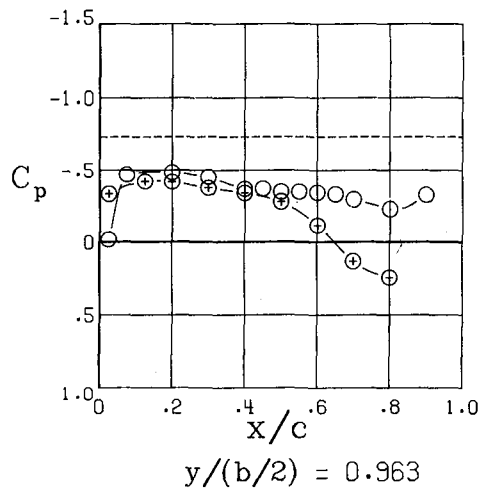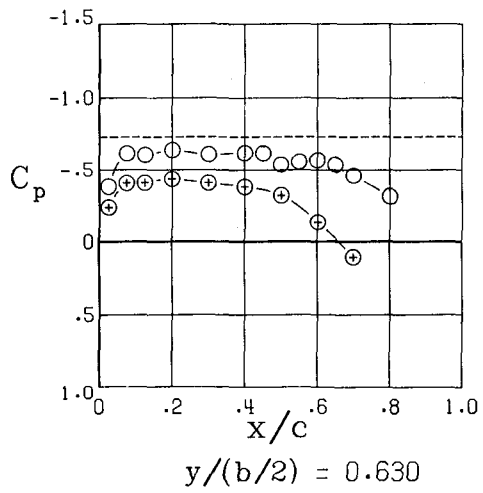
$$\alpha = -2.1^{o}$$

(a) Continued.

Figure 12.- Continued.

Legend:
- ○ Upper surface
- ⊕ Lower surface
- ------ $C_{p,sonic}$

$y/(b/2) = 0.259$

$y/(b/2) = 0.444$

$y/(b/2) = 0.815$

$y/(b/2) = 0.630$

$y/(b/2) = 0.963$
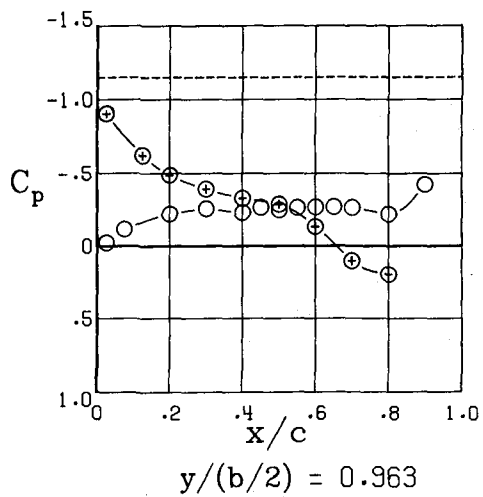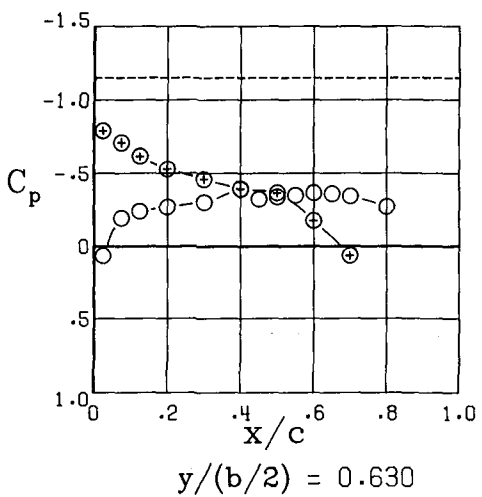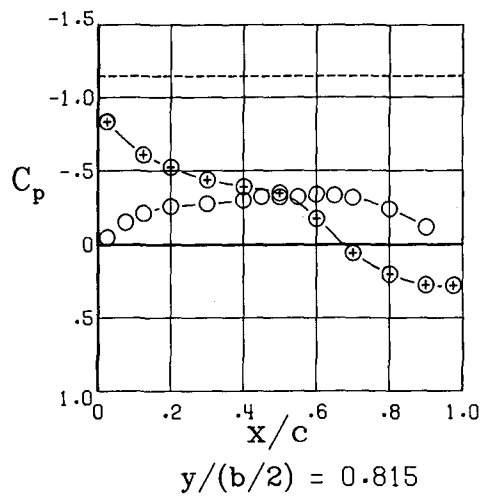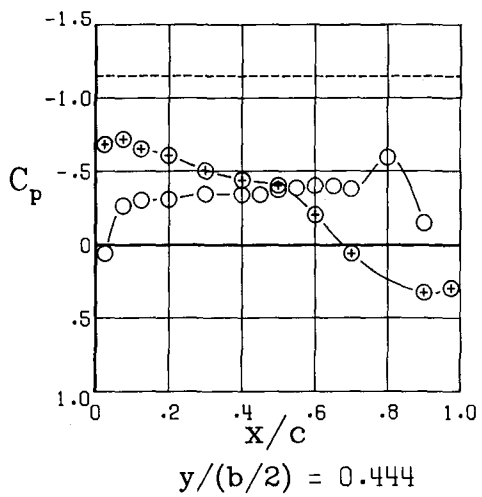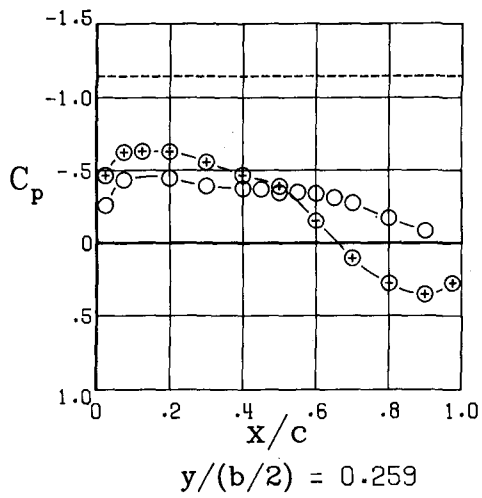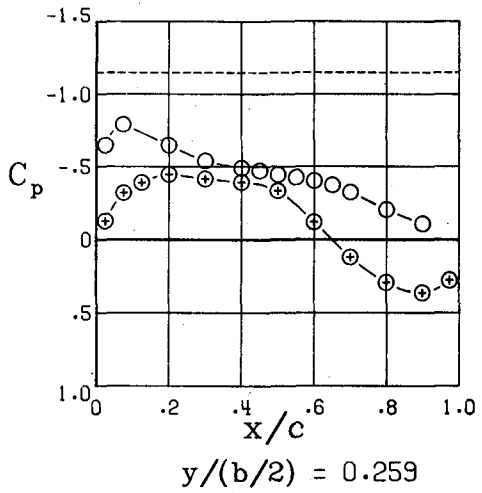
$\alpha = -0.1^{\circ}$

(a) Continued.

Figure 12.- Continued.

$y/(b/2) = 0.259$

$y/(b/2) = 0.444$

$y/(b/2) = 0.815$

$y/(b/2) = 0.630$

$y/(b/2) = 0.963$

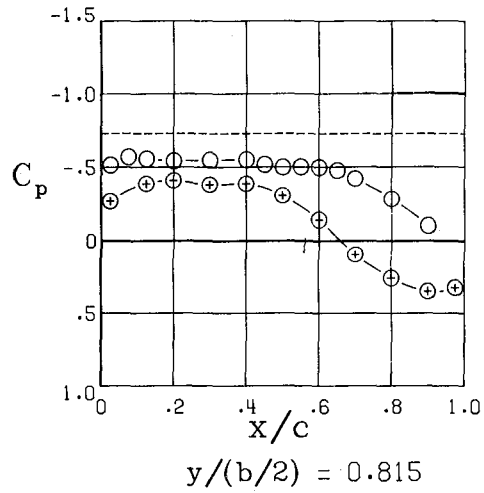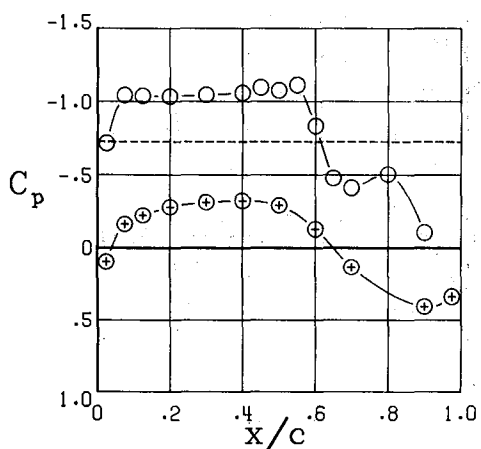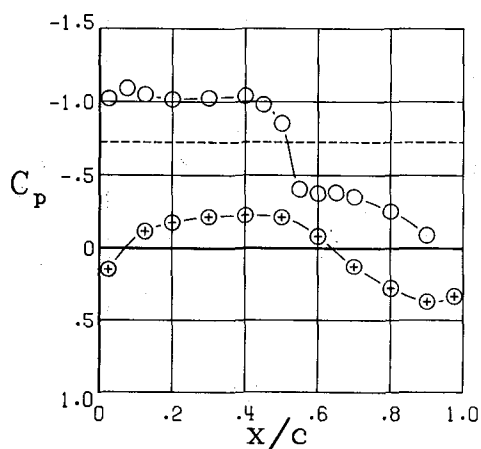$\alpha = 1.9^O$

(a) Continued.

Figure 12.- Continued.

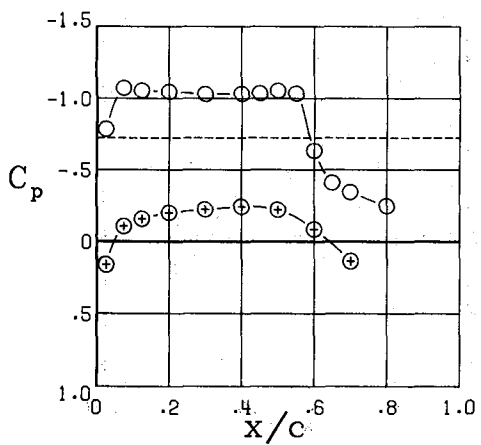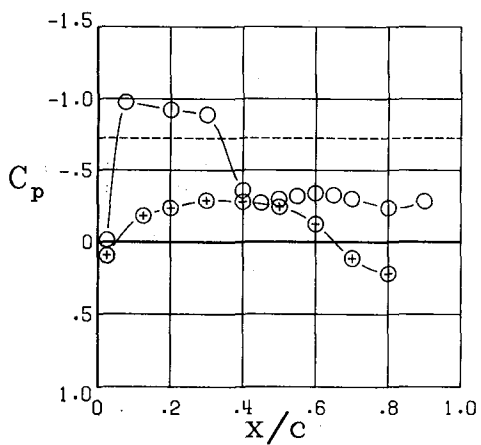O   Upper surface
⊕   Lower surface
-----   $C_{p,sonic}$

$y/(b/2) = 0.259$

$y/(b/2) = 0.444$

$y/(b/2) = 0.815$

$y/(b/2) = 0.630$

$y/(b/2) = 0.963$

$\alpha = 4.0^0$

(a) Concluded.

Figure 12.- Continued.

$\alpha = -4.1^{o}$
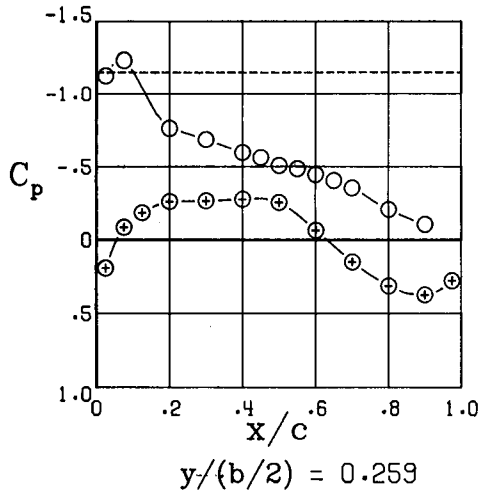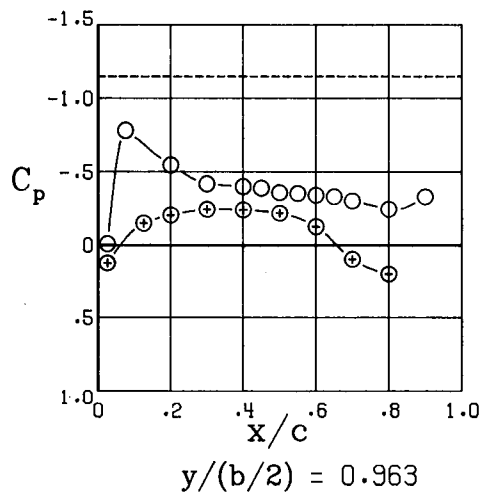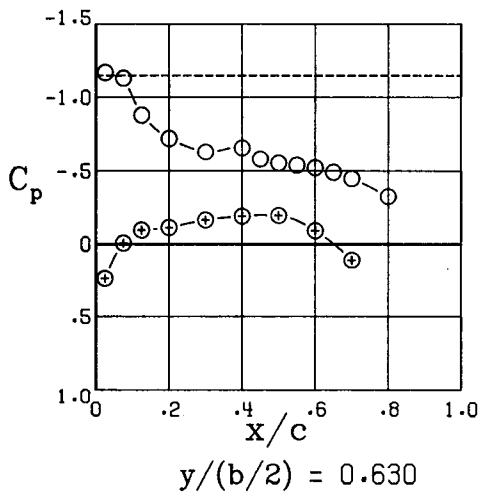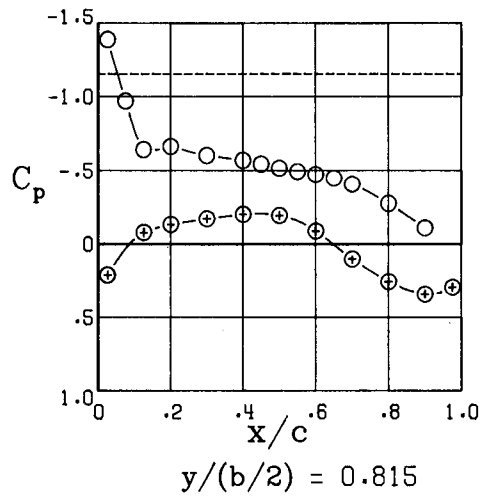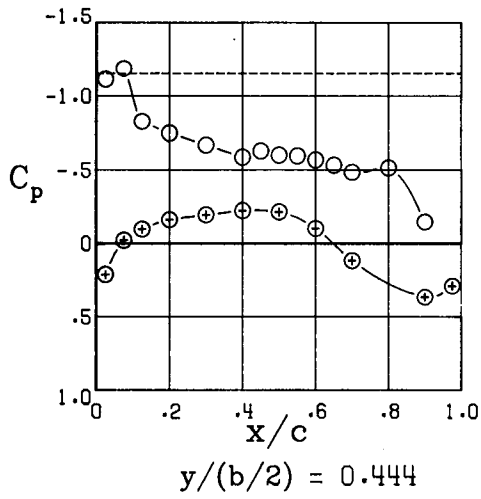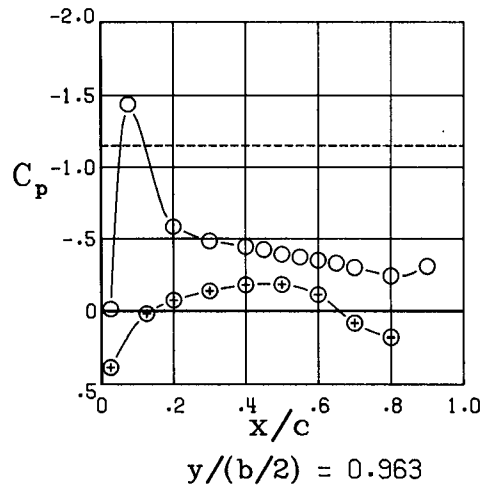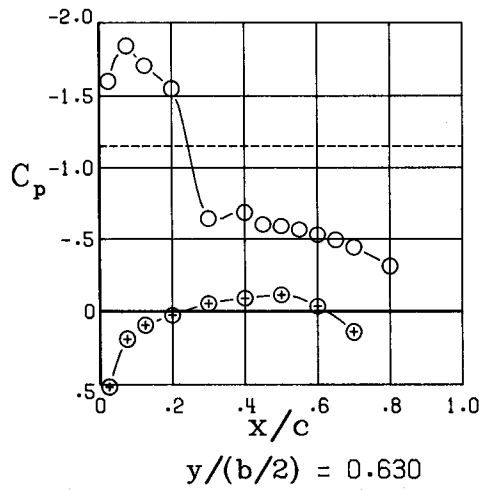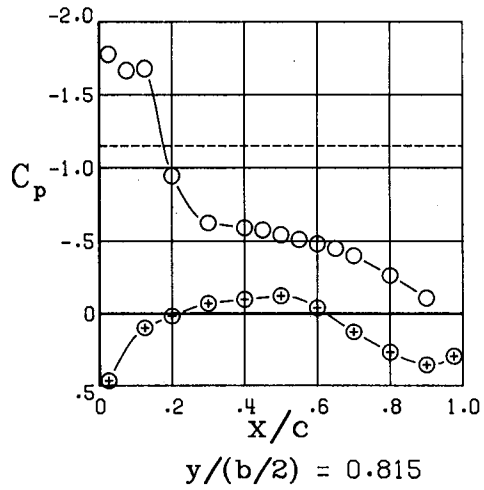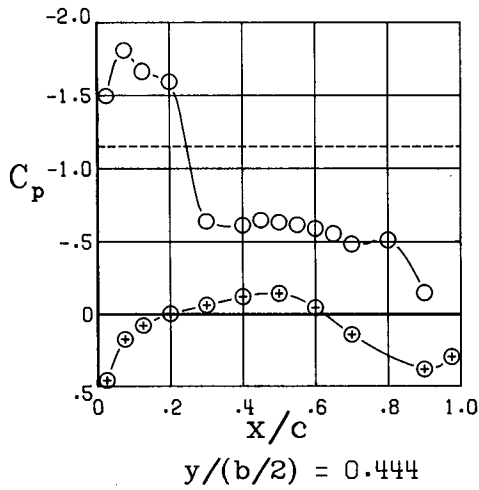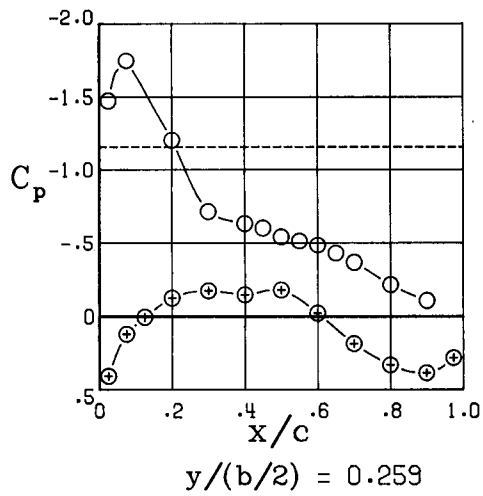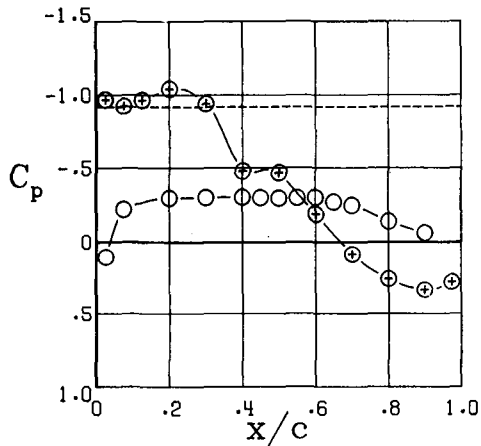
(b)  M = 0.75.

Figure 12.- Continued.

$\circ$   Upper surface
$\oplus$   Lower surface
-----   $C_{p,sonic}$

$y/(b/2) = 0.259$

$y/(b/2) = 0.444$
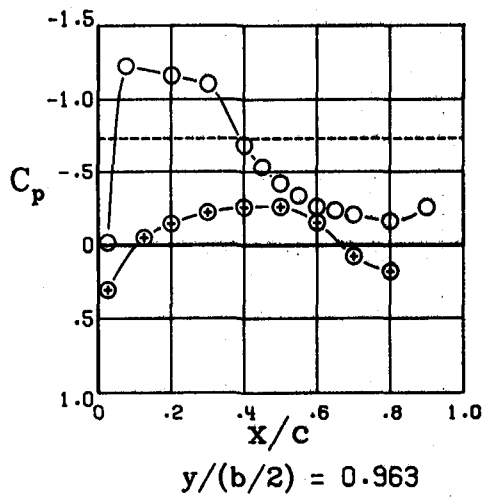
$y/(b/2) = 0.815$

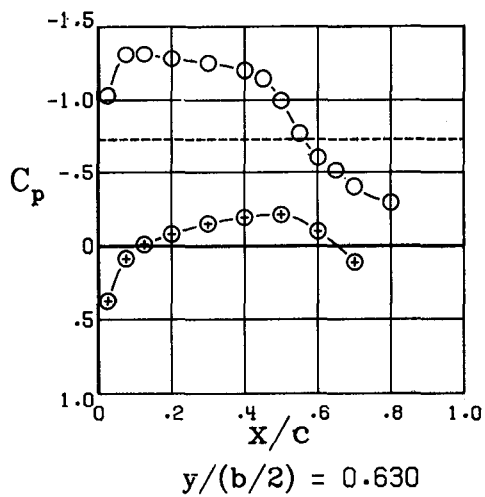$y/(b/2) = 0.630$

$y/(b/2) = 0.963$

$\alpha = -2.1^{\circ}$

(b) Continued.

Figure 12.- Continued.

O  Upper surface
⊕  Lower surface
------  $C_{p,sonic}$

$y/(b/2) = 0.259$

$y/(b/2) = 0.444$
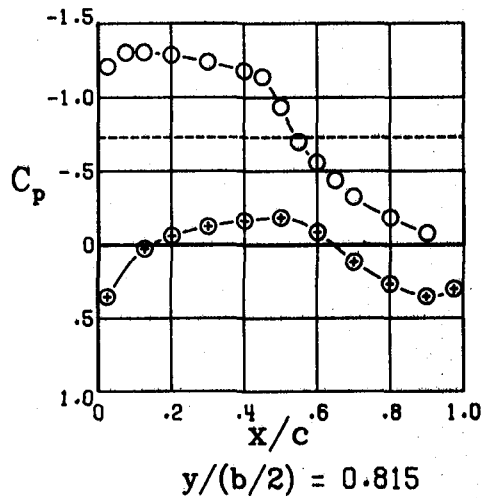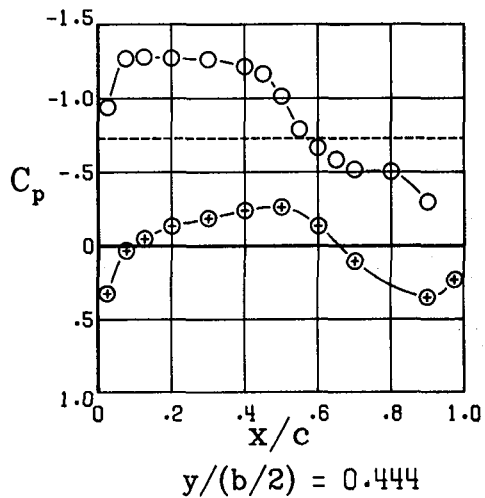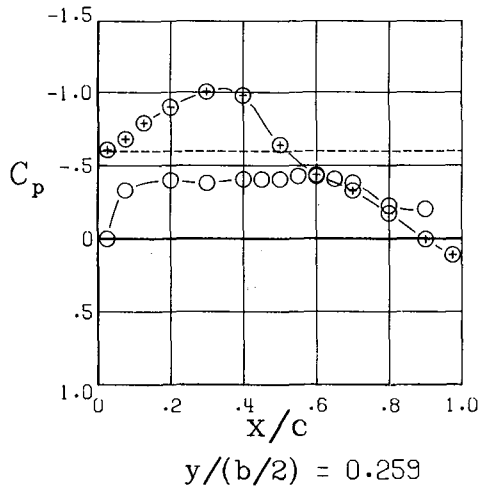
$y/(b/2) = 0.815$

$y/(b/2) = 0.630$

$y/(b/2) = 0.963$

$\alpha = -0.1^{o}$

(b) Continued.

Figure 12.- Continued.

$$\alpha = 2.0^{o}$$

(b) Continued.

Figure 12.- Continued.
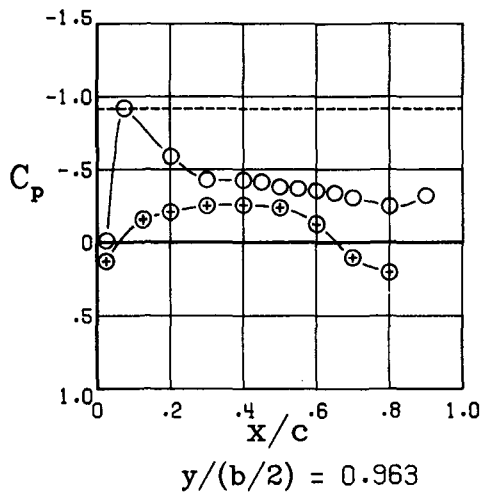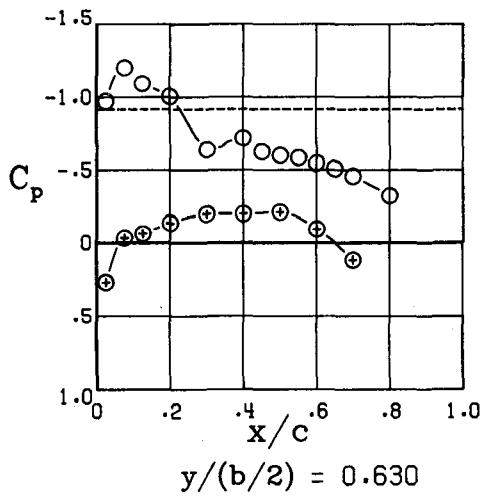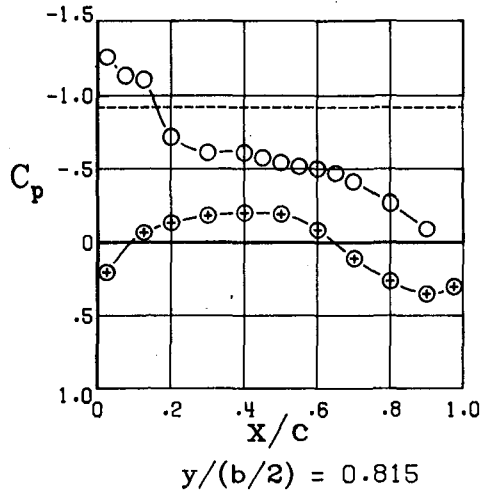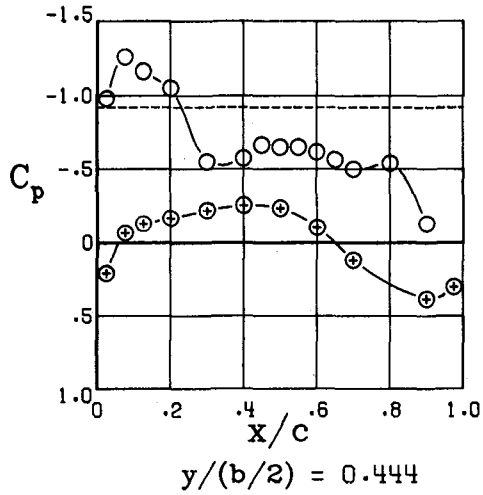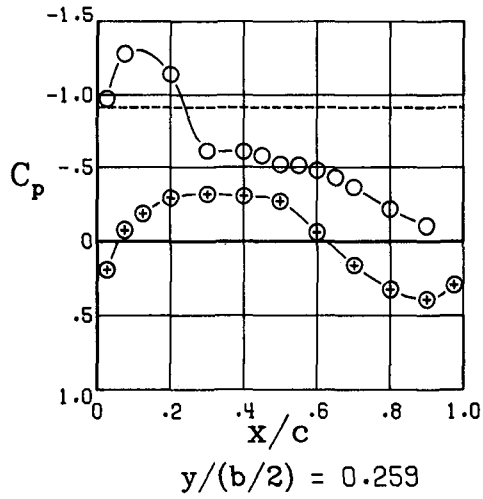
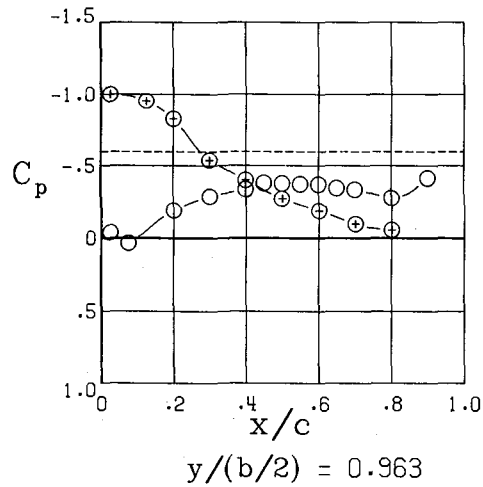y/(b/2) = 0.259

y/(b/2) = 0.444

y/(b/2) = 0.815
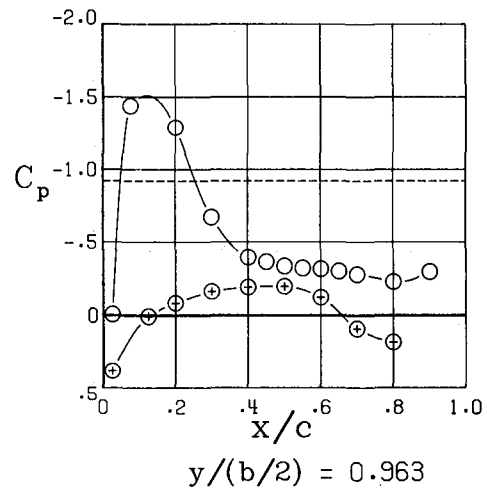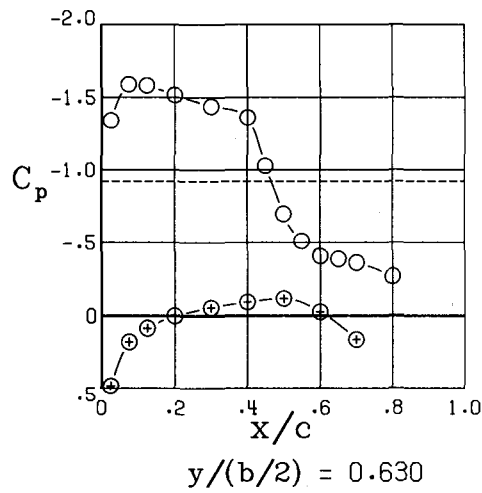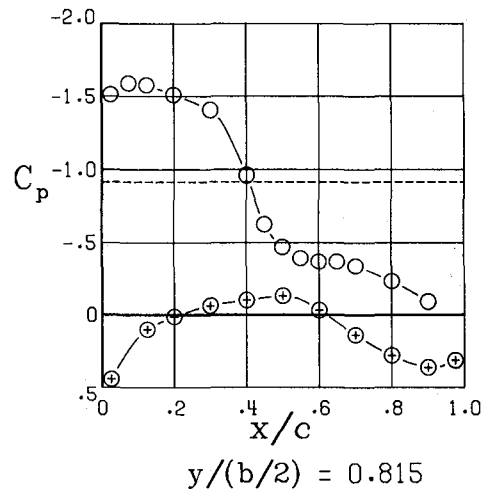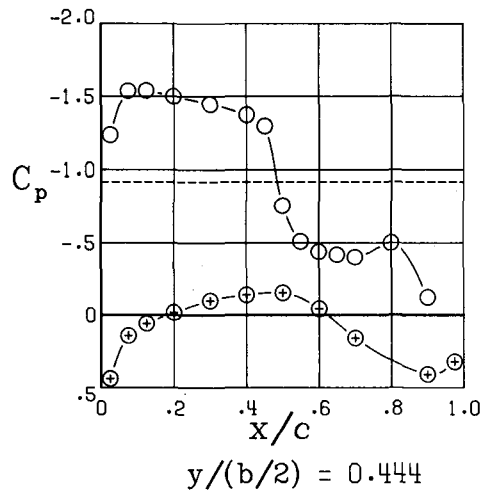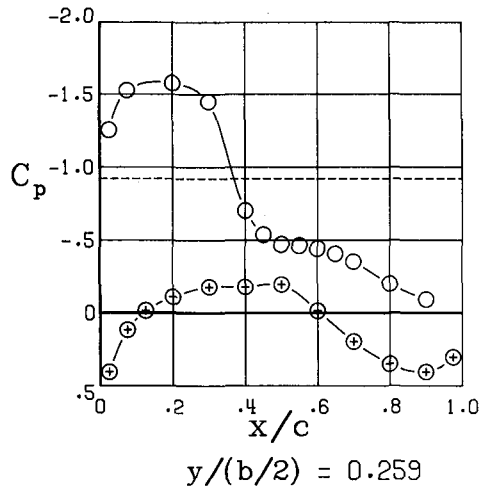
y/(b/2) = 0.630

y/(b/2) = 0.963

$\alpha = 4.0^0$

(b) Concluded.
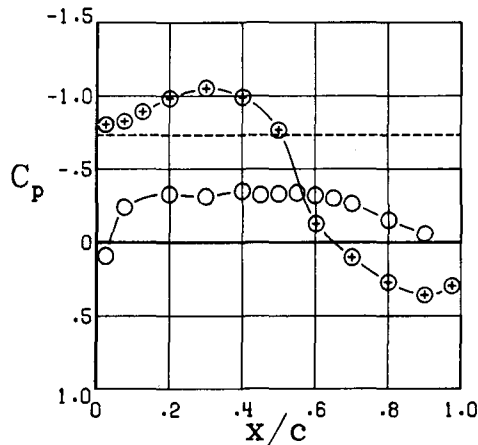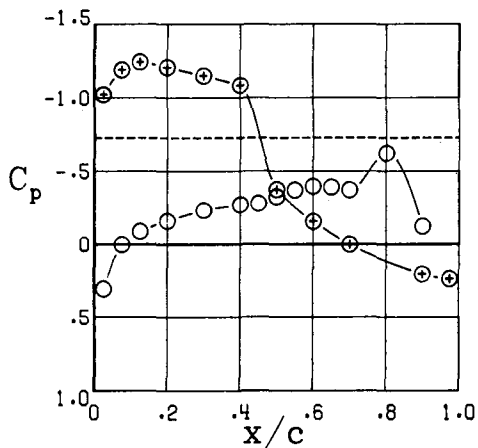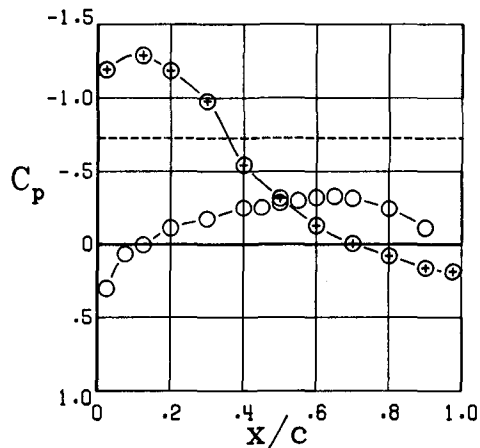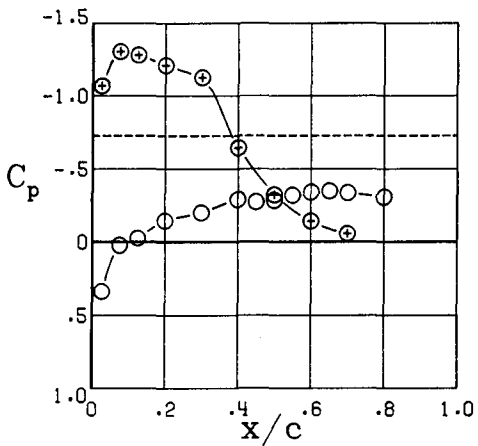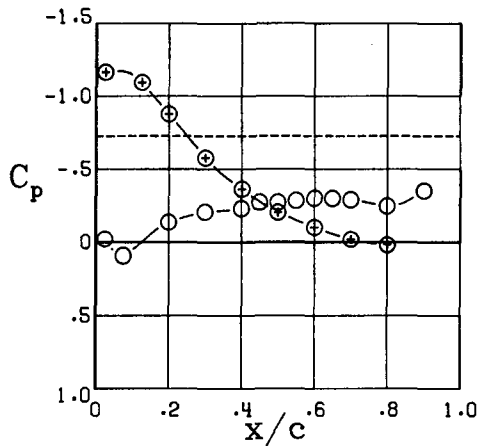
Figure 12.- Continued.

$\alpha = -4.1^\circ$

(c)   M = 0.80.

Figure 12.- Continued.

O    Upper surface
⊕    Lower surface
-----    $C_{p,sonic}$

$y/(b/2) = 0.259$

$y/(b/2) = 0.444$

$y/(b/2) = 0.815$

$y/(b/2) = 0.630$

$y/(b/2) = 0.963$

$\alpha = -2.1^{o}$

(c) Continued.

Figure 12.- Continued.

O  Upper surface
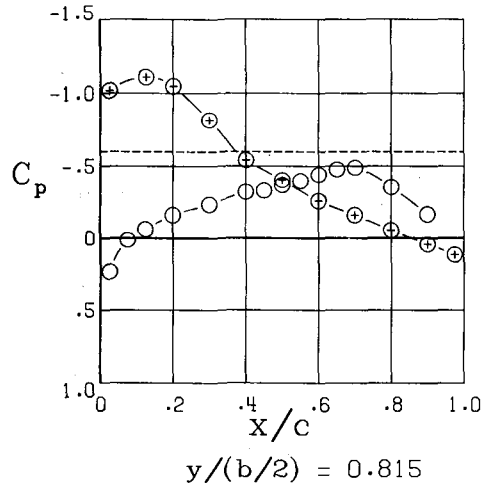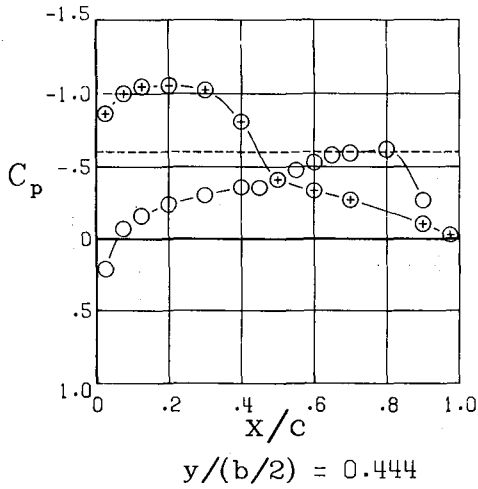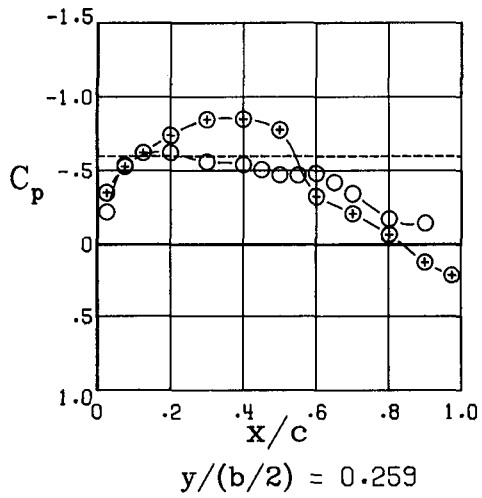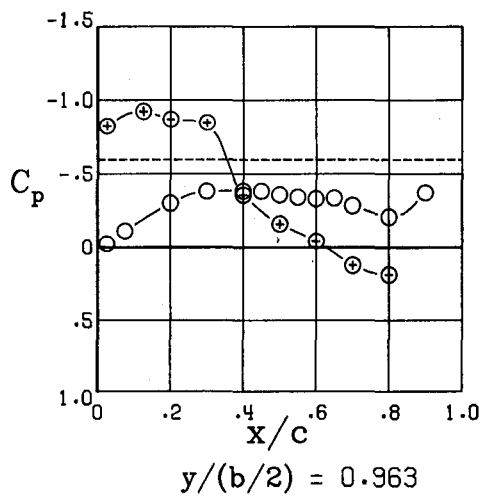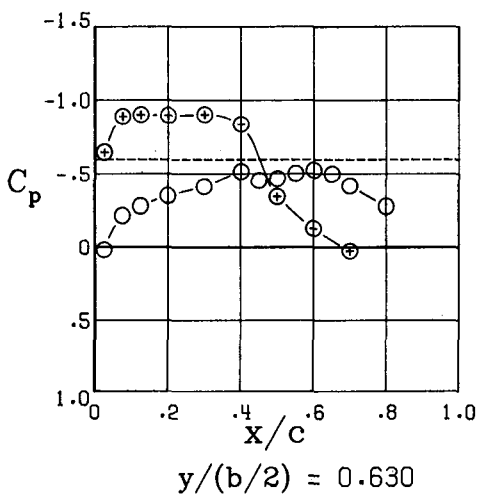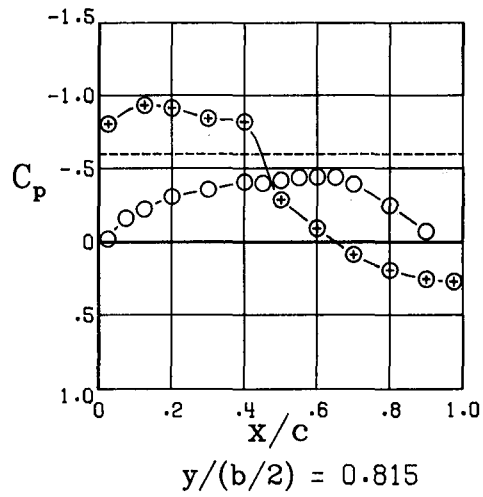⊕  Lower surface
------  $C_{p,sonic}$

$y/(b/2) = 0.259$

$y/(b/2) = 0.444$

$y/(b/2) = 0.815$

$y/(b/2) = 0.630$

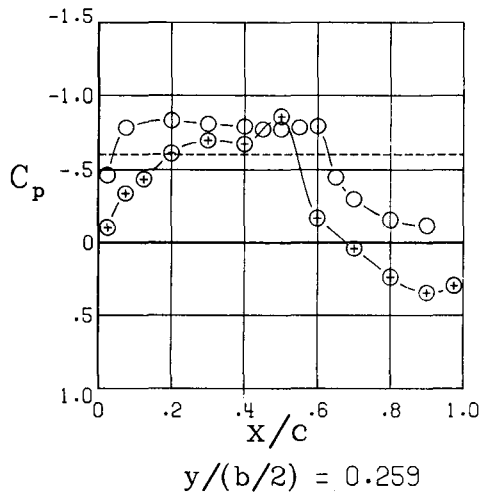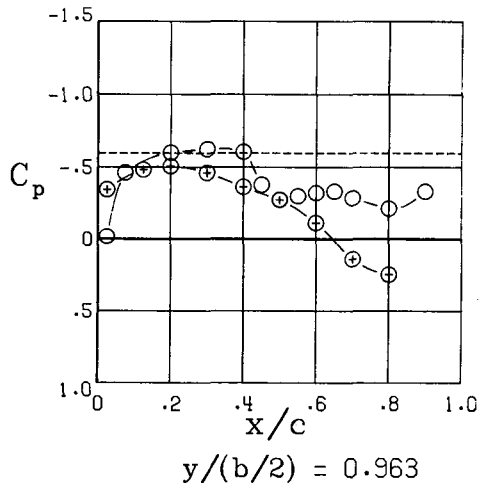$y/(b/2) = 0.963$

$\alpha = -0.1^{\circ}$

(c) Continued.

Figure 12.- Continued.

O   Upper surface
⊕   Lower surface
-----   $C_{p,sonic}$

y/(b/2) = 0.259

y/(b/2) = 0.444

y/(b/2) = 0.815

y/(b/2) = 0.630

y/(b/2) = 0.963

$\alpha = 1.9^0$

(c) Continued.

Figure 12.- Continued.

Legend:
- O Upper surface
- ⊕ Lower surface
- - - - - $C_{p,sonic}$

$y/(b/2) = 0.259$

$y/(b/2) = 0.444$

$y/(b/2) = 0.815$

$y/(b/2) = 0.630$

$y/(b/2) = 0.963$

$\alpha = 4.0^0$

(c) Concluded.

Figure 12.- Continued.

O   Upper surface
⊕   Lower surface
-----   $C_{p,sonic}$

y/(b/2) = 0.259

y/(b/2) = 0.444

y/(b/2) = 0.815

y/(b/2) = 0.630

y/(b/2) = 0.963

$\alpha = -4.1^0$

(d)   M = 0.84.

Figure 12.- Continued.

$y/(b/2) = 0.259$

$y/(b/2) = 0.444$

$y/(b/2) = 0.815$

$y/(b/2) = 0.630$
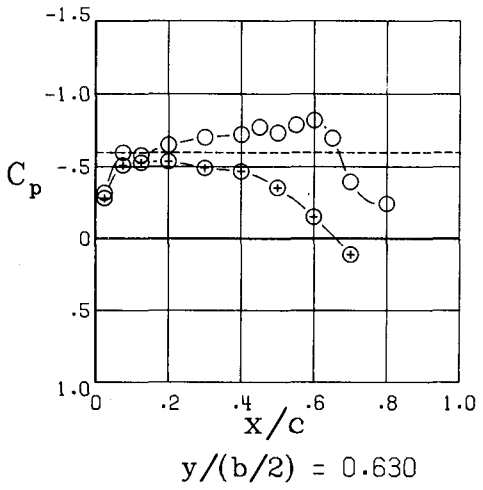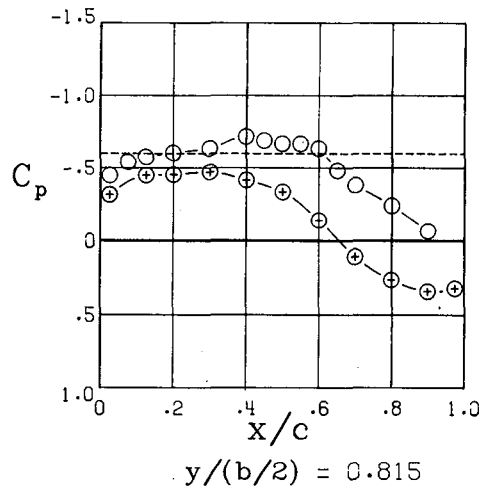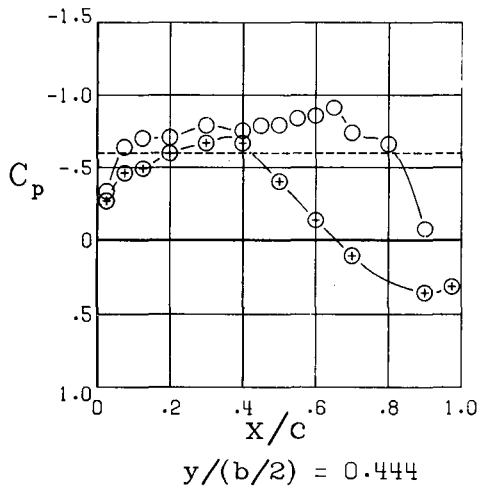
$y/(b/2) = 0.963$

○   Upper surface
⊕   Lower surface
------   $C_{p,sonic}$

$\alpha = -2.1^0$

(d) Continued.

Figure 12.- Continued.

$y/(b/2) = 0.259$
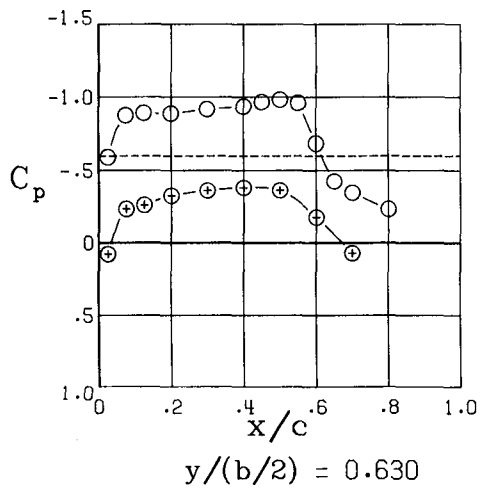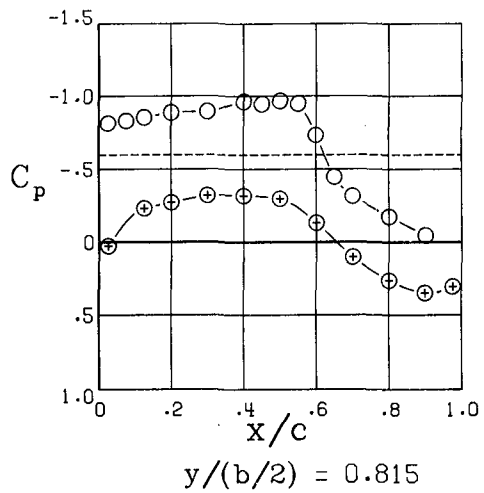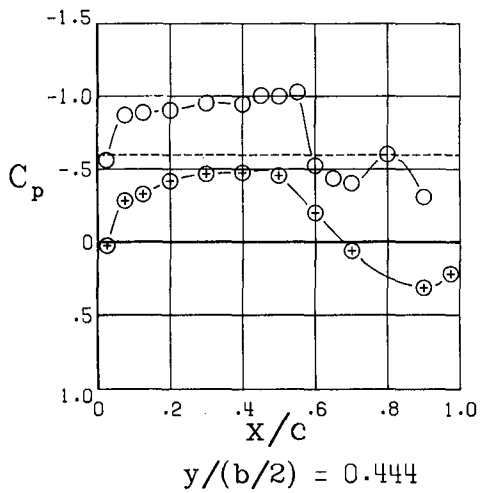
$y/(b/2) = 0.444$

$y/(b/2) = 0.815$

$y/(b/2) = 0.630$

$y/(b/2) = 0.963$

$\alpha = -0.1^{o}$

(d) Continued.

Figure 12.- Continued.

$$y/(b/2) = 0.259$$

○   Upper surface
⊕   Lower surface
-----   $C_{p,sonic}$

$$y/(b/2) = 0.444$$

$$y/(b/2) = 0.815$$

$$y/(b/2) = 0.630$$

$$y/(b/2) = 0.963$$

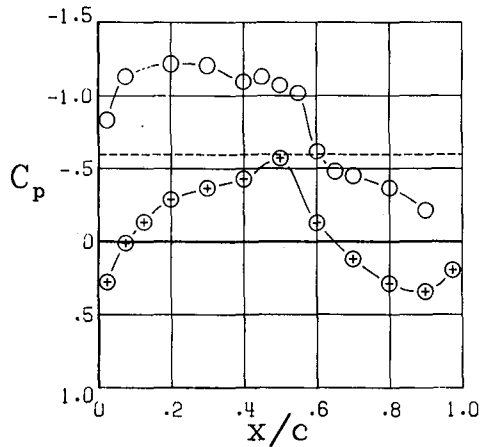$$\alpha = 1.9^0$$

(d) Continued.

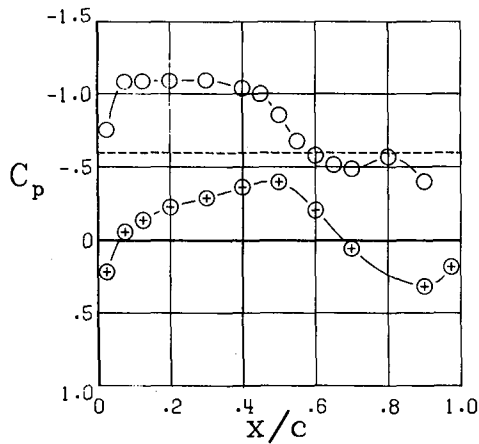Figure 12.- Continued.

$\alpha = 3.9^\circ$

(d) Continued.
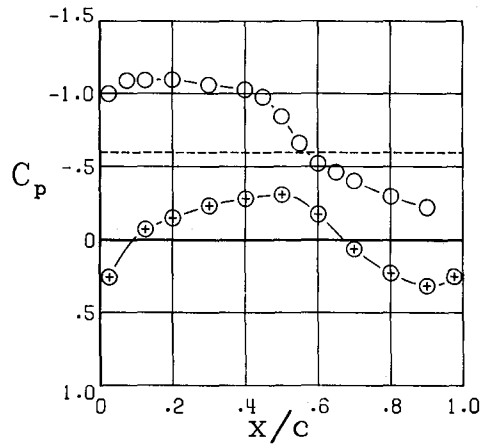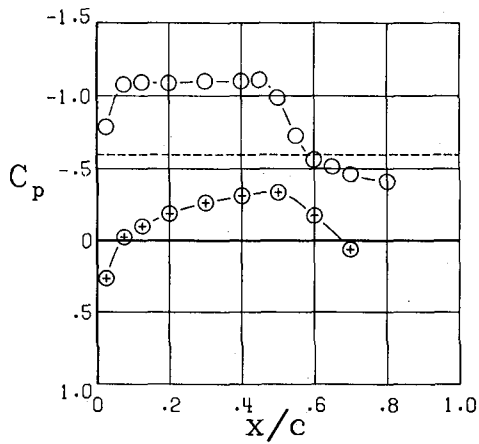
Figure 12.- Continued.

$y/(b/2) = 0.259$
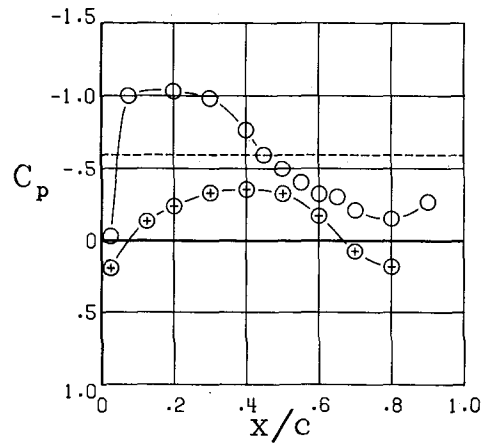
O  Upper surface
⊕  Lower surface
-----  $C_{p,sonic}$

$y/(b/2) = 0.444$

$y/(b/2) = 0.815$

$y/(b/2) = 0.630$

$y/(b/2) = 0.963$
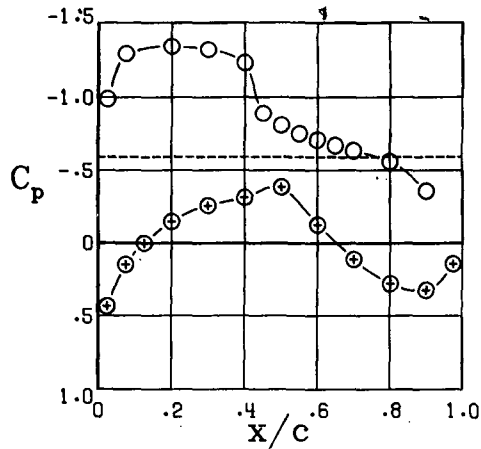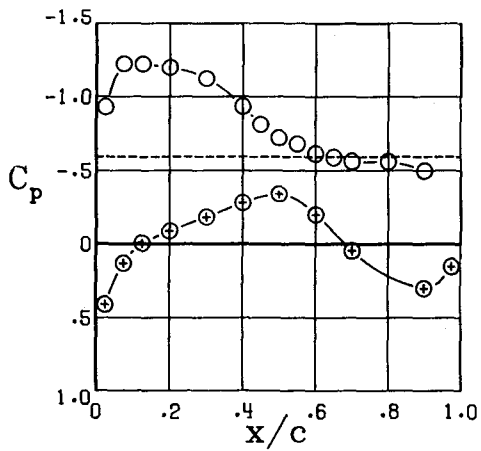
$\alpha = 5.9^o$

(d) Concluded.

Figure 12.- Continued.
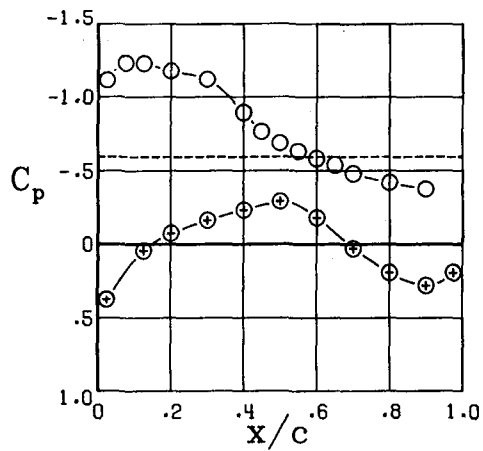
Legend:
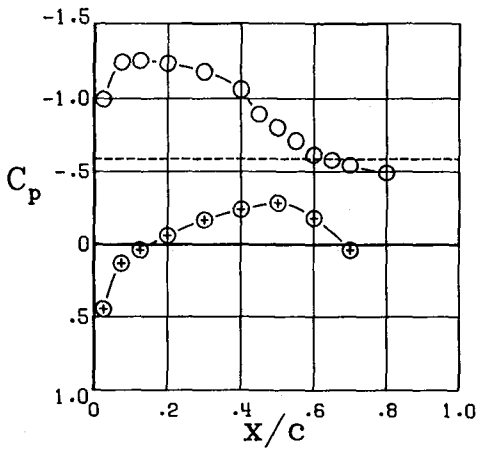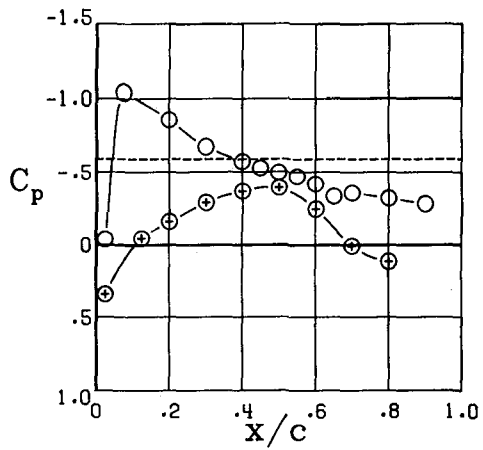○   Upper surface
⊕   Lower surface
-----   $C_{p,sonic}$

$y/(b/2) = 0.259$

$y/(b/2) = 0.444$

$y/(b/2) = 0.815$

$y/(b/2) = 0.630$

$y/(b/2) = 0.963$

$\alpha = -4.1^0$

(e)   M = 0.86.

Figure 12.- Continued.

○   Upper surface
⊕   Lower surface
------   $C_{p,sonic}$

y/(b/2) = 0.259

y/(b/2) = 0.444

y/(b/2) = 0.815

y/(b/2) = 0.630

y/(b/2) = 0.963

$\alpha = -2.1^0$

(e) Continued.

Figure 12.- Continued.

50

O  Upper surface

⊕  Lower surface

------  $C_{p,sonic}$

$C_p$

$x/c$

$y/(b/2) = 0.259$

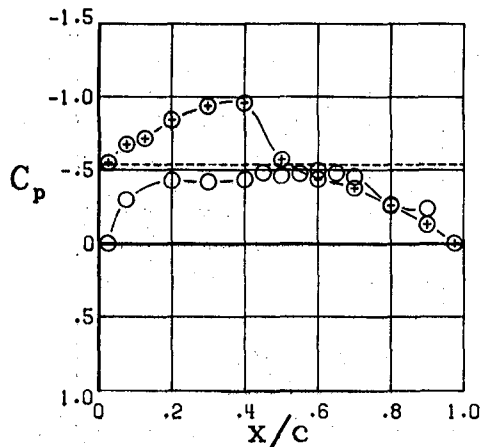$y/(b/2) = 0.444$

$y/(b/2) = 0.815$

$y/(b/2) = 0.630$

$y/(b/2) = 0.963$

$\alpha = -0.1^o$

(e) Continued.

Figure 12.- Continued.

$y/(b/2) = 0.259$

$y/(b/2) = 0.444$

$y/(b/2) = 0.815$

$y/(b/2) = 0.630$

$y/(b/2) = 0.963$

$\alpha = 1.9°$

(e) Continued.

Figure 12.- Continued.

$y/(b/2) = 0.259$

$y/(b/2) = 0.444$

$y/(b/2) = 0.815$

$y/(b/2) = 0.630$

$y/(b/2) = 0.963$

$\alpha = 3.9^0$

(e) Continued.

Figure 12.- Continued.
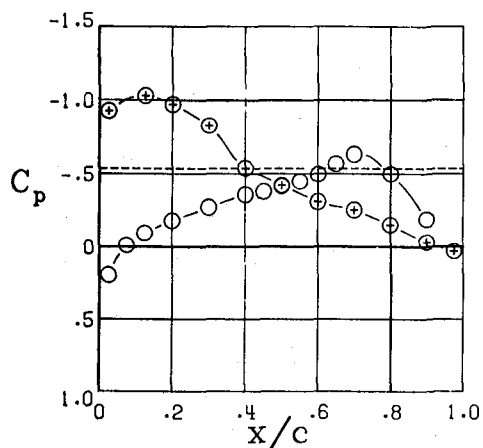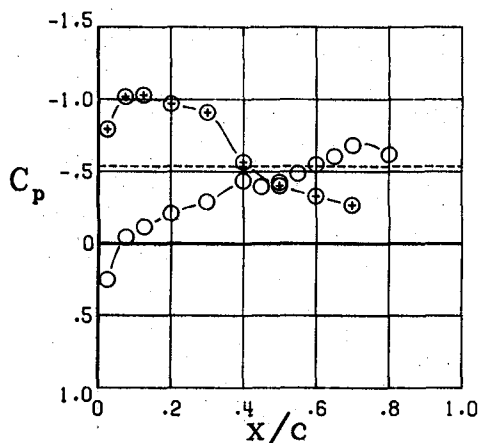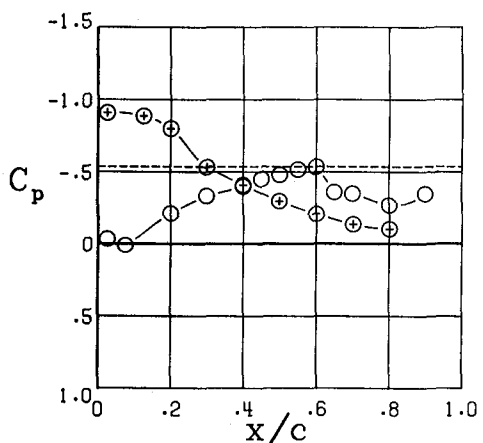
O    Upper surface
⊕    Lower surface
-----    $C_{p,sonic}$

$y/(b/2) = 0.259$

$y/(b/2) = 0.444$

$y/(b/2) = 0.815$

$y/(b/2) = 0.630$

$y/(b/2) = 0.963$

$\alpha = 5.9^{o}$

(e) Continued.

Figure 12.- Continued.

O  Upper surface
⊕  Lower surface
------  $C_{p,sonic}$

y/(b/2) = 0.259

y/(b/2) = 0.444

y/(b/2) = 0.815

y/(b/2) = 0.630

y/(b/2) = 0.963

$\alpha = 7.9^{\circ}$

(e) Concluded.

Figure 12.- Continued.

O  Upper surface
⊕  Lower surface
------  $C_{p,sonic}$

$y/(b/2) = 0.259$
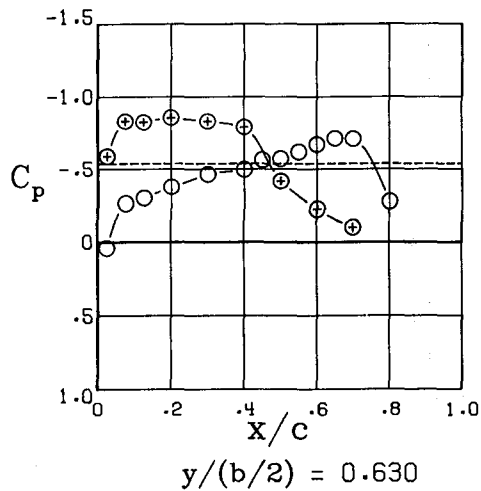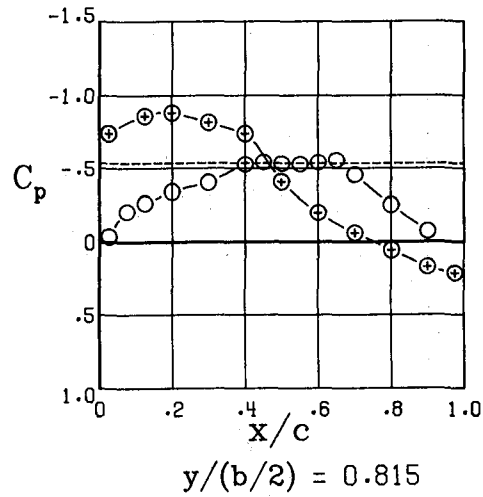
$y/(b/2) = 0.444$

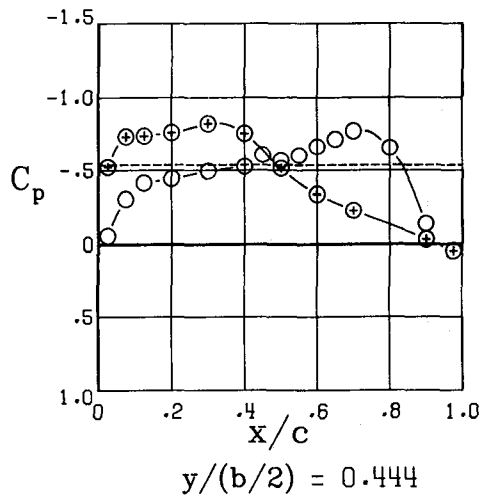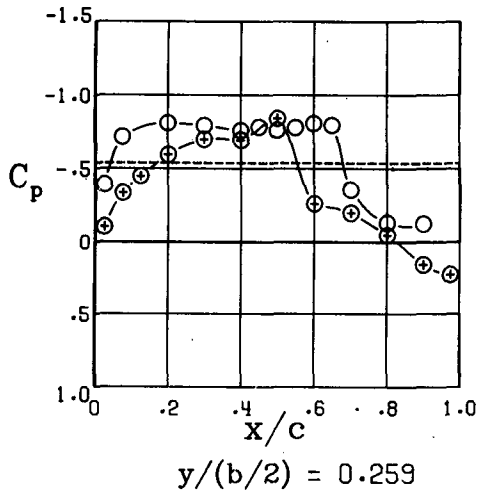$y/(b/2) = 0.815$

$y/(b/2) = 0.630$

$y/(b/2) = 0.963$

$\alpha = -4.1^{0}$

(f)  M = 0.90.

Figure 12.- Continued.

○   Upper surface
⊕   Lower surface
------   $C_{p,sonic}$

$y/(b/2) = 0.259$
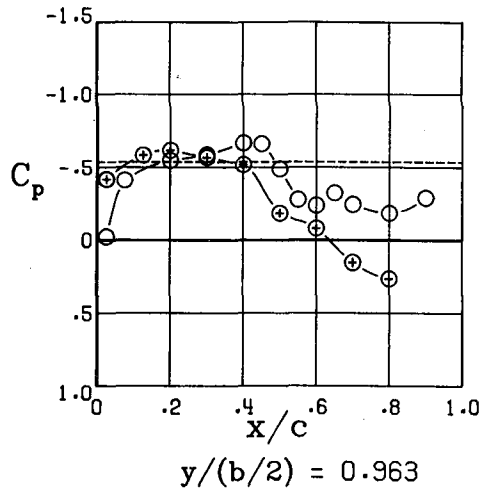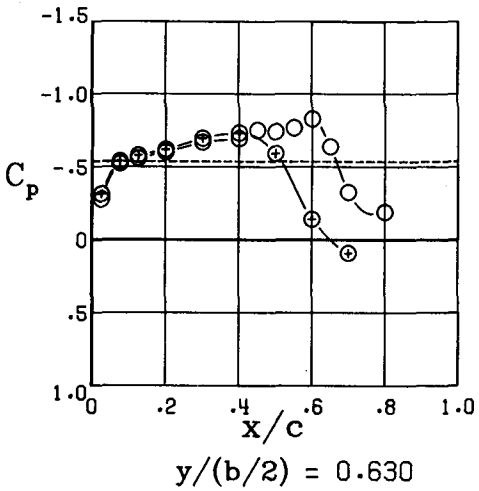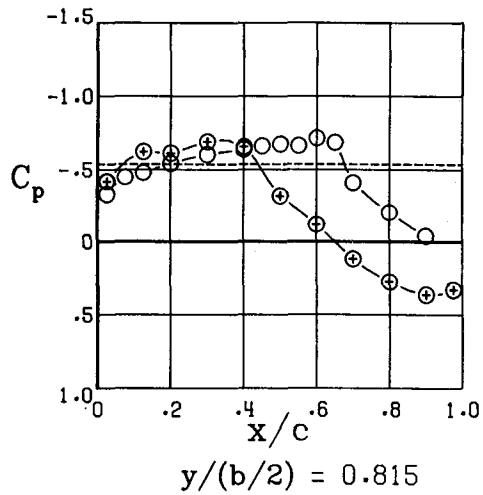
$y/(b/2) = 0.444$

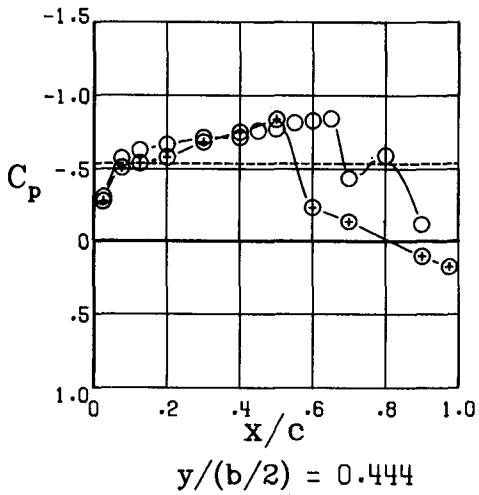$y/(b/2) = 0.815$

$y/(b/2) = 0.630$
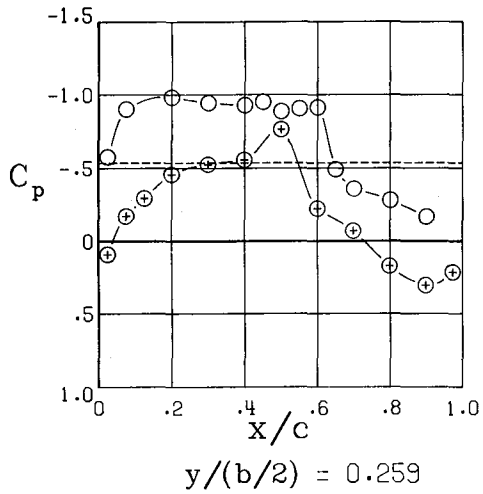
$y/(b/2) = 0.963$

$\alpha = -2.1^0$

(f) Continued.

Figure 12.- Continued.

O   Upper surface
⊕   Lower surface
-----   $C_{p,sonic}$

$y/(b/2) = 0.259$

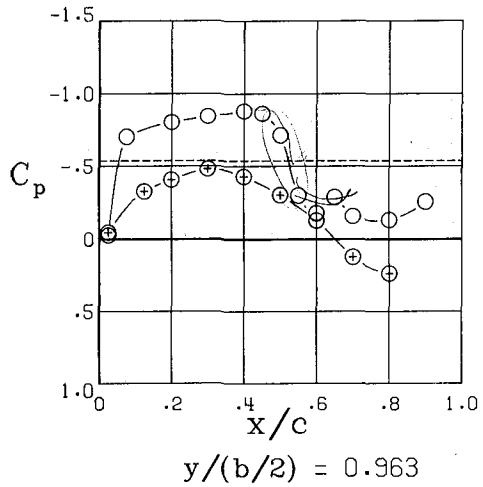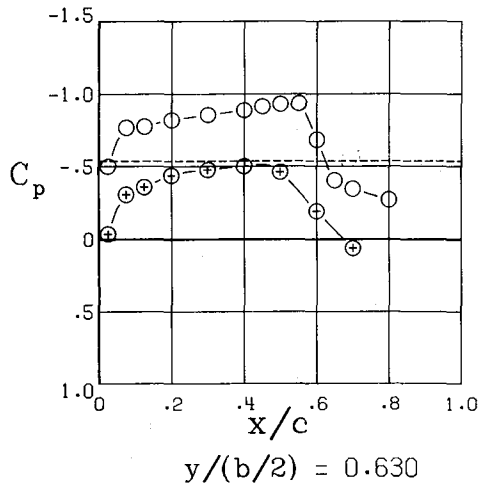$y/(b/2) = 0.444$

$y/(b/2) = 0.815$

$y/(b/2) = 0.630$

$y/(b/2) = 0.963$

$\alpha = -0.1^{\circ}$

(f) Continued.

Figure 12.- Continued.

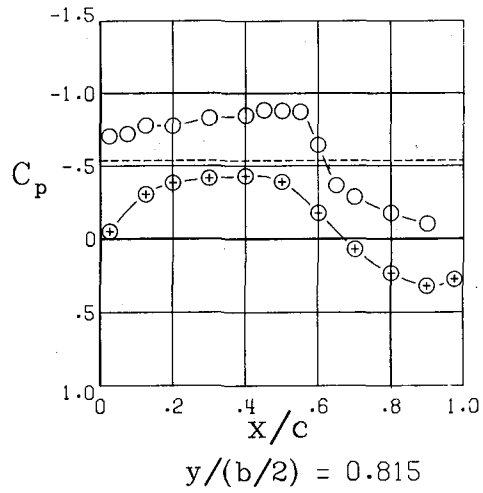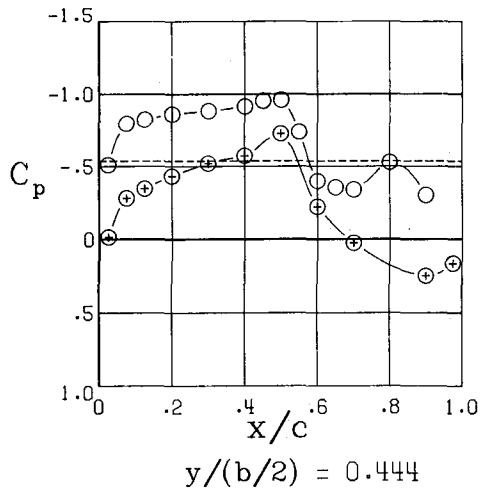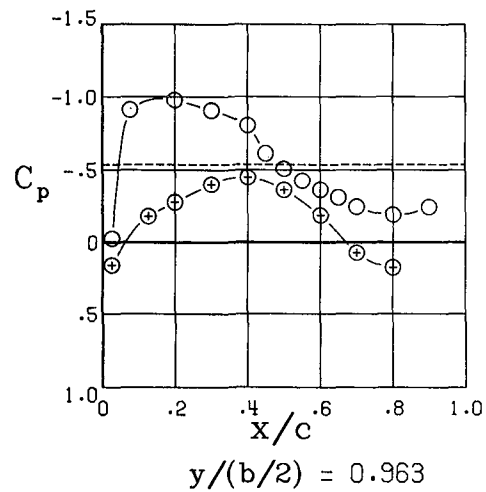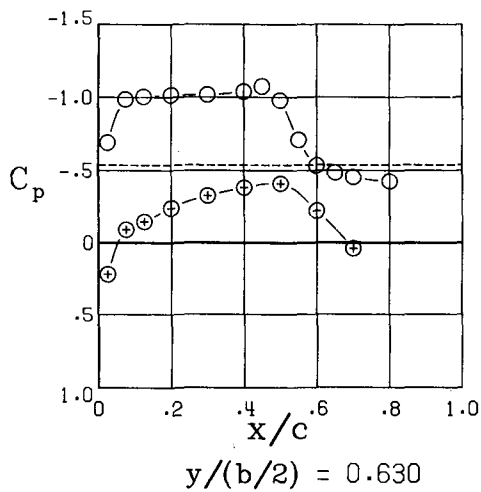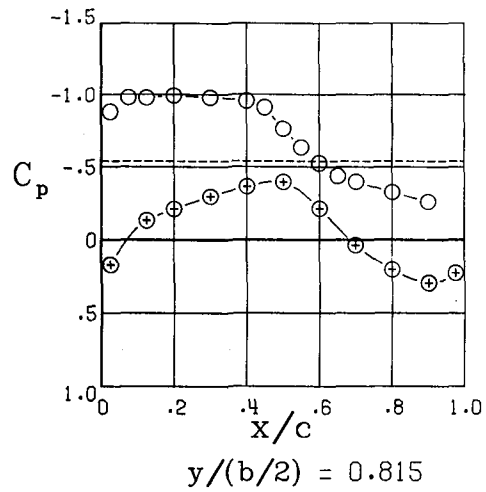O   Upper surface
⊕   Lower surface
------   $C_{p,sonic}$

$y/(b/2) = 0.259$

$y/(b/2) = 0.444$

$y/(b/2) = 0.815$

$y/(b/2) = 0.630$

$y/(b/2) = 0.963$

$\alpha = 2.0^0$

(f) Continued.

Figure 12.- Continued.

y/(b/2) = 0.259



y/(b/2) = 0.444



y/(b/2) = 0.815



y/(b/2) = 0.630



y/(b/2) = 0.963

$\alpha = 3.9^0$

(f) Continued.

Figure 12.- Continued.

○ Upper surface
⊕ Lower surface
----- $C_{p,sonic}$

$y/(b/2) = 0.259$

$y/(b/2) = 0.444$

$y/(b/2) = 0.815$

$y/(b/2) = 0.630$

$y/(b/2) = 0.963$

$\alpha = 5.9^{o}$

(f) Continued.

Figure 12.- Continued.

y/(b/2) = 0.259

y/(b/2) = 0.444

y/(b/2) = 0.815

y/(b/2) = 0.630

y/(b/2) = 0.963

$\alpha = 7.9^0$

(f) Concluded.

Figure 12.- Continued.

O  Upper surface
⊕  Lower surface
-----  $C_{p,sonic}$

$y/(b/2) = 0.259$

$y/(b/2) = 0.444$

$y/(b/2) = 0.815$

$y/(b/2) = 0.630$

$y/(b/2) = 0.963$

$\alpha = -4.1^0$

(g)   $M = 0.92$.

Figure 12.- Continued.

$y/(b/2) = 0.259$

$y/(b/2) = 0.444$

$y/(b/2) = 0.815$
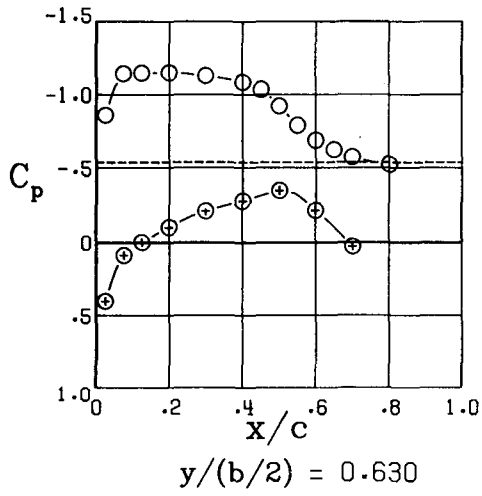
$y/(b/2) = 0.630$

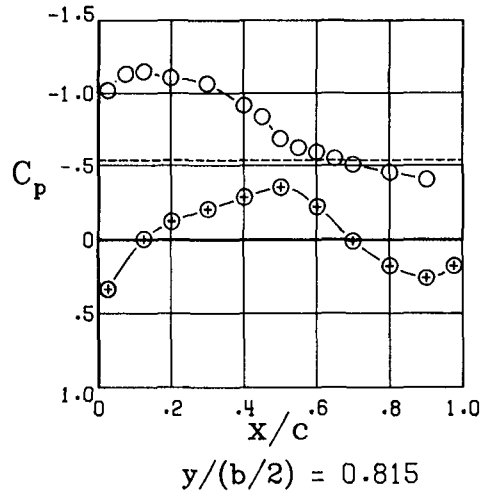$y/(b/2) = 0.963$

$\alpha = -2.1^{\circ}$

(g) Continued.

Figure 12.- Continued.

$\alpha = -0.1^o$

(g) Continued.

Figure 12.- Continued.

$y/(b/2) = 0.259$

$y/(b/2) = 0.444$

$y/(b/2) = 0.815$

$y/(b/2) = 0.630$

$y/(b/2) = 0.963$

○   Upper surface

⊕   Lower surface
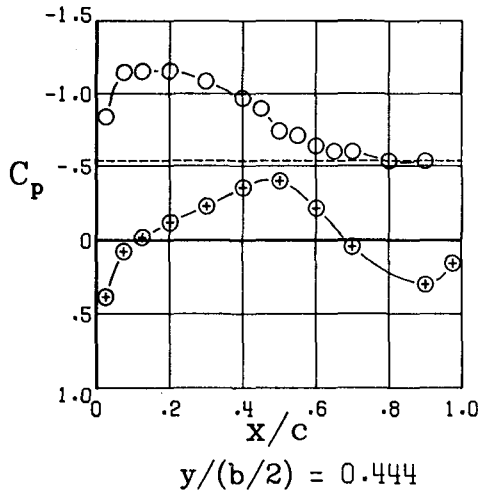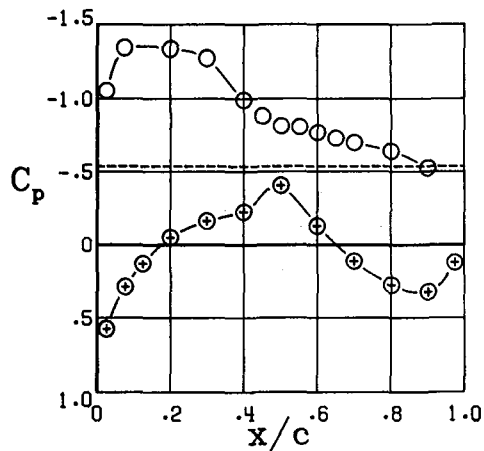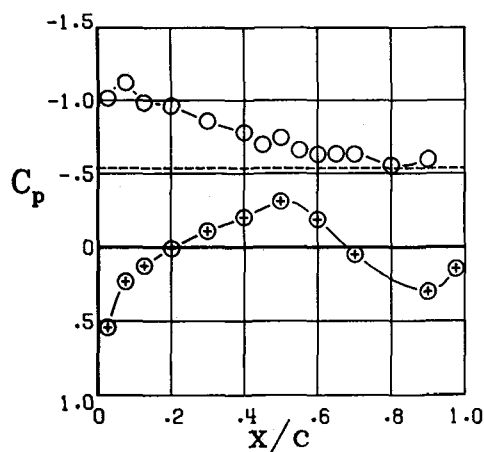
----- $C_{p,sonic}$

$\alpha = 1.9^o$
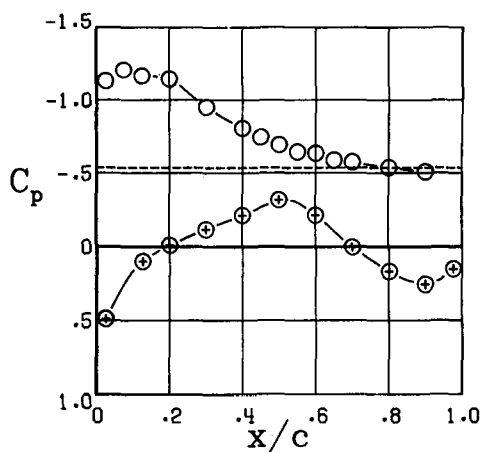
(g) Continued.

Figure 12.- Continued.
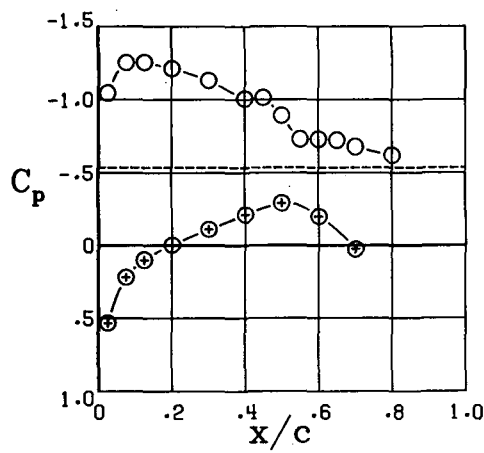
66

$y/(b/2) = 0.259$
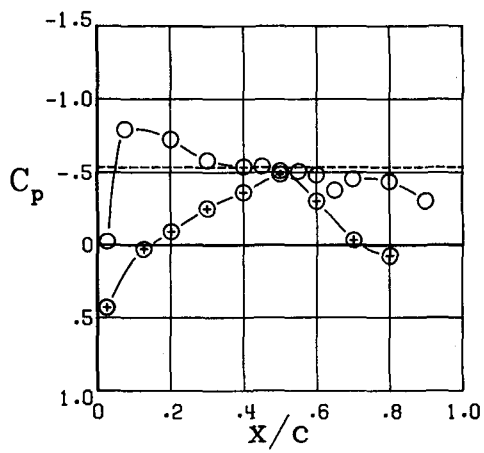
○ Upper surface
⊕ Lower surface
----- $C_{p,sonic}$

$y/(b/2) = 0.444$

$y/(b/2) = 0.815$

$y/(b/2) = 0.630$

$y/(b/2) = 0.963$
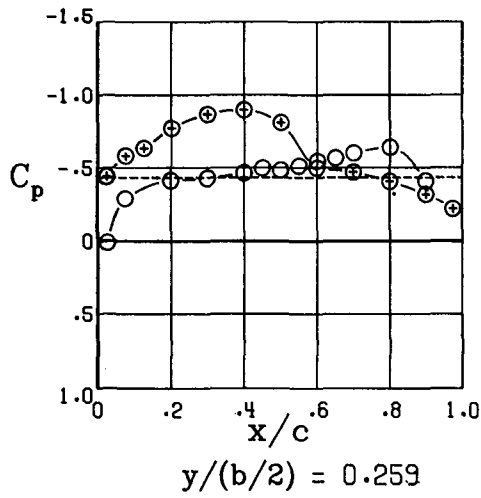
$\alpha = 3.9^{0}$
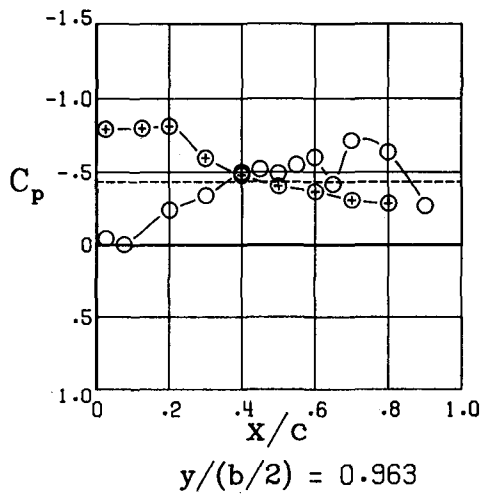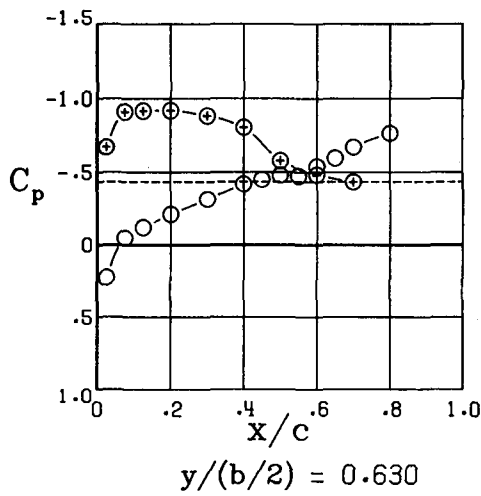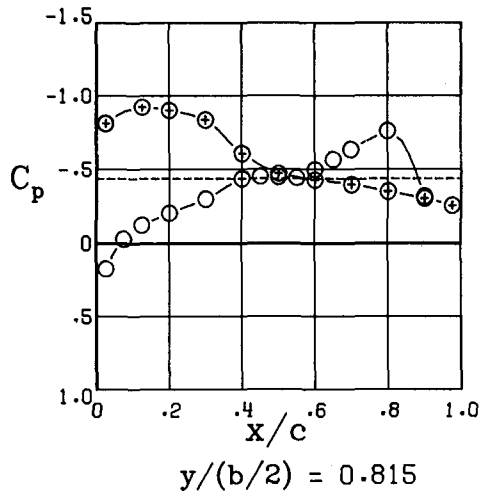
(g) Continued.

Figure 12.- Continued.

O Upper surface
⊕ Lower surface
------ $C_{p,sonic}$

y/(b/2) = 0.259

y/(b/2) = 0.444

y/(b/2) = 0.815

y/(b/2) = 0.630

y/(b/2) = 0.963

$\alpha = 5.9^0$

(g) Concluded.

Figure 12.- Concluded.

$\alpha = -4.1^\circ$

(a)  M = 0.70.

Figure 13.- Wing pressure distributions for model configuration B.

$\alpha = -2.1°$

(a) Continued.

Figure 13.- Continued.

O    Upper surface
⊕    Lower surface
------  $C_{p,sonic}$

y/(b/2) = 0.259

y/(b/2) = 0.444

y/(b/2) = 0.815

y/(b/2) = 0.630

y/(b/2) = 0.963

$\alpha = -0.1^o$

(a) Continued.

Figure 13.- Continued.

O   Upper surface
⊕   Lower surface
------   $C_{p,sonic}$

y/(b/2) = 0.259

y/(b/2) = 0.444

y/(b/2) = 0.815

y/(b/2) = 0.630

y/(b/2) = 0.963

$\alpha = 1.9°$

(a) Continued.

Figure 13.- Continued.

Legend:
○ Upper surface
⊕ Lower surface
----- $C_{p,sonic}$

$y/(b/2) = 0.259$

$y/(b/2) = 0.444$

$y/(b/2) = 0.815$

$y/(b/2) = 0.630$

$y/(b/2) = 0.963$

$\alpha = 3.9^{0}$

(a) Concluded.

Figure 13.- Continued.

○ Upper surface

⊕ Lower surface

----- $C_{p,sonic}$

$y/(b/2) = 0.259$

$y/(b/2) = 0.444$

$y/(b/2) = 0.815$

$y/(b/2) = 0.630$

$y/(b/2) = 0.963$

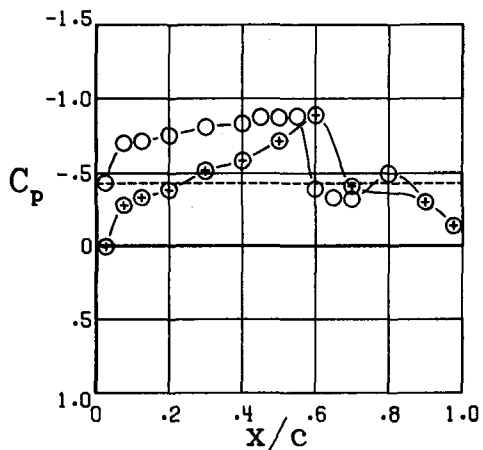$\alpha = -4.1^{o}$

(b)   M = 0.75.

Figure 13.- Continued.

74

O Upper surface
⊕ Lower surface
----- $C_{p,sonic}$

y/(b/2) = 0.259

y/(b/2) = 0.444

y/(b/2) = 0.815

y/(b/2) = 0.630

y/(b/2) = 0.963

$\alpha = -2.1^{0}$
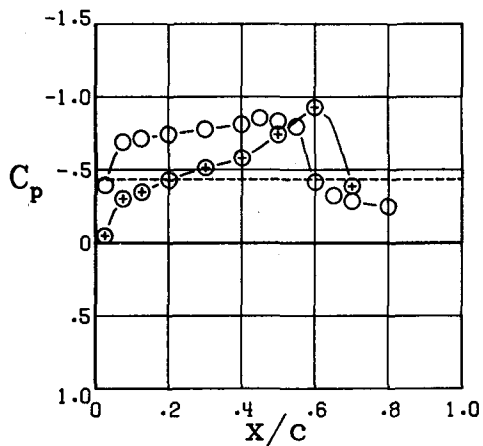
(b) Continued.

Figure 13.- Continued.

O    Upper surface
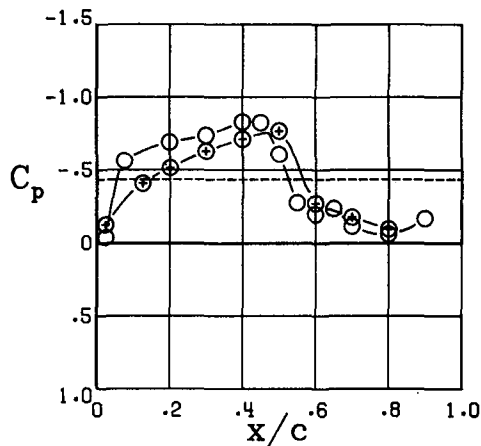⊕    Lower surface
-----    $C_{p,sonic}$

$y/(b/2) = 0.259$

$y/(b/2) = 0.444$

$y/(b/2) = 0.815$

$y/(b/2) = 0.630$

$y/(b/2) = 0.963$

$\alpha = -0.1^{o}$

(b) Continued.

Figure 13.- Continued.

Legend:
○ Upper surface
⊕ Lower surface
------ $C_{p,sonic}$

$y/(b/2) = 0.259$
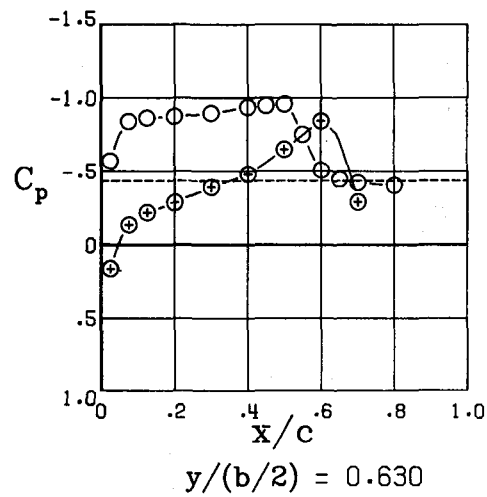
$y/(b/2) = 0.444$

$y/(b/2) = 0.815$

$y/(b/2) = 0.630$

$y/(b/2) = 0.963$

$\alpha = 2.0°$

(b) Continued.

Figure 13.- Continued.

Figure 13.- Continued.

Legend:

○ Upper surface
⊕ Lower surface
------ $C_{p,sonic}$
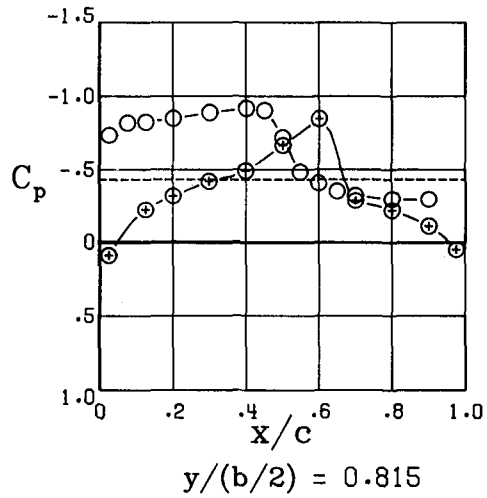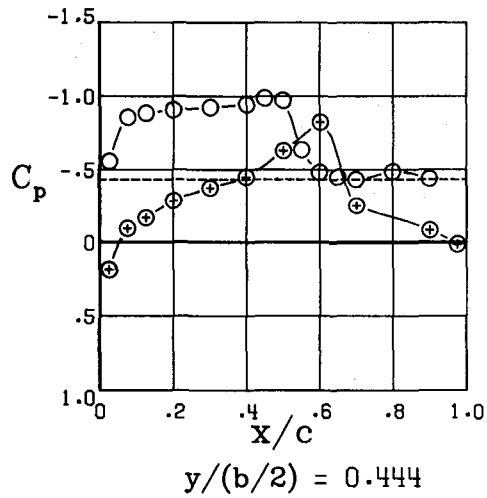
$y/(b/2) = 0.259$

$y/(b/2) = 0.444$

$y/(b/2) = 0.815$

-0.43464

$y/(b/2) = 0.630$

$y/(b/2) = 0.963$

$\alpha = -4.1°$

(c)   M = 0.80.

Figure 13.- Continued.

Legend:
○ Upper surface
⊕ Lower surface
----- $C_{p,sonic}$
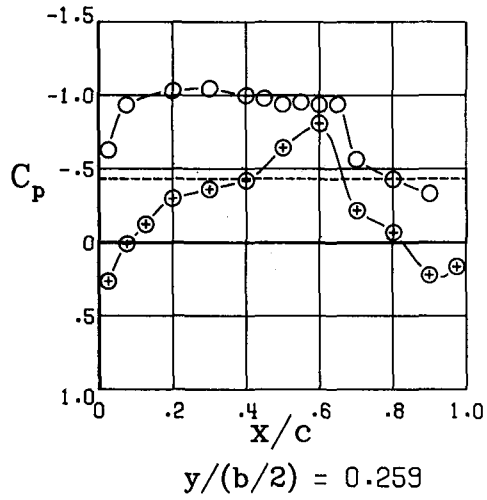
$y/(b/2) = 0.259$

$y/(b/2) = 0.444$

$y/(b/2) = 0.815$

$y/(b/2) = 0.630$

$y/(b/2) = 0.963$

$\alpha = -2.1^{o}$

(c) Continued.

Figure 13.- Continued.

-1.5
-1.0
$C_p$ -.5
0
.5
1.0
0    .2    .4    .6    .8    1.0
x/c

y/(b/2) = 0.259

○ Upper surface
⊕ Lower surface
------ $C_{p,sonic}$

-1.5
-1.0
$C_p$ -.5
0
.5
1.0
0    .2    .4    .6    .8    1.0
x/c

y/(b/2) = 0.444

-1.5
-1.0
$C_p$ -.5
0
.5
1.0
0    .2    .4    .6    .8    1.0
x/c

y/(b/2) = 0.815

-1.5
-1.0
$C_p$ -.5
0
.5
1.0
0    .2    .4    .6    .8    1.0
x/c

y/(b/2) = 0.630

-1.5
-1.0
$C_p$ -.5
0
.5
1.0
0    .2    .4    .6    .8    1.0
x/c

y/(b/2) = 0.963

$\alpha = -0.1^o$

(c) Continued.

Figure 13.- Continued.

81

O    Upper surface
⊕    Lower surface
-----   $C_{p,sonic}$

$y/(b/2) = 0.259$

$y/(b/2) = 0.444$

$y/(b/2) = 0.815$

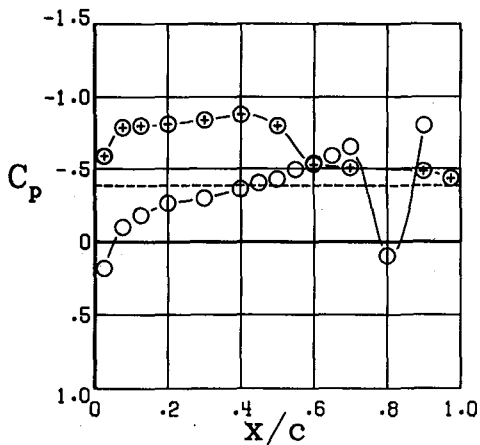$y/(b/2) = 0.630$

$y/(b/2) = 0.963$

$\alpha = 1.9^{o}$
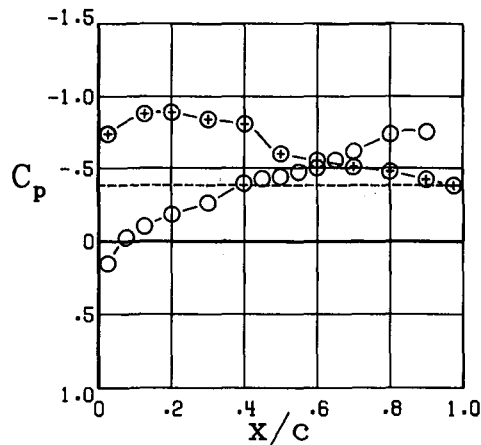
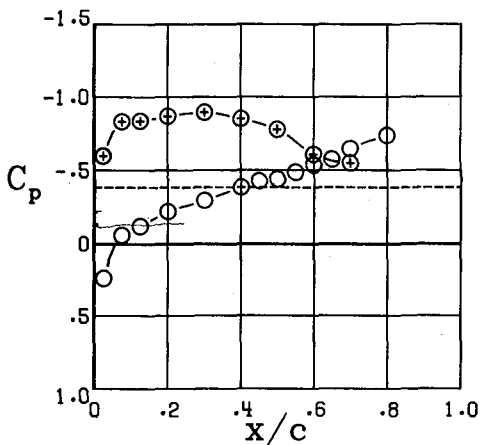(c) Continued.

Figure 13.- Continued.

$y/(b/2) = 0.259$

○ Upper surface
⊕ Lower surface
------ $C_{p,sonic}$

$y/(b/2) = 0.444$

$y/(b/2) = 0.815$

$y/(b/2) = 0.630$

$y/(b/2) = 0.963$

$\alpha = 3.9^0$

(c) Concluded.

Figure 13.- Continued.

O   Upper surface
⊕   Lower surface
-----   $C_{p,sonic}$

y/(b/2) = 0.259
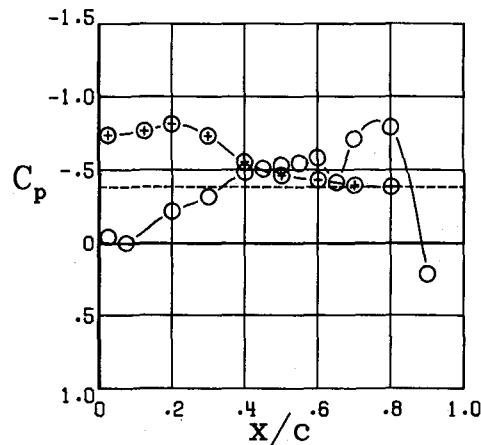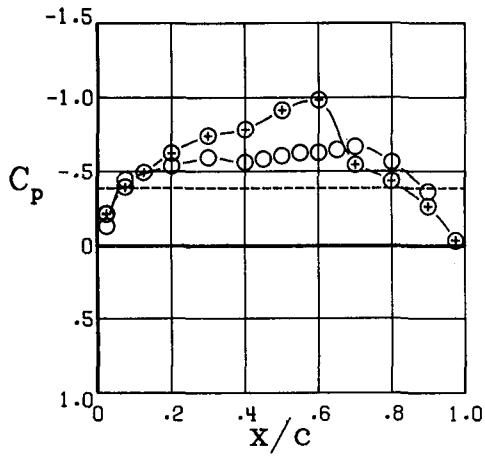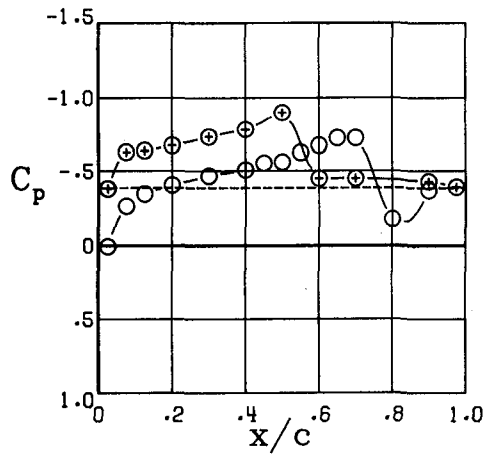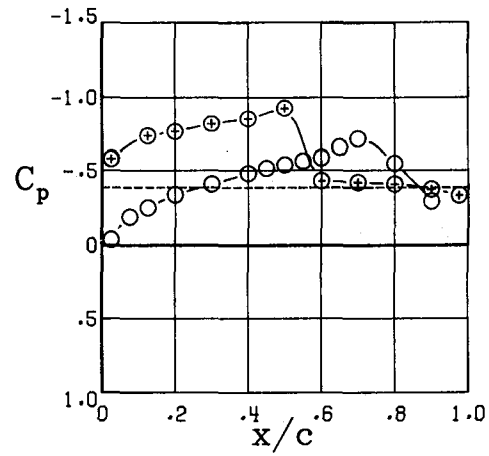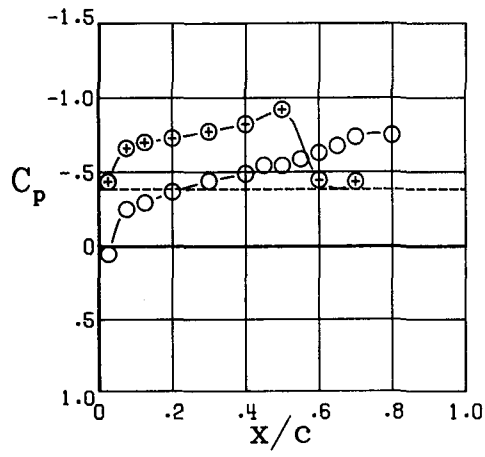
y/(b/2) = 0.444

y/(b/2) = 0.815

y/(b/2) = 0.630

y/(b/2) = 0.963

$\alpha = -4.1^o$

(d)   M = 0.84.

Figure 13.- Continued.

y/(b/2) = 0.259

Legend:
○  Upper surface
⊕  Lower surface
------ $C_{p,\text{sonic}}$

y/(b/2) = 0.444

y/(b/2) = 0.815

y/(b/2) = 0.630

y/(b/2) = 0.963

$\alpha = -2.1°$

(d) Continued.

Figure 13.- Continued.

y/(b/2) = 0.259

y/(b/2) = 0.444

y/(b/2) = 0.815

y/(b/2) = 0.630

y/(b/2) = 0.963

$\alpha = -0.1^o$
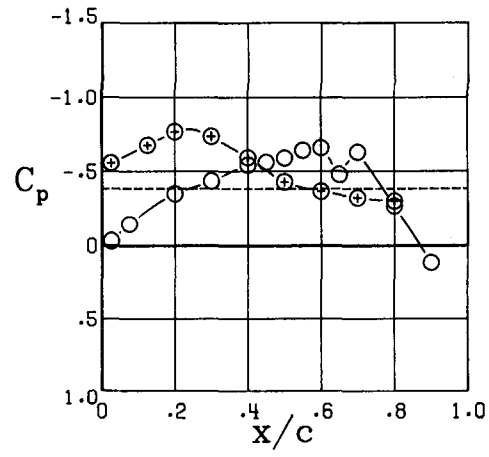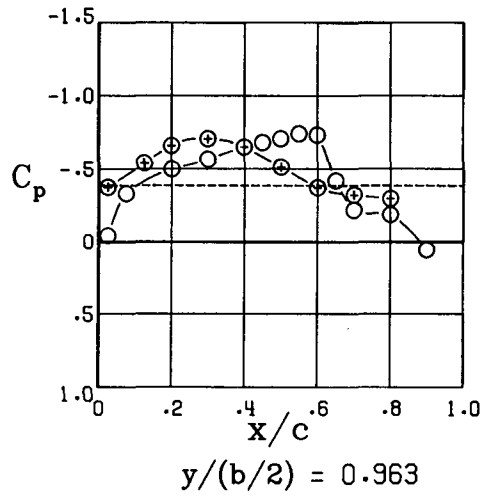
(d) Continued.

Figure 13.- Continued.

$y/(b/2) = 0.259$

$y/(b/2) = 0.444$

$y/(b/2) = 0.815$

$y/(b/2) = 0.630$

$y/(b/2) = 0.963$

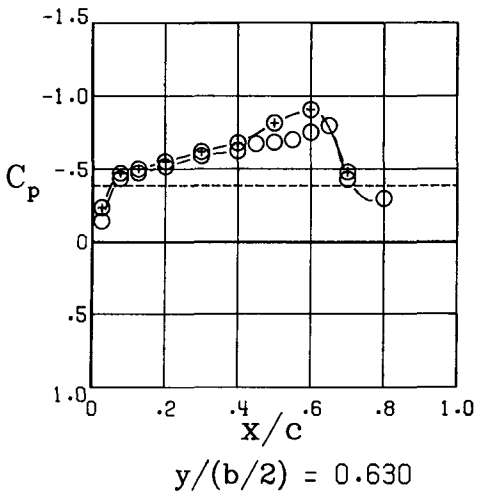$\alpha = 1.9^0$

(d) Continued.

Figure 13.- Continued.

Figure 13.- Continued.

o    Upper surface
⊕    Lower surface
-----  $C_{p,sonic}$

$y/(b/2) = 0.259$

$y/(b/2) = 0.444$

$y/(b/2) = 0.815$

$y/(b/2) = 0.630$

$y/(b/2) = 0.963$

$\alpha = 3.9^0$

(d) Continued.

Figure 13.- Continued.

$y/(b/2) = 0.259$

$y/(b/2) = 0.444$

$y/(b/2) = 0.815$

$y/(b/2) = 0.630$

$y/(b/2) = 0.963$

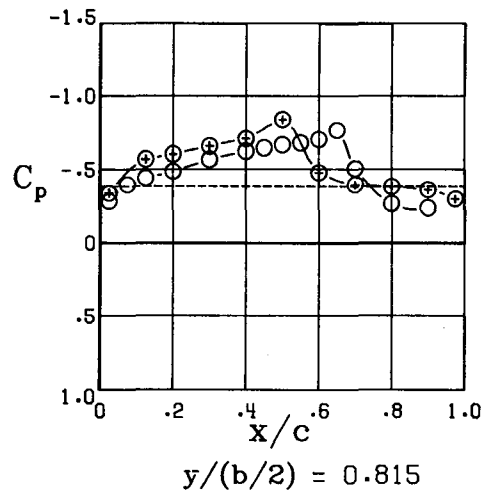$\alpha = 5.9°$

(d) Concluded.

Figure 13.- Continued.
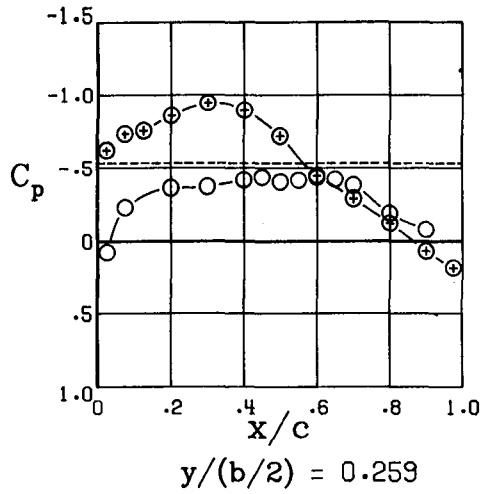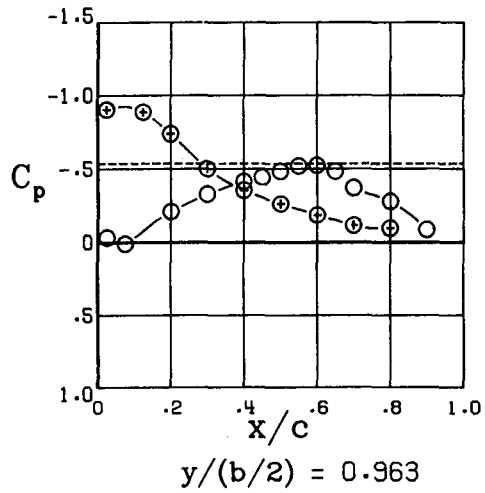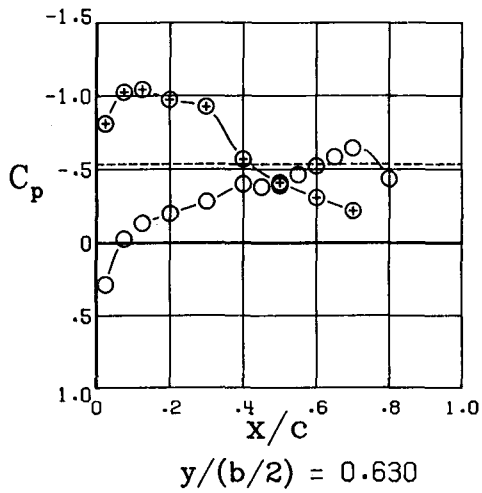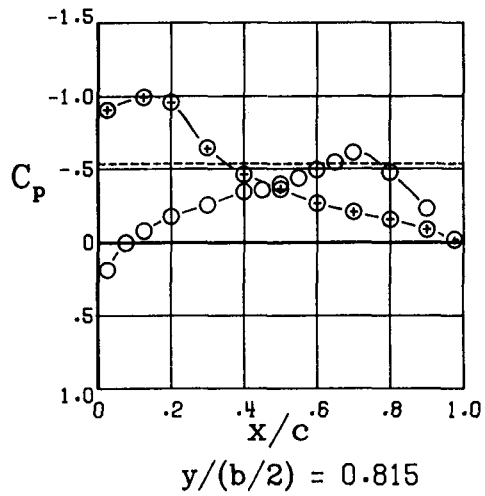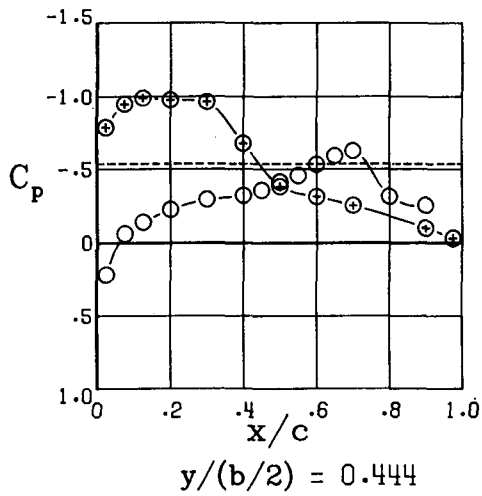
O  Upper surface
⊕  Lower surface
----- $C_{p,sonic}$

y/(b/2) = 0.259

y/(b/2) = 0.444

y/(b/2) = 0.815

y/(b/2) = 0.630

y/(b/2) = 0.963

$\alpha = -4.1^{\circ}$

(e)  M = 0.86.

Figuer 13.- Continued.

90

y/(b/2) = 0.259



y/(b/2) = 0.444



y/(b/2) = 0.815



y/(b/2) = 0.630



y/(b/2) = 0.963

$\alpha = -2.1°$

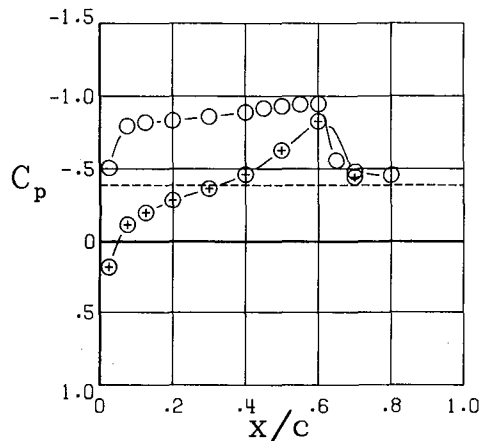(e) Continued.

Figure 13.- Continued.

O    Upper surface
⊕    Lower surface
------ $C_{p,sonic}$

$y/(b/2) = 0.259$

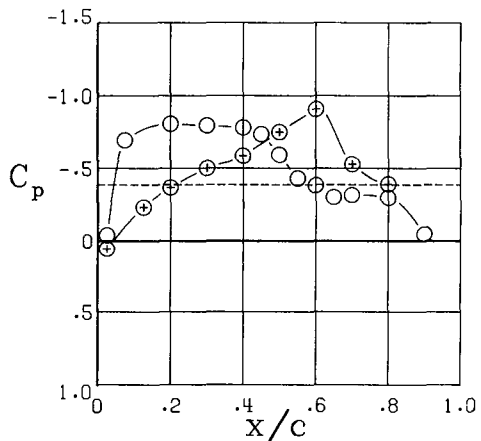$y/(b/2) = 0.444$

$y/(b/2) = 0.815$

$y/(b/2) = 0.630$

$y/(b/2) = 0.963$

$\alpha = -0.1°$

(e) Continued.

Figure 13.- Continued.

O    Upper surface
⊕    Lower surface
----- $C_{p,sonic}$

$y/(b/2) = 0.259$

$y/(b/2) = 0.444$

$y/(b/2) = 0.815$

$y/(b/2) = 0.630$

$y/(b/2) = 0.963$

$\alpha = 1.9^{0}$

(e) Continued.

Figure 13.- Continued.

O  Upper surface
⊕  Lower surface
------  $C_{p,sonic}$

$y/(b/2) = 0.259$

$y/(b/2) = 0.444$

$y/(b/2) = 0.815$

$y/(b/2) = 0.630$

$y/(b/2) = 0.963$

$\alpha = 3.9^0$

(e) Continued.

Figure 13.- Continued.

94
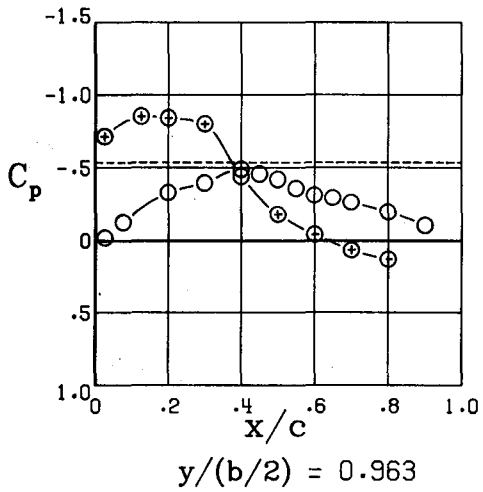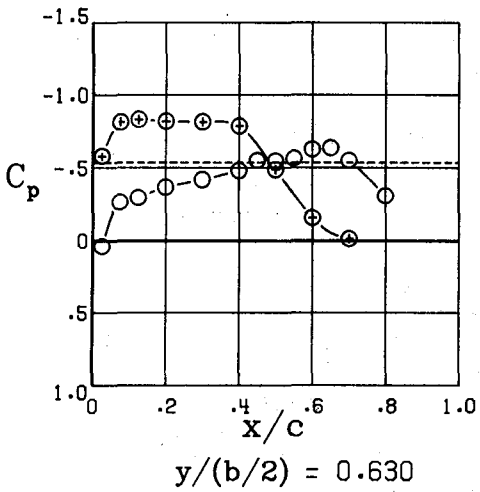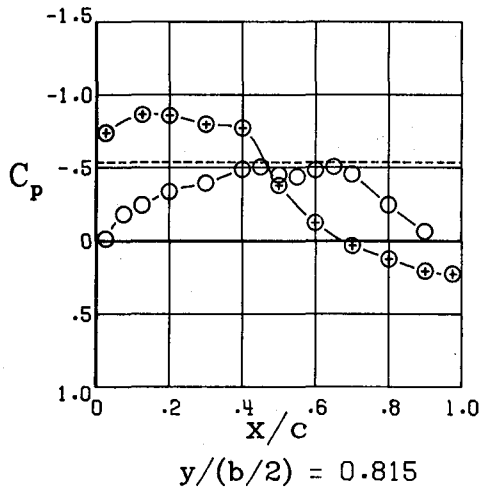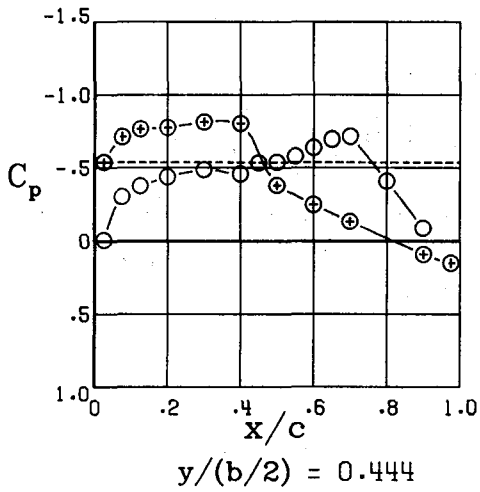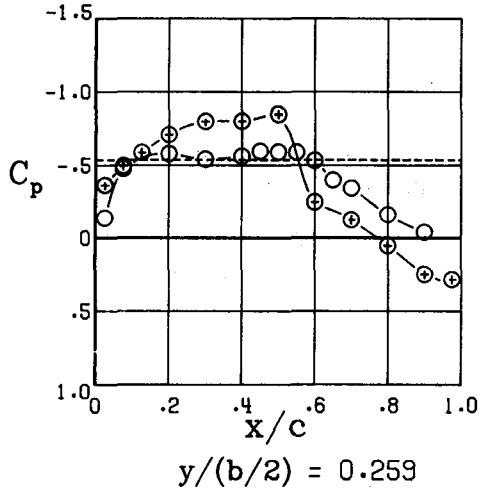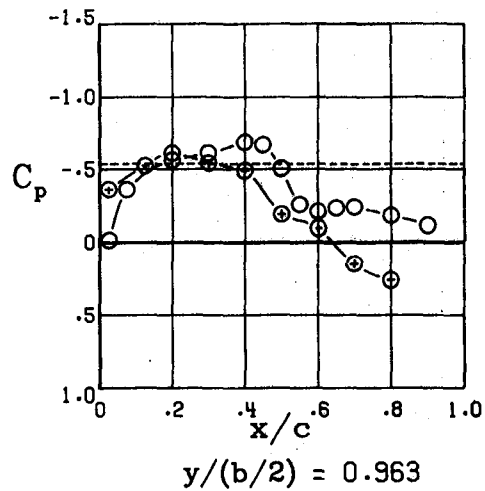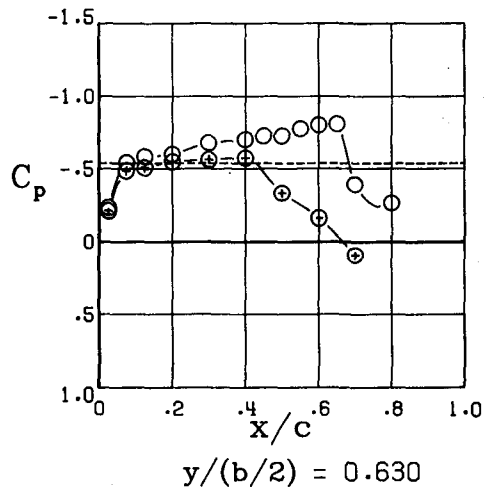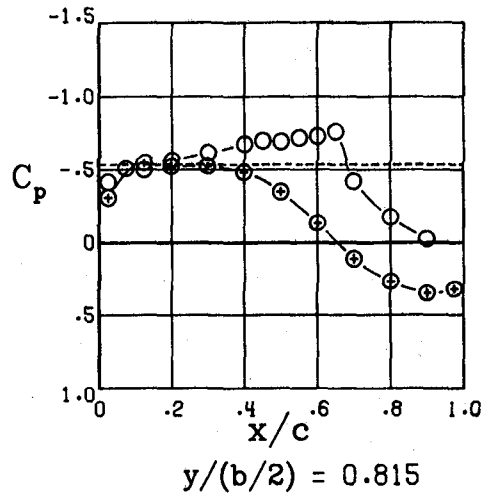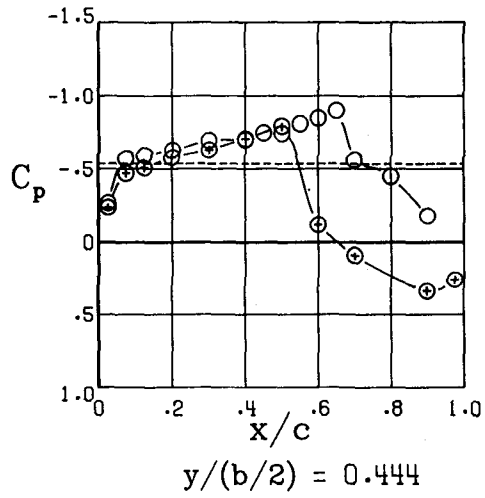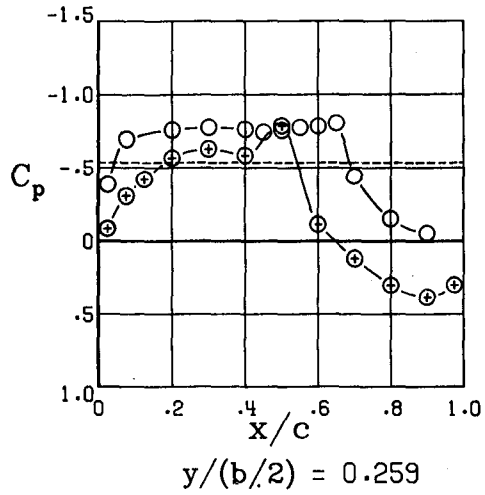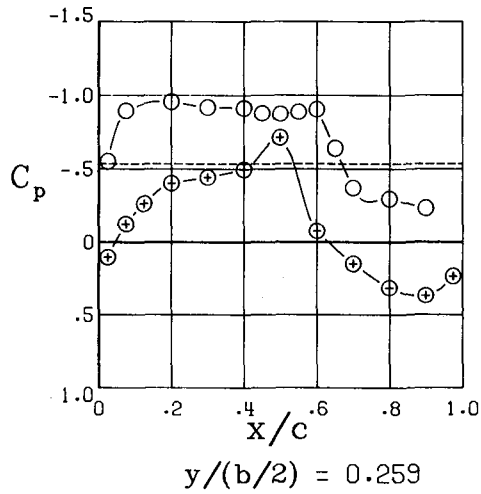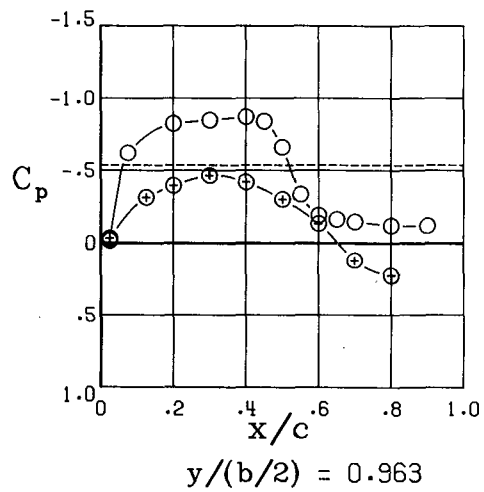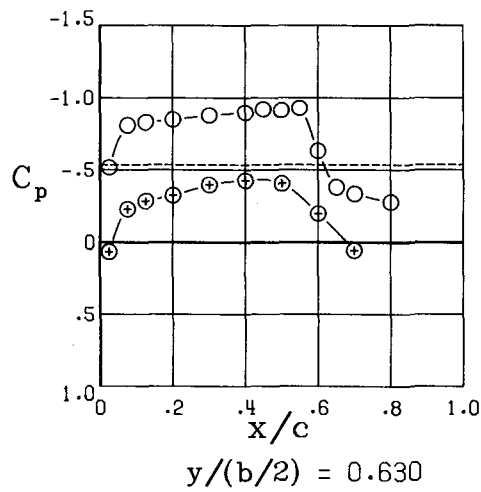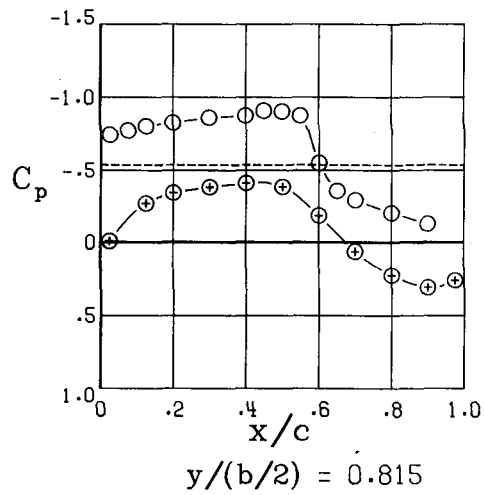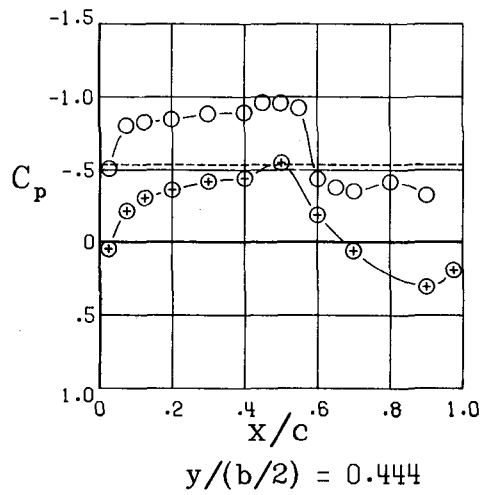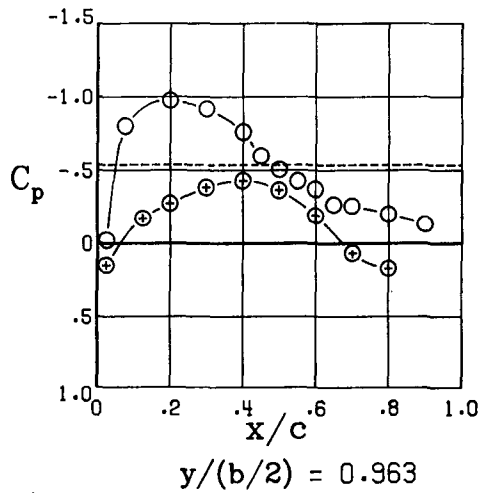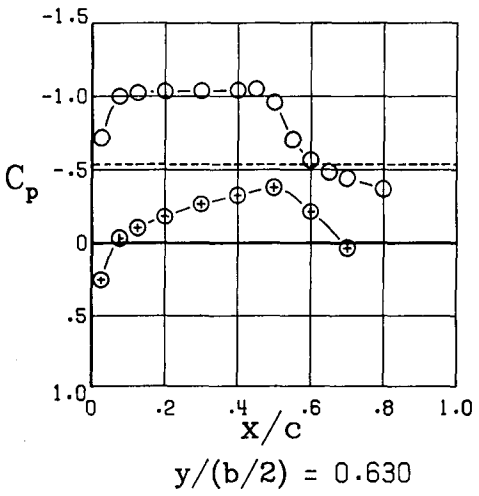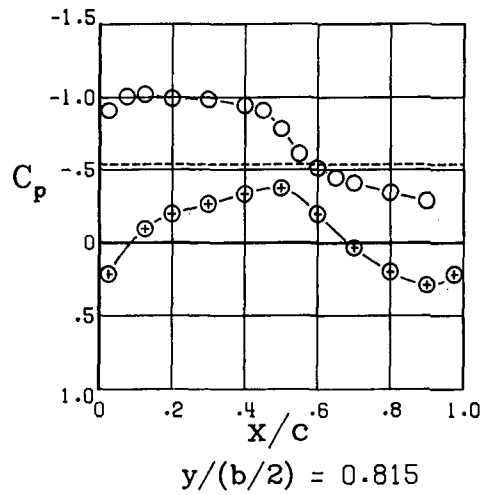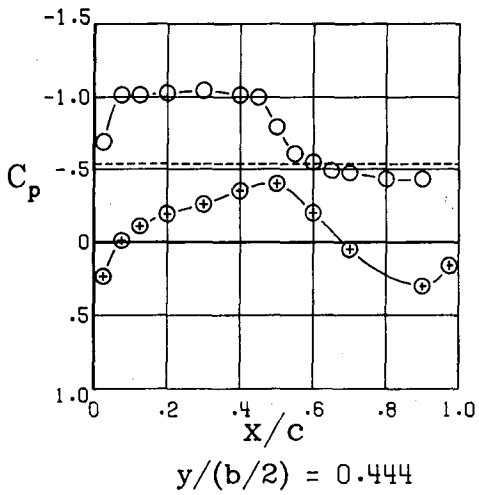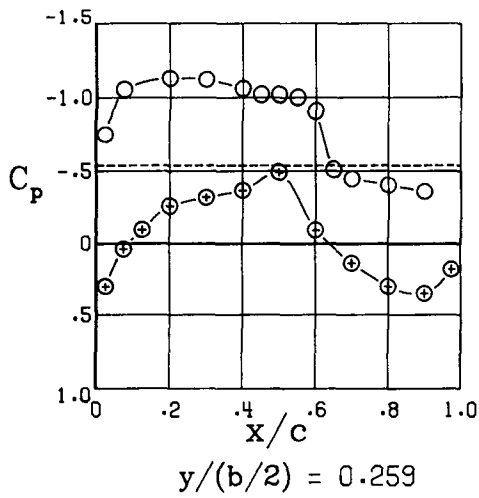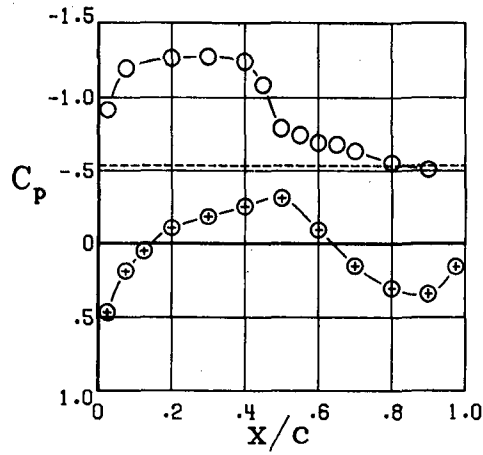
O   Upper surface
⊕   Lower surface
----- $C_{p,sonic}$
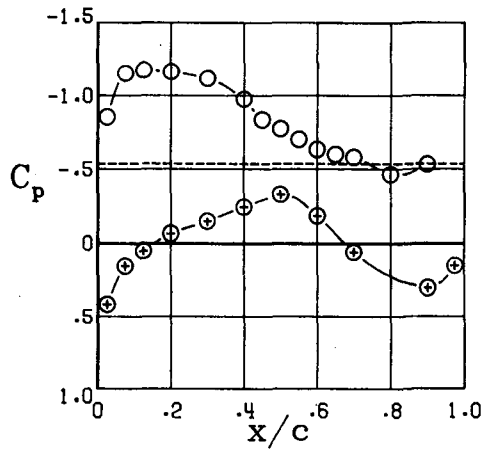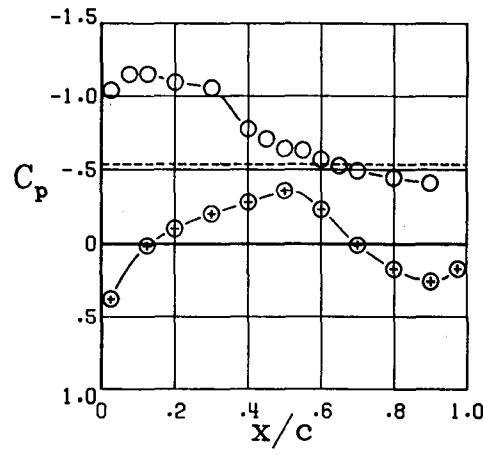
$y/(b/2) = 0.259$
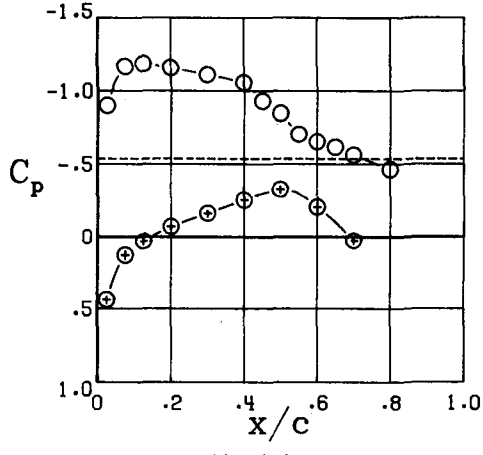
$y/(b/2) = 0.444$
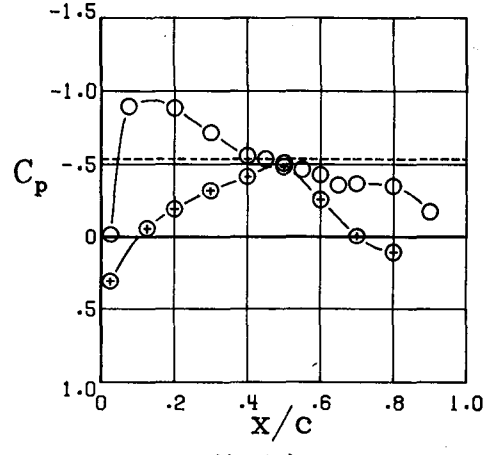
$y/(b/2) = 0.815$

$y/(b/2) = 0.630$

$y/(b/2) = 0.963$

$\alpha = 5.9°$

(e) Continued.

Figure 13.- Continued.
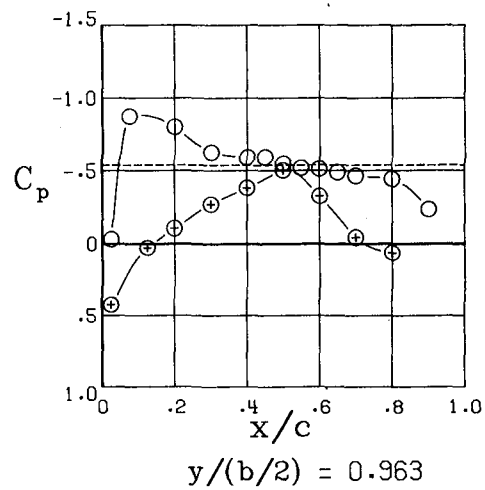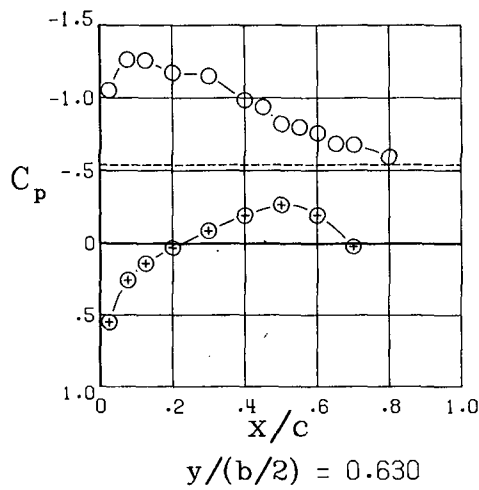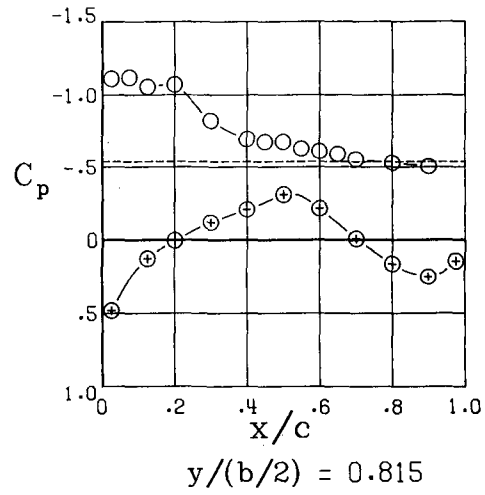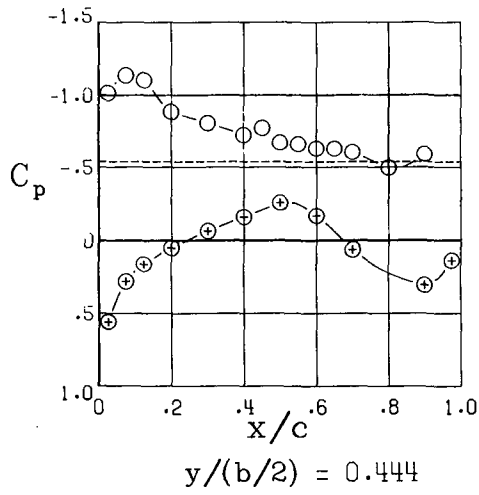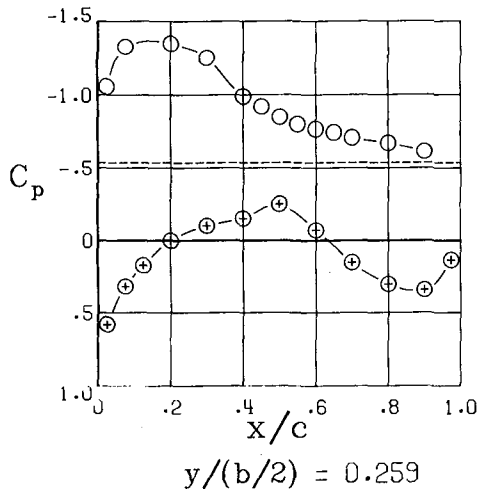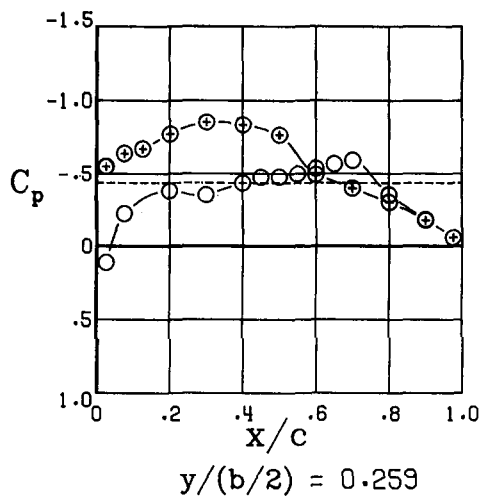
O    Upper surface
⊕    Lower surface
------  $C_{p,sonic}$

$y/(b/2) = 0.259$

$y/(b/2) = 0.444$

$y/(b/2) = 0.815$

$y/(b/2) = 0.630$

$y/(b/2) = 0.963$

$\alpha = 8.0^0$
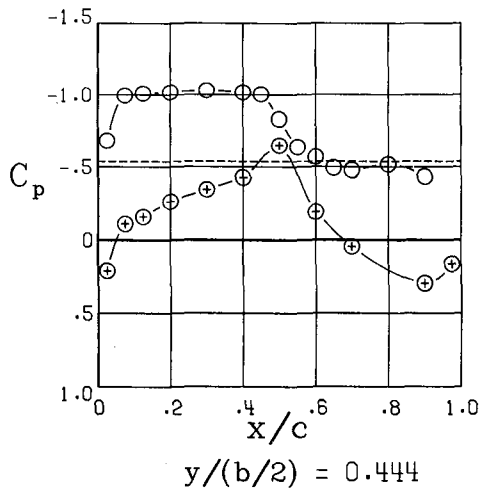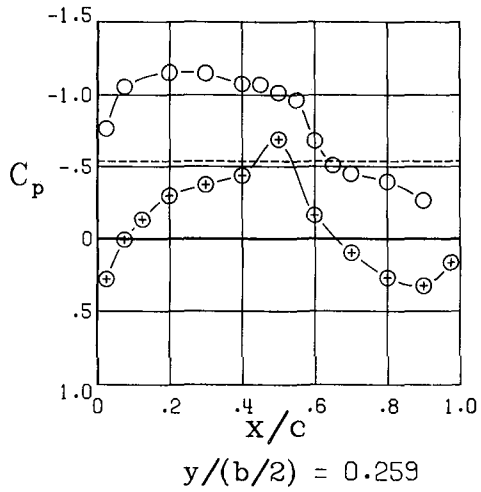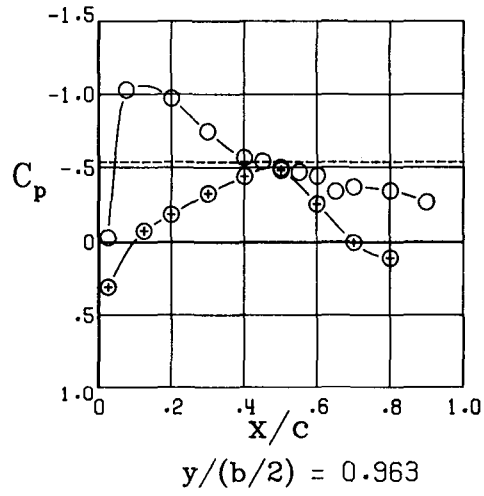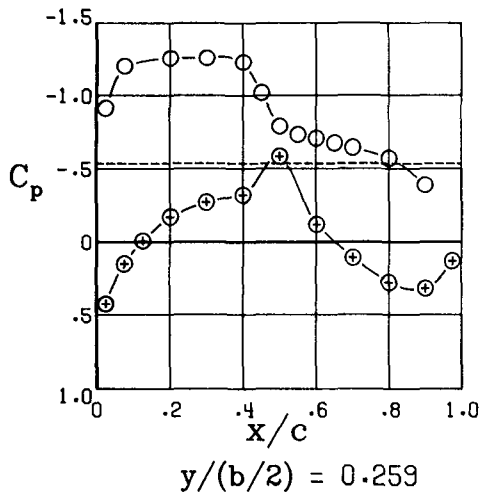
(e) Concluded.

Figure 13.- Continued.

O   Upper surface
⊕   Lower surface
-----   $C_{p,sonic}$

$y/(b/2) = 0.259$

$y/(b/2) = 0.444$

$y/(b/2) = 0.815$

$y/(b/2) = 0.630$

$y/(b/2) = 0.963$

$\alpha = -4.1°$

(f)   M = 0.90.

Figure 13.- Continued.
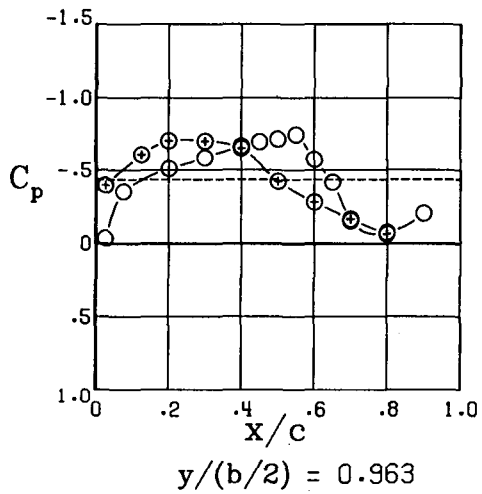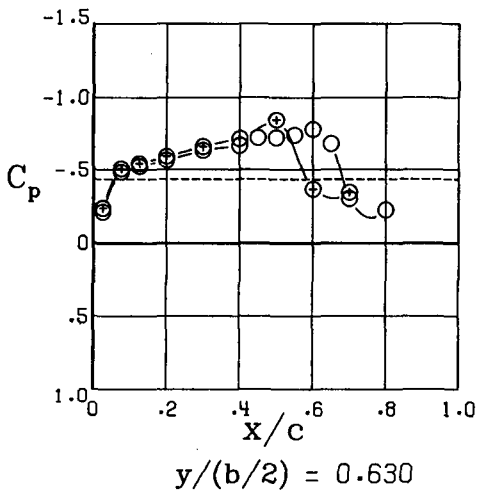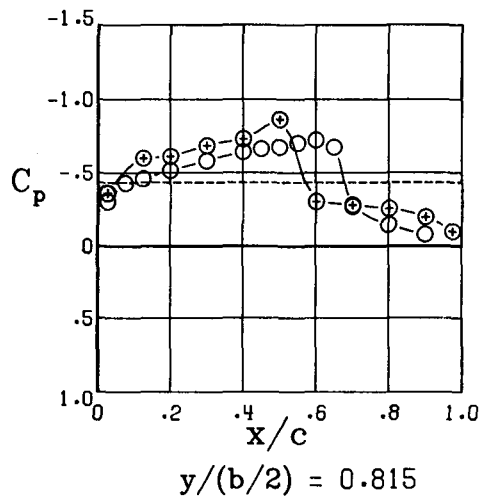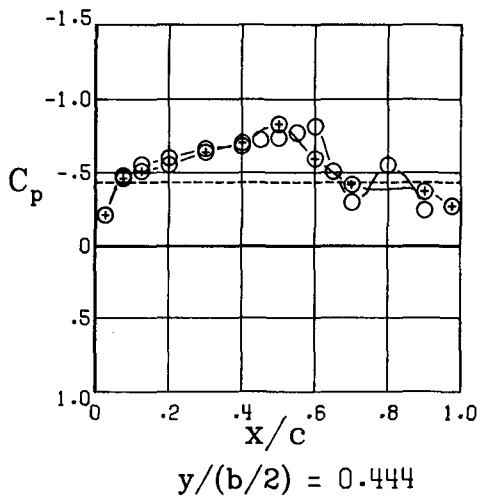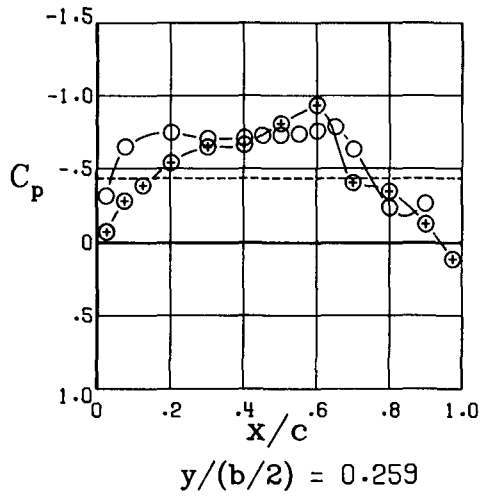
O   Upper surface

⊕   Lower surface

------   $C_{p,sonic}$

$y/(b/2) = 0.259$

$y/(b/2) = 0.444$

$y/(b/2) = 0.815$

$y/(b/2) = 0.630$

$y/(b/2) = 0.963$

$\alpha = -2.1°$

(f) Continued.

Figure 13.- Continued.

$$C_{p}$$

○ Upper surface
⊕ Lower surface
------ $C_{p,sonic}$

y/(b/2) = 0.259

y/(b/2) = 0.444

y/(b/2) = 0.815

y/(b/2) = 0.630

y/(b/2) = 0.963

α = -0.1°

(f) Continued.

Figure 13.- Continued.

O   Upper surface
⊕   Lower surface
------   $C_{p,sonic}$

$y/(b/2) = 0.259$

$y/(b/2) = 0.444$

$y/(b/2) = 0.815$

$y/(b/2) = 0.630$

$y/(b/2) = 0.963$

$\alpha = 1.9^0$

(f) Continued.

Figure 13.- Continued.

O Upper surface
⊕ Lower surface
------ $C_{p,sonic}$

$y/(b/2) = 0.259$

$y/(b/2) = 0.444$

$y/(b/2) = 0.815$

$y/(b/2) = 0.630$

$y/(b/2) = 0.963$

$\alpha = 3.9°$

(f) Continued.

Figure 13.- Continued.

○  Upper surface
⊕  Lower surface
------  $C_{p,sonic}$

y/(b/2) = 0.259

y/(b/2) = 0.444

y/(b/2) = 0.815

y/(b/2) = 0.630

y/(b/2) = 0.963

$\alpha = 5.9^{o}$
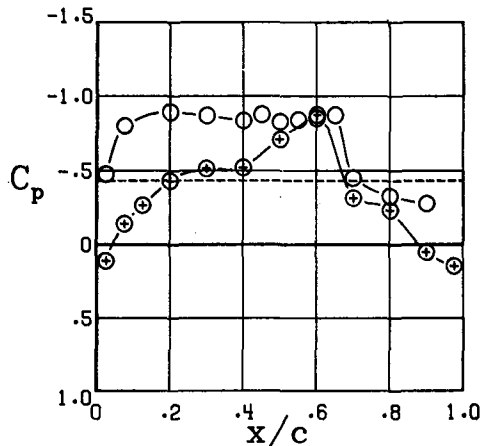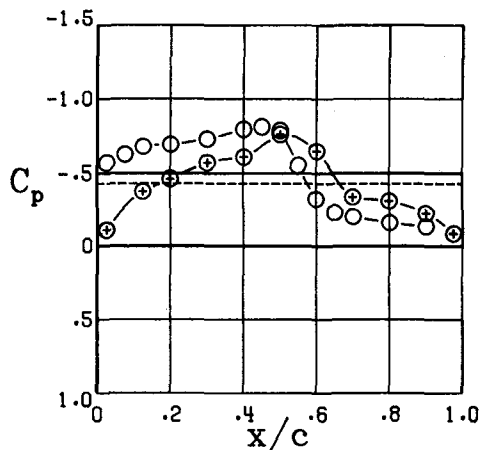
(f) Continued.

Figure 13.- Continued.
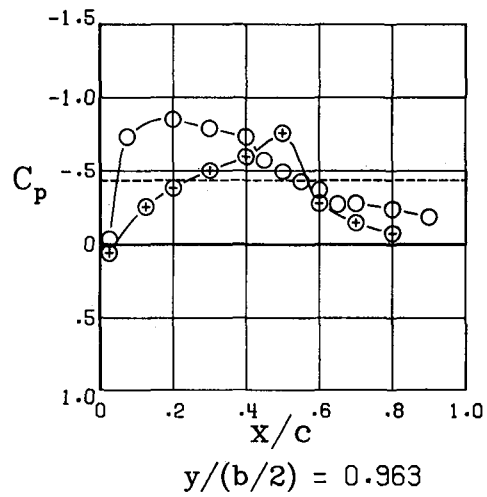
O   Upper surface
⊕   Lower surface
-----   $C_{p,sonic}$
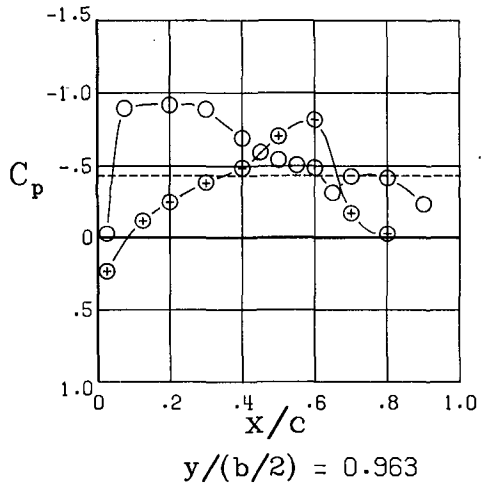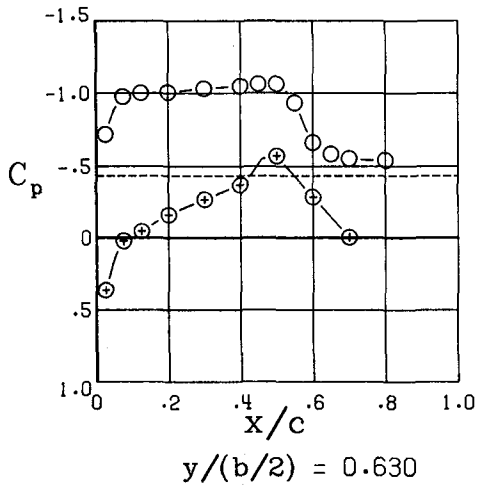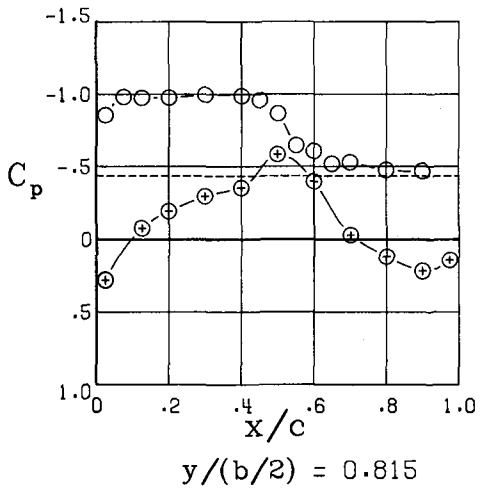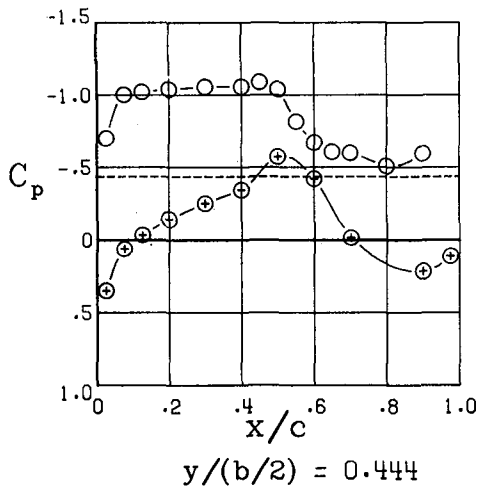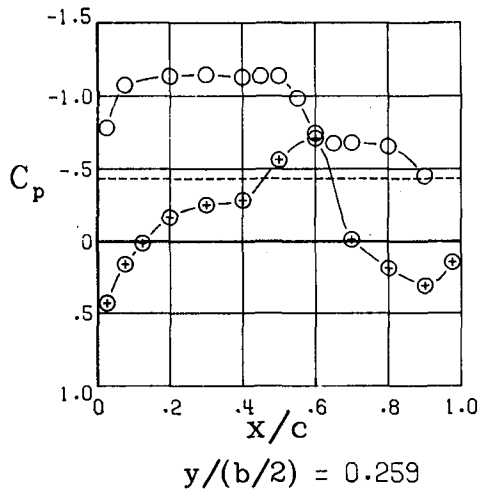
y/(b/2) = 0.259

y/(b/2) = 0.444

y/(b/2) = 0.815
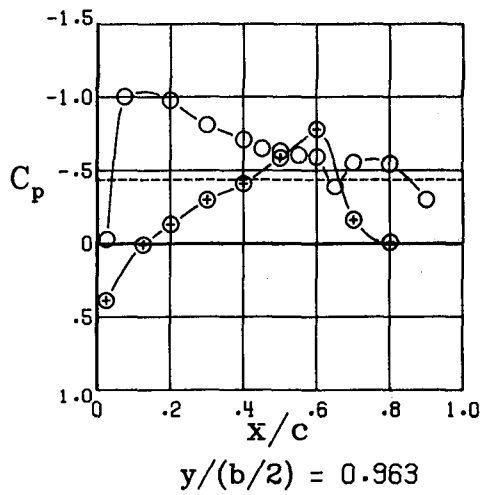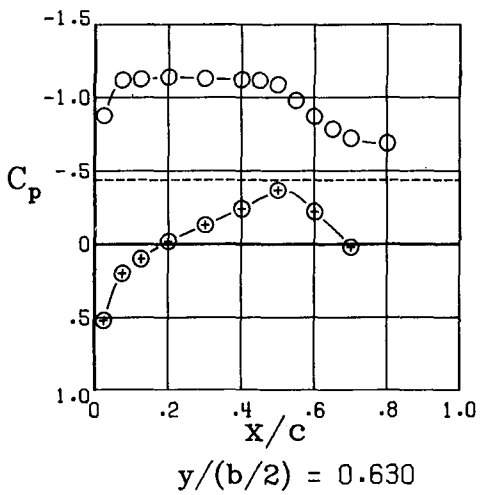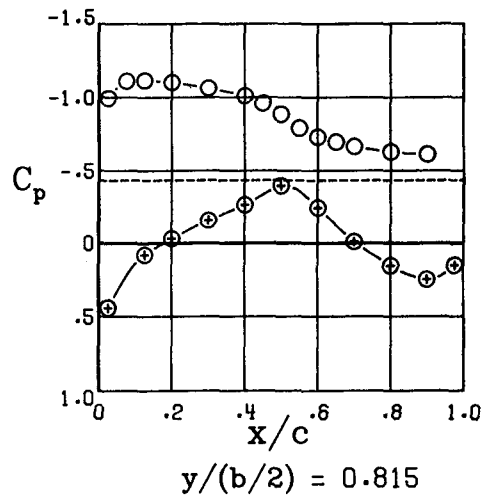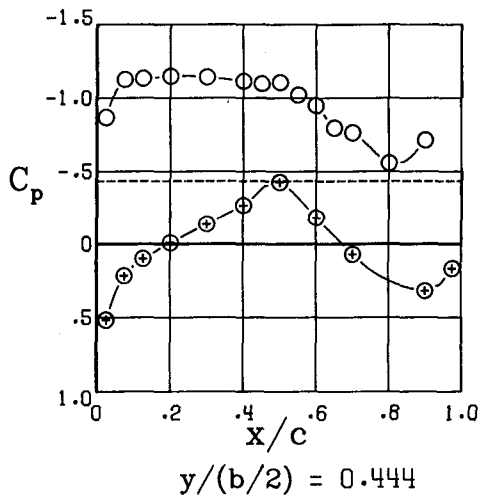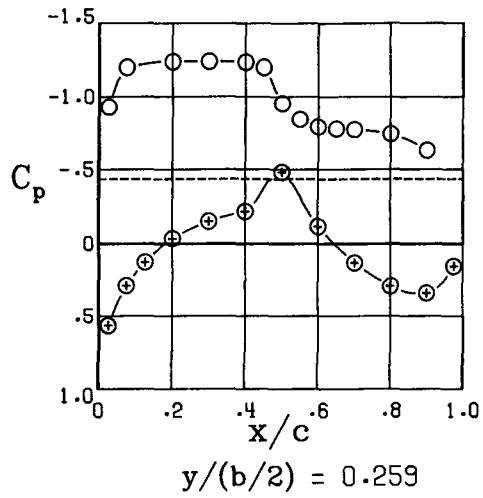
y/(b/2) = 0.630

y/(b/2) = 0.963

α = 7.9°

(f) Concluded.

Figure 13.- Continued.
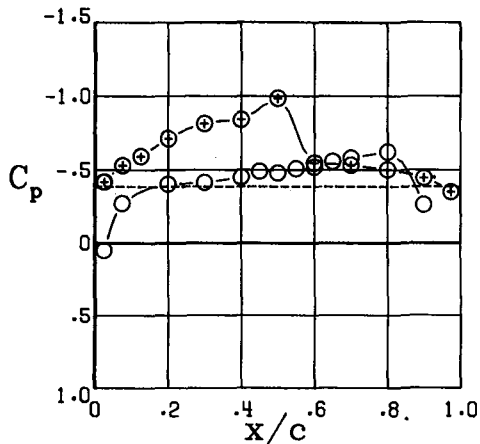
O    Upper surface
⊕    Lower surface
------    $C_{p,sonic}$

$y/(b/2) = 0.259$

$y/(b/2) = 0.444$

$y/(b/2) = 0.815$

$y/(b/2) = 0.630$

$y/(b/2) = 0.963$

$\alpha = -4.1°$

(g)    M = 0.92.

Figure 13.- Continued.

O  Upper surface
⊕  Lower surface
-----  $C_{p,sonic}$

$y/(b/2) = 0.259$

$y/(b/2) = 0.444$

$y/(b/2) = 0.815$

$y/(b/2) = 0.630$

$y/(b/2) = 0.963$

$\alpha = -2.1°$

(g) Continued.

Figure 13.- Continued.

O   Upper surface
⊕   Lower surface
----  $C_{p,sonic}$

$y/(b/2) = 0.259$

$y/(b/2) = 0.444$

$y/(b/2) = 0.815$

$y/(b/2) = 0.630$

$y/(b/2) = 0.963$

$\alpha = -0.1°$

(g) Continued.

Figure 13.- Continued.

Legend:
O   Upper surface
⊕   Lower surface
----- $C_{p,sonic}$

y/(b/2) = 0.259

y/(b/2) = 0.444

y/(b/2) = 0.815

y/(b/2) = 0.630

y/(b/2) = 0.963

$\alpha = 1.9°$

(g) Continued.

Figure 13.- Continued.

Figure 13.- Continued.

O  Upper surface
⊕  Lower surface
-----  $C_{p,sonic}$

$y/(b/2) = 0.259$

$y/(b/2) = 0.444$

$y/(b/2) = 0.815$

$y/(b/2) = 0.630$

$y/(b/2) = 0.963$

$\alpha = 4.0^0$

(g) Continued.

Figure 13.- Continued.

$y/(b/2) = 0.259$

O  Upper surface
⊕  Lower surface
------ $C_{p,sonic}$

$y/(b/2) = 0.444$

$y/(b/2) = 0.815$

$y/(b/2) = 0.630$

$y/(b/2) = 0.963$

$\alpha = 6.0^0$
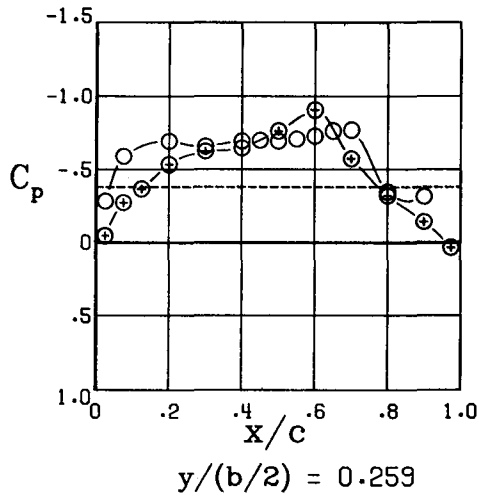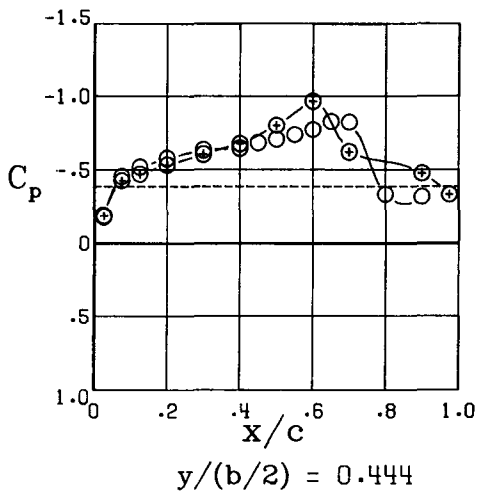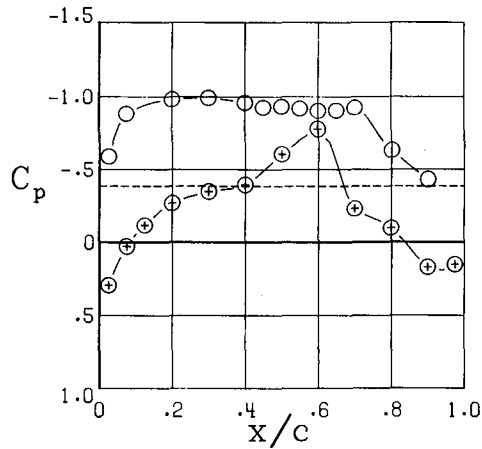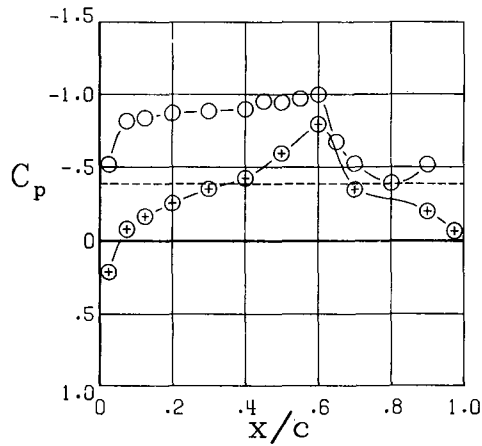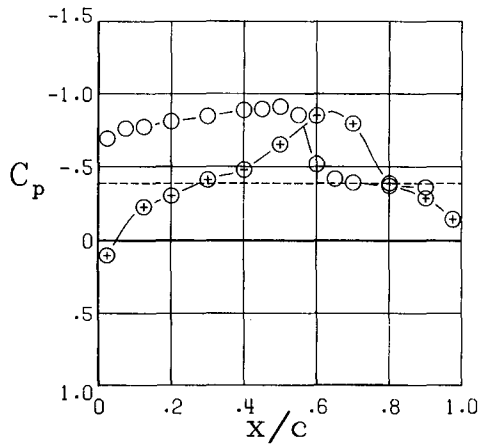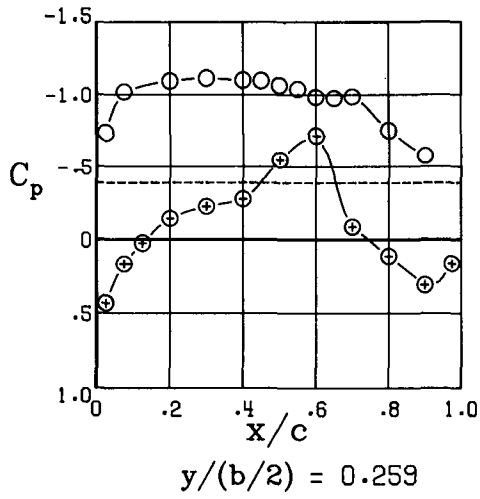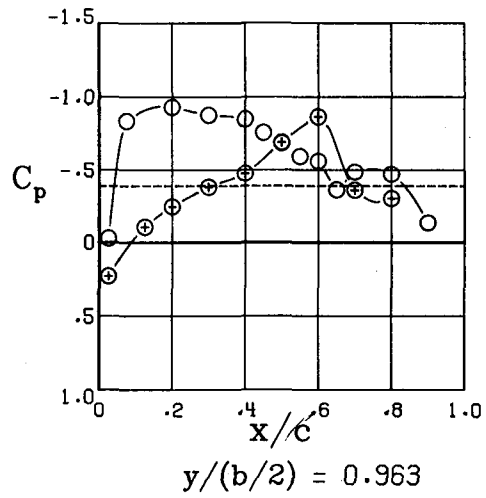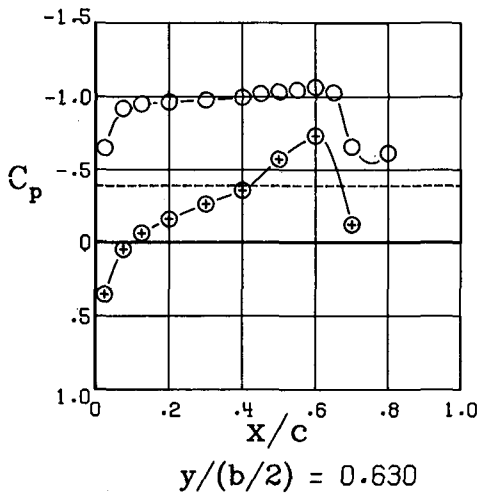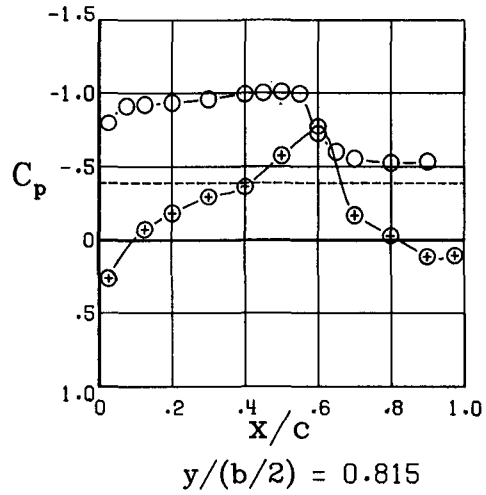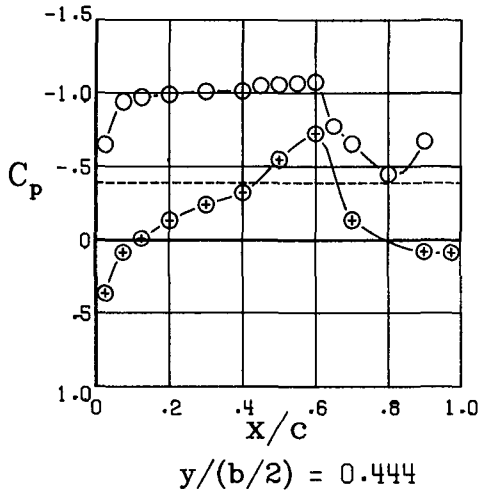
(g) Concluded.

Figure 13.- Concluded.
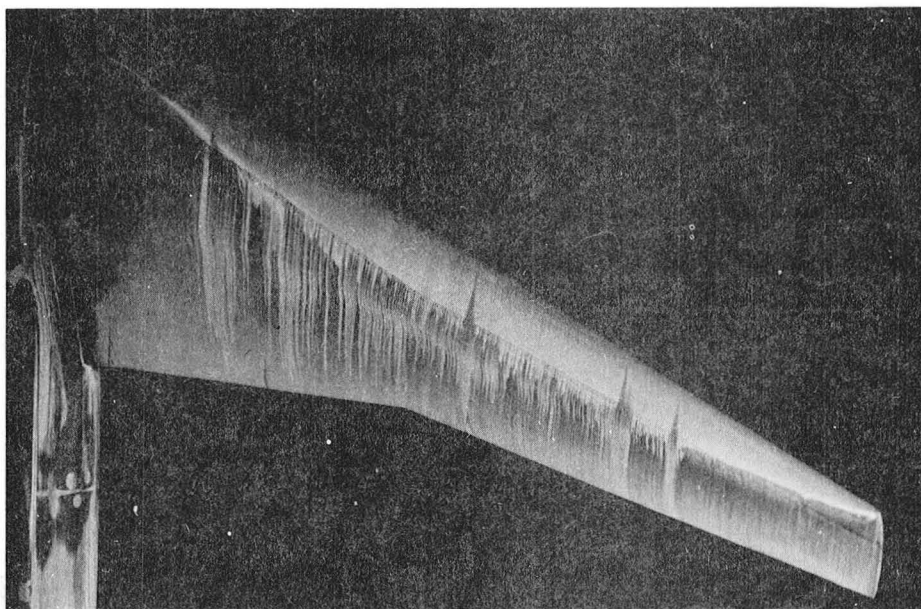
Upper surface
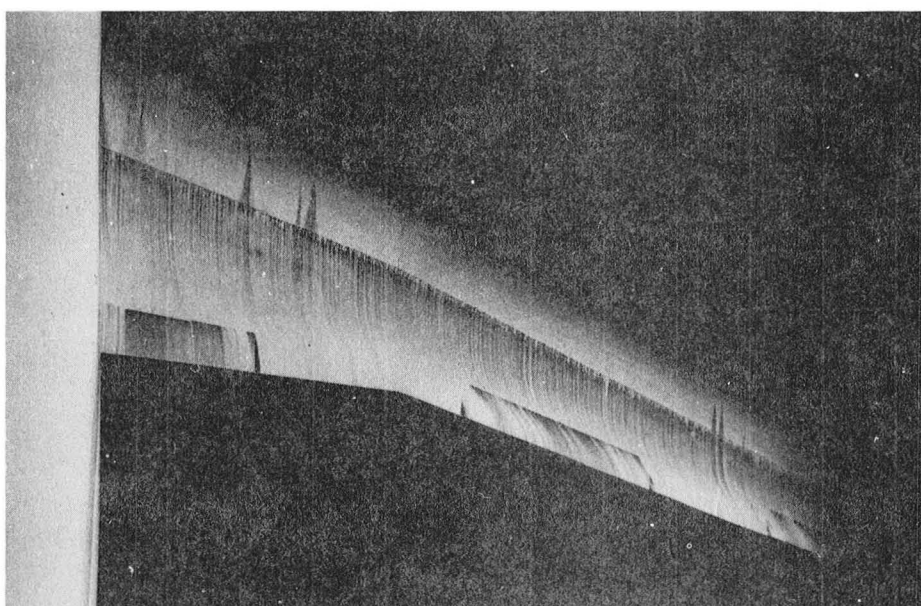


Lower surface

L-83-69

(a)  $\alpha = 1.5°$;  $C_L = 0.564$.

Figure 14.- Fluorescent-oil flow visualization photographs of model
configuration A.  M = 0.80.
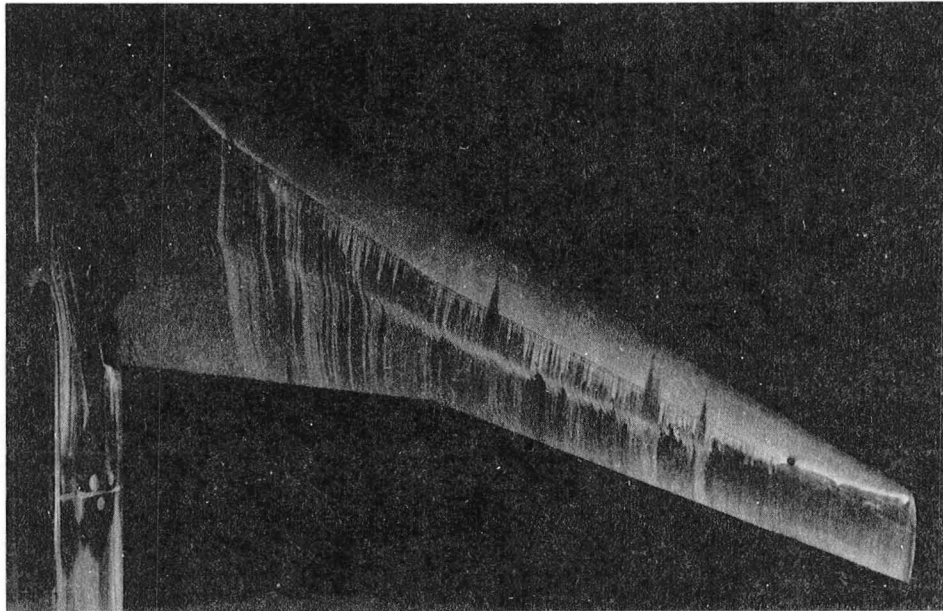
Upper surface
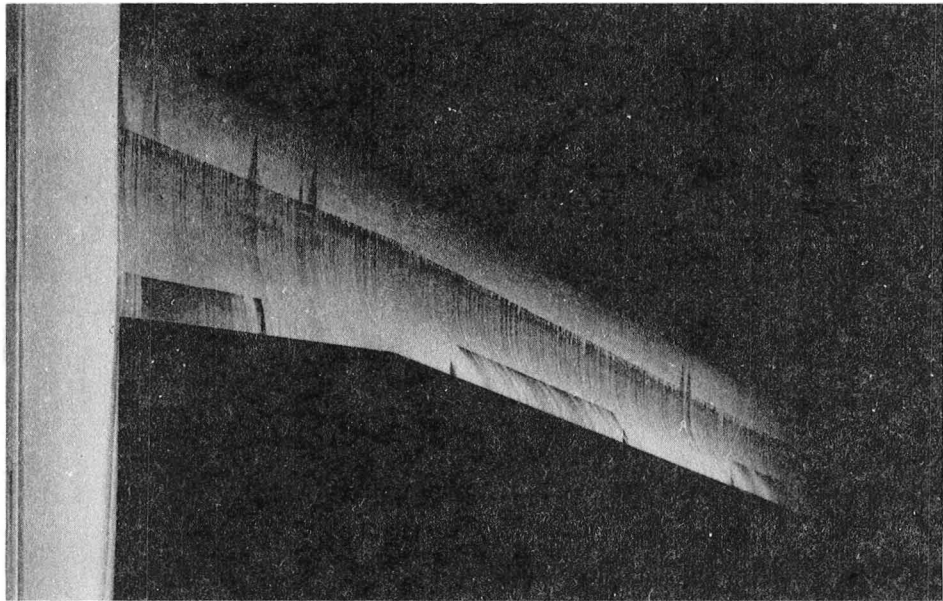


Lower surface

L-83-70

(b)   $\alpha = 1.9°$;   $C_L = 0.627$.

Figure 14.- Continued.
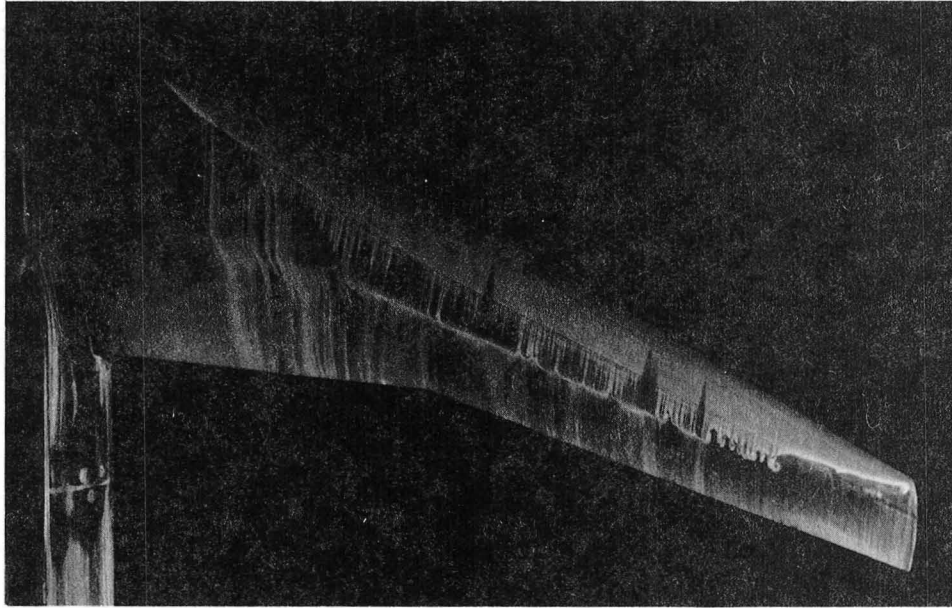
Upper surface
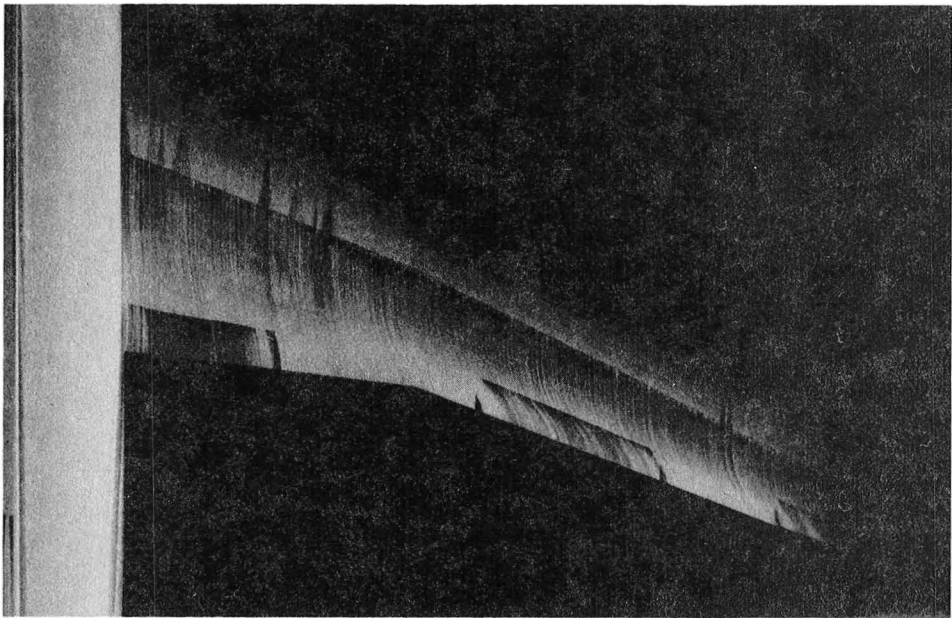


Lower surface

L-83-71

(c)  $\alpha = 2.4°$;  $C_L = 0.724$.

Figure 14.- Concluded.

112
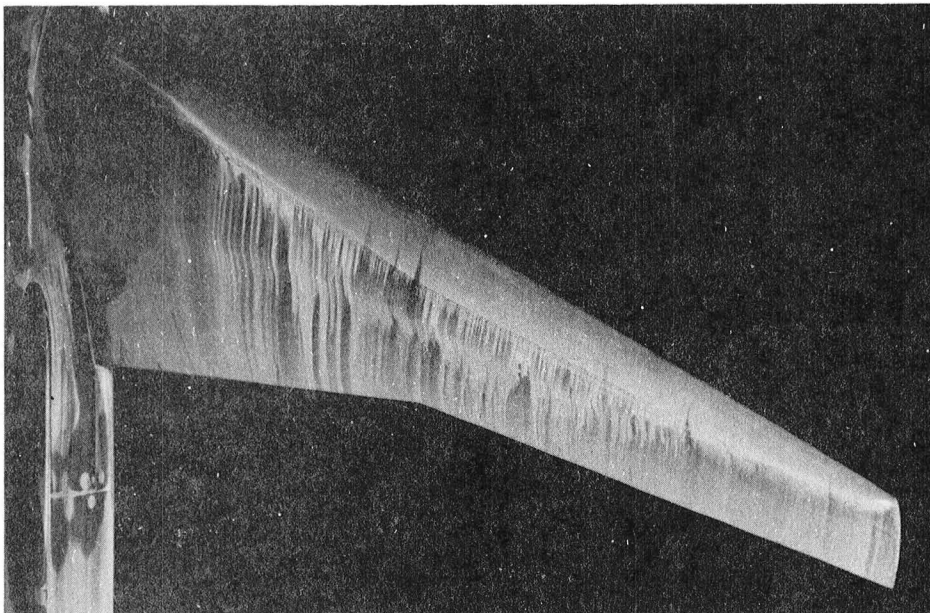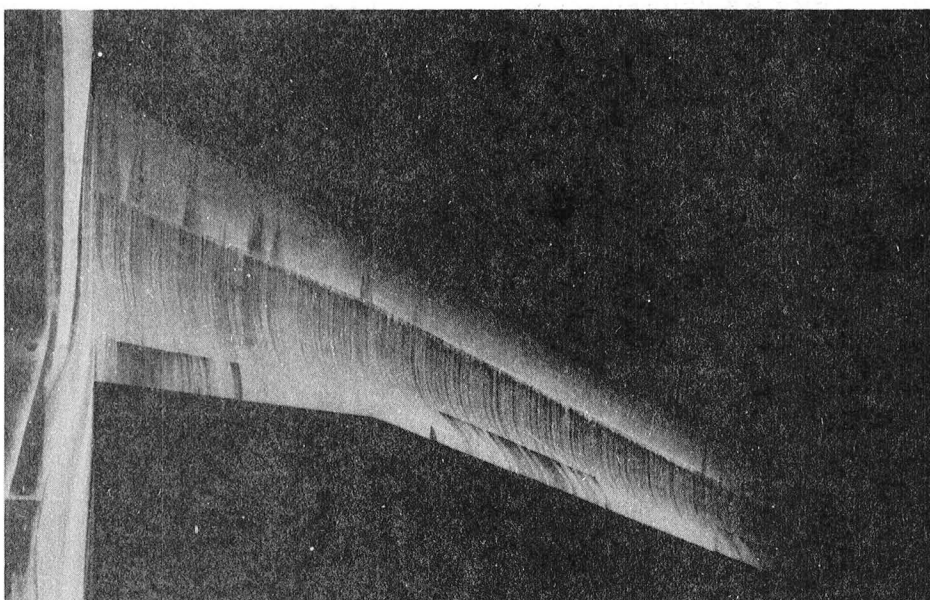
Upper surface



Lower surface

L-83-72

(a)  $\alpha = 1.4°$;   $C_L = 0.528$.

Figure 15.- Fluorescent-oil flow visualization photographs of model
configuration B.  M = 0.80.
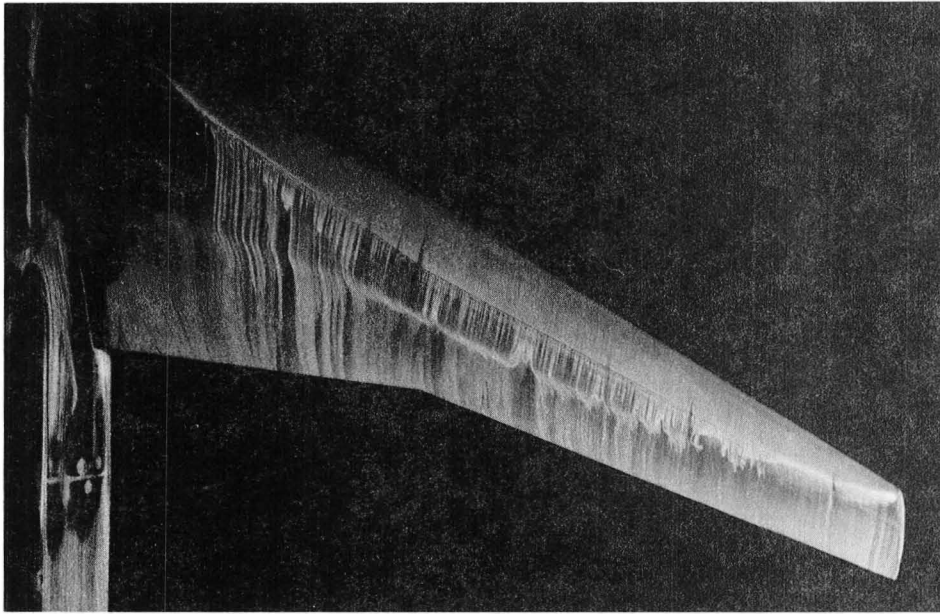
Upper surface
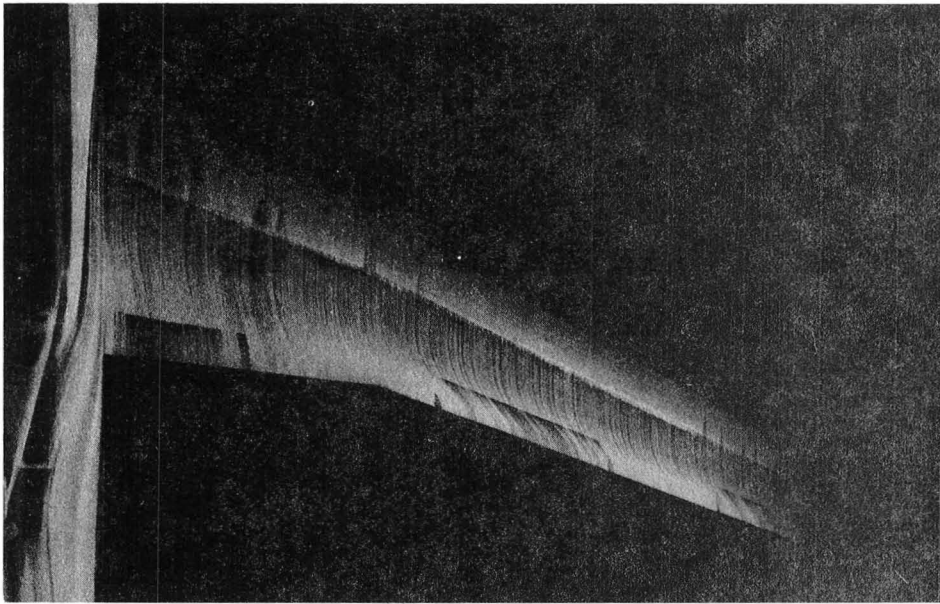


Lower surface

L-83-73

(b)  $\alpha = 1.9°$;  $C_L = 0.612$.

Figure 15.- Continued.
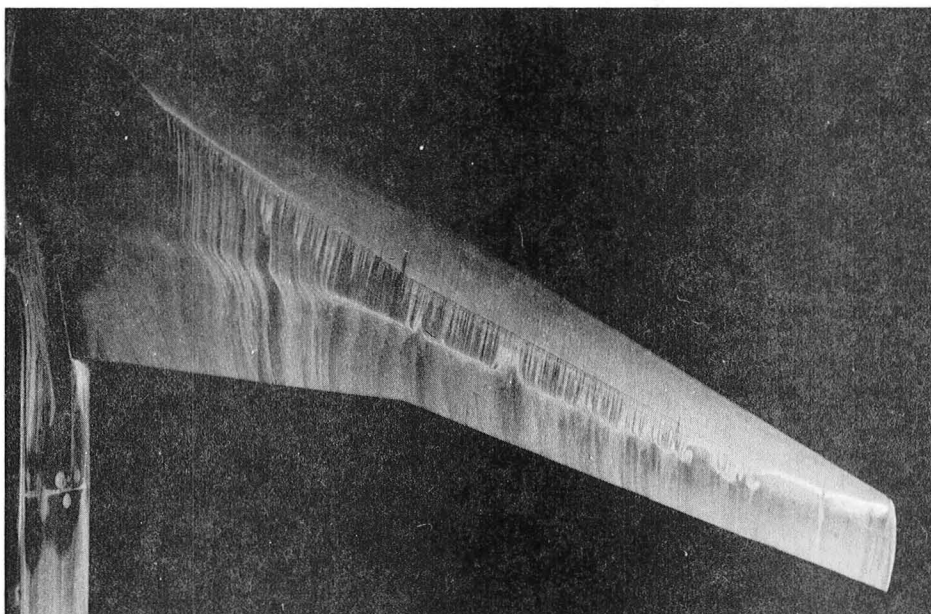
Upper surface
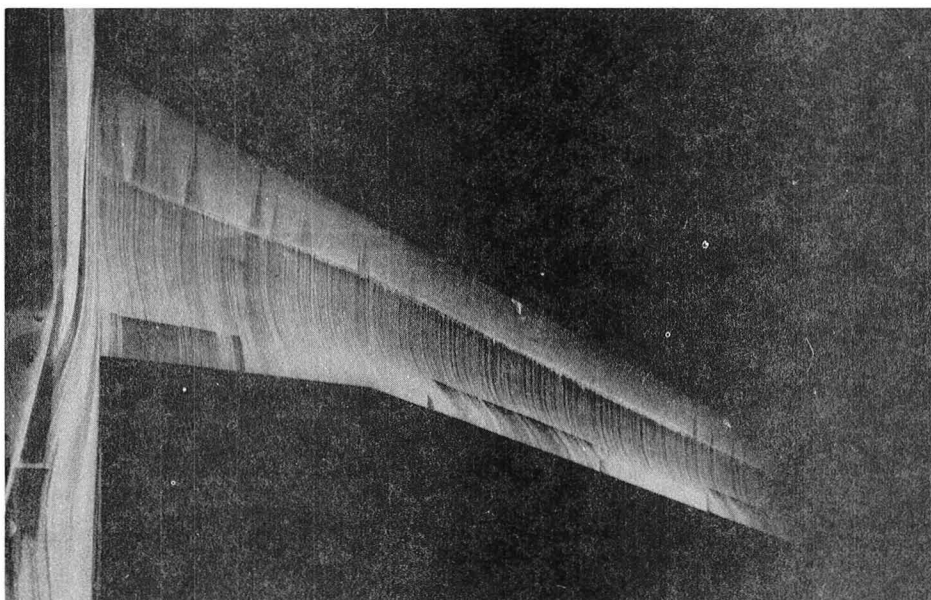


Lower surface

L-83-74

(c)   $\alpha = 2.4°$;   $C_L = 0.694$.
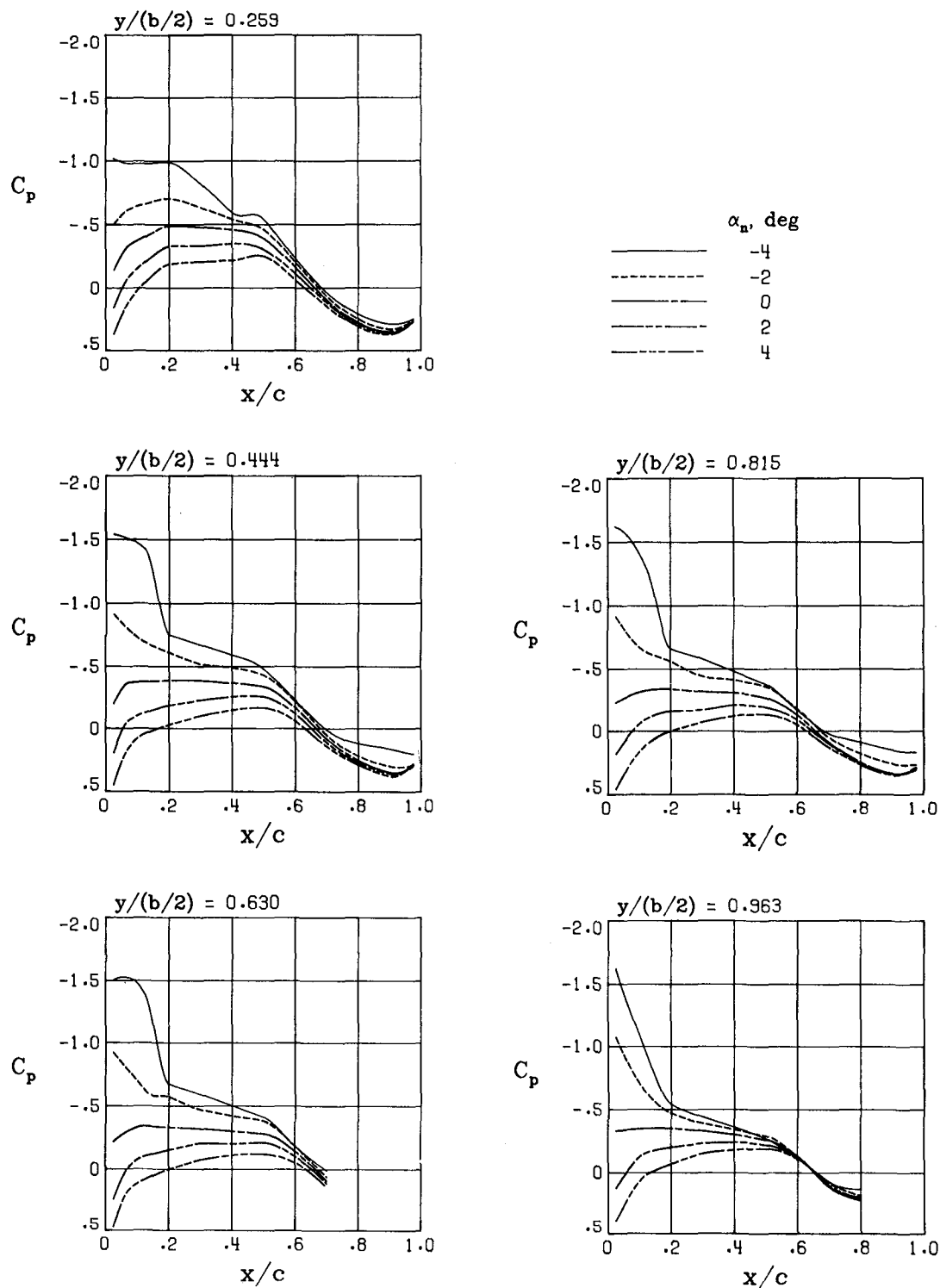
Figure 15.- Concluded.
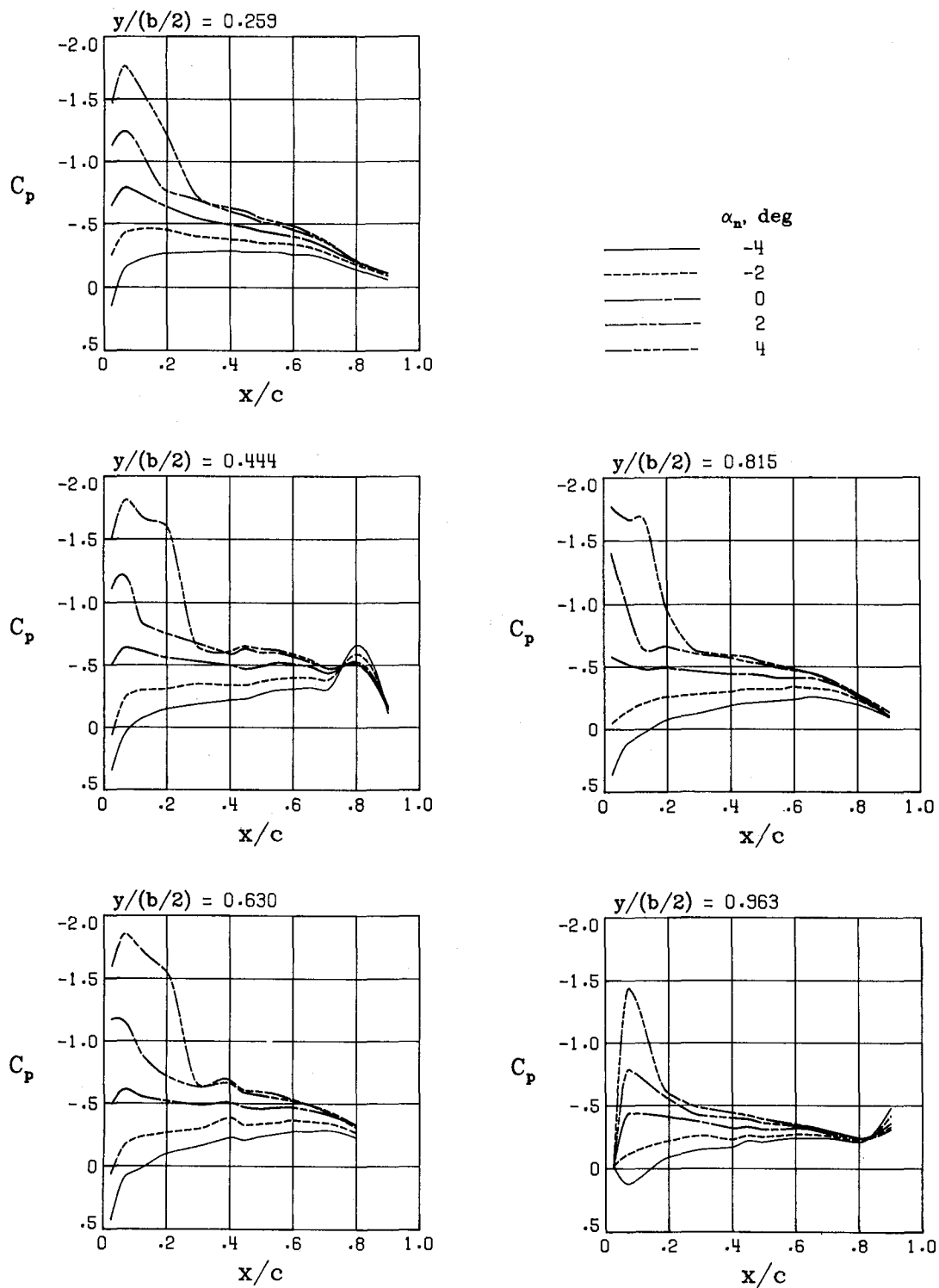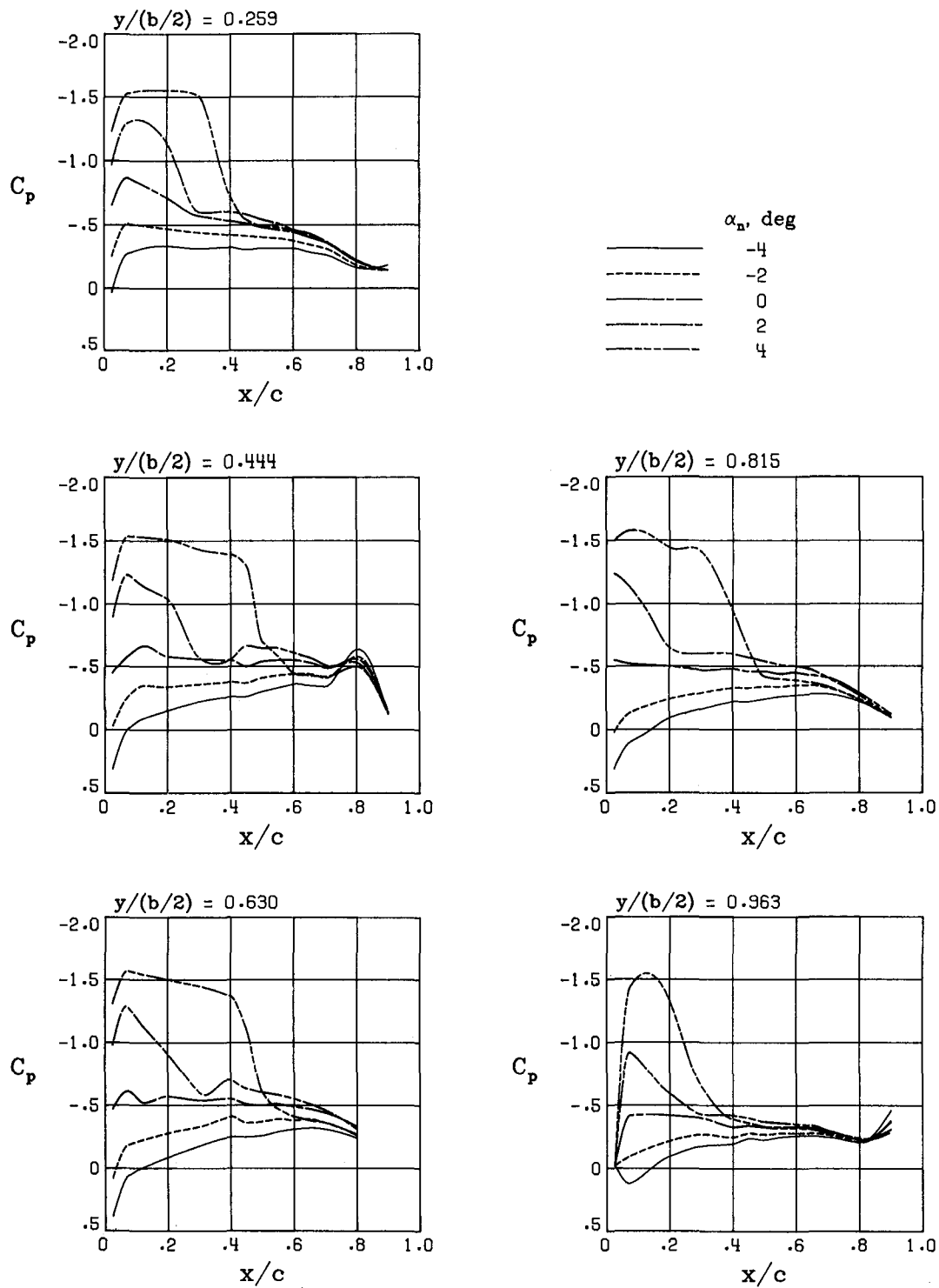
Upper surface pressures

(a)   M = 0.70.

Figure 16.- Effect of angle of attack on wing-surface pressure
distributions for model configuration A.
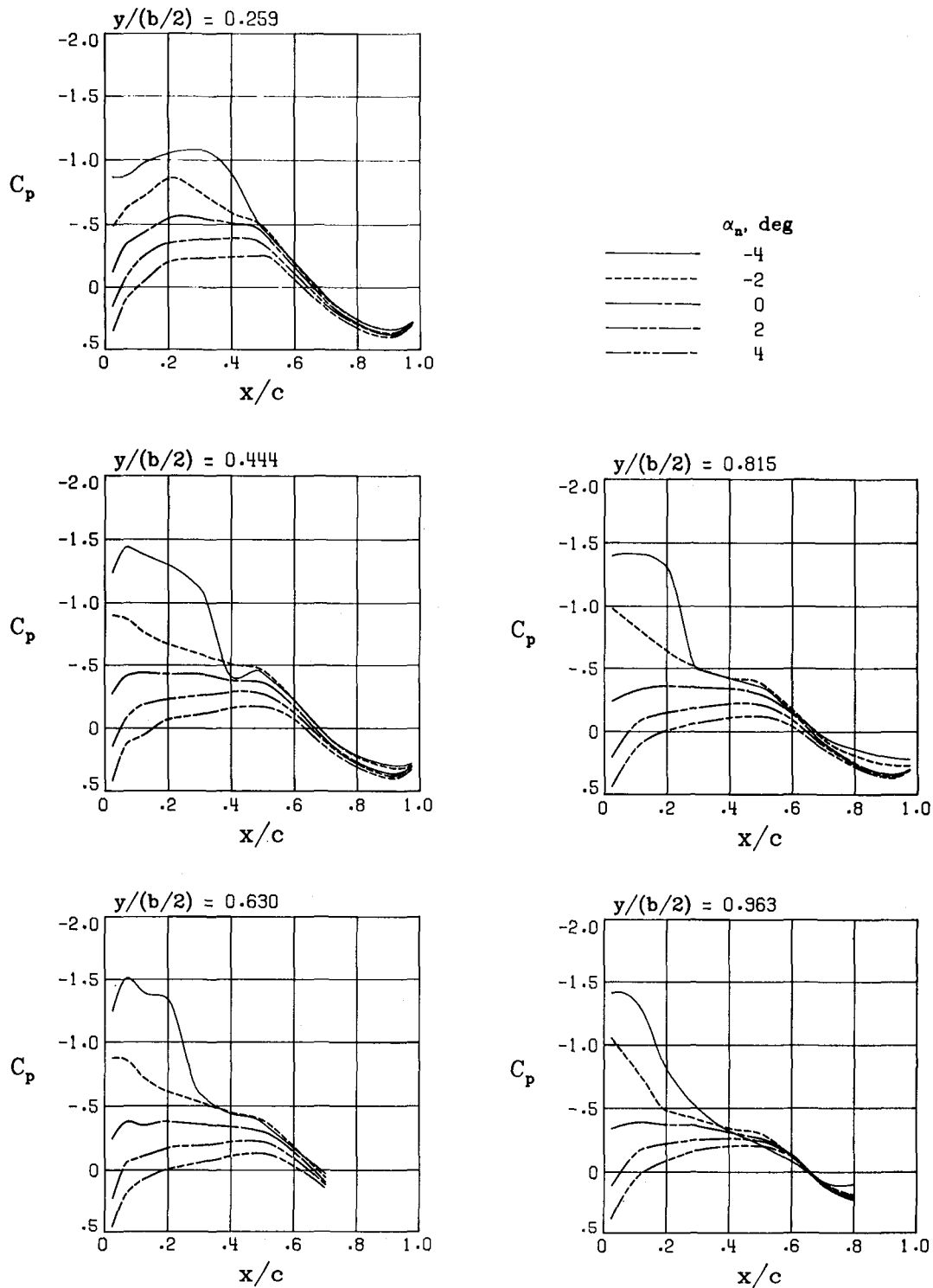
Lower surface pressures
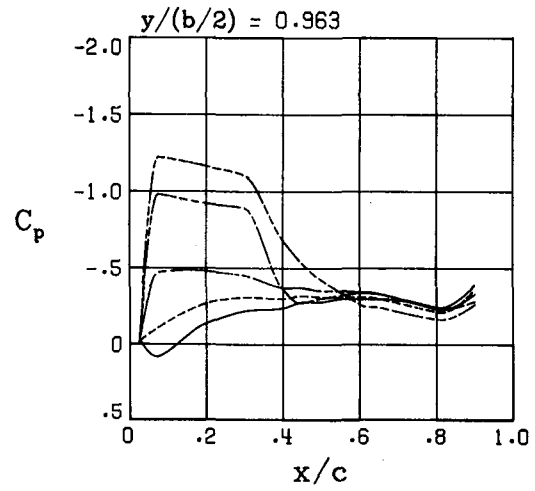
(a) Concluded.

Figure 16.- Continued.

y/(b/2) = 0.259

y/(b/2) = 0.444

y/(b/2) = 0.815

y/(b/2) = 0.630

y/(b/2) = 0.963

$\alpha_n$, deg

$-4$
$-2$
$0$
$2$
$4$
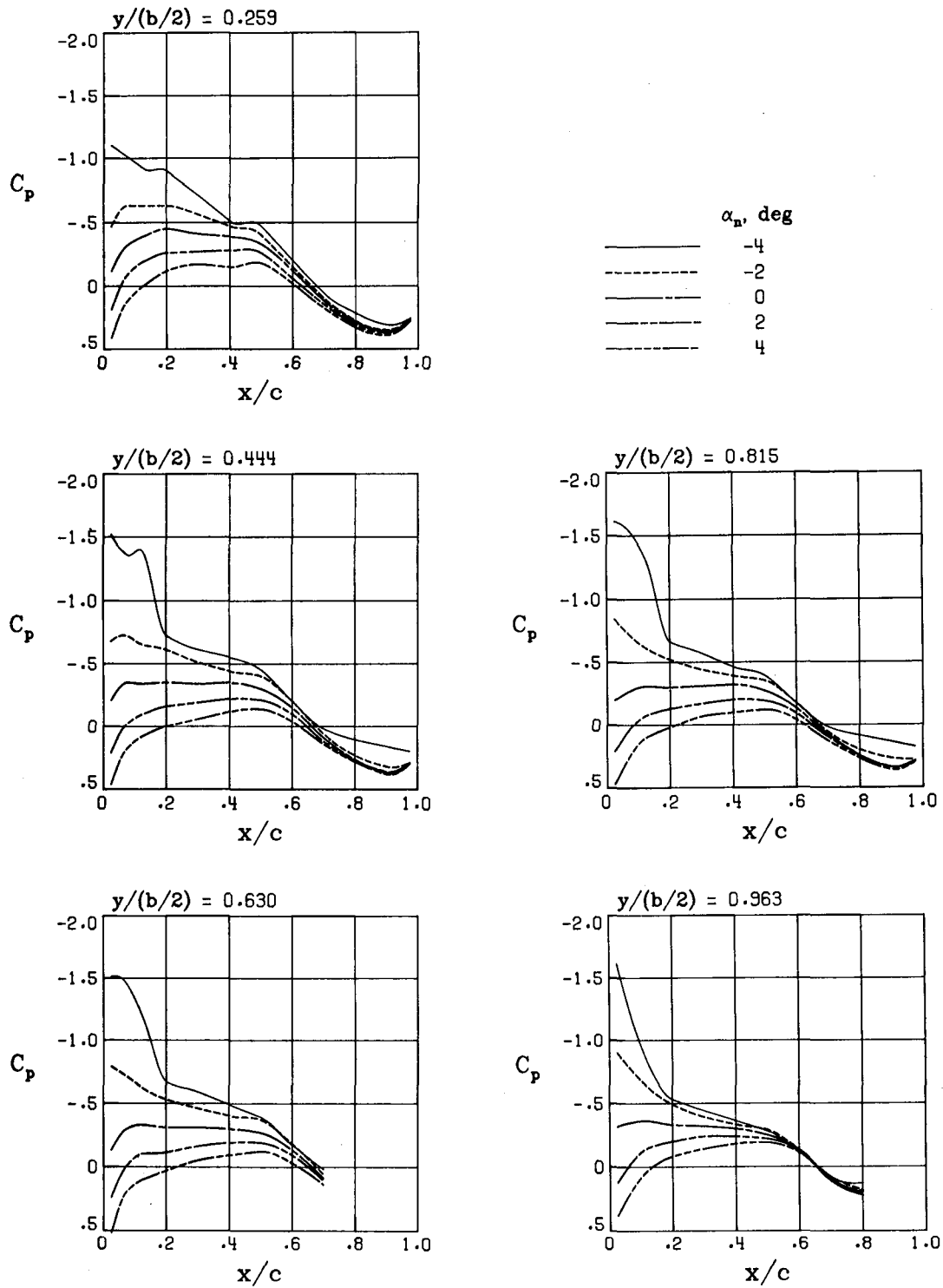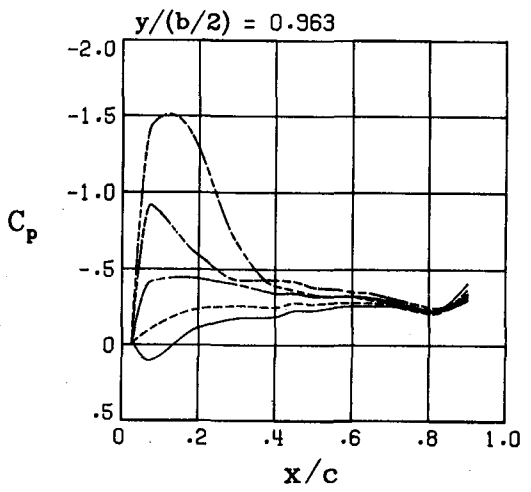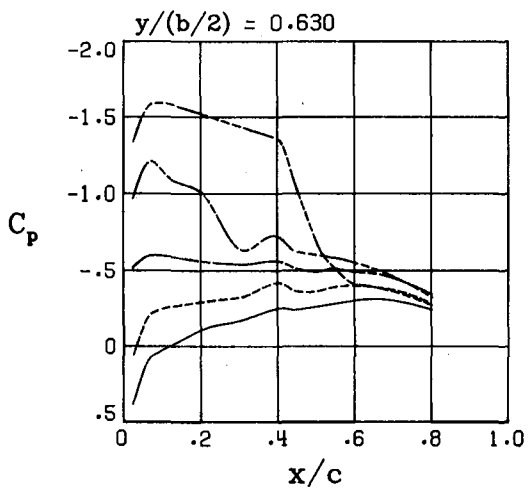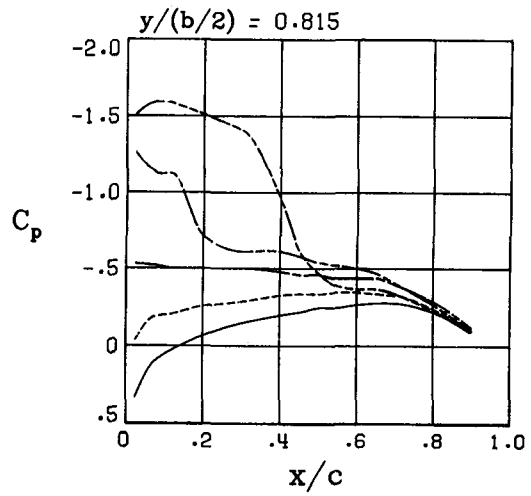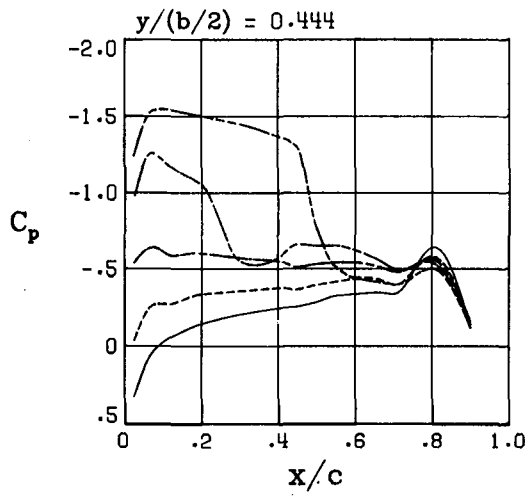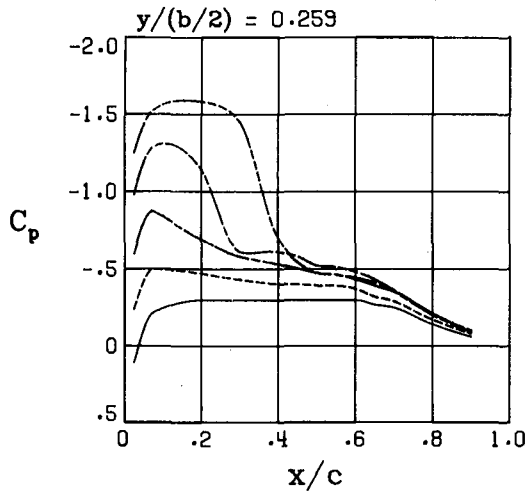
Upper surface pressures

(b)   M = 0.75.

Figure 16.- Continued.
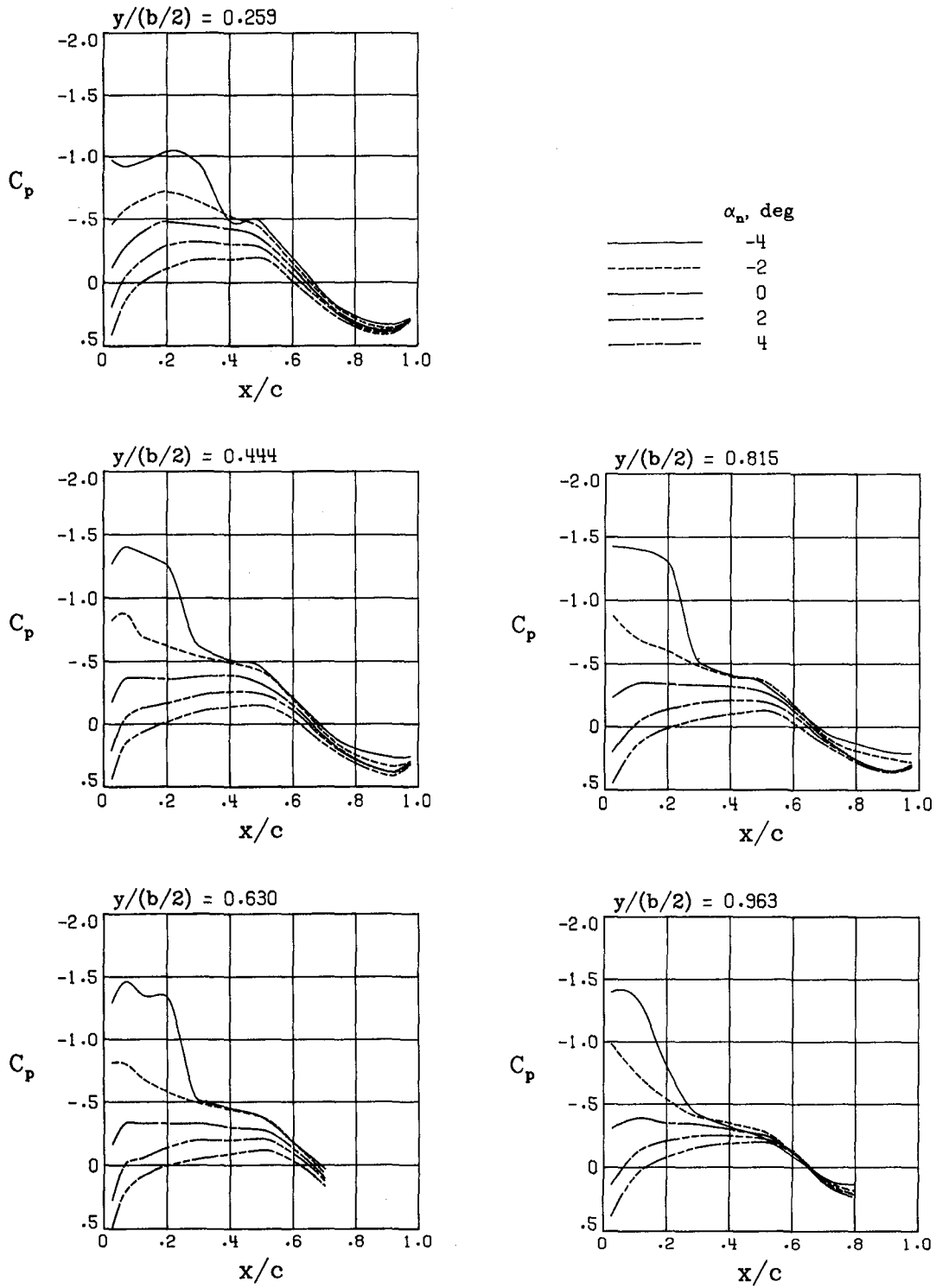
y/(b/2) = 0.259

$C_p$

x/c

$\alpha_n$, deg
−4
−2
0
2
4

y/(b/2) = 0.444

$C_p$

x/c

y/(b/2) = 0.815

$C_p$

x/c

y/(b/2) = 0.630

$C_p$

x/c

y/(b/2) = 0.963

$C_p$

x/c

Lower surface pressures

(b) Concluded.

Figure 16.- Continued.

119
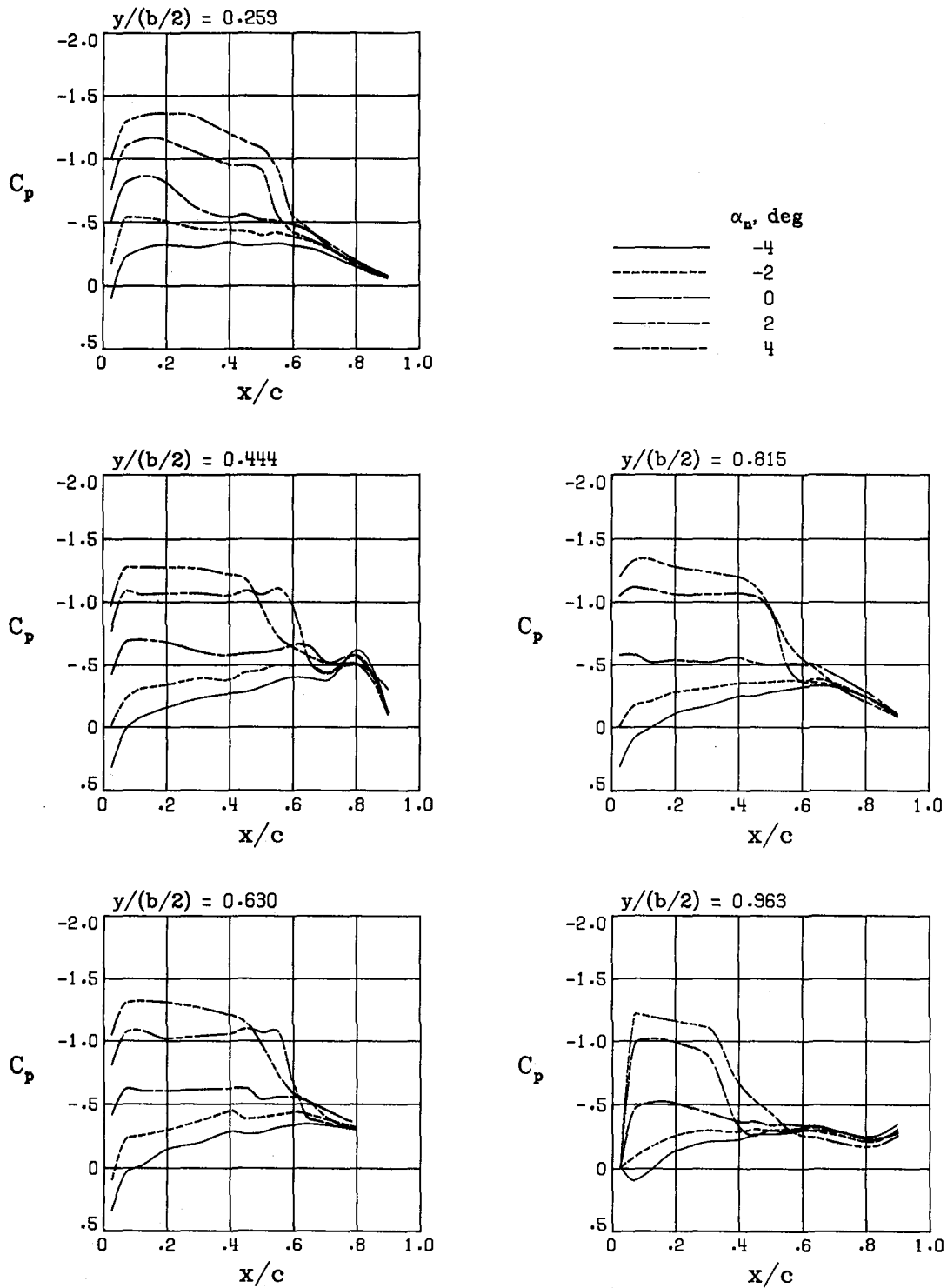
Upper surface pressures

(c)  M = 0.80.

Figure 16.- Continued.
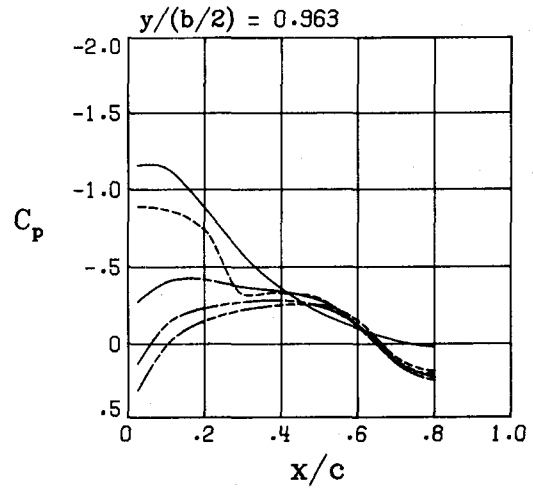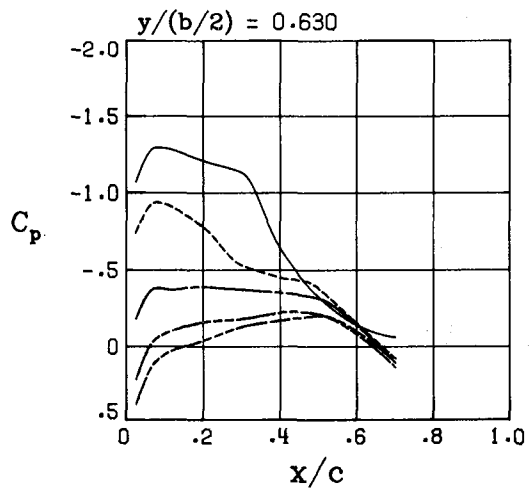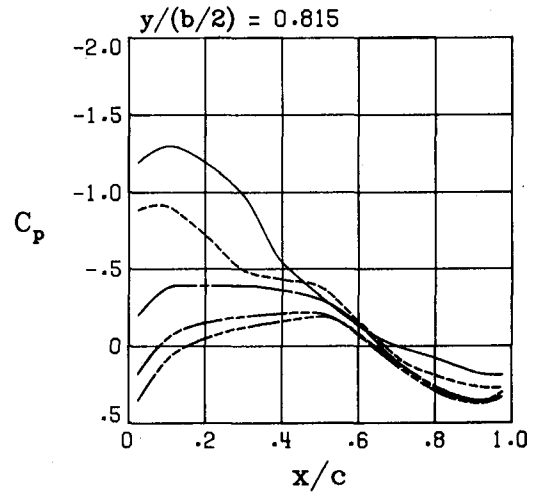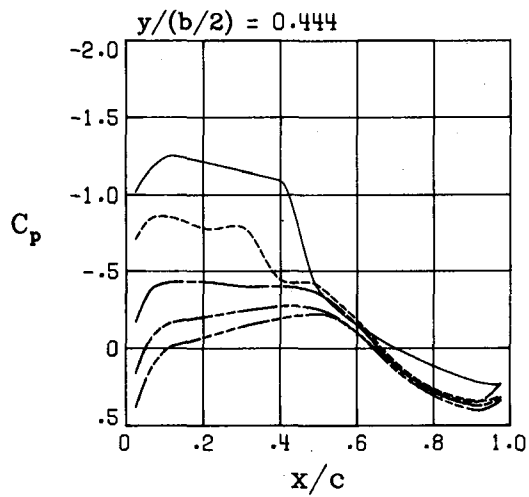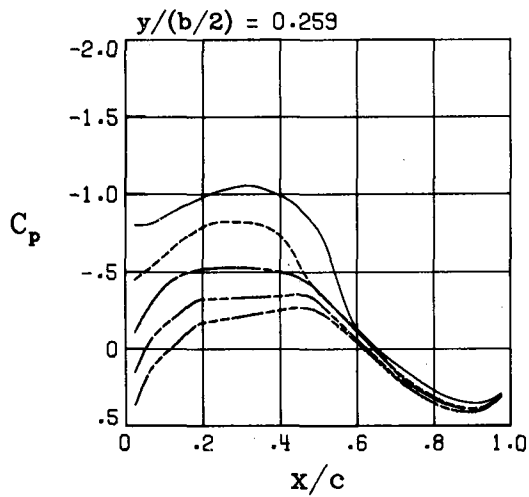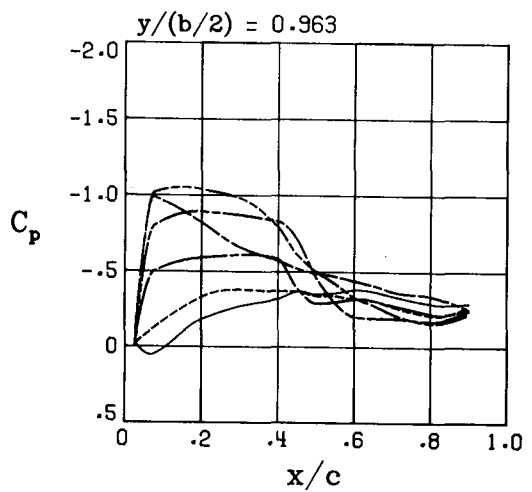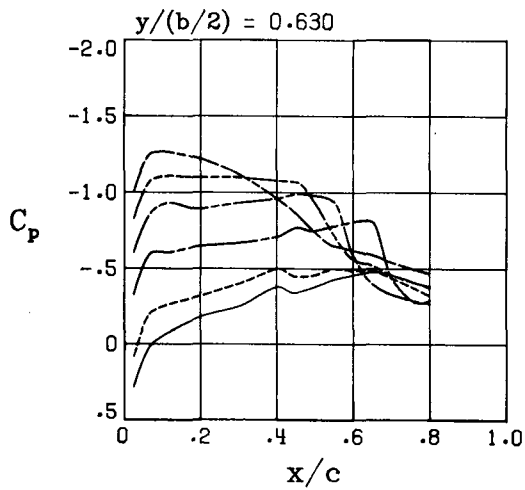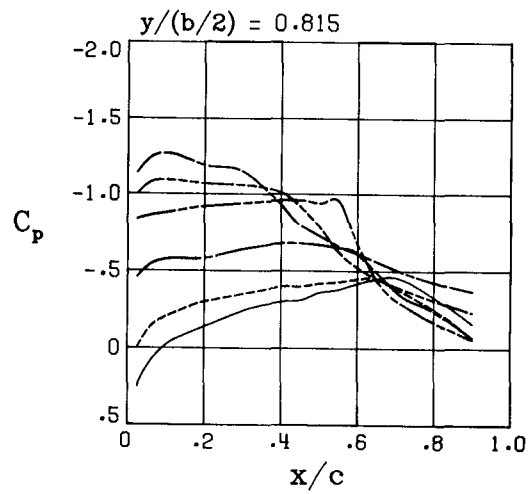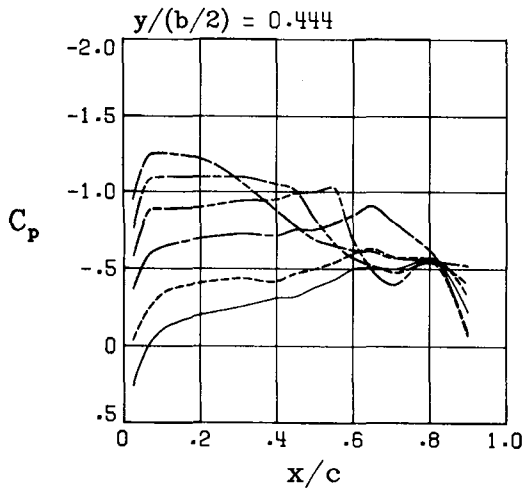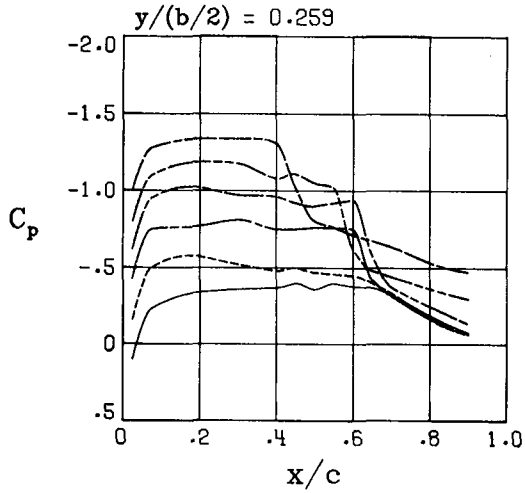
y/(b/2) = 0.259

y/(b/2) = 0.444

y/(b/2) = 0.815

y/(b/2) = 0.630

y/(b/2) = 0.963

$\alpha_n$, deg

−4

−2

0

2

4

Lower surface pressures

(c) Concluded.

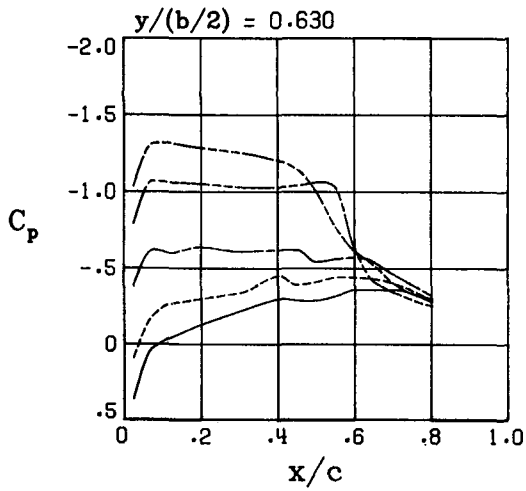Figure 16.− Continued.

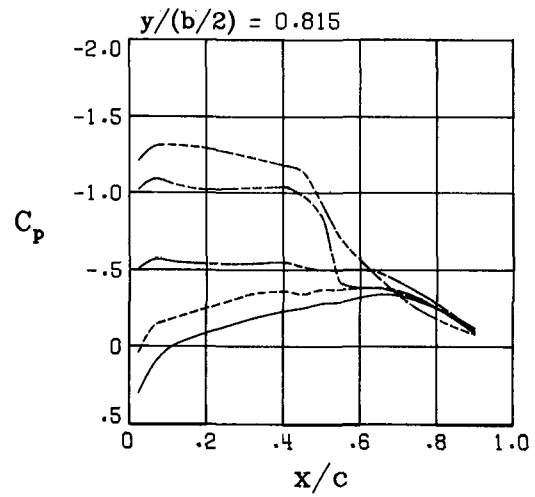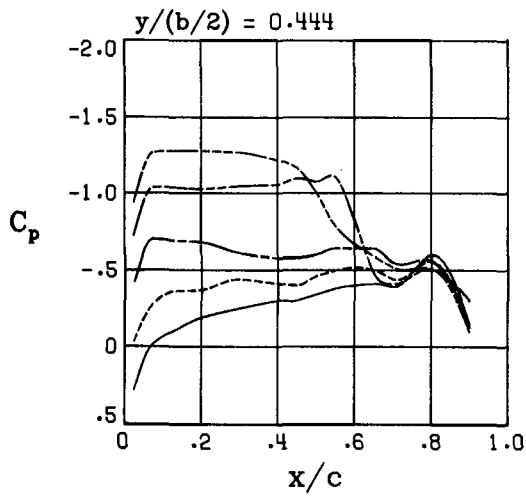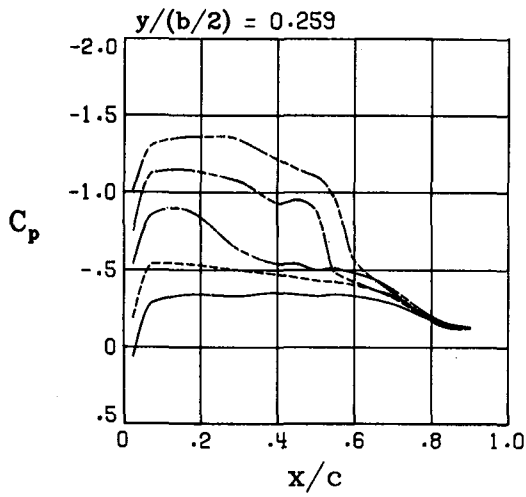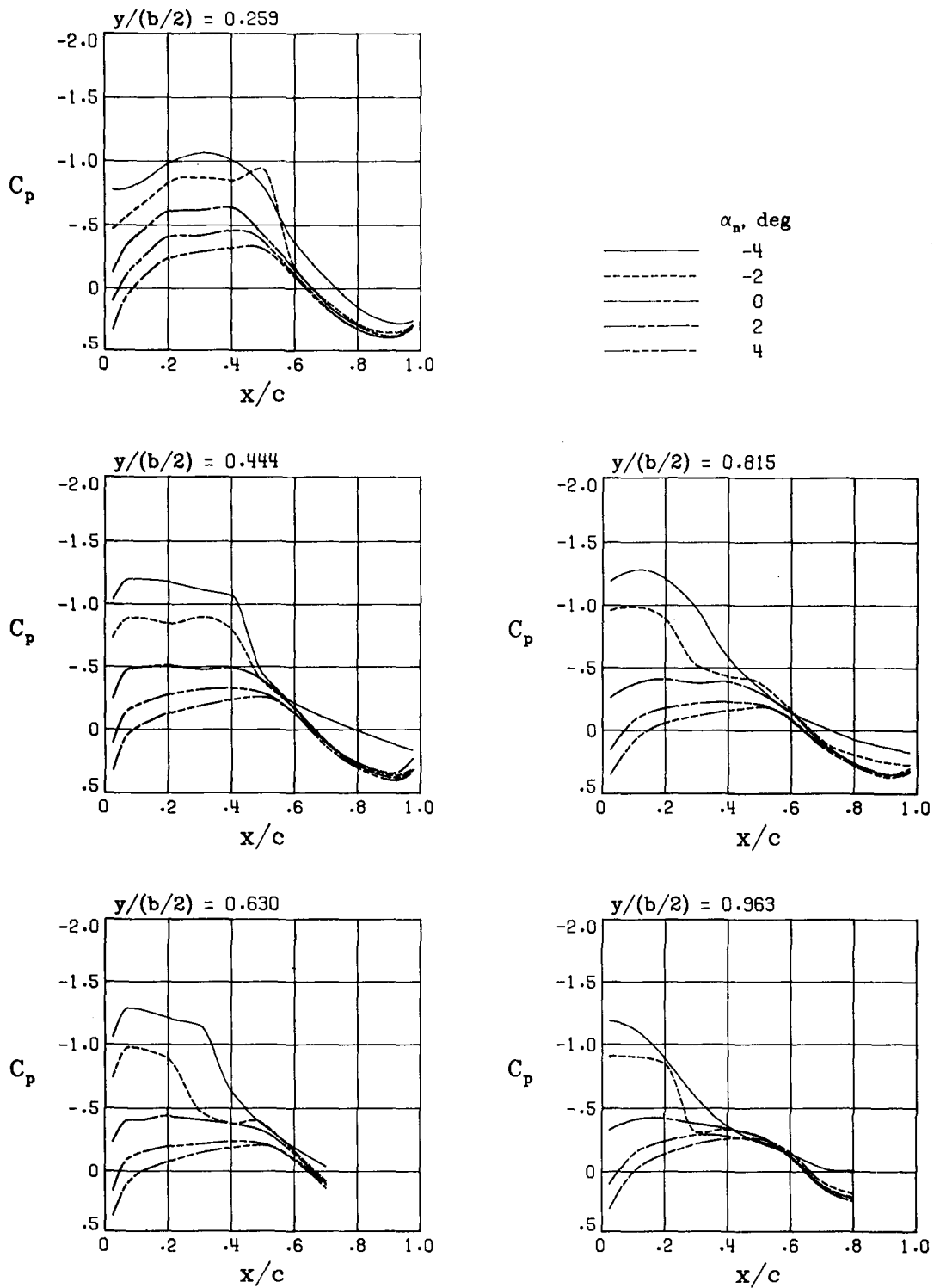Upper surface pressures

(d) M = 0.84.

Figure 16.- Continued.

Lower surface pressures
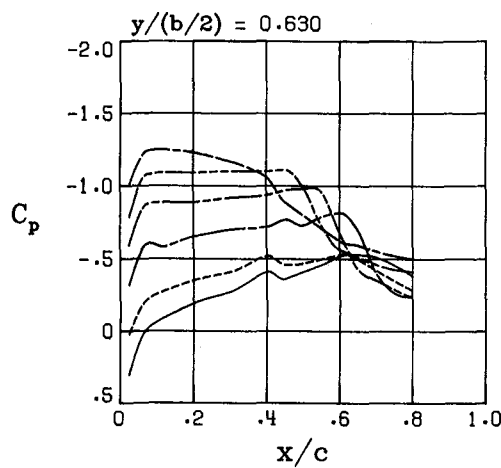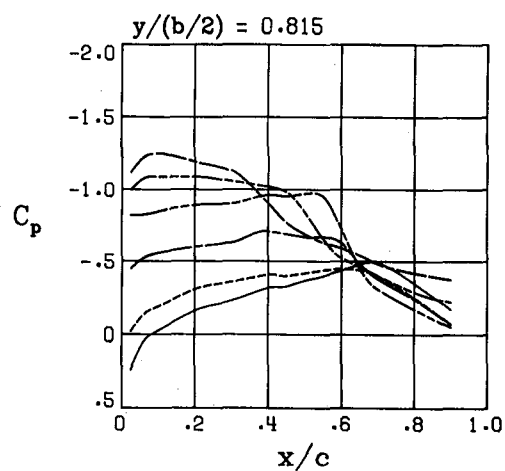
(d) Concluded.

Figure 16.- Continued.

y/(b/2) = 0.259

$C_p$

-2.0
-1.5
-1.0
-.5
0
.5

0  .2  .4  .6  .8  1.0

x/c

$\alpha_n$, deg

—————  -4
- - - - -  -2
— — —  0
— · —  2
— — —  4
— — —  6
— — —  8

y/(b/2) = 0.444

$C_p$

-2.0
-1.5
-1.0
-.5
0
.5

0  .2  .4  .6  .8  1.0

x/c

y/(b/2) = 0.815

$C_p$

-2.0
-1.5
-1.0
-.5
0
.5

0  .2  .4  .6  .8  1.0

x/c

y/(b/2) = 0.630

$C_p$

-2.0
-1.5
-1.0
-.5
0
.5

0  .2  .4  .6  .8  1.0

x/c

y/(b/2) = 0.963

$C_p$

-2.0
-1.5
-1.0
-.5
0
.5

0  .2  .4  .6  .8  1.0

x/c
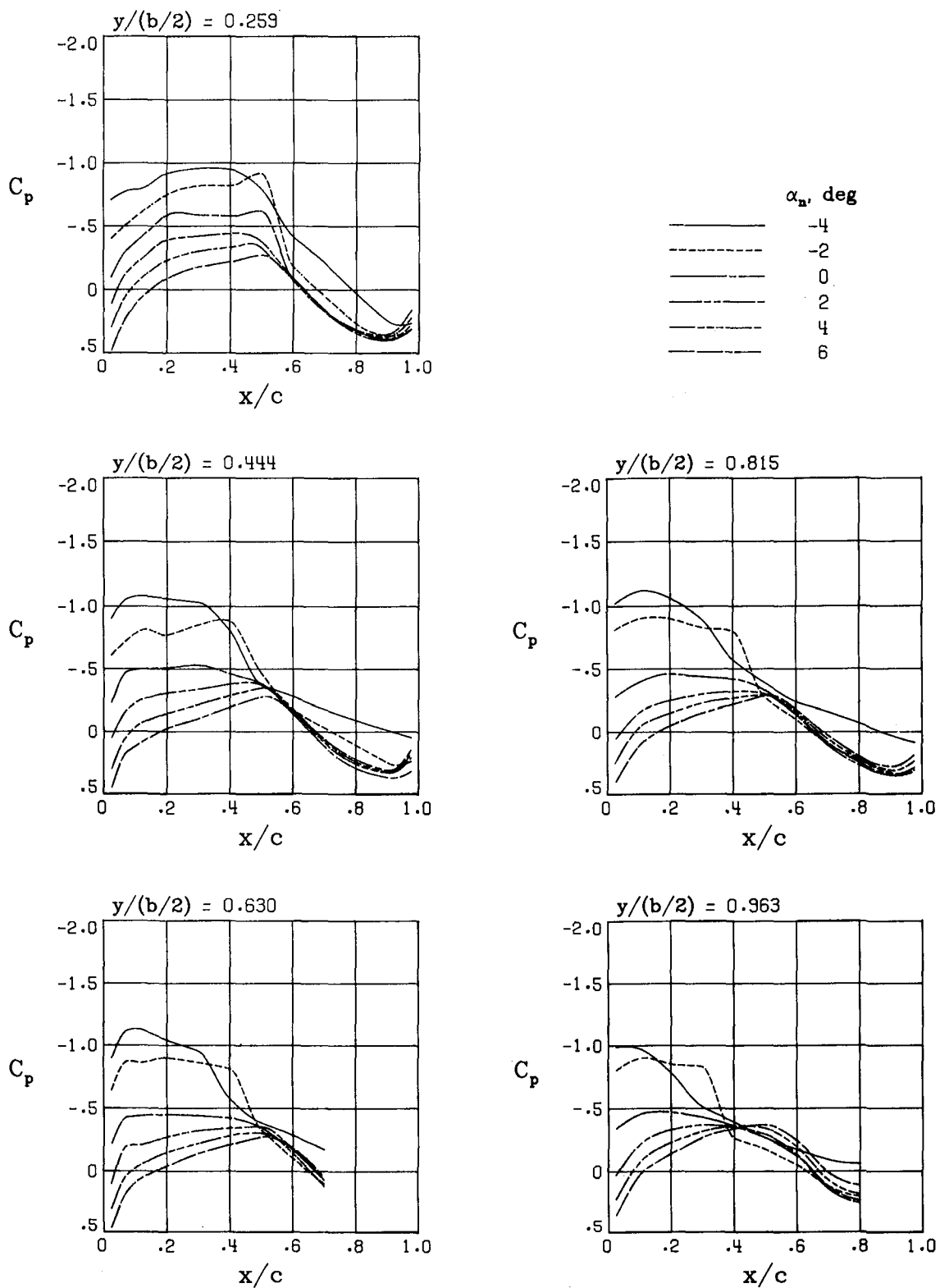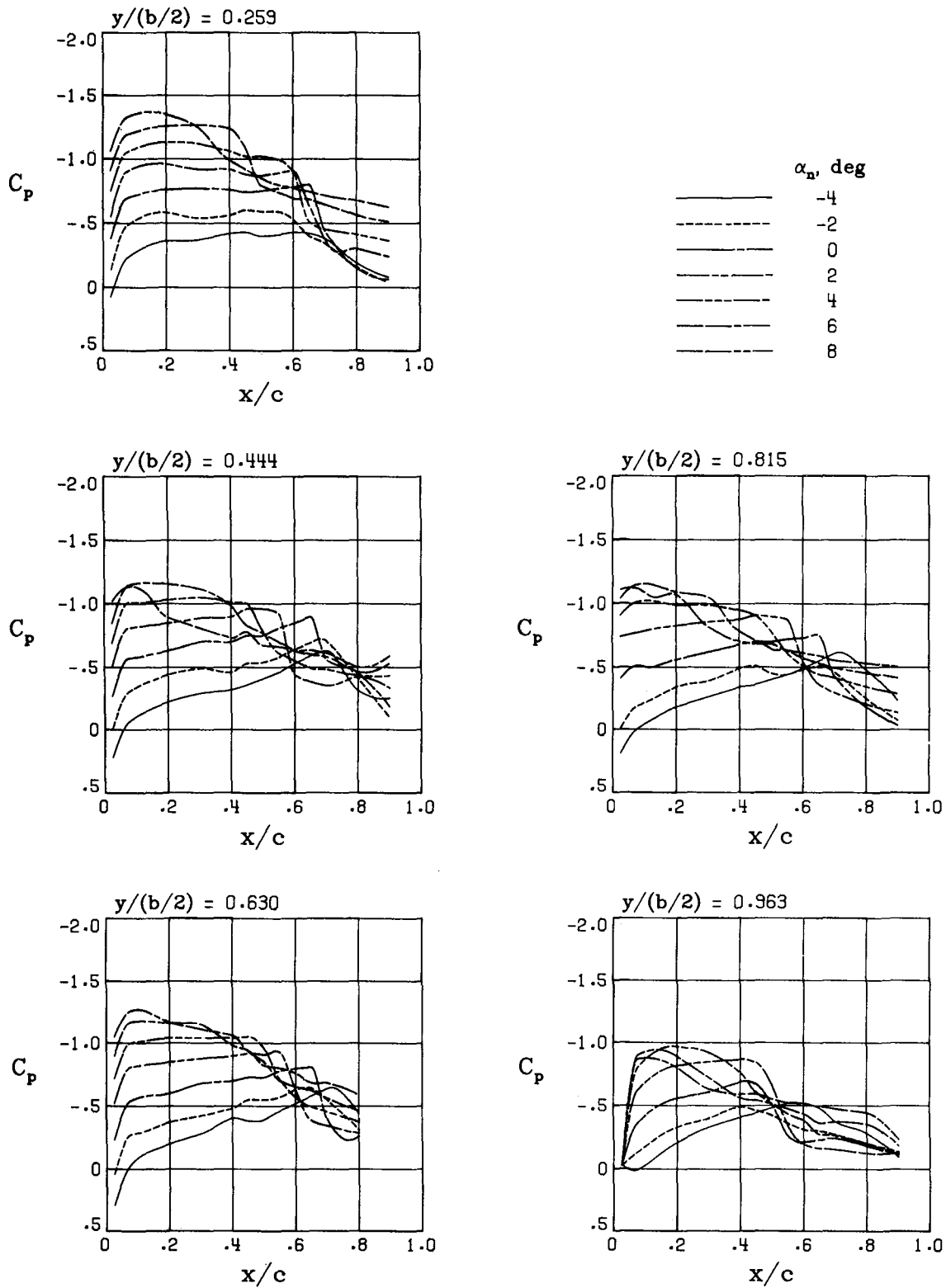
Upper surface pressures

(e)  M = 0.86.

Figure 16.- Continued.
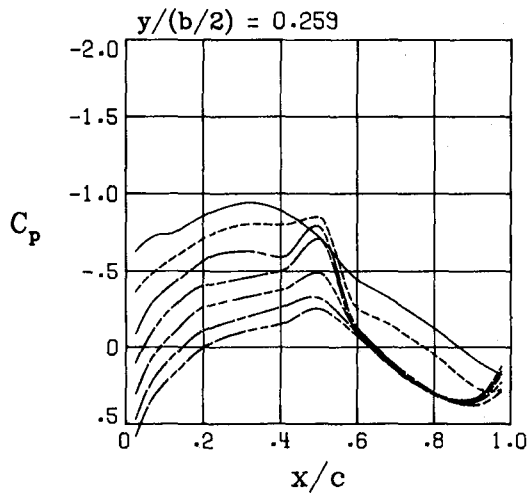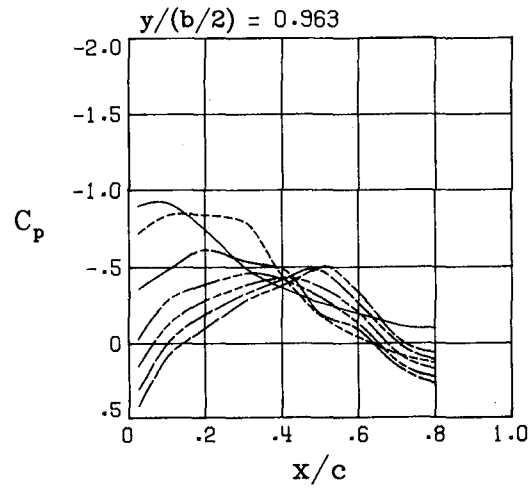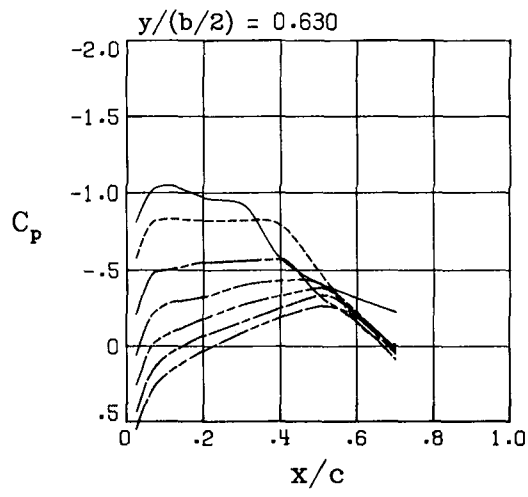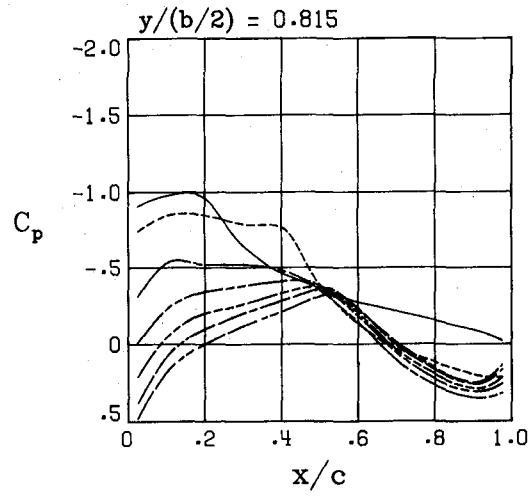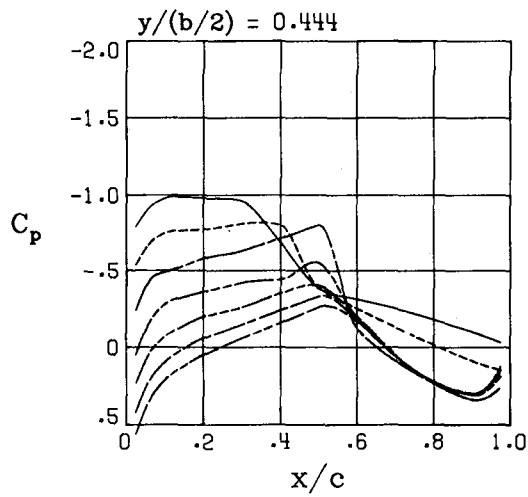
Lower surface pressures

(e) Concluded.

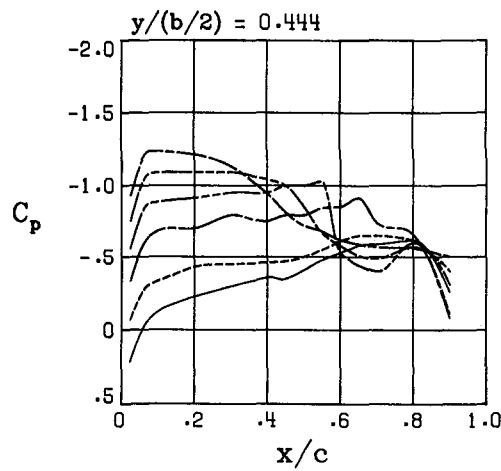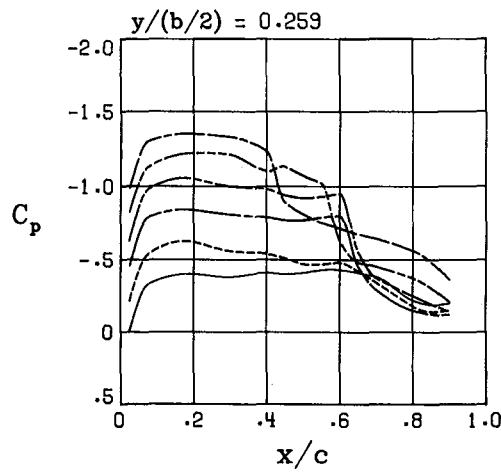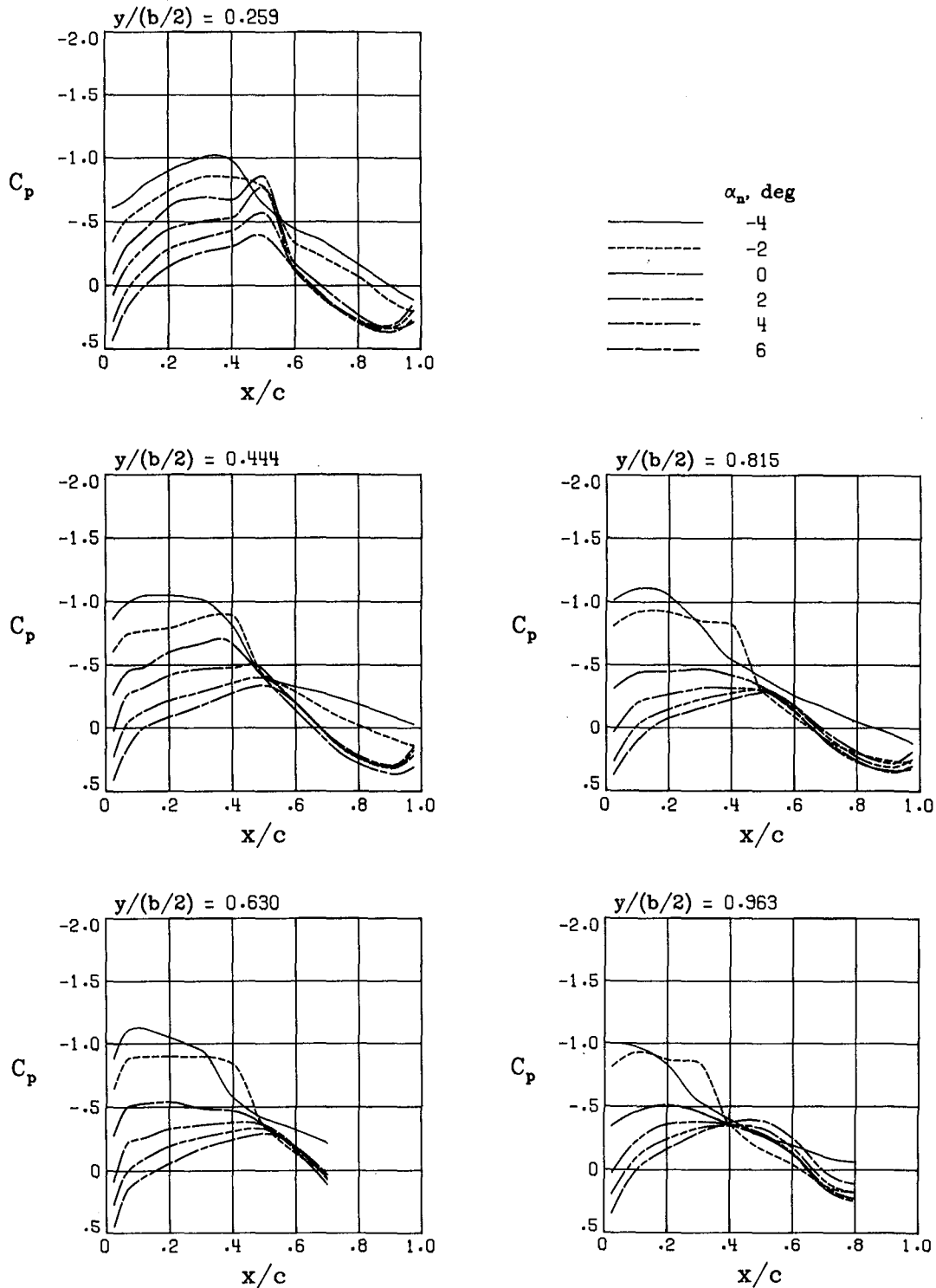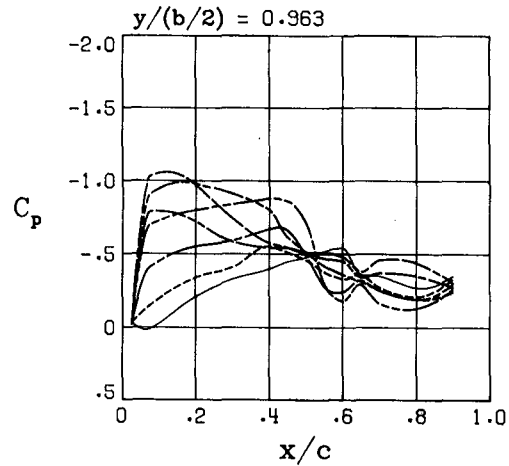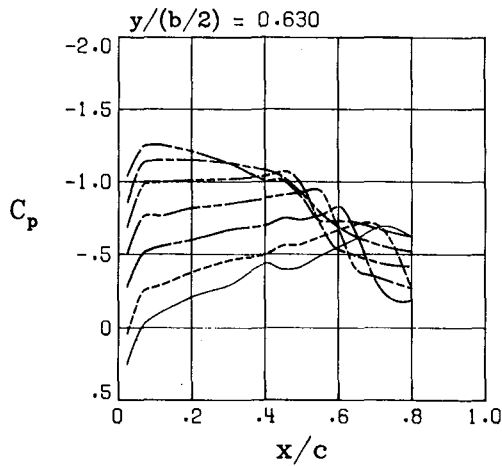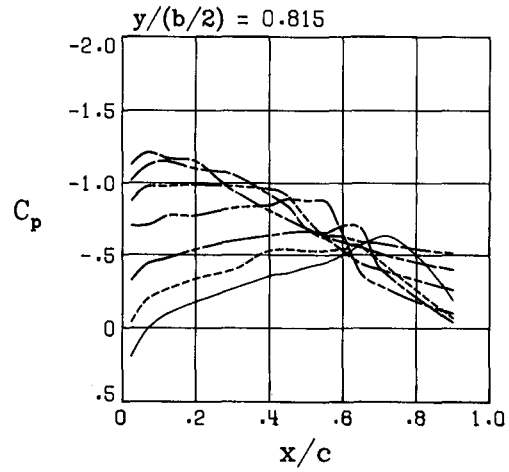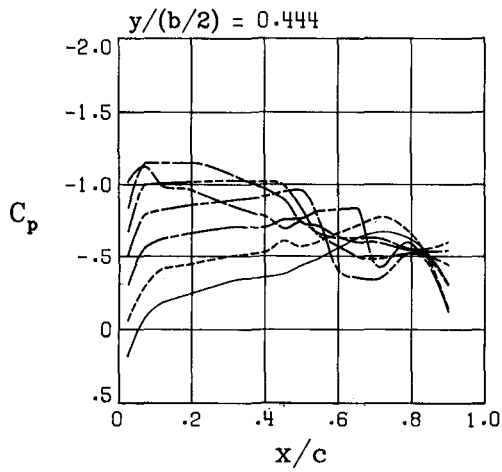Figure 16.- Continued.
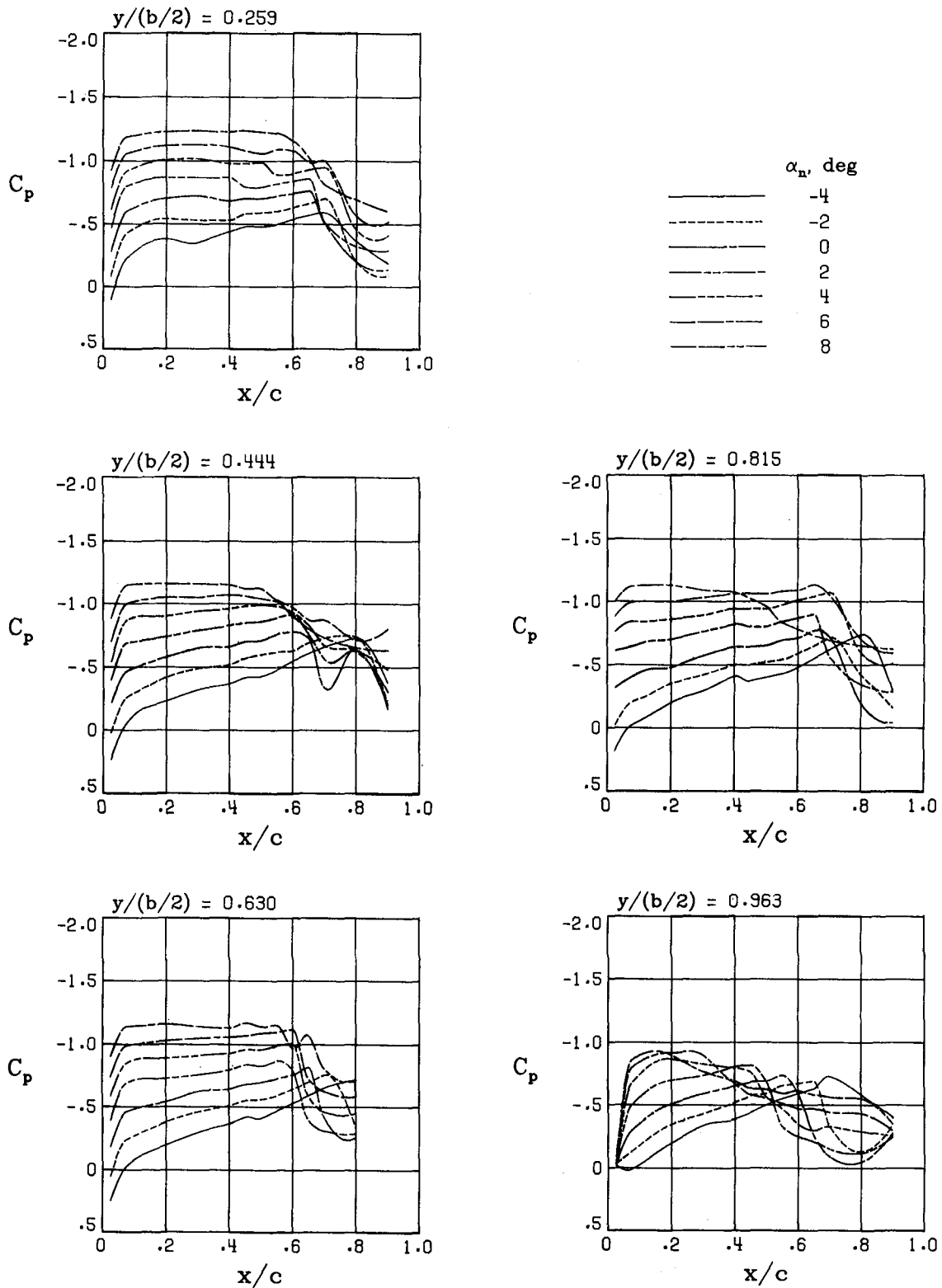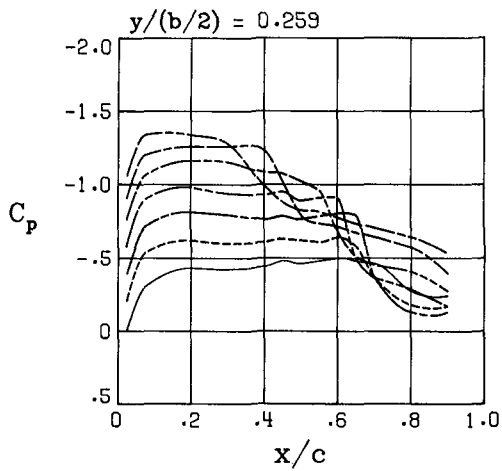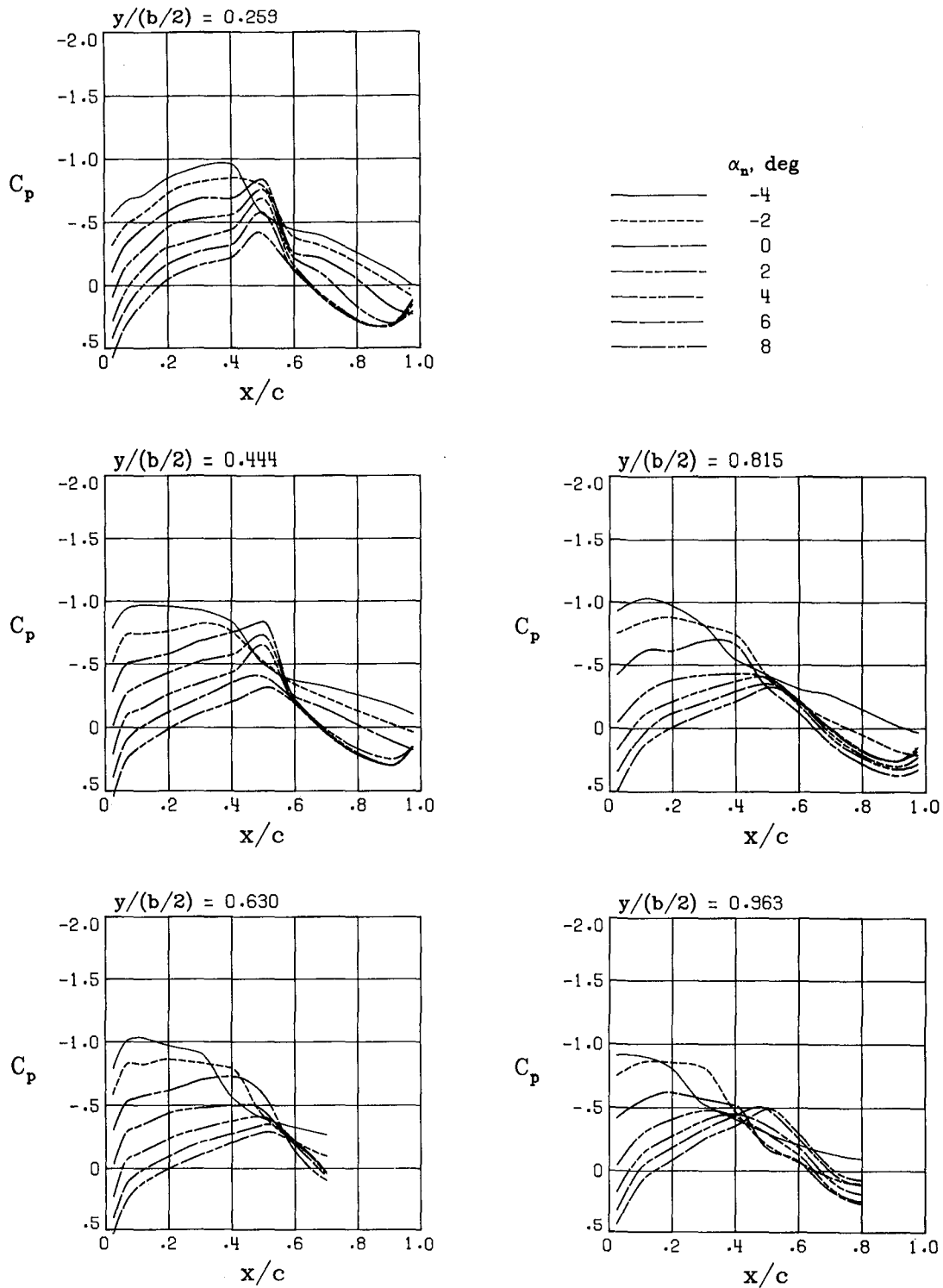
Upper surface pressures

(f)   M = 0.90.

Figure 16.- Continued.
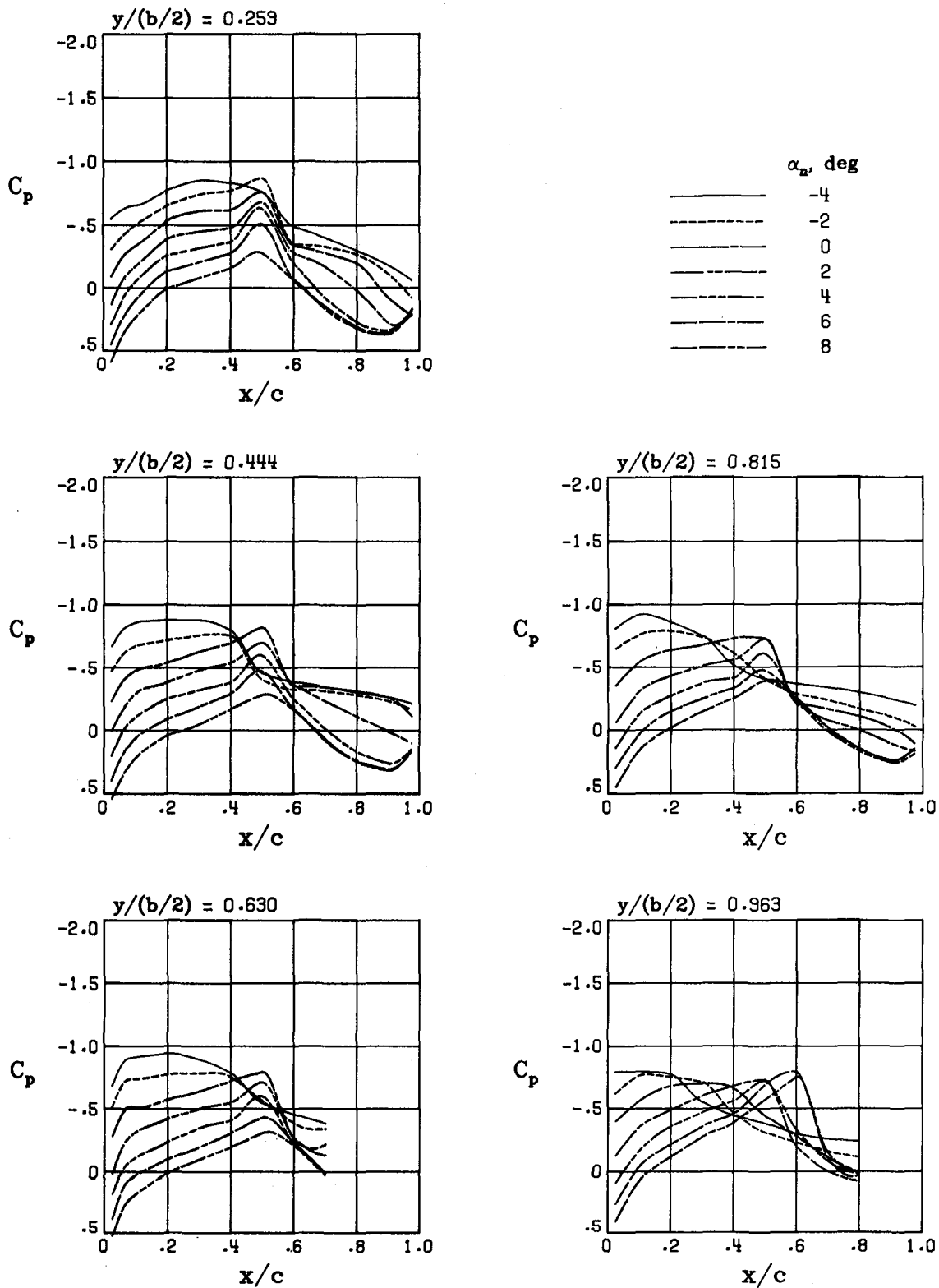
Lower surface pressures

(f) Concluded.

Figure 16.- Continued.
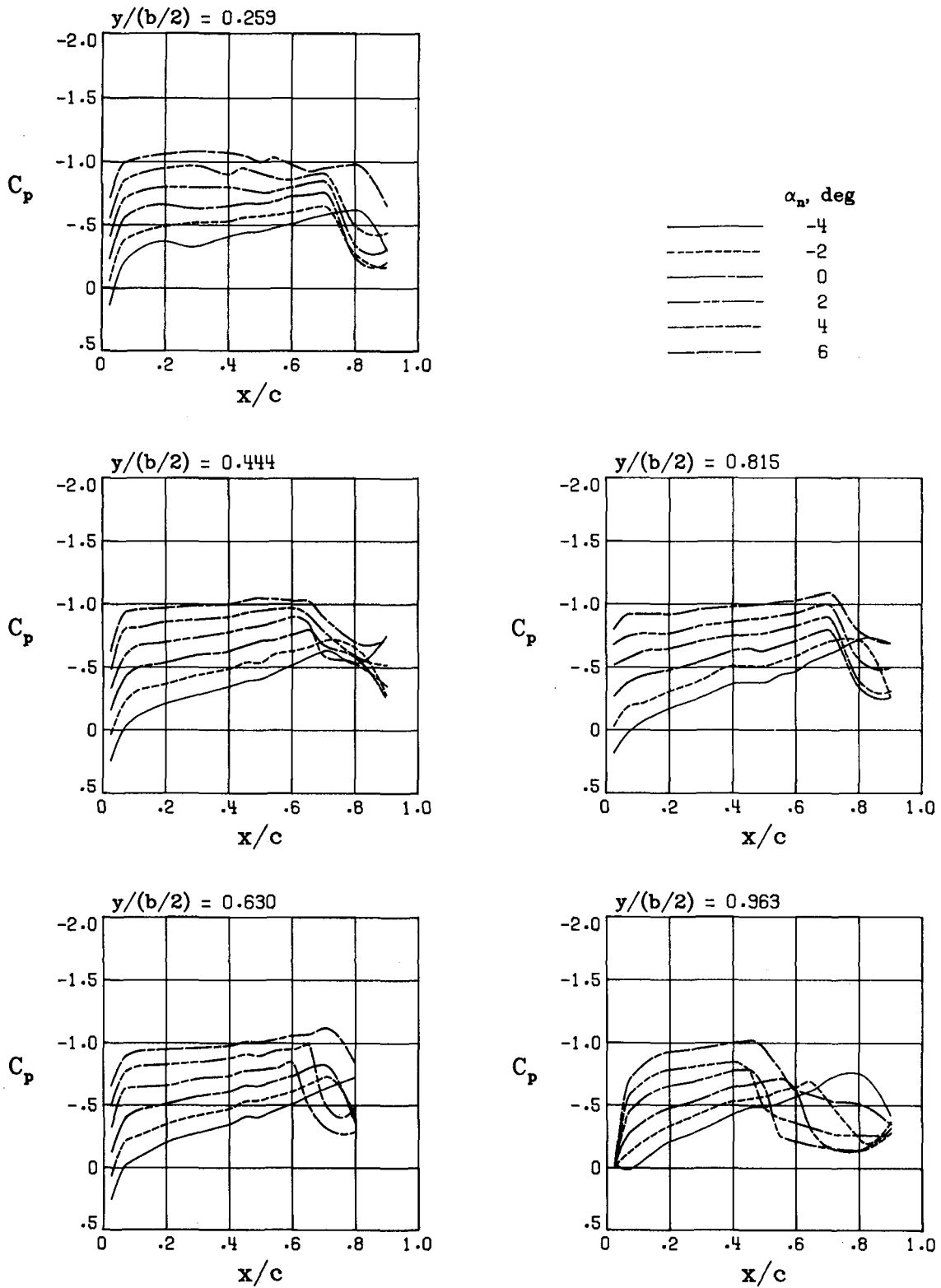
Upper surface pressures

(g)   M = 0.92.

Figure 16.- Continued.
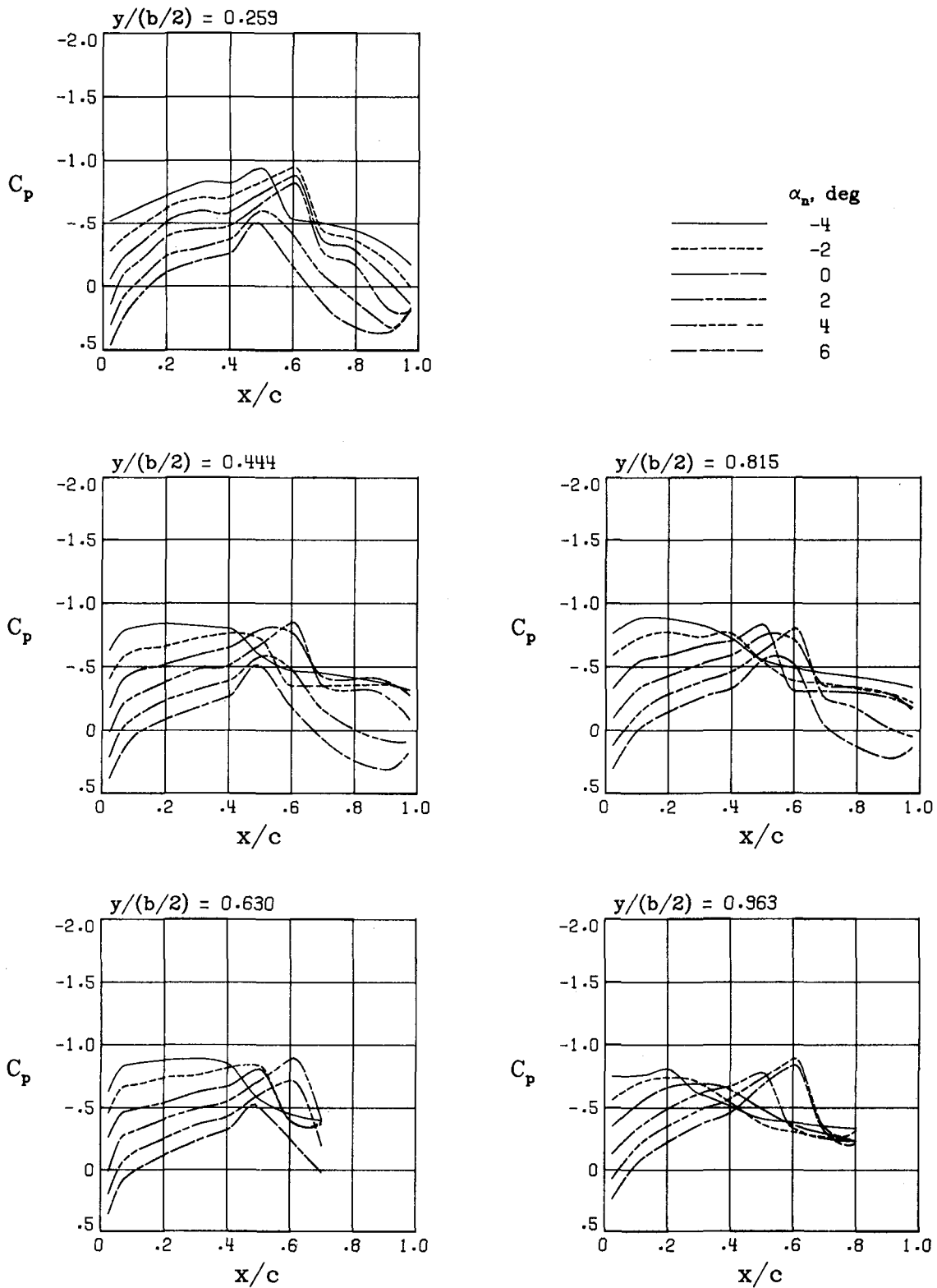
Lower surface pressures

(g) Concluded.

Figure 16.- Concluded.
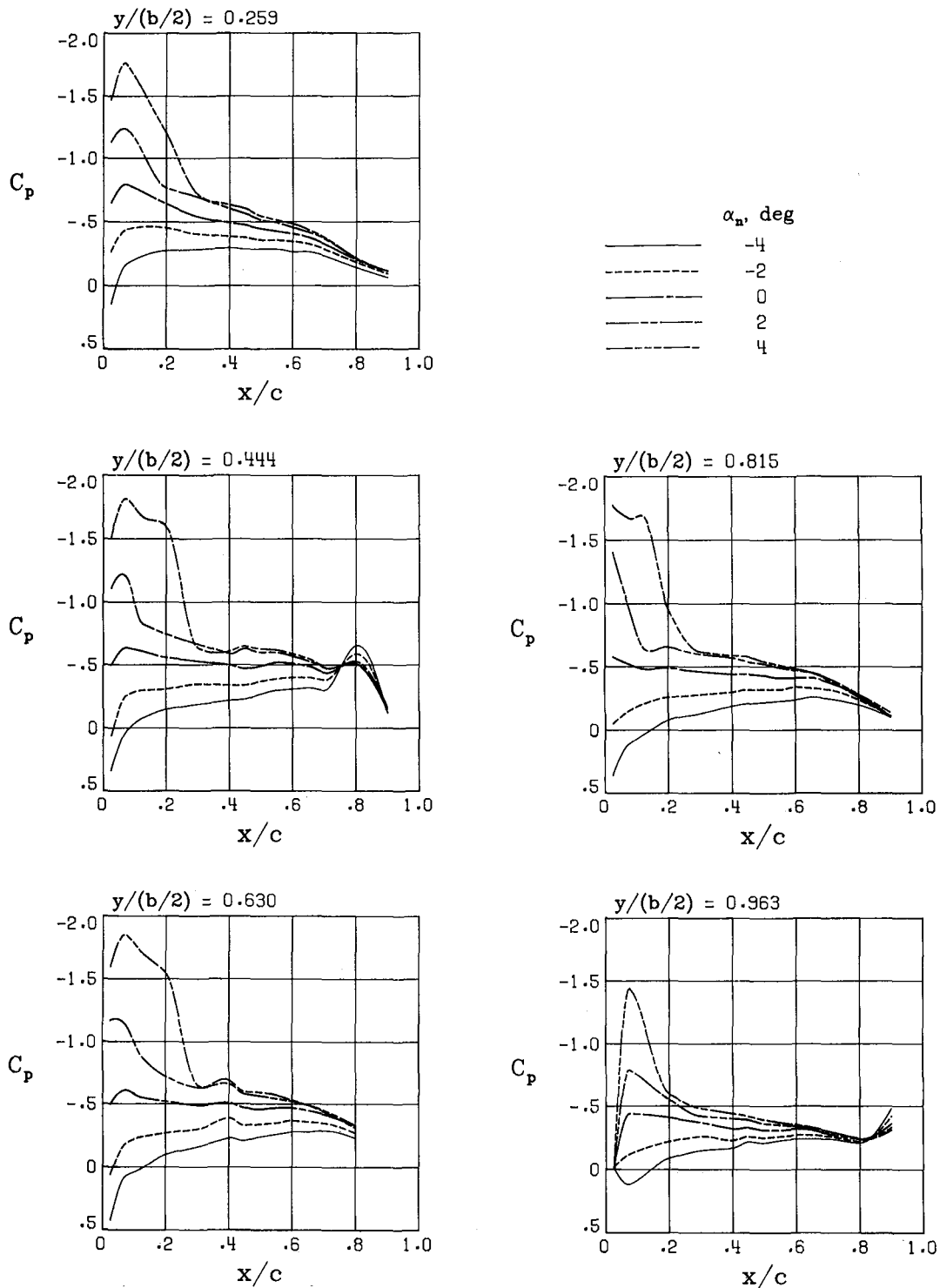
Upper surface pressures

(a)   M = 0.70.

Figure 17.- Effect of angle of attack on wing-surface pressure distributions
for model configuration B.

130

Lower surface pressures

(a) Concluded.

Figure 17.- Continued.
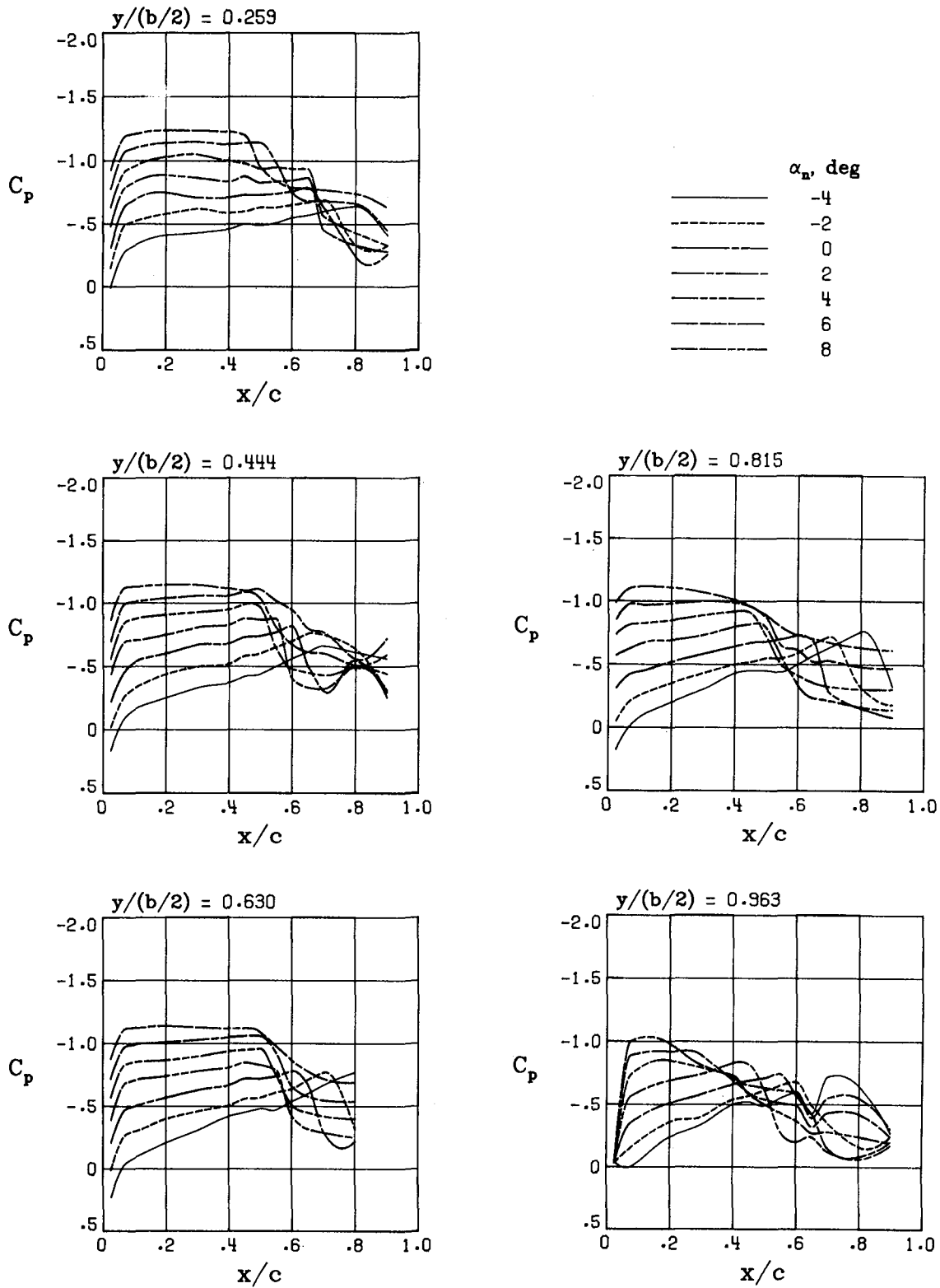
Upper surface pressures

(b)  M = 0.75.

Figure 17.- Continued.
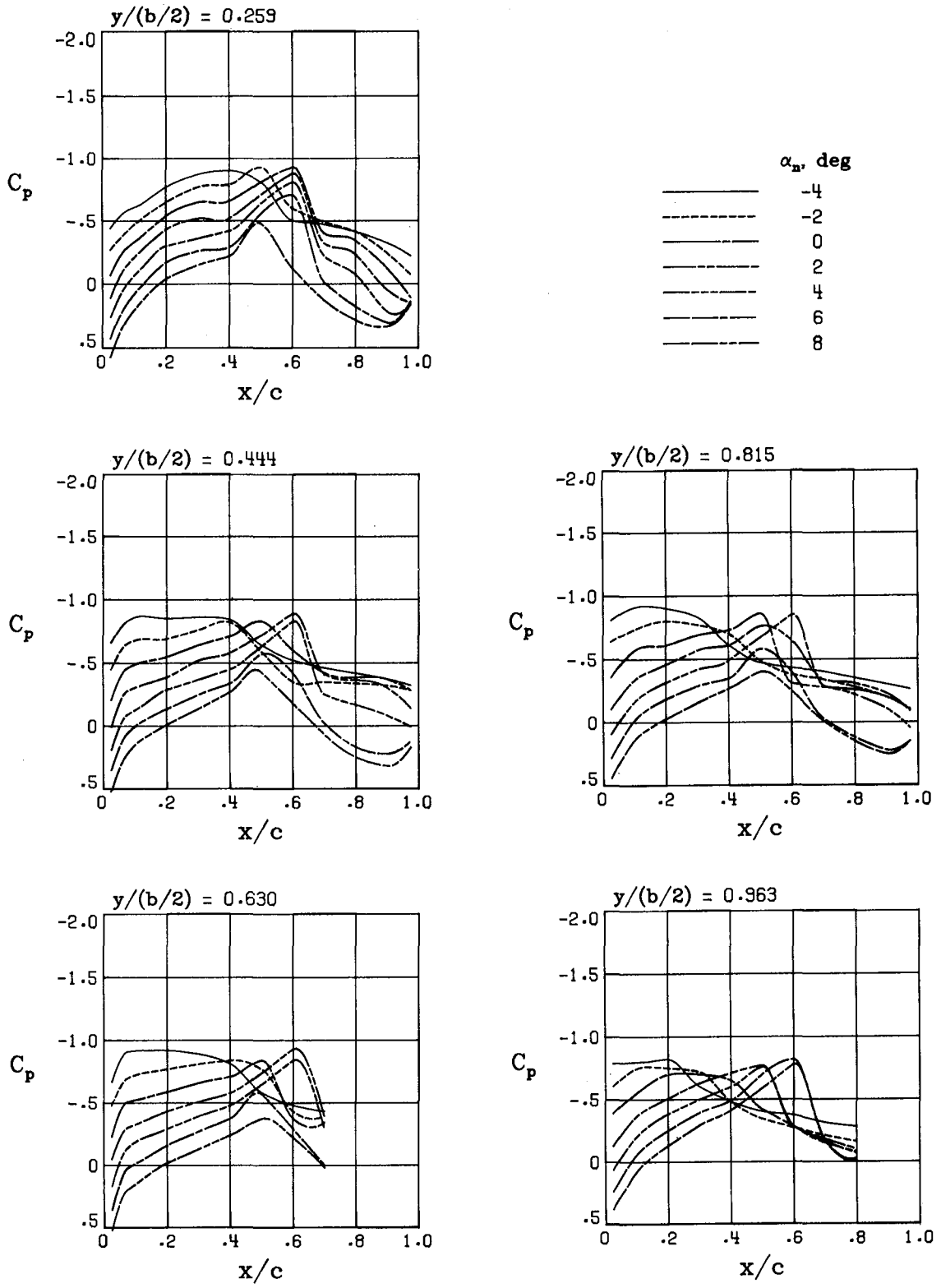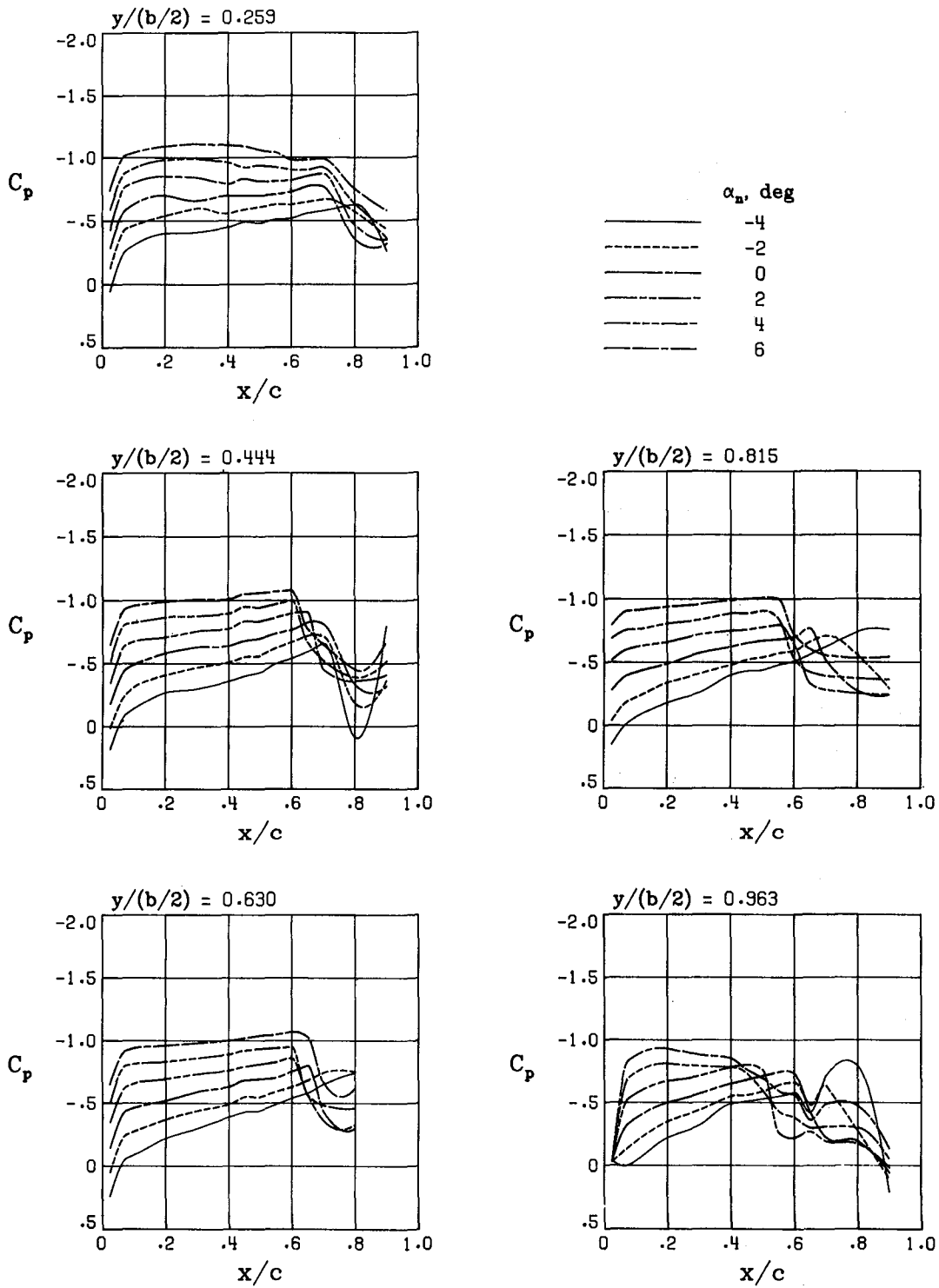
Lower surface pressures

(b) Concluded.

Figure 17.- Continued.

Upper surface pressures

(c)  M = 0.80.

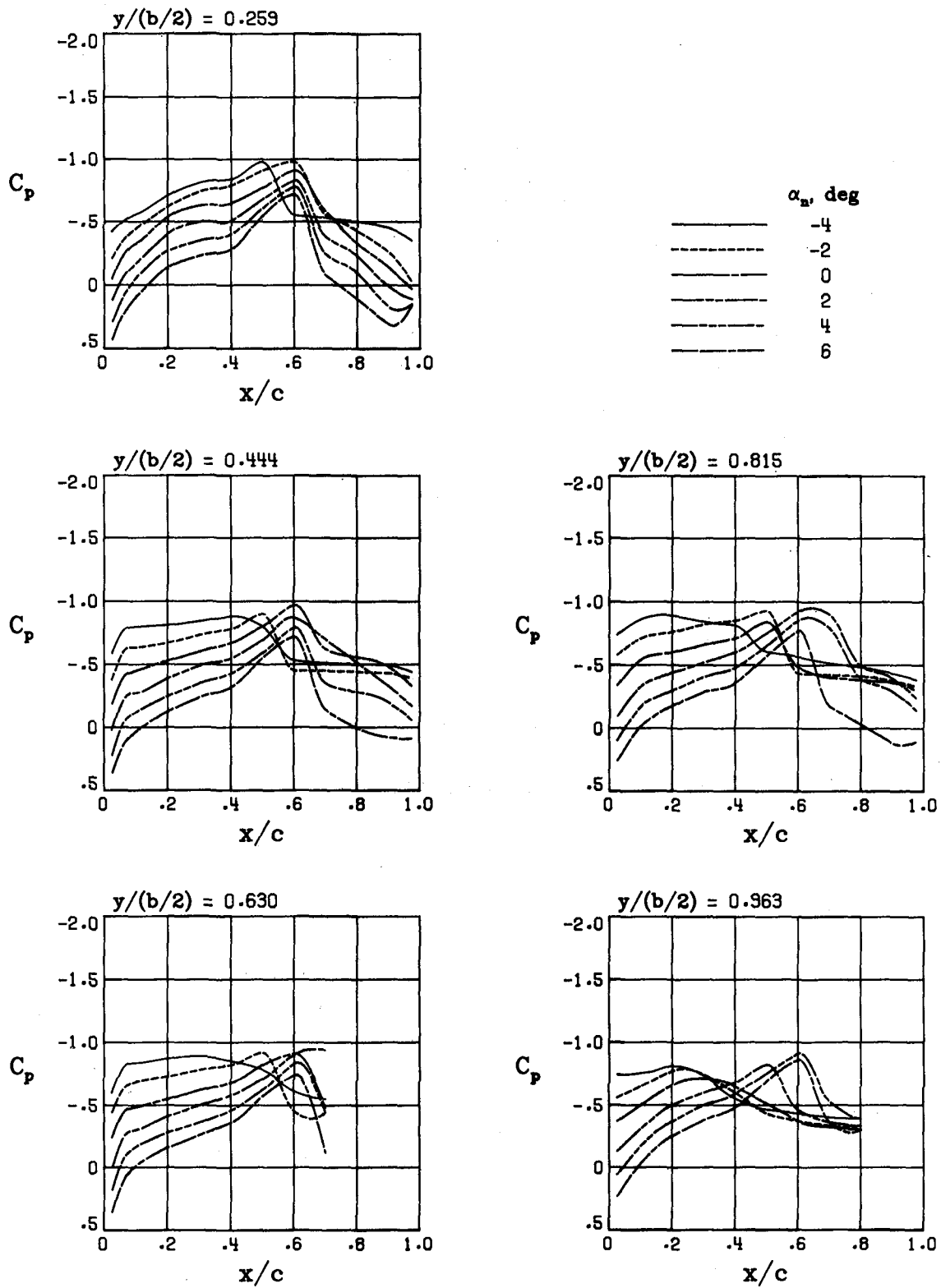Figure 17.- Continued.

Lower surface pressures

(c) Concluded.

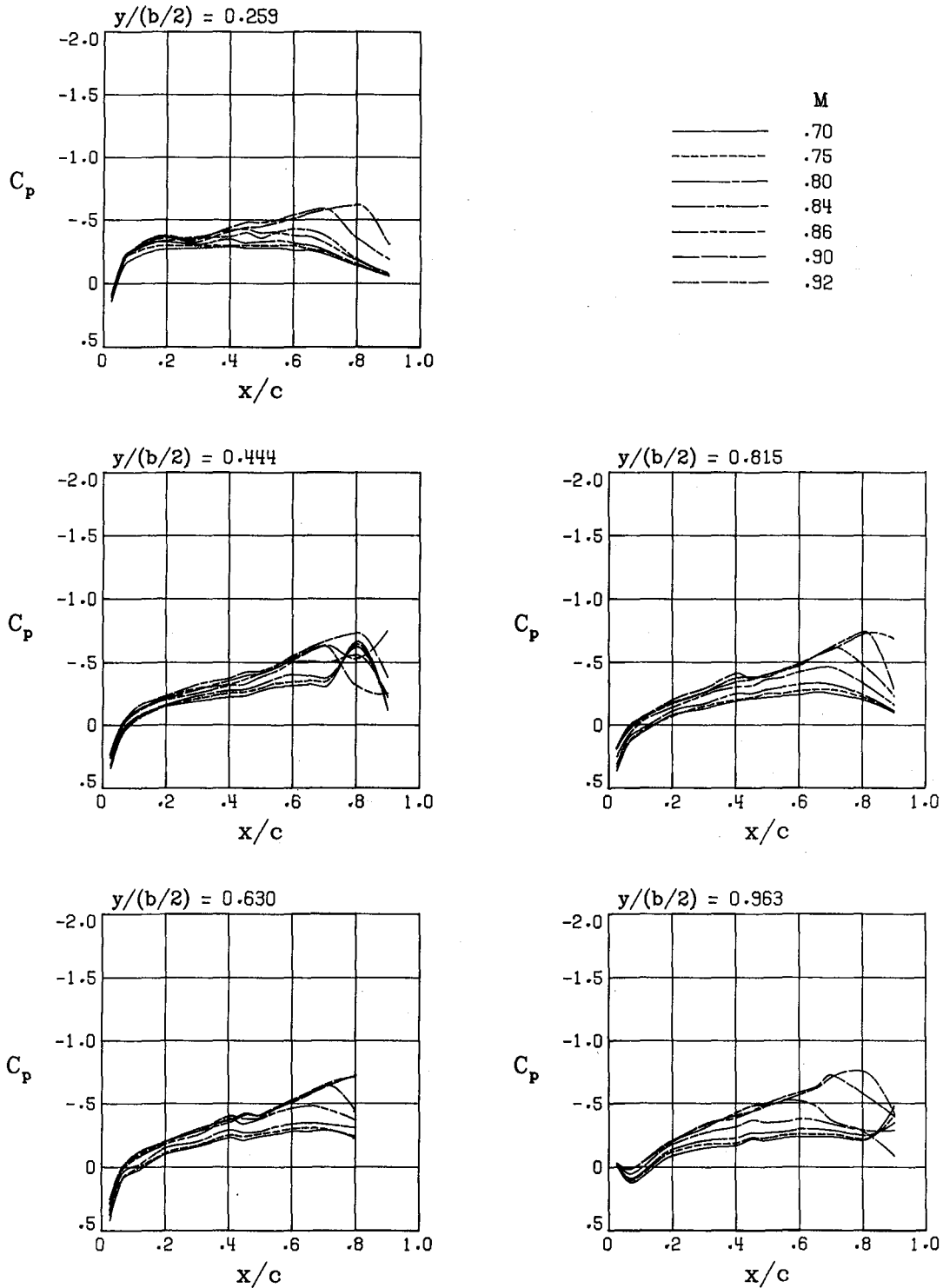Figure 17.- Continued.
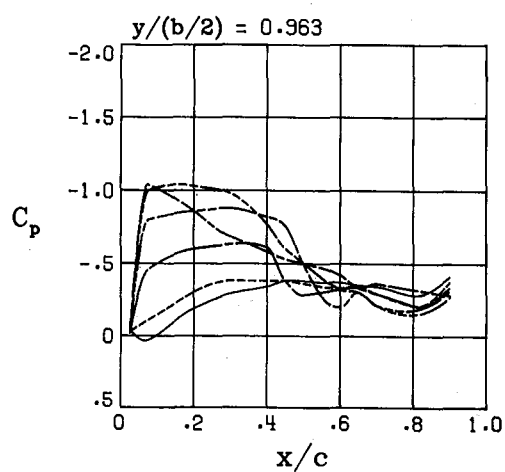
Upper surface pressures

(d)   M = 0.84.

Figure 17.- Continued.

Lower surface pressures

(d) Concluded.

Figure 17.- Continued.

Upper surface pressures

(e)   M = 0.86.

Figure 17.- Continued.

Lower surface pressures

(e) Concluded.
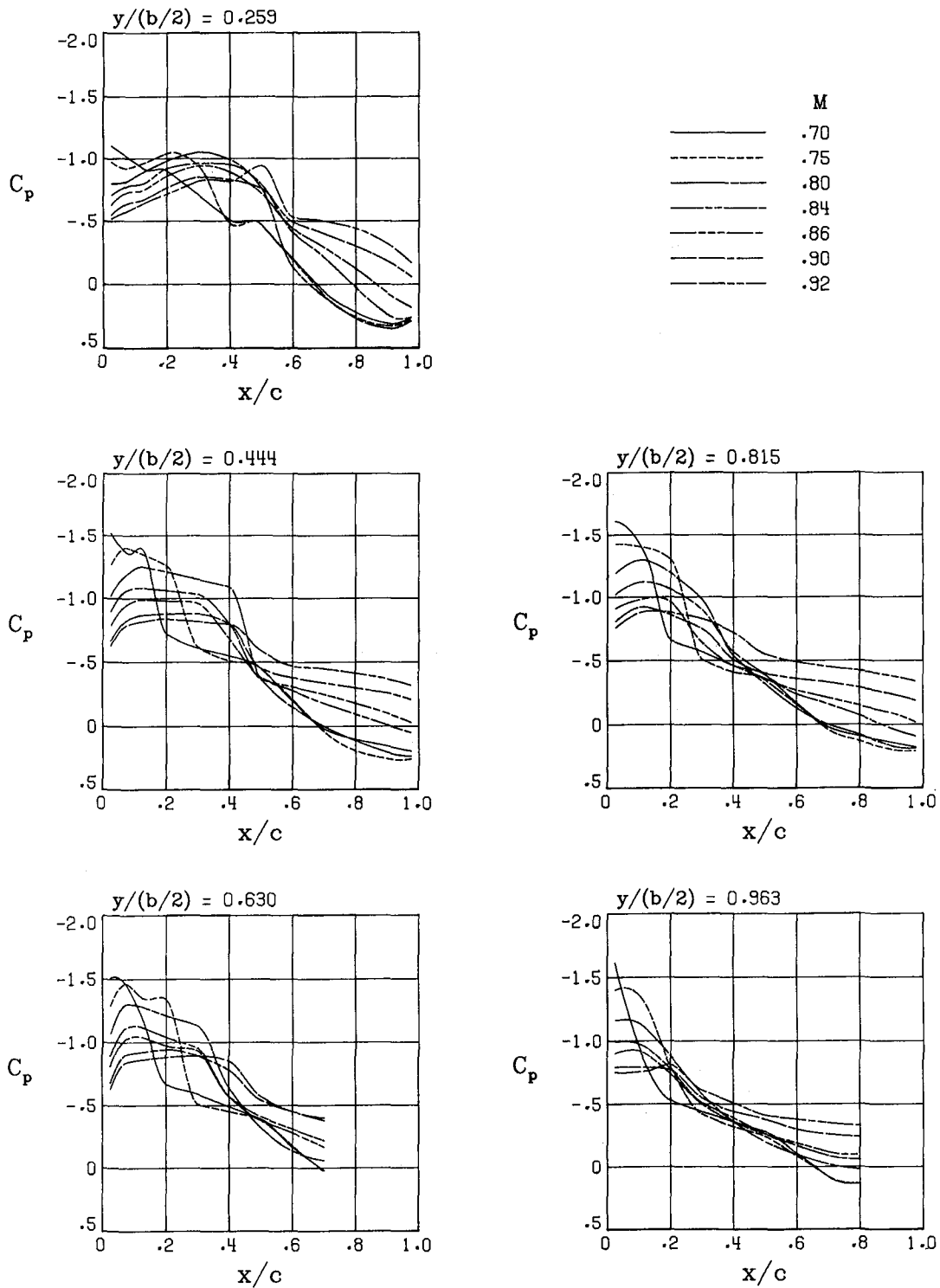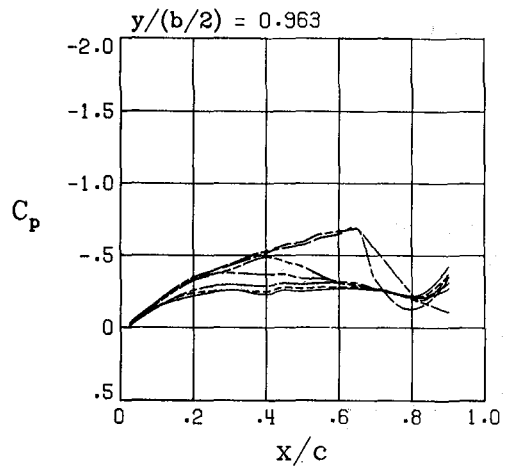
Figure 17.- Continued.

Upper surface pressures

(f)  M = 0.90.

Figure 17.- Continued.

$$\frac{y}{b/2} = 0.259$$

$C_p$

$$\frac{x}{c}$$

$$\alpha_n, \text{ deg}$$

| | |
|---|---|
| ——— | -4 |
| - - - - - | -2 |
| —·—·— | 0 |
| —··—··— | 2 |
| – – – | 4 |
| ——— | 6 |
| ——— | 8 |

$$\frac{y}{b/2} = 0.444$$

$C_p$

$$\frac{x}{c}$$

$$\frac{y}{b/2} = 0.815$$

$C_p$

$$\frac{x}{c}$$

$$\frac{y}{b/2} = 0.630$$

$C_p$

$$\frac{x}{c}$$

$$\frac{y}{b/2} = 0.963$$

$C_p$

$$\frac{x}{c}$$

Lower surface pressures

(f) Concluded.

Figure 17.- Continued.

Upper surface pressures

(g)   M = 0.92.

Figure 17.- Continued.

Lower surface pressures

(g) Concluded.

Figure 17.- Concluded.
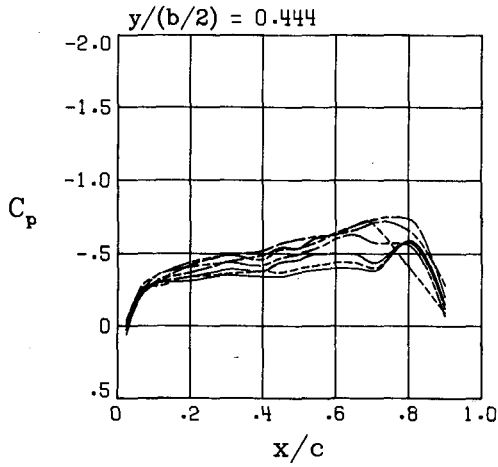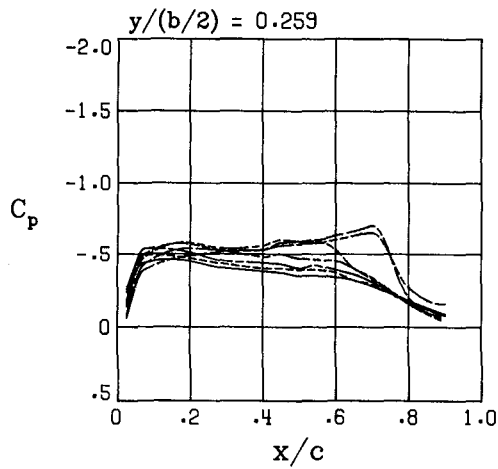
Upper surface pressures

(a)   $\alpha_n = -4°$.

Figure 18.- Effect of Mach number on wing-surface pressure distributions for model configuration A.
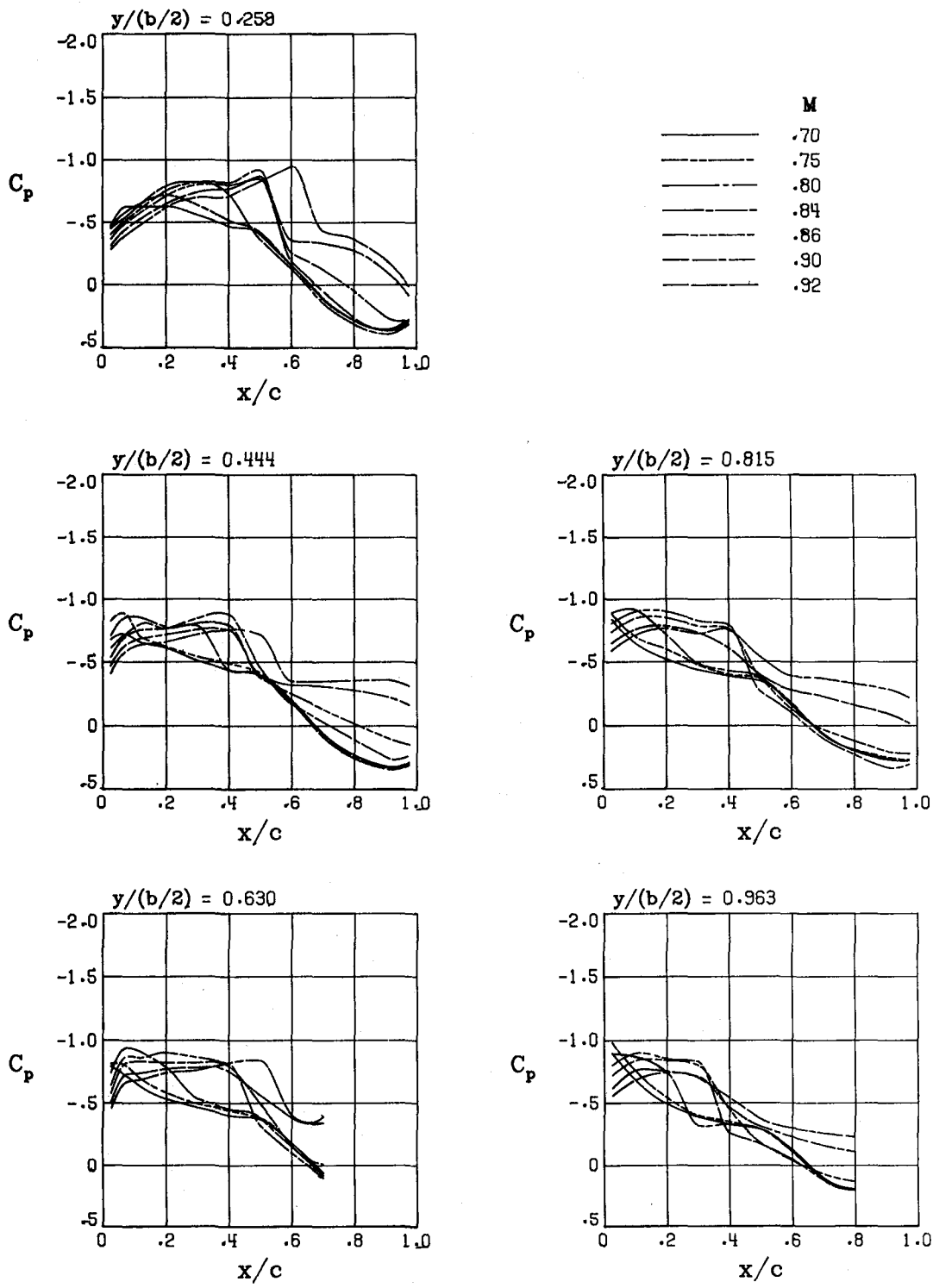
Lower surface pressures

(a) Concluded.

Figure 18.- Continued.
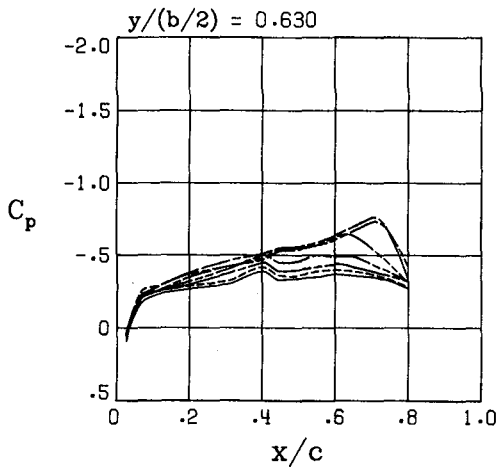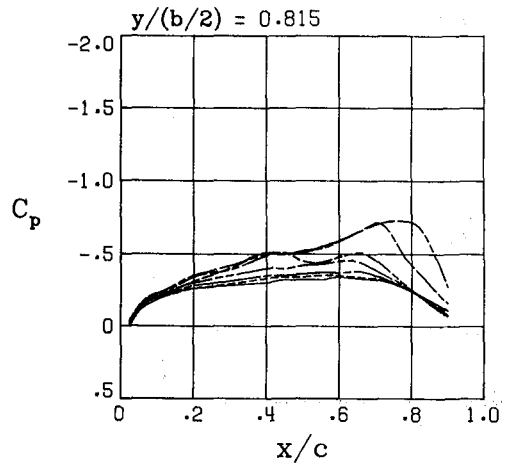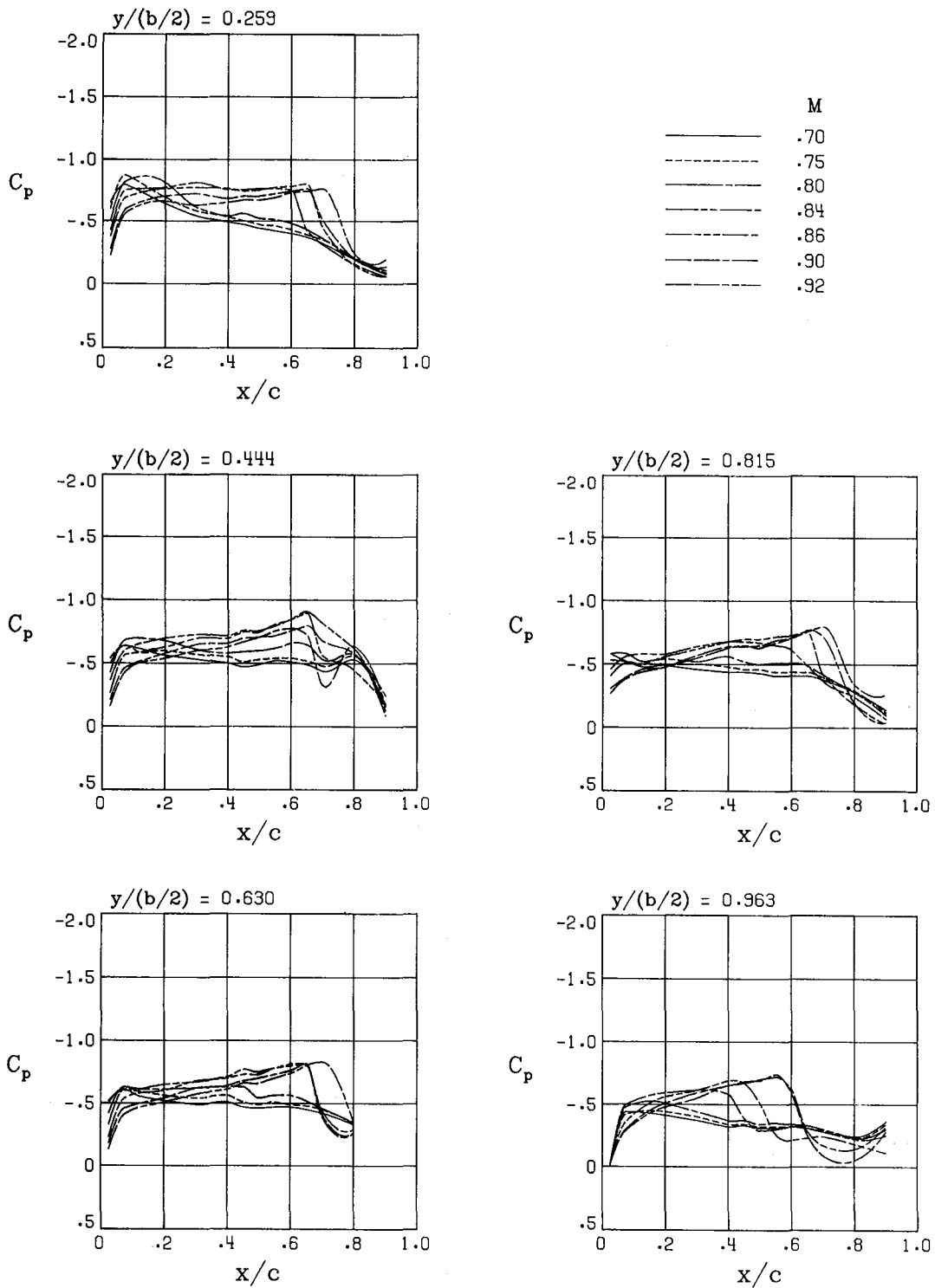
Upper surface pressures

(b)  $\alpha_n = -2°$.

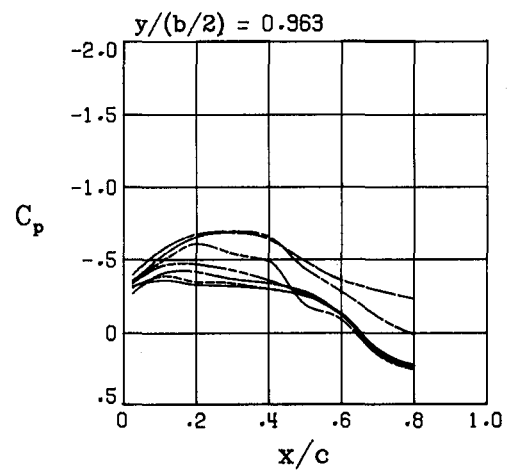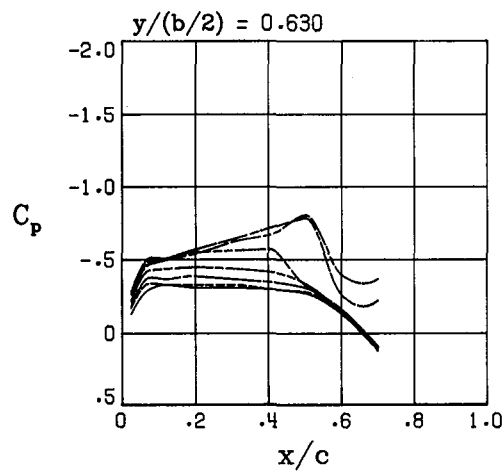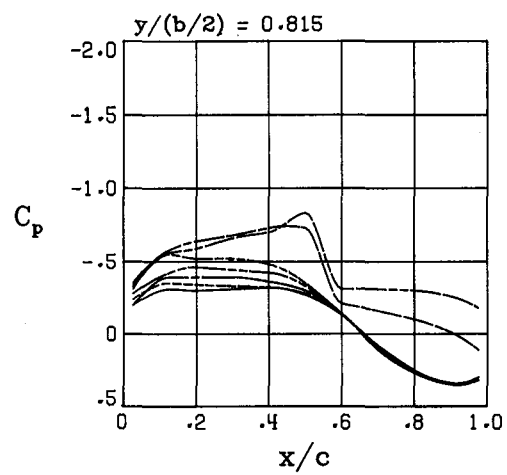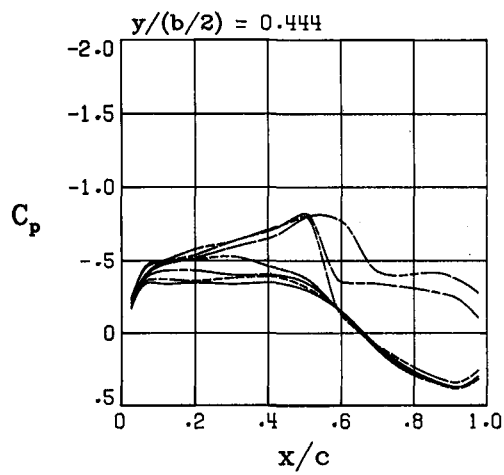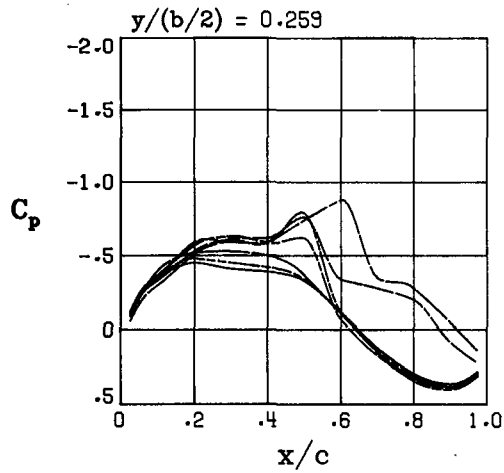Figure 18.- Continued.

Lower surface pressures

(b) Concluded.

Figure 18.- Continued.

Upper surface pressures

(c)  $\alpha_n = 0°$.
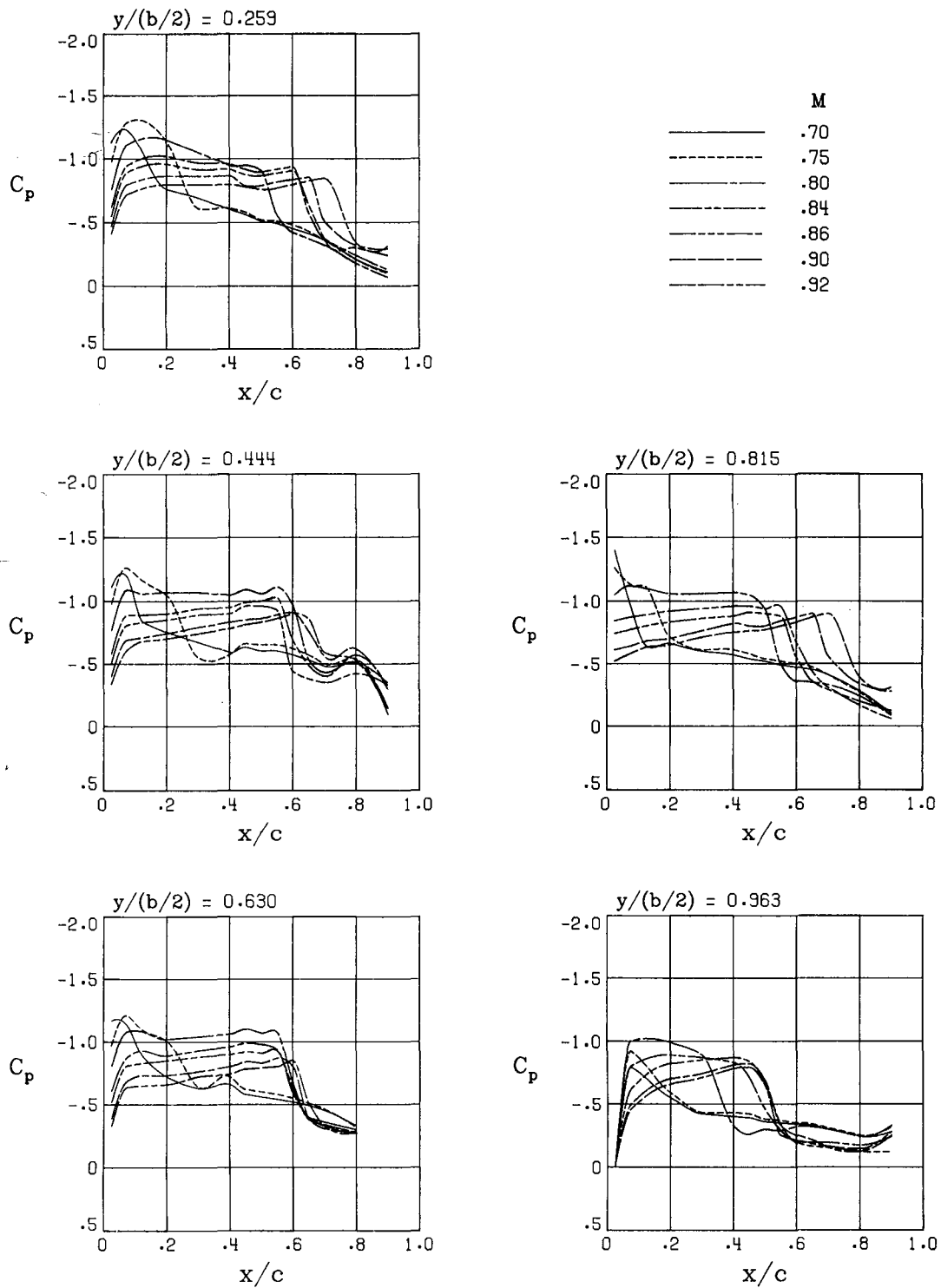
Figure 18.- Continued.

Lower surface pressures

(c) Concluded.
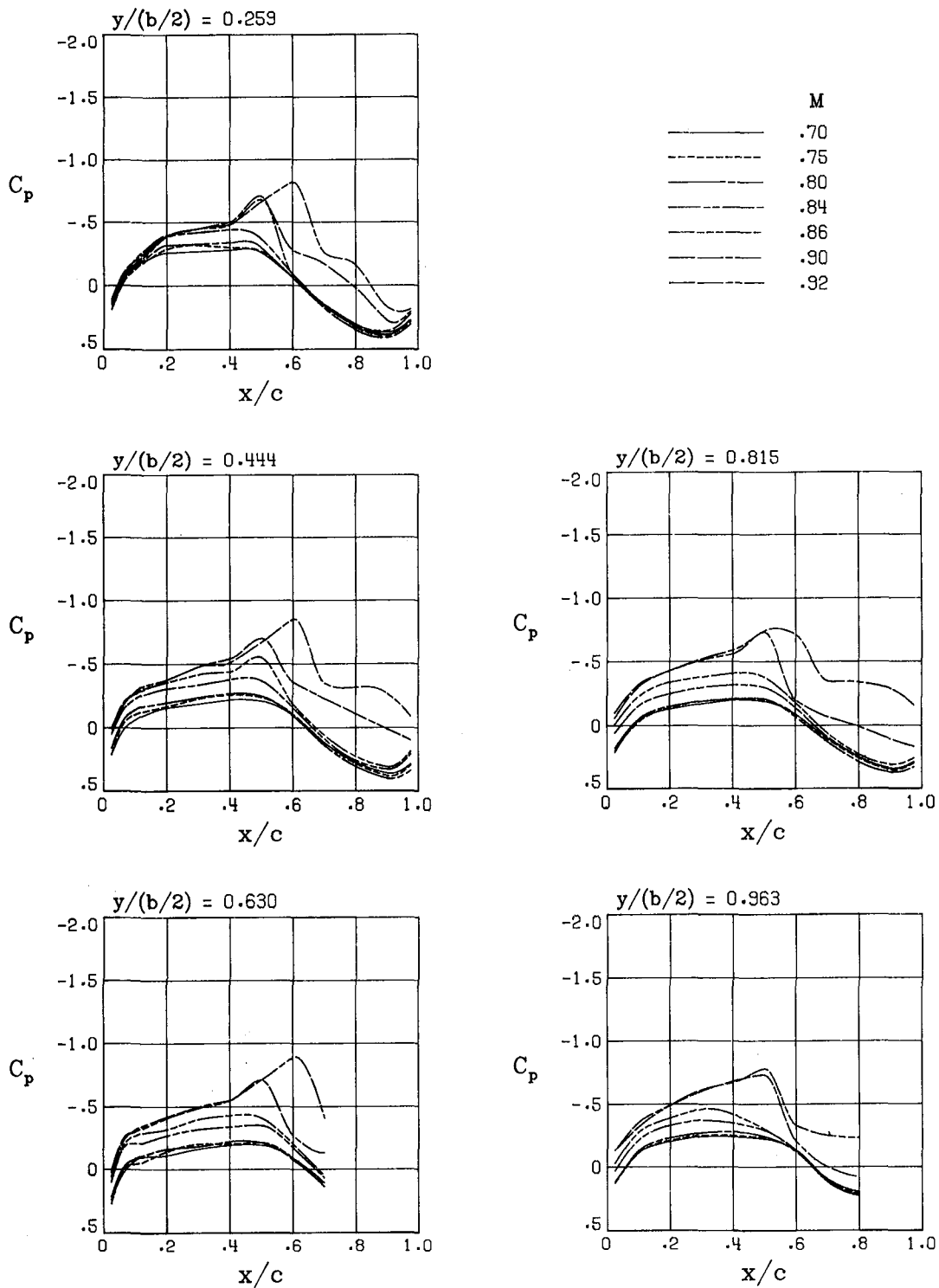
Figure 18.- Continued.
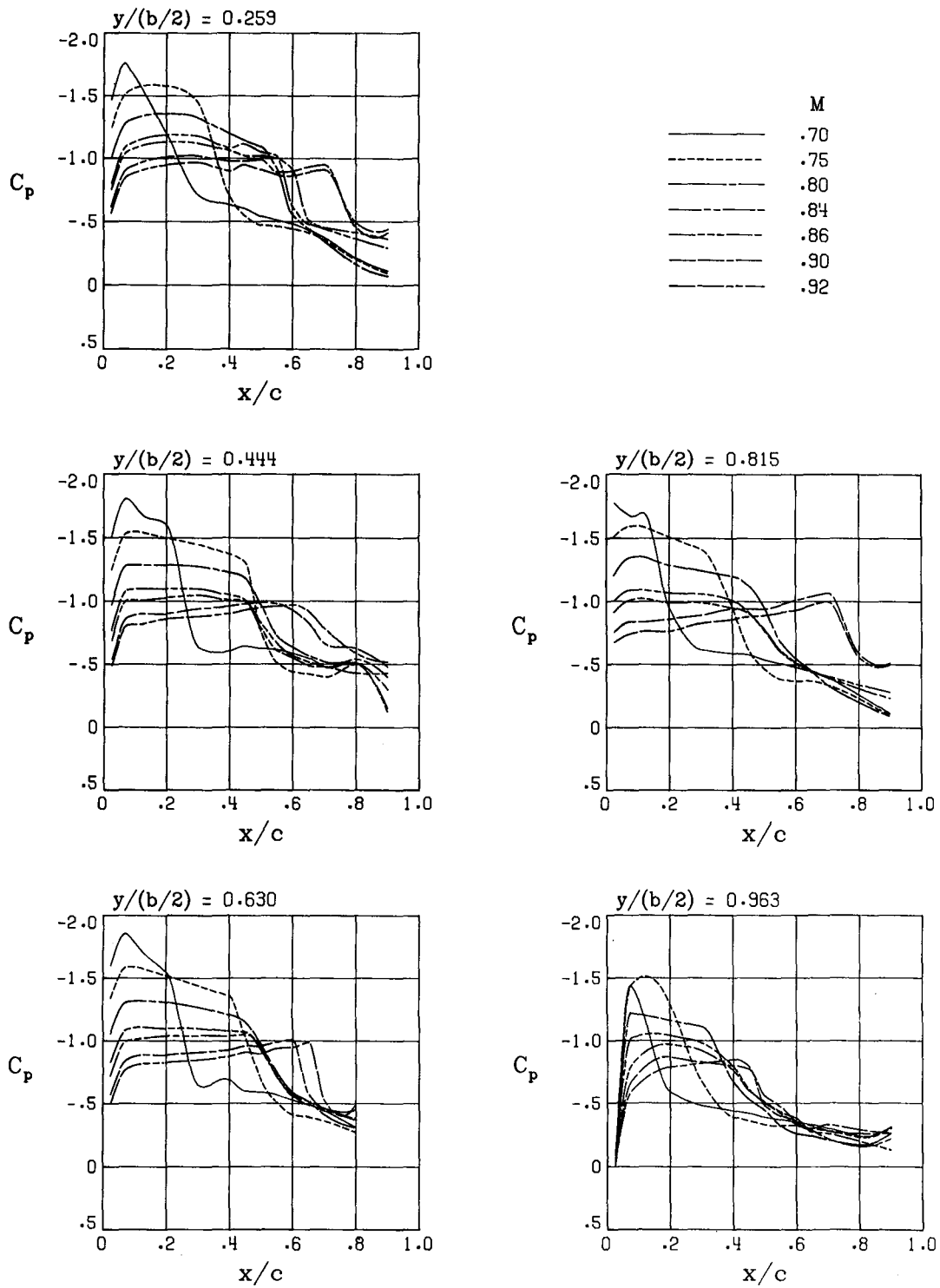
Upper surface pressures

(d) $\alpha_n = 2°$.

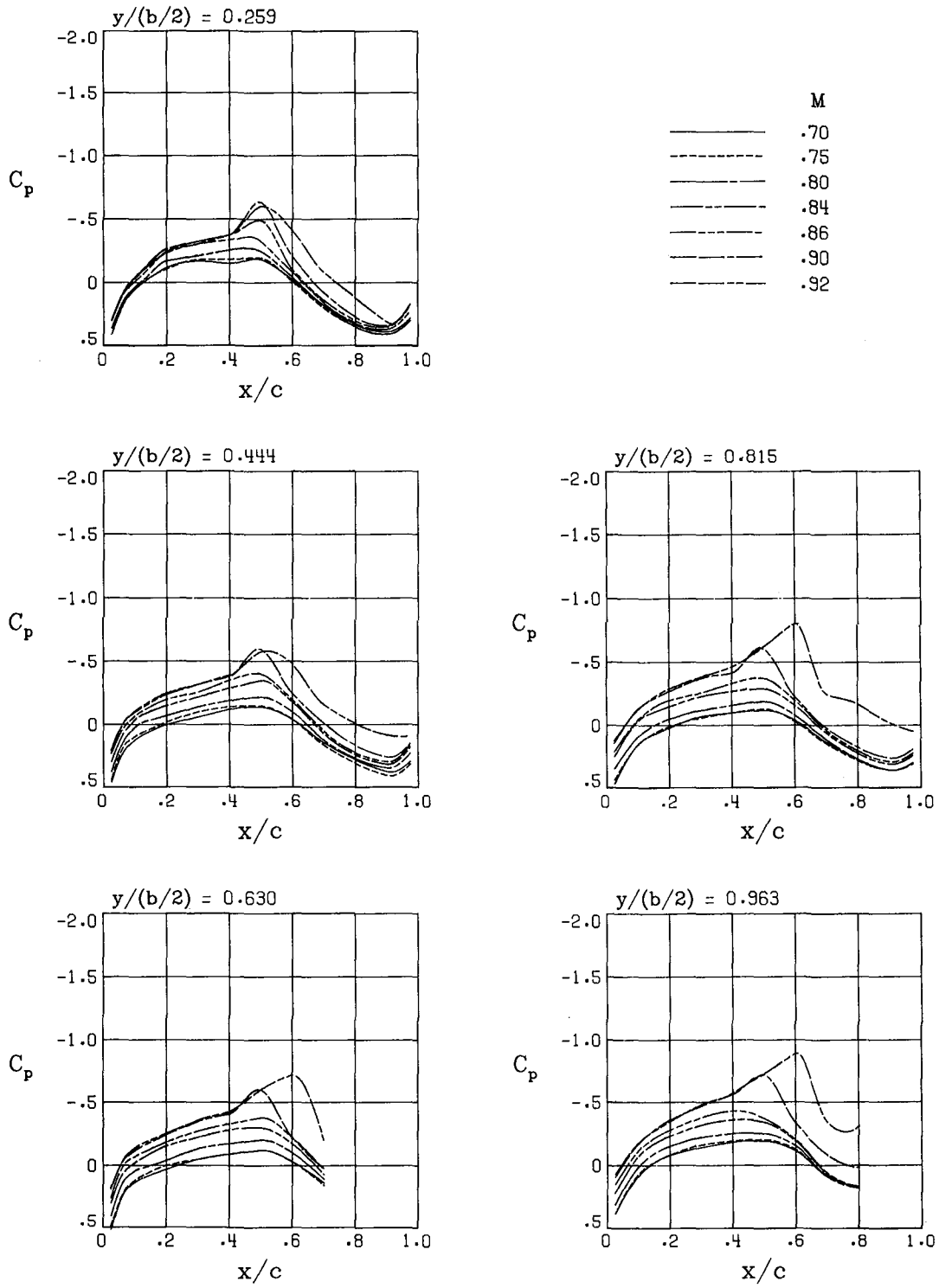Figure 18.- Continued.

Lower surface pressures

(d) Concluded.

Figure 18.- Continued.
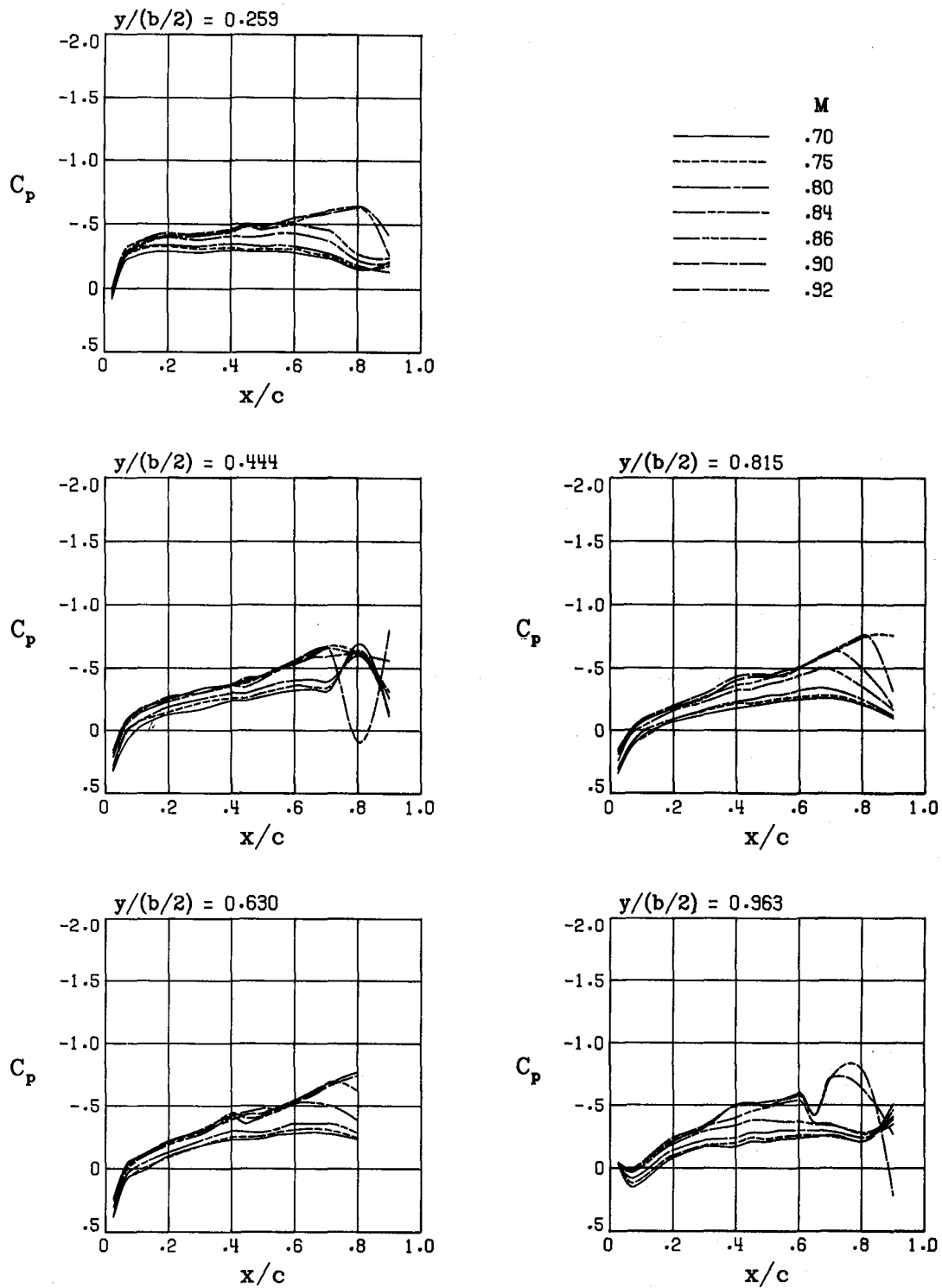
Upper surface pressures

(e)  $\alpha_n = 4°$.

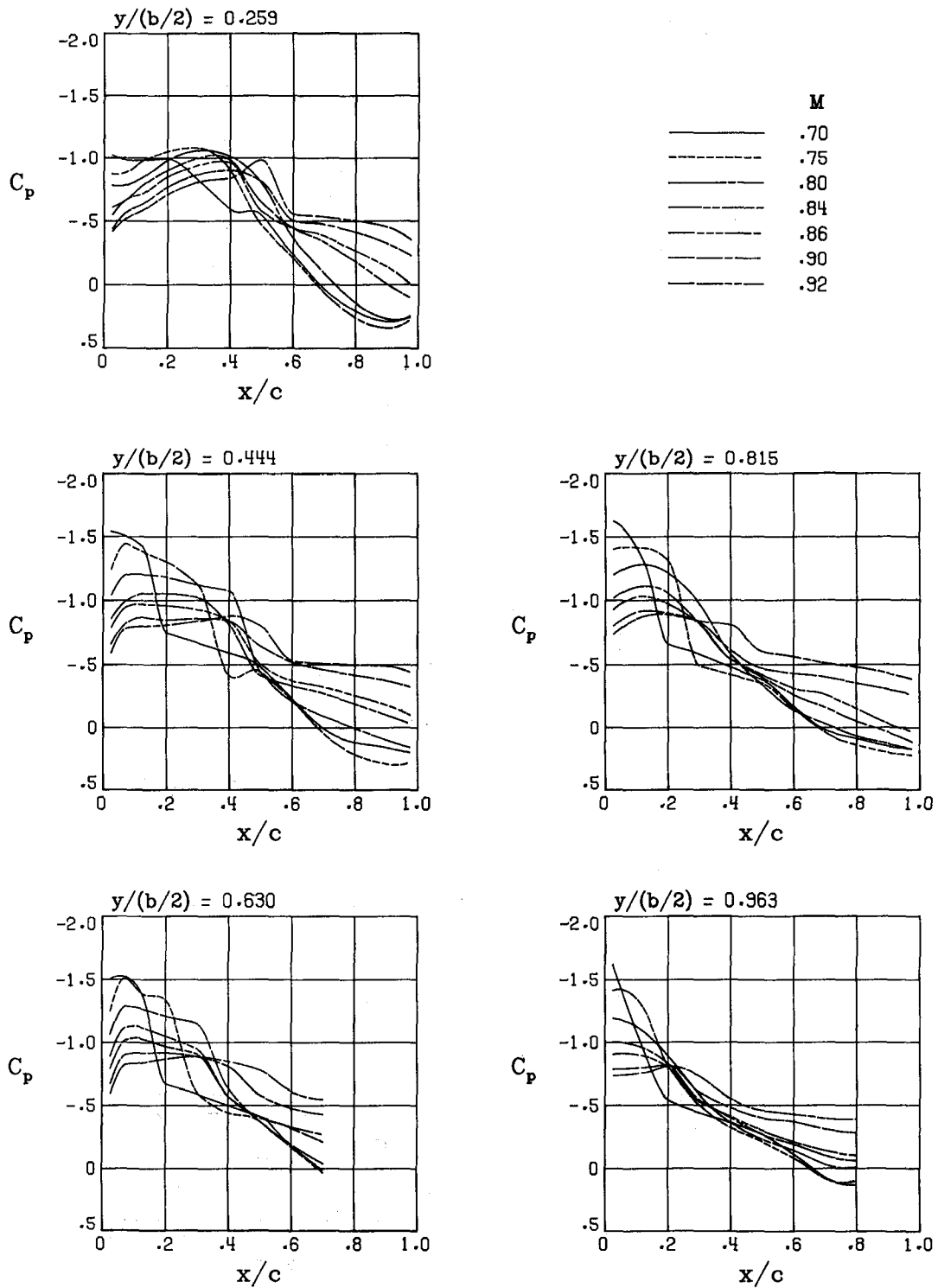Figure 18.- Continued.

Lower surface pressures

(e) Concluded.

Figure 18.- Concluded.

Upper surface pressures

(a)  $\alpha_n = -4°$.

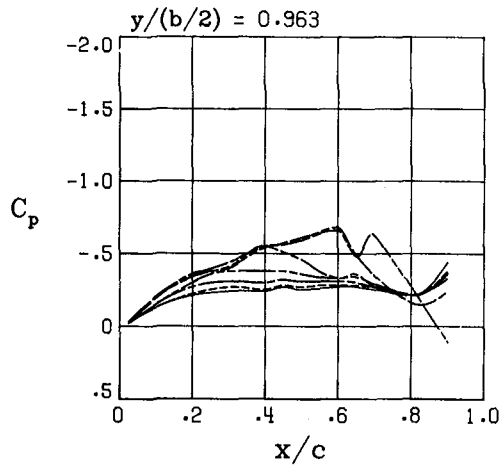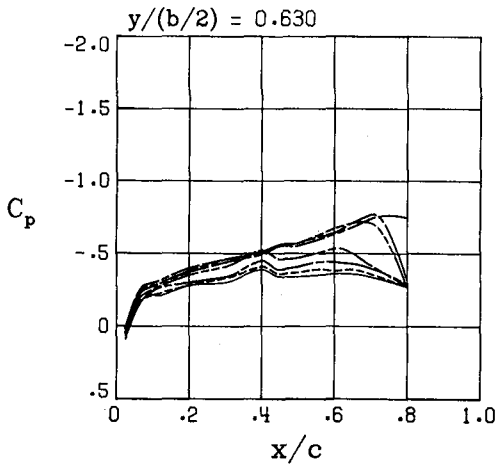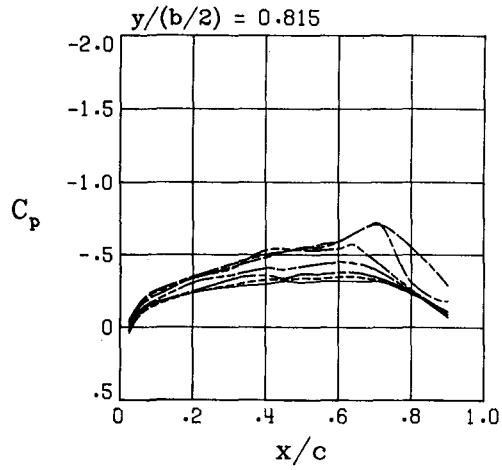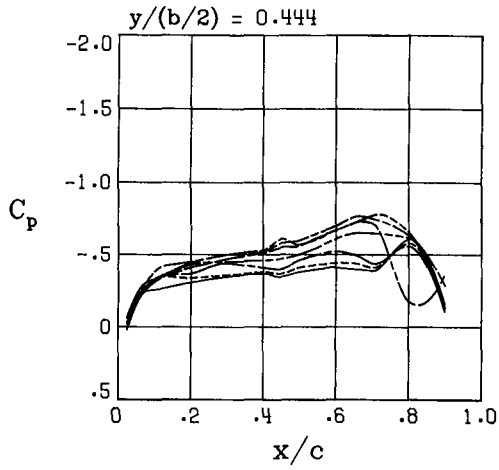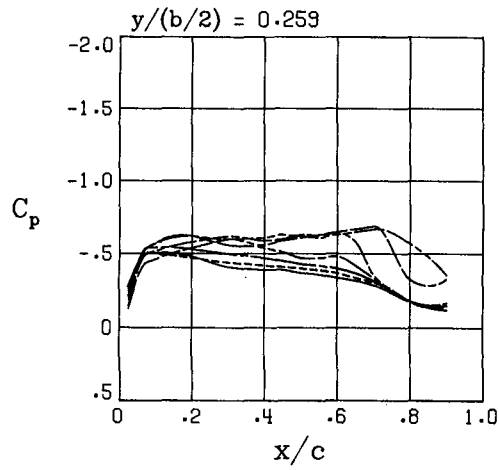Figure 19.- Effect of Mach number on wing-surface pressure distributions
for model configuration B.

Lower surface pressures

(a) Concluded.

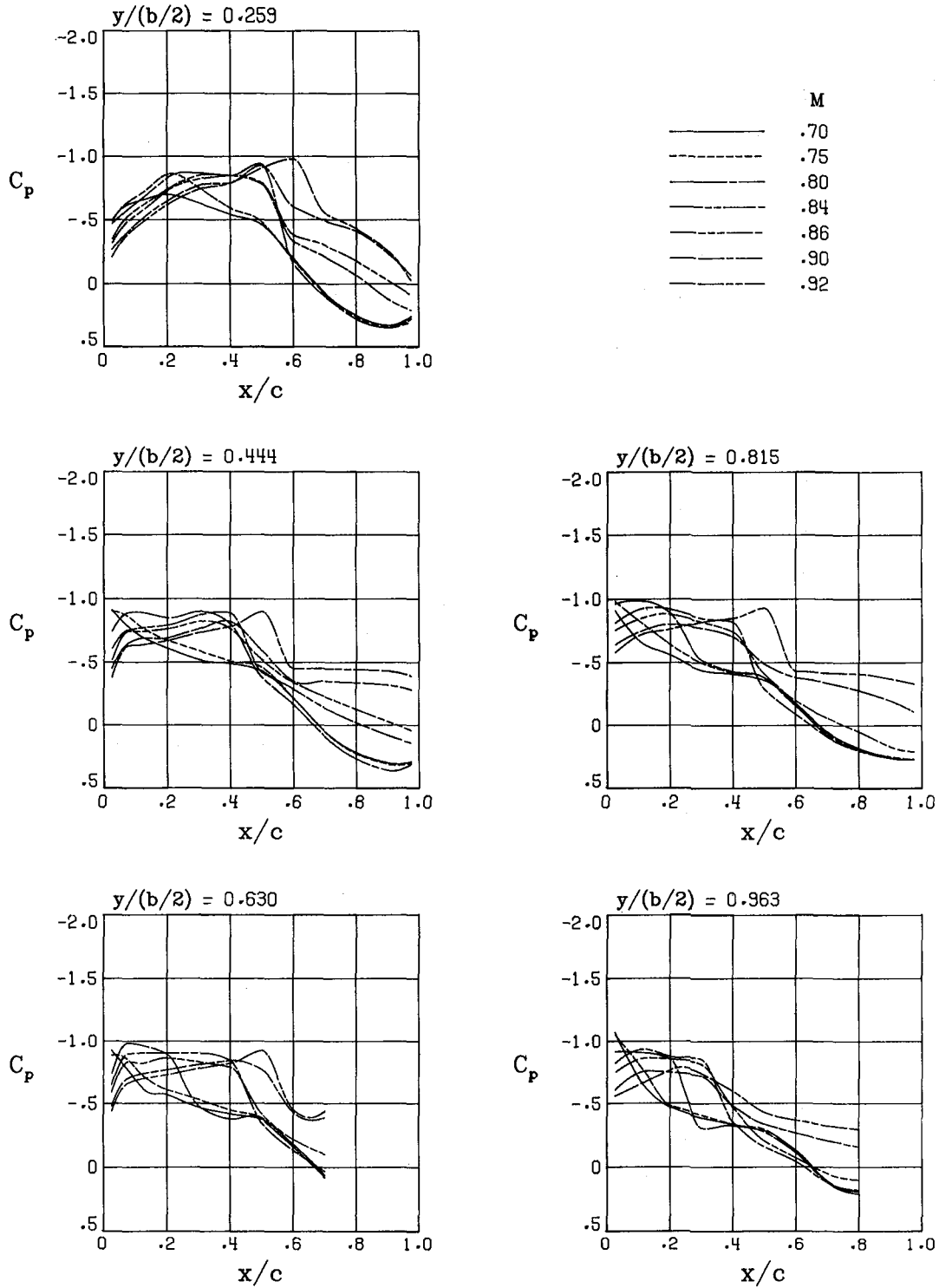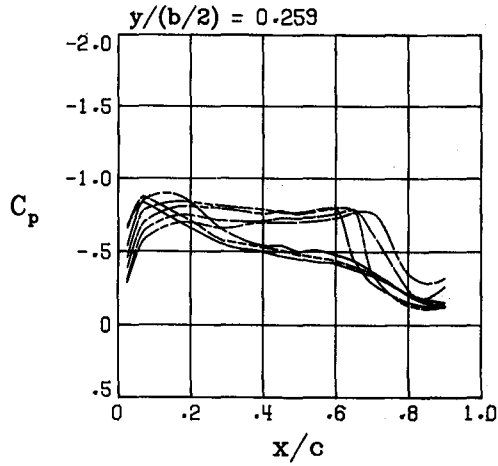Figure 19.- Continued.

Upper surface pressures

(b) $\alpha_n = -2°$.

Figure 19.- Continued.

Lower surface pressures

(b) Concluded.

Figure 19.- Continued.
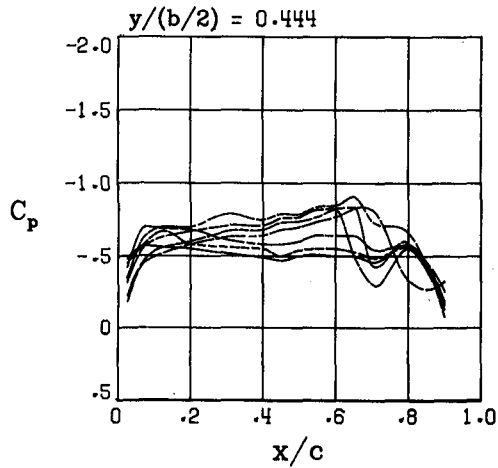
Upper surface pressures

(c)  $\alpha_n$ = 0°.

Figure 19.- Continued.

y/(b/2) = 0.259

$C_p$

-2.0
-1.5
-1.0
-.5
0
.5

0    .2    .4    .6    .8    1.0

x/c

M
——————— .70
- - - - - - .75
—— — —— .80
— —— —— .84
— — — — .86
—— —— —— .90
——— ——— .92

y/(b/2) = 0.444

$C_p$

-2.0
-1.5
-1.0
-.5
0
.5

0    .2    .4    .6    .8    1.0

x/c

y/(b/2) = 0.815

$C_p$

-2.0
-1.5
-1.0
-.5
0
.5

0    .2    .4    .6    .8    1.0

x/c

y/(b/2) = 0.630

$C_p$

-2.0
-1.5
-1.0
-.5
0
.5

0    .2    .4    .6    .8    1.0

x/c

y/(b/2) = 0.963

$C_p$

-2.0
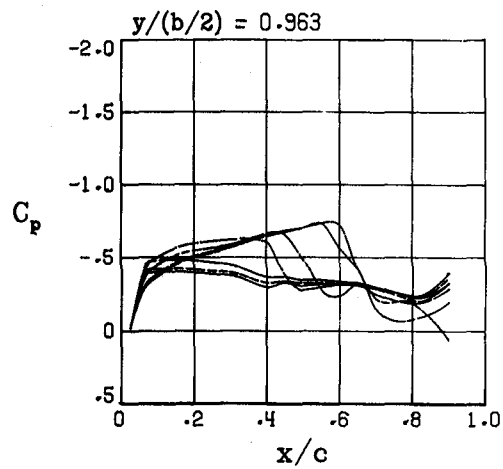-1.5
-1.0
-.5
0
.5

0    .2    .4    .6    .8    1.0

x/c

Lower surface pressures

(c) Concluded.

Figure 19.- Continued.

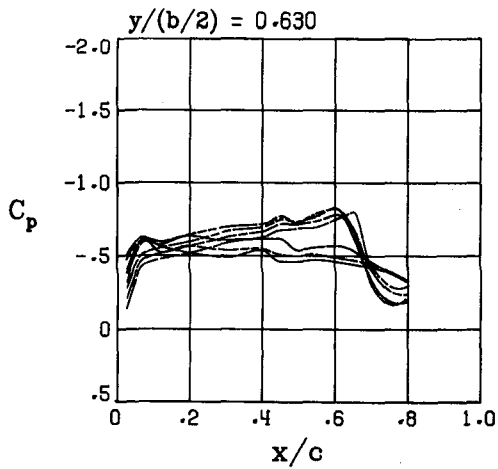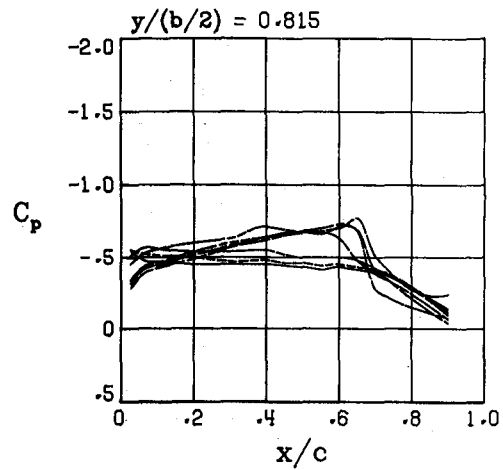Upper surface pressures

(d)  $\alpha_n = 2°$.

Figure 19.- Continued.
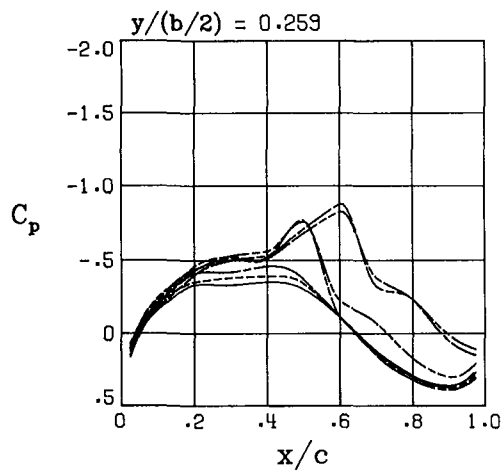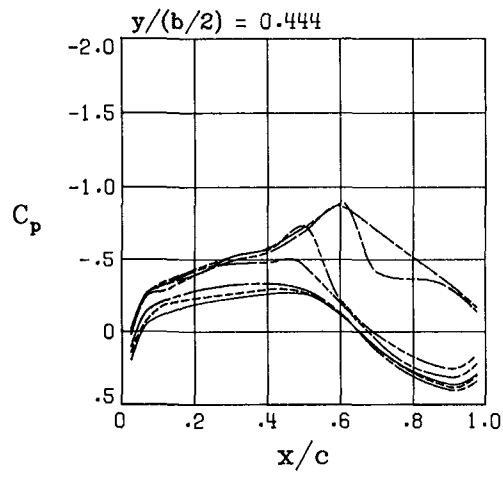
y/(b/2) = 0.259

$C_p$

x/c

M
.70
.75
.80
.84
.86
.90
.92

y/(b/2) = 0.444

$C_p$

x/c

y/(b/2) = 0.815

$C_p$

x/c

y/(b/2) = 0.630

$C_p$

x/c

y/(b/2) = 0.963

$C_p$

x/c

Lower surface pressures

(d) Concluded.

Figure 19.- Continued.

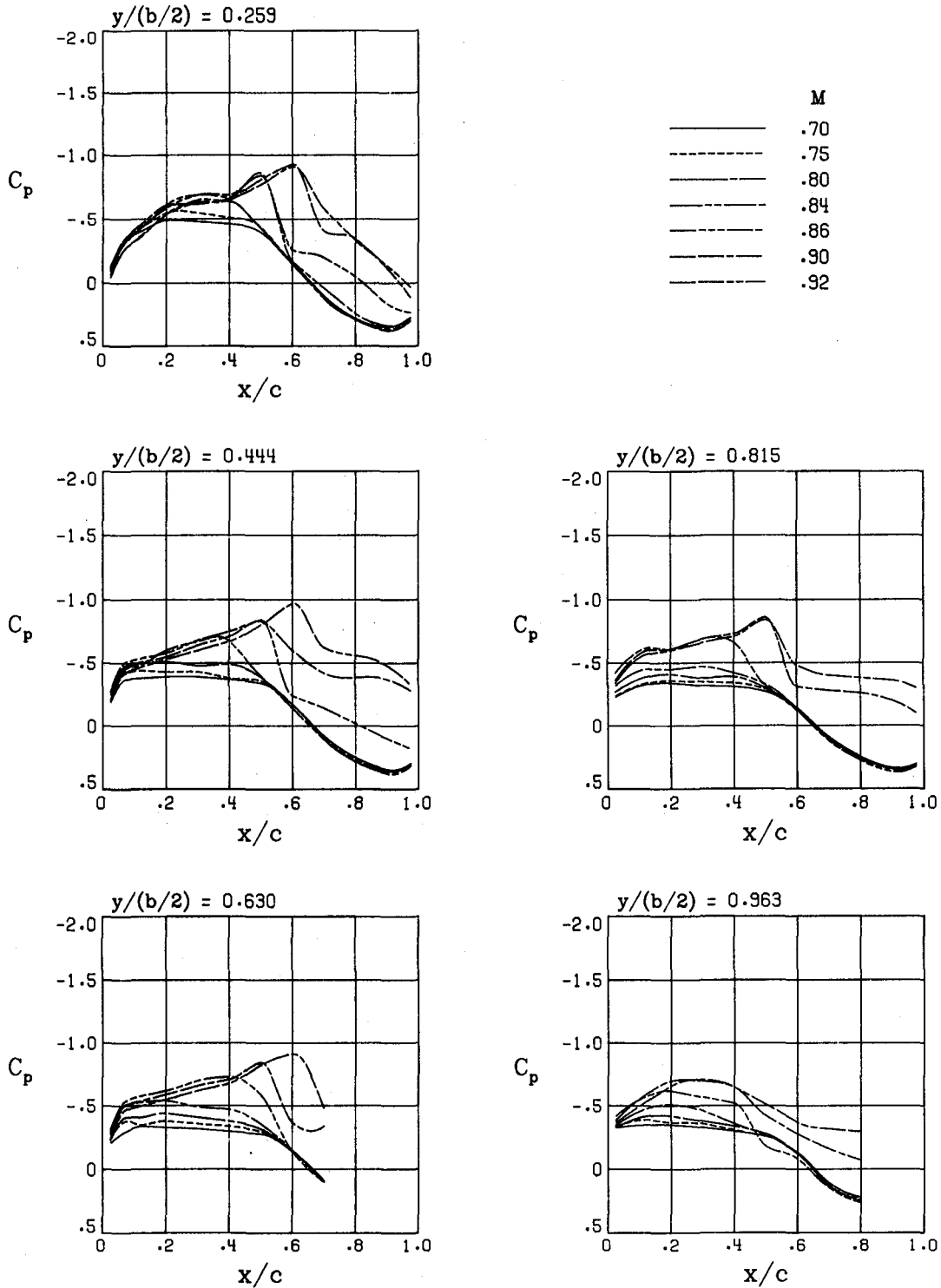Upper surface pressures
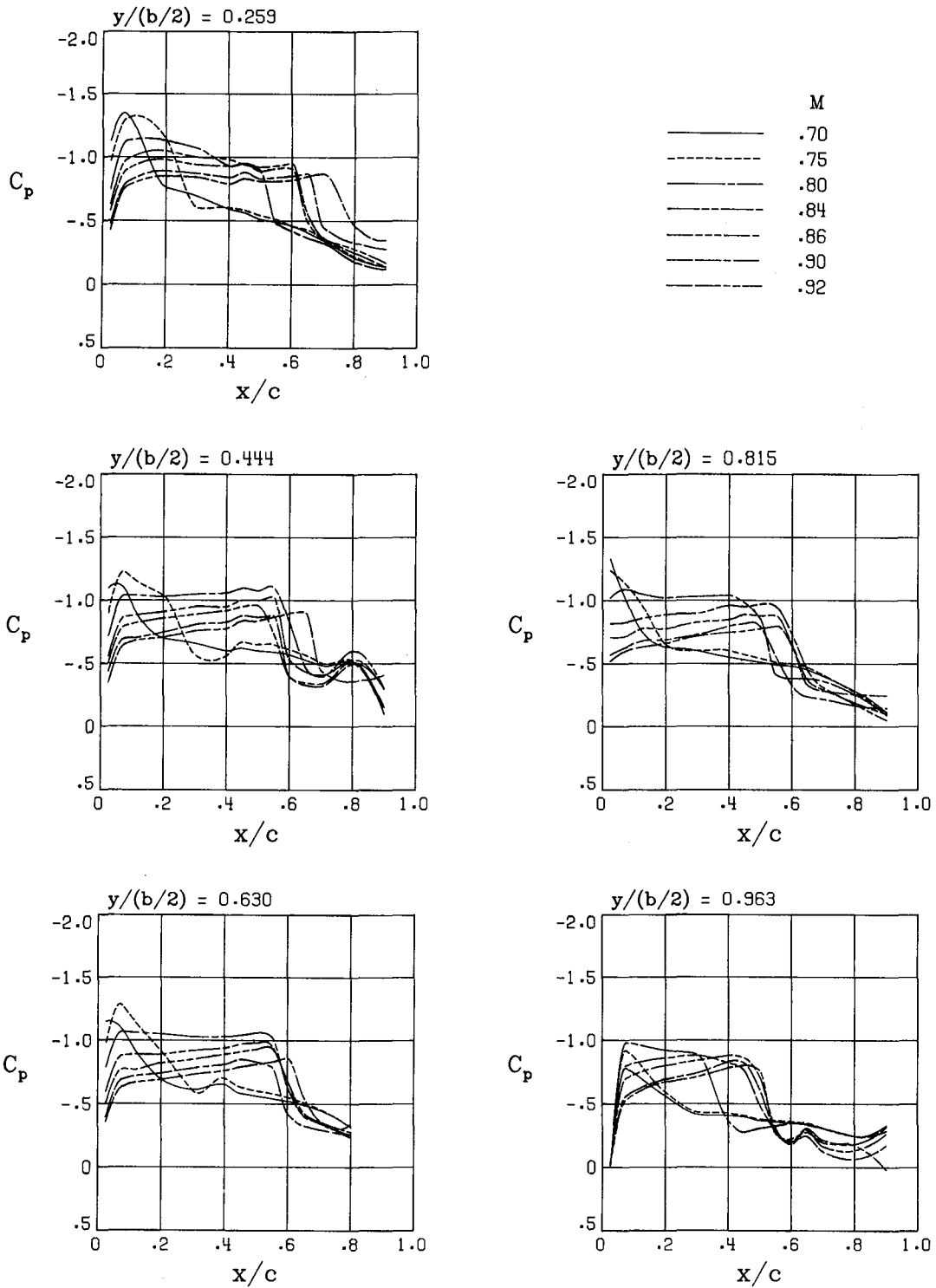
(e)  $\alpha_n$ = 4°.

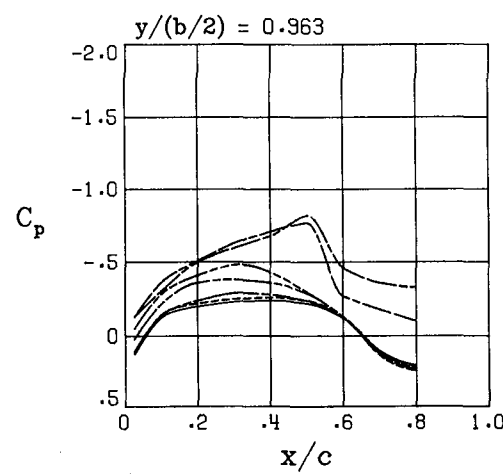Figure 19.- Continued.
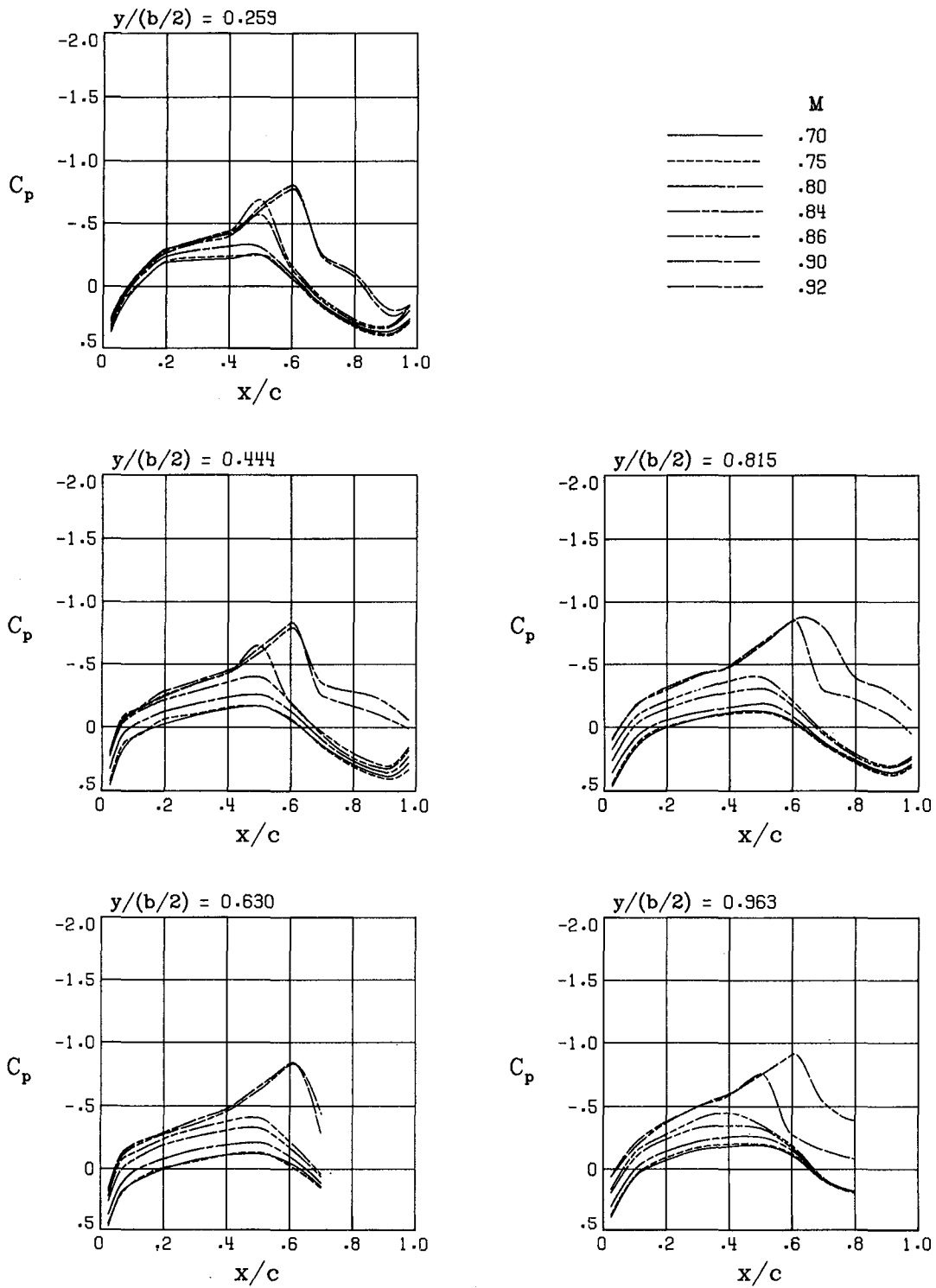
Lower surface pressures
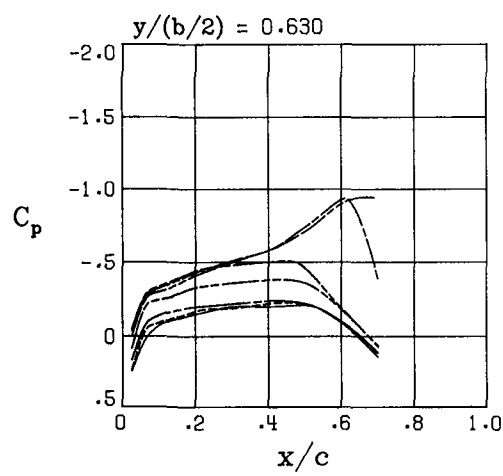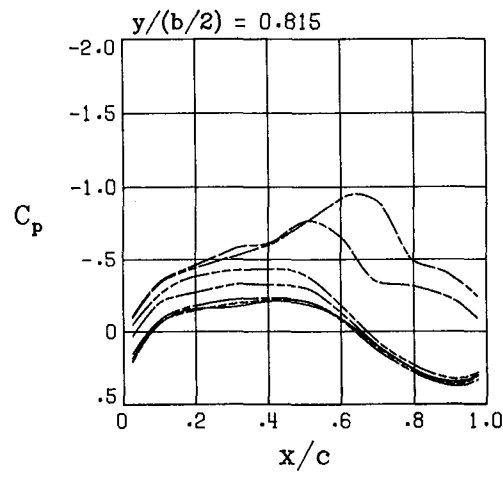
(e) Concluded.

Figure 19.- Concluded.
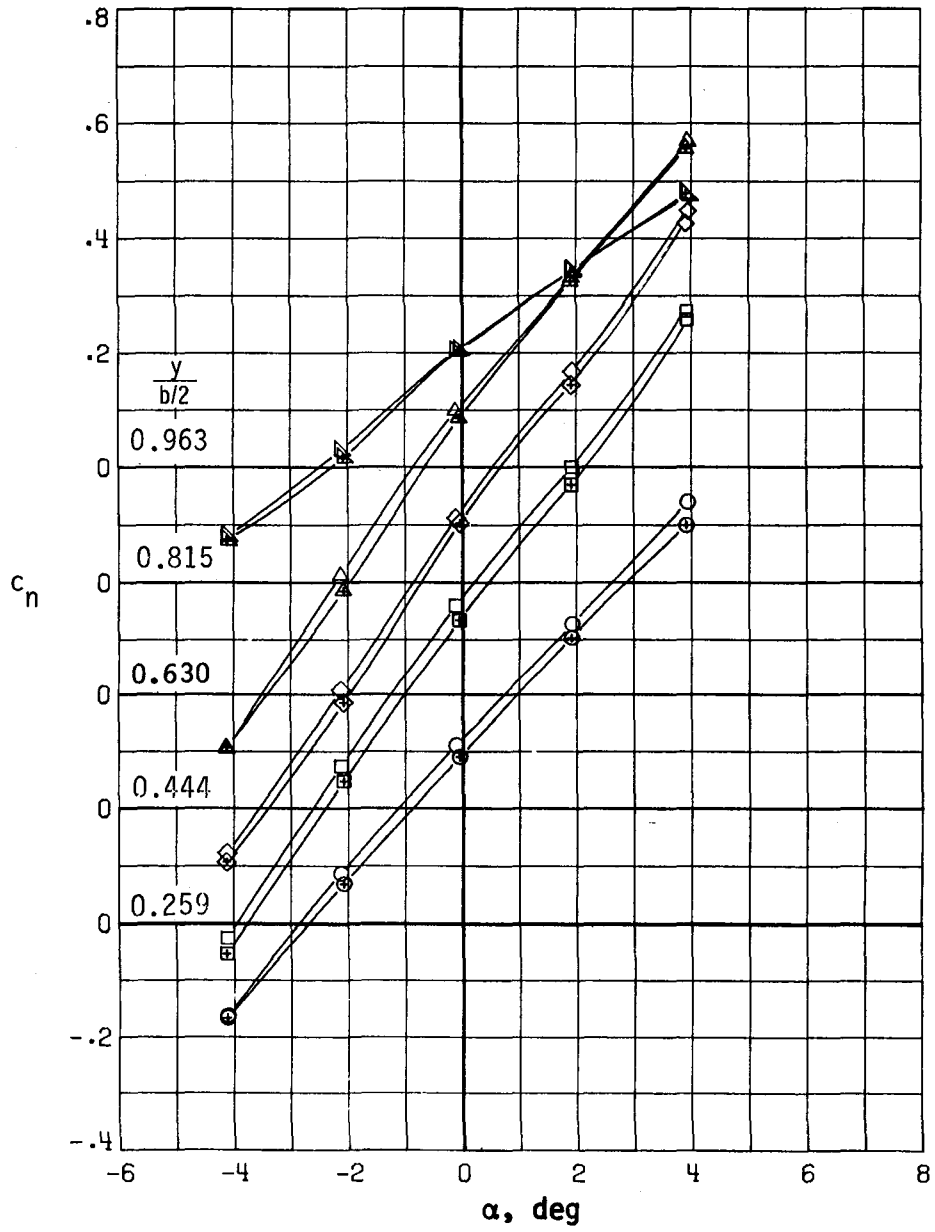
(a)  M = 0.70.

Figure 20.- Variation of wing-section normal-force coefficient with angle
of attack for model configurations A and B.

Model configuration

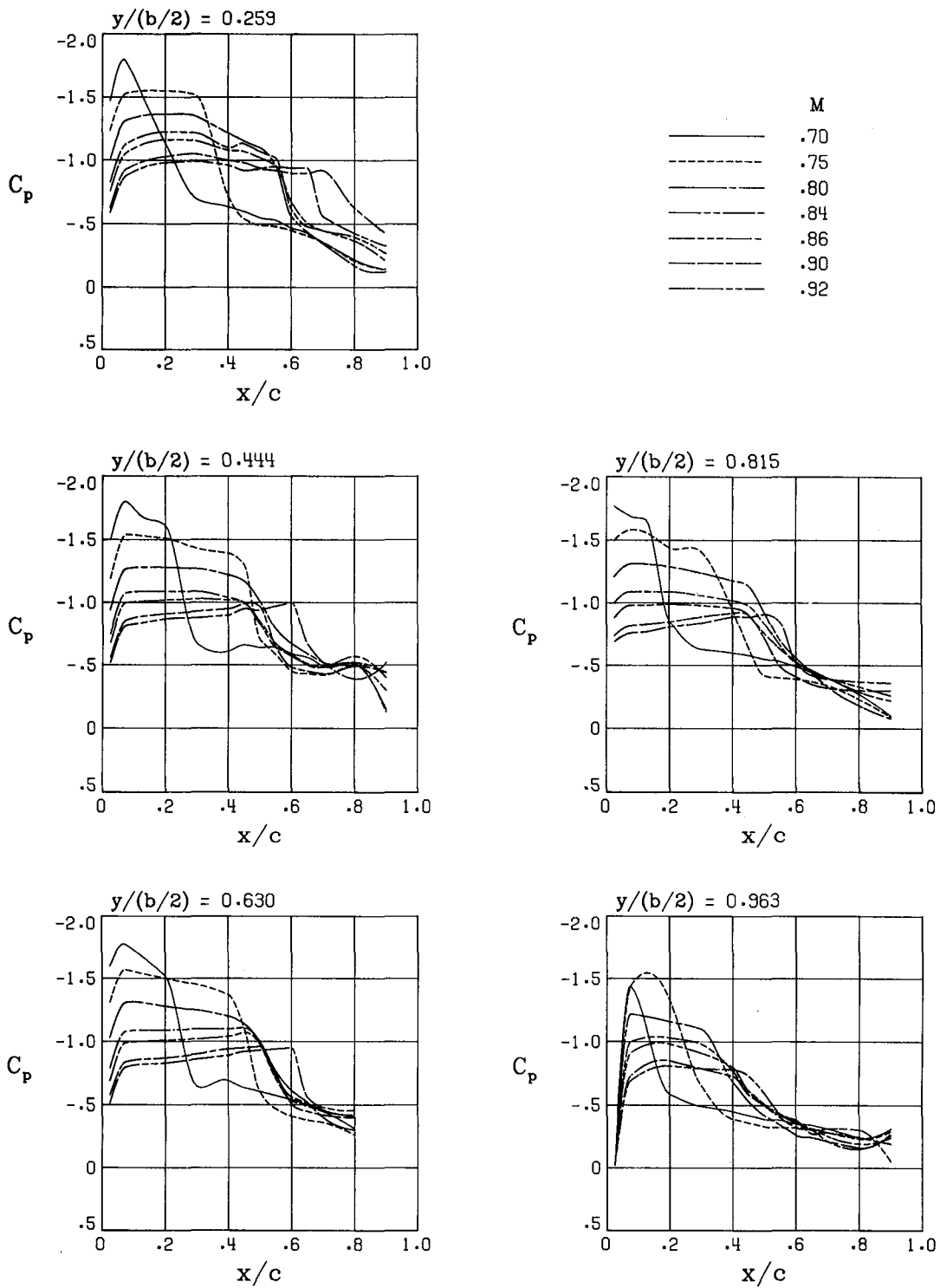| A | B | $\dfrac{y}{b/2}$ |
|---|---|---|
| ○ | ⊕ | 0.259 |
| □ | ⊞ | .444 |
| ◇ | ⬦ | .630 |
| △ | ◭ | .815 |
| ◁ | ◮ | .963 |



$c_n$

$\dfrac{y}{b/2}$

0.963

0.815

0.630

0.444

0.259

$\alpha$, deg

(b)   M = 0.75.

Figure 20.- Continued.

(c)   M = 0.80.

Figure 20.- Continued.

Model configuration

| A | B | $\frac{y}{b/2}$ |
|---|---|---|
| ◯ | ⊕ | 0.259 |
| ◻ | ⊞ | .444 |
| ◇ | ⬖ | .630 |
| △ | ◬ | .815 |
| ◺ | ◺ | .963 |

(d)   M = 0.84.

Figure 20.- Continued.
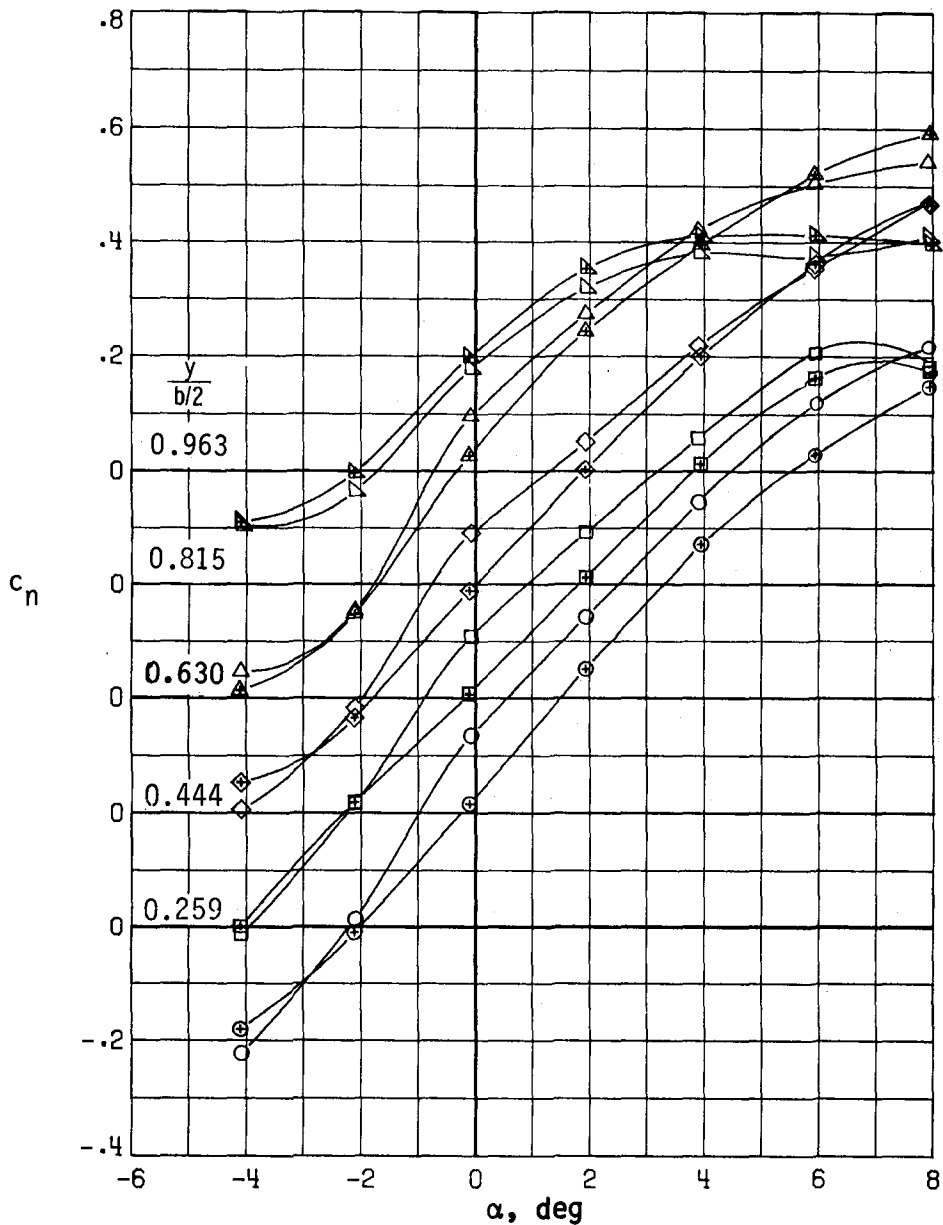
(e)  M = 0.86.

Figure 20.- Continued.

Model configuration

| A | B | $\frac{y}{b/2}$ |
|---|---|---|
| ◯ | ⊕ | 0.259 |
| ▢ | ⊞ | .444 |
| ◇ | ⬦ | .630 |
| △ | ▲ | .815 |
| ◁ | ◀ | .963 |

(f)  M = 0.90.

Figure 20.- Continued.

## Model configuration

| A | B | $\dfrac{y}{b/2}$ |
|---|---|---|
| ○ | ⊕ | 0.259 |
| □ | ⊞ | .444 |
| ◇ | ◈ | .630 |
| △ | ▲ | .815 |
| ◁ | ◣ | .963 |
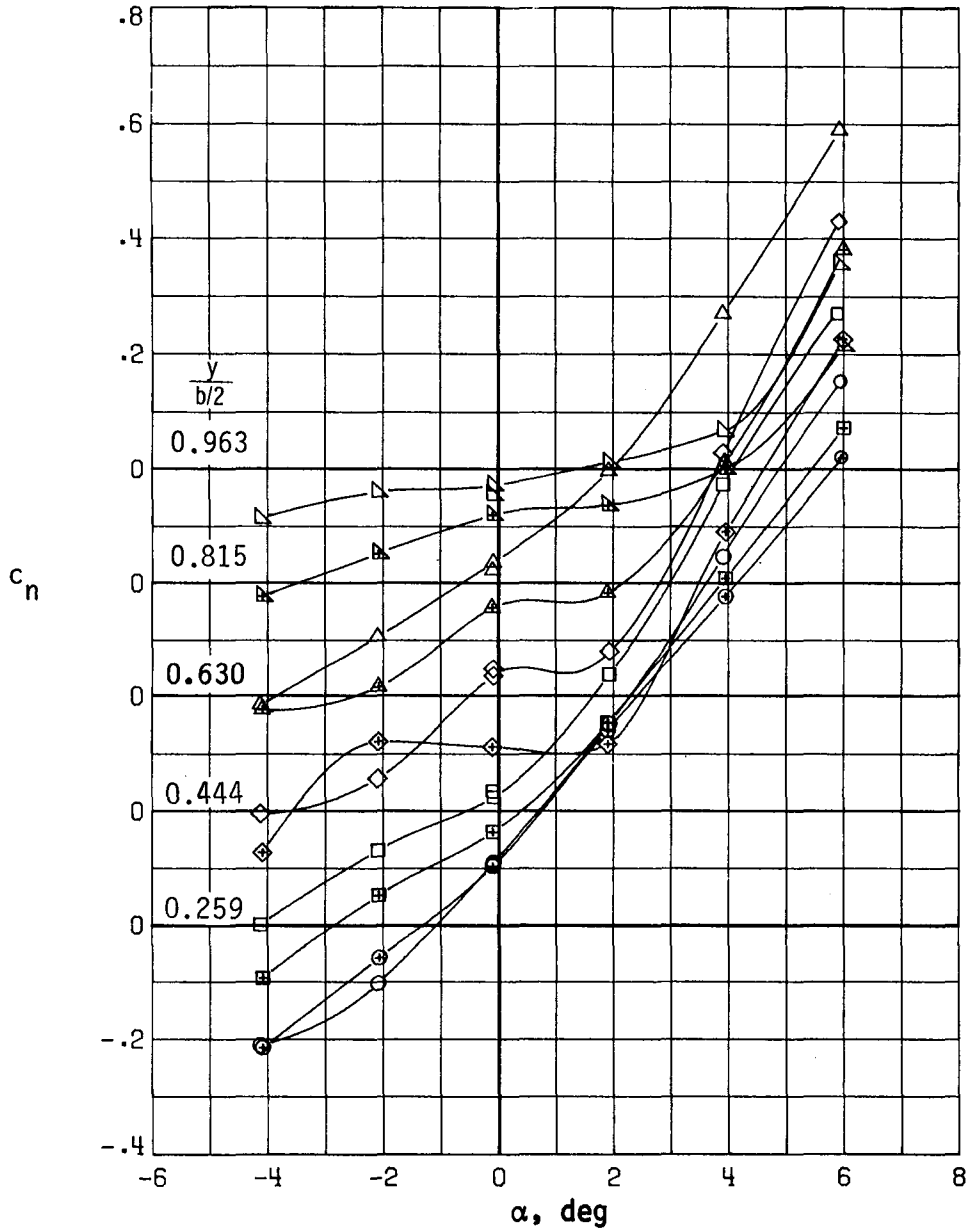


(g)   M = 0.92.

Figure 20.- Concluded.

(a)   M = 0.70.

Figure 21.- Variation of wing-section pitching-moment coefficient with angle of attack for model configurations A and B.

171

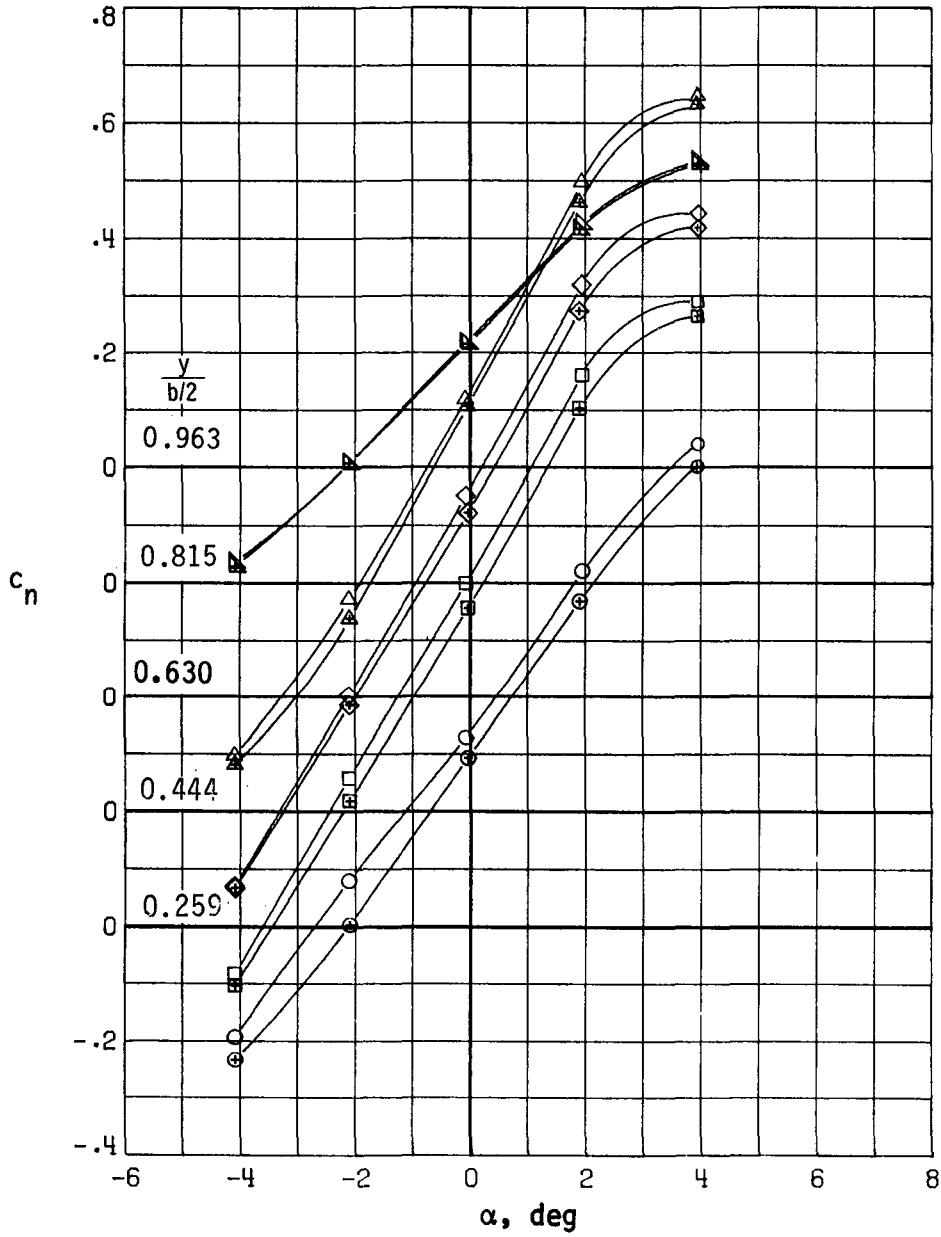(b)  M = 0.75.

Figure 21.- Continued.

(c)  M = 0.80.

Figure 21.- Continued.

Model configuration

| A | B | $\dfrac{y}{b/2}$ |
|---|---|---|
| ◯ | ⊕ | 0.259 |
| ▢ | ⊞ | .444 |
| ◇ | ⬖ | .630 |
| △ | ▲ | .815 |
| ◁ | ◀ | .963 |



(d)  M = 0.84.

Figure 21.- Continued.
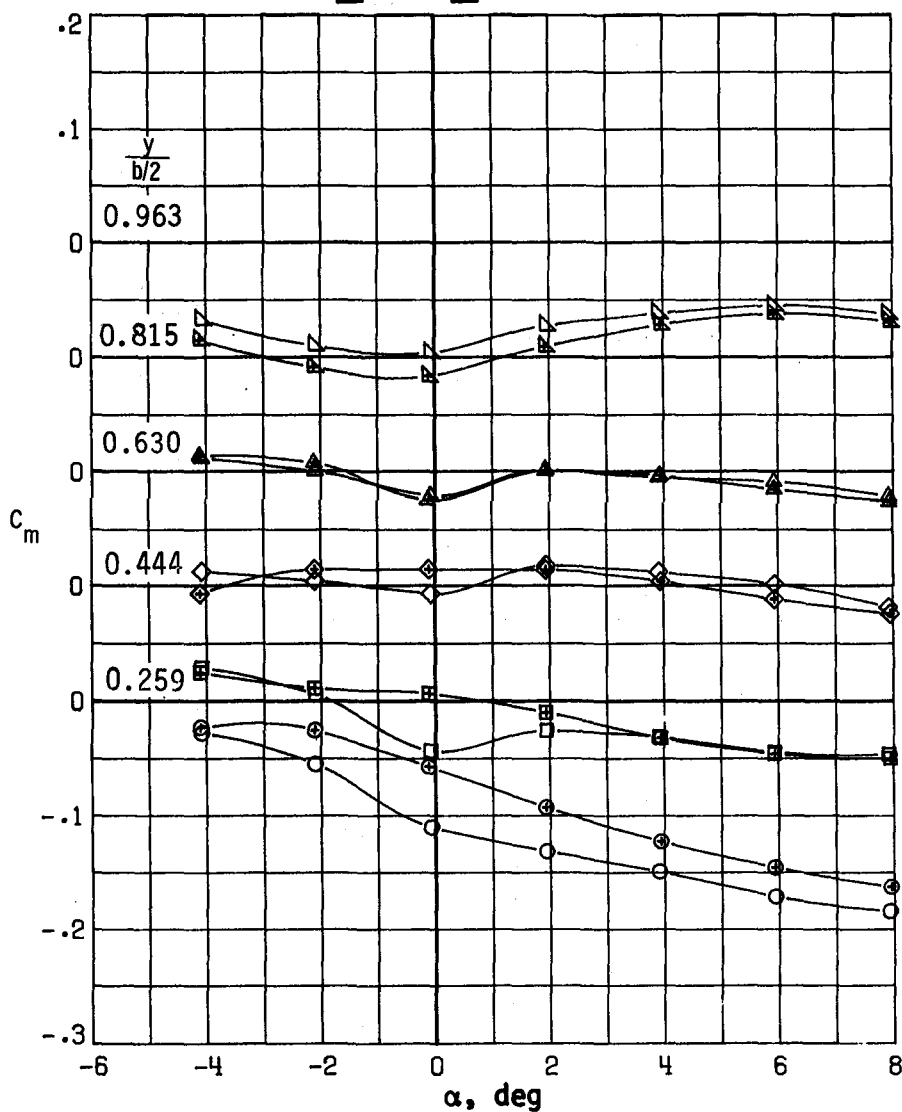
(e)  M = 0.86.

Figure 21.- Continued.

Model configuration

| A | B | $\frac{y}{b/2}$ |
|---|---|---|
| ○ | ⊕ | 0.259 |
| □ | ⊞ | .444 |
| ◇ | ⬦ | .630 |
| △ | ◭ | .815 |
| ◺ | ◹ | .963 |

(f)  M = 0.90.

Figure 21.- Continued.

Model configuration

|  | A | B | $\dfrac{y}{b/2}$ |
|---|---|---|---|
|  | ◯ | ⊕ | 0.259 |
|  | ☐ | ⊞ | .444 |
|  | ◇ | ⬦ | .630 |
|  | △ | ▲ | .815 |
|  | ◸ | ◿ | .963 |
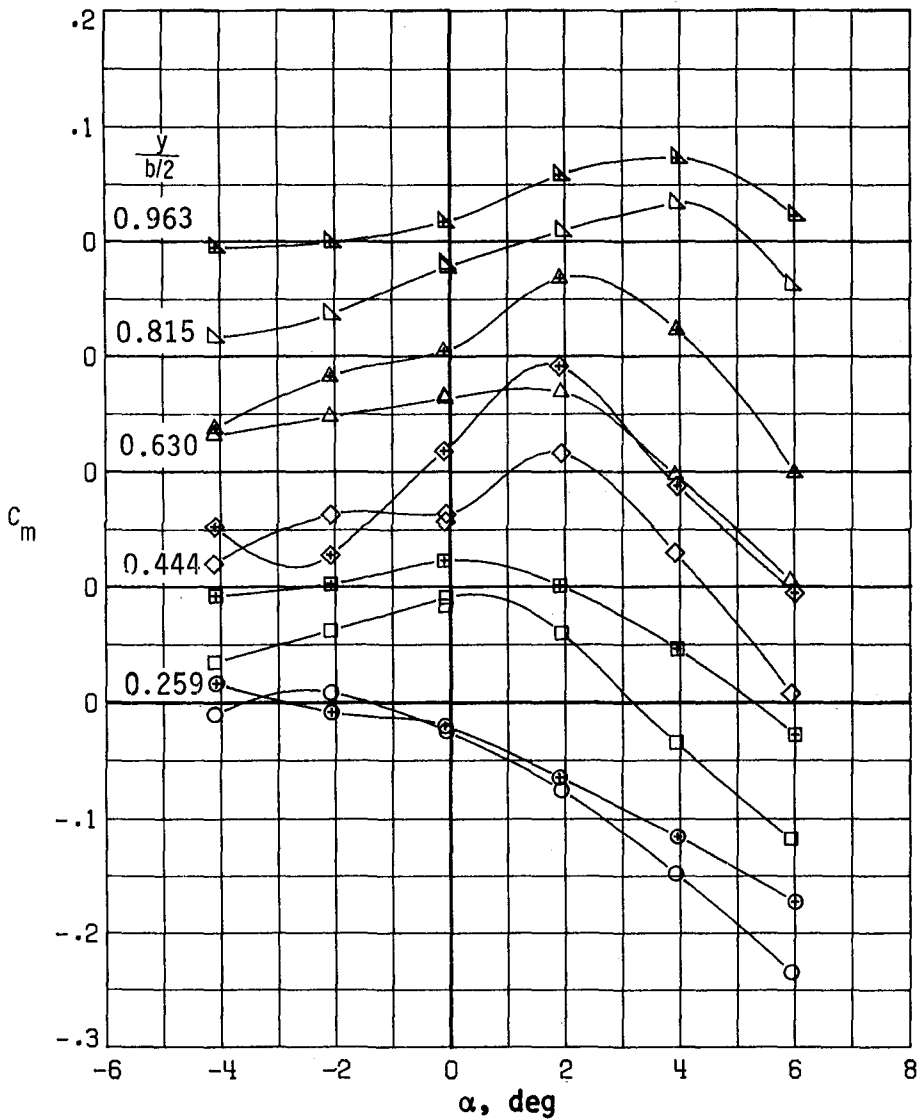


(g)   M = 0.92.

Figure 21.- Concluded.

177
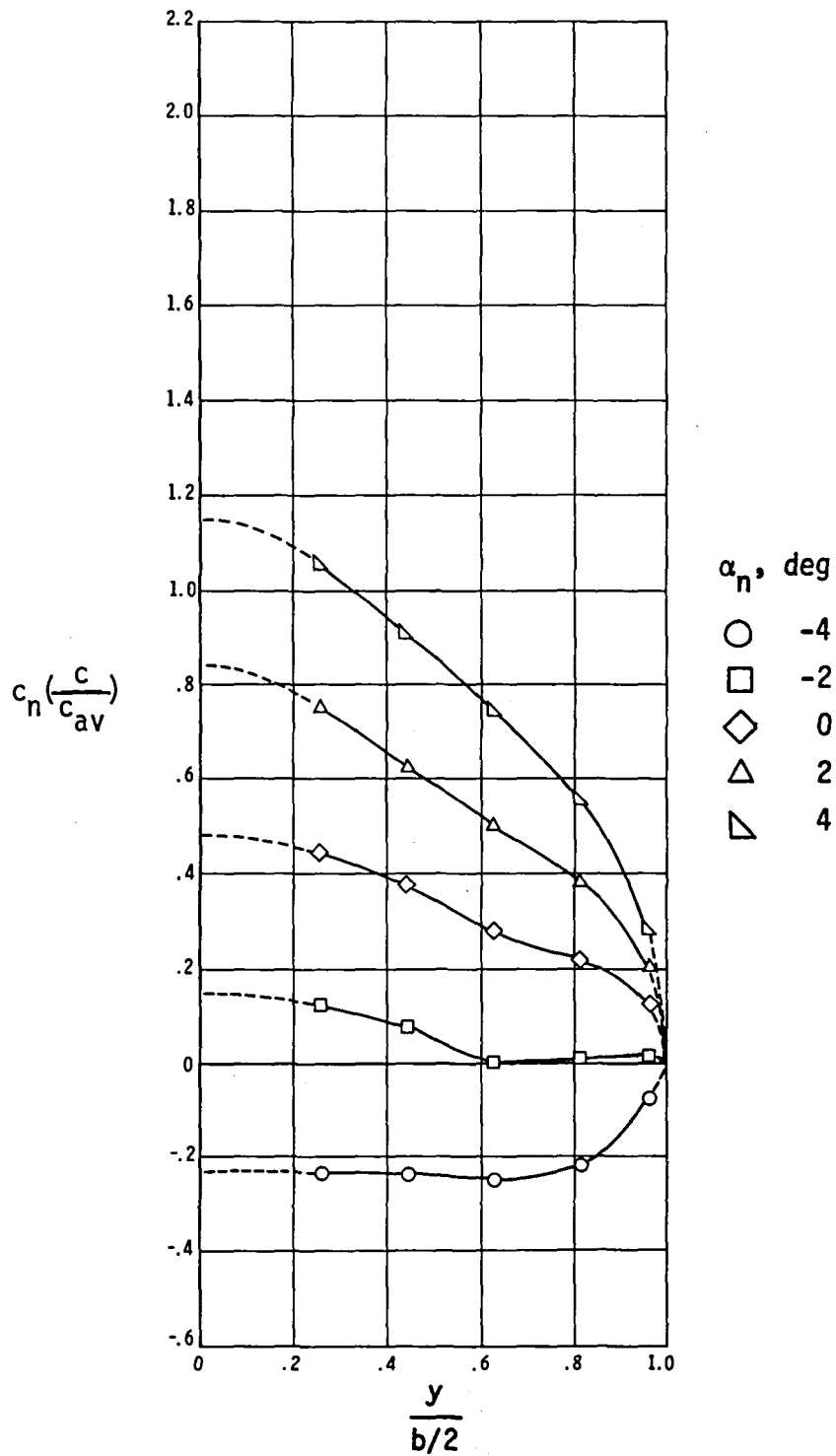
Model configuration A

(a)  M = 0.70.

Figure 22.- Variation of wing-panel loading with angle of attack.

Model configuration B

(a) Concluded.

Figure 22.- Continued.

Model configuration A

(b)  M = 0.75.

Figure 22.- Continued.

Model configuration B

(b) Concluded.

Figure 22.- Continued.

Model configuration A

(c)  M = 0.80.

Figure 22.- Continued.

Model configuration B

(c) Concluded.

Figure 22.- Continued.

$$c_n\left(\frac{c}{c_{av}}\right)$$

$\alpha_n$, deg

○ -4
□ -2
◇ 0
△ 2
▷ 4
▢ 6

$$\frac{y}{b/2}$$

Model configuration A

(d)   M = 0.84.

Figure 22.- Continued.

Model configuration B

(d) Concluded.

Figure 22.- Continued.

Model configuration A

(e)  M = 0.86.

Figure 22.- Continued.

Model configuration B

(e) Concluded.

Figure 22.- Continued.

Model configuration A

(f)   M = 0.90.

Figure 22.- Continued.

Model configuration B

(f) Concluded.

Figure 22.- Continued.

Model configuration A

(g)   M = 0.92.

Figure 22.- Continued.
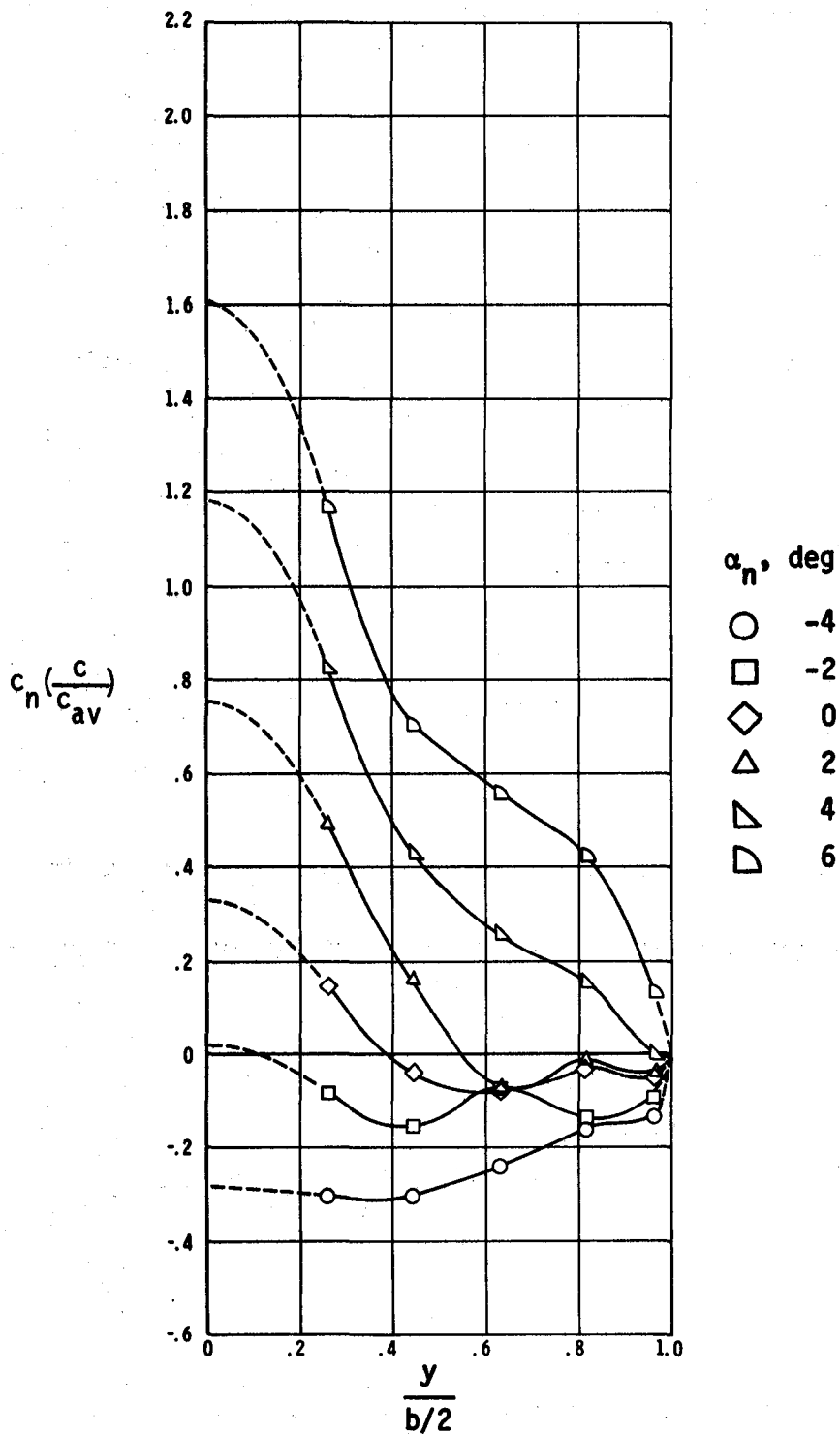
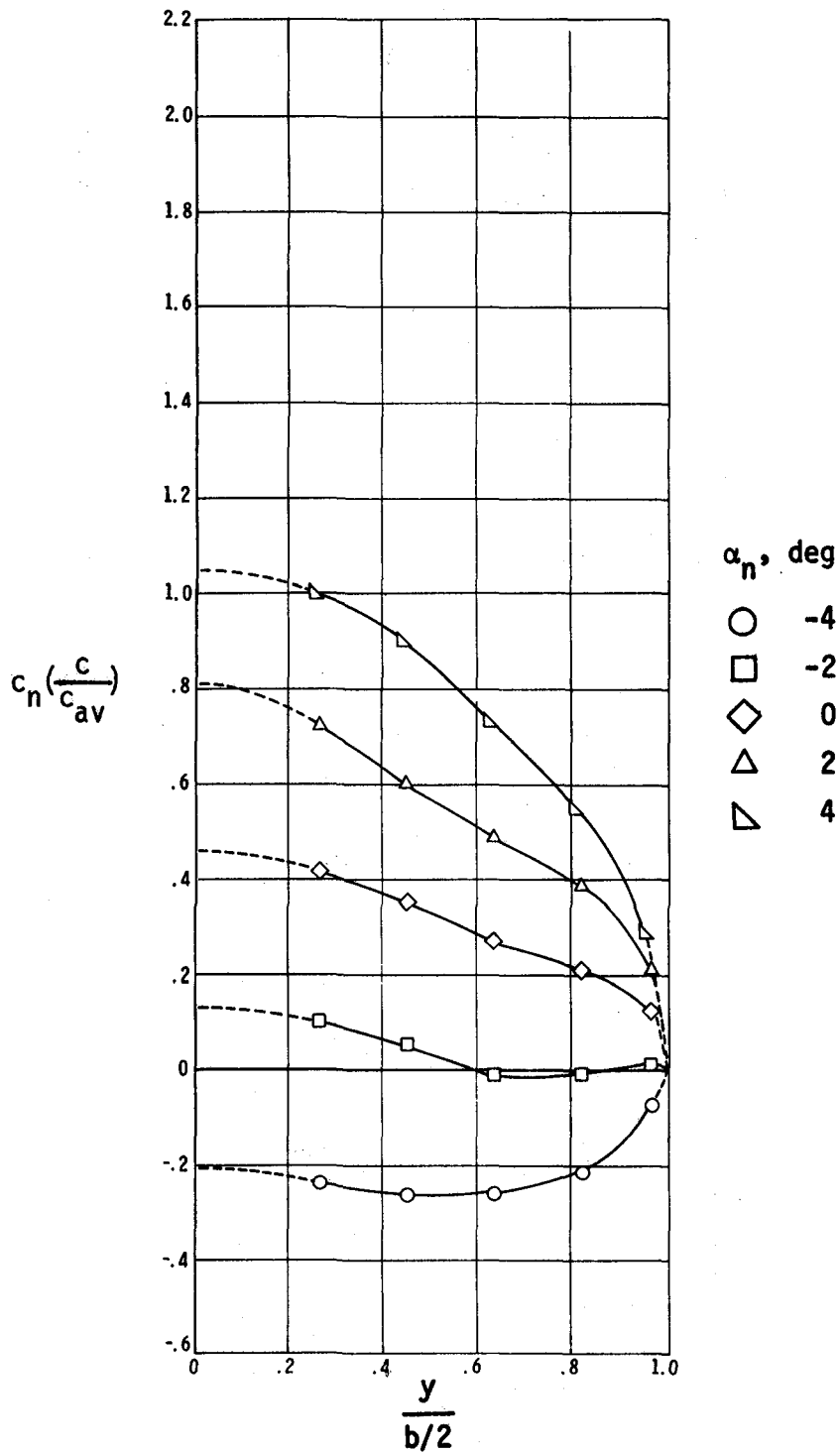Model configuration B

(g) Concluded.

Figure 22.- Concluded.
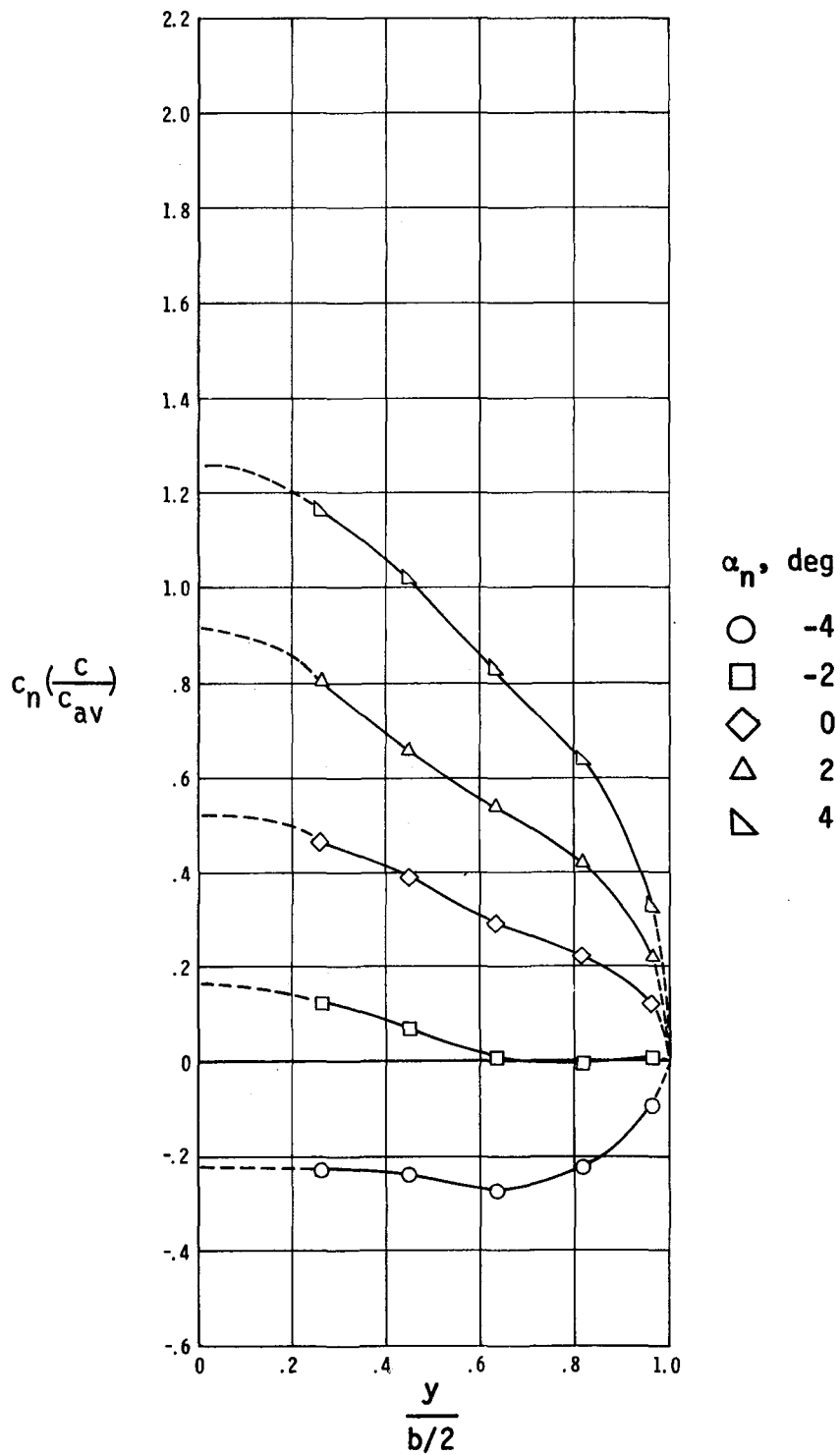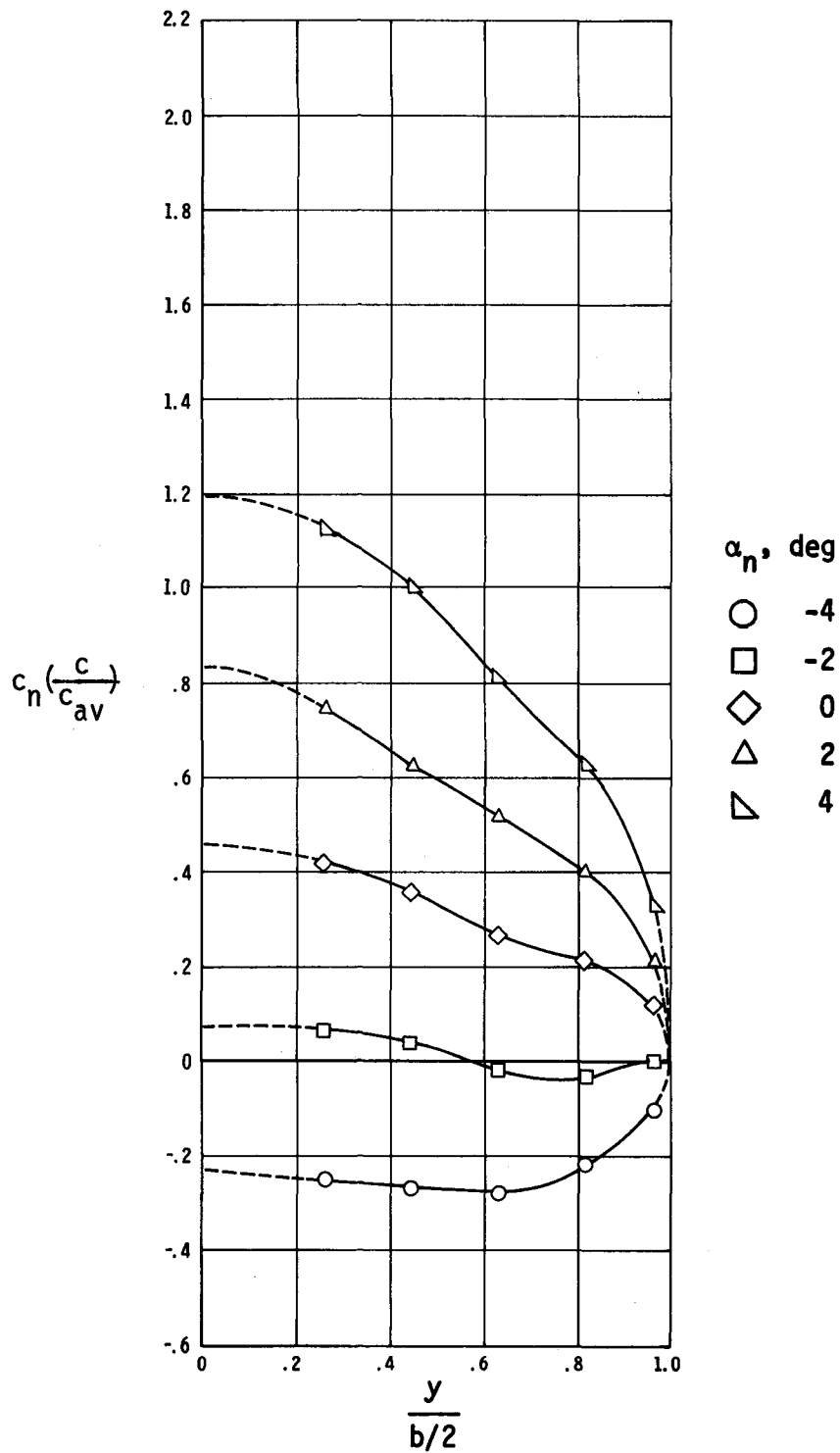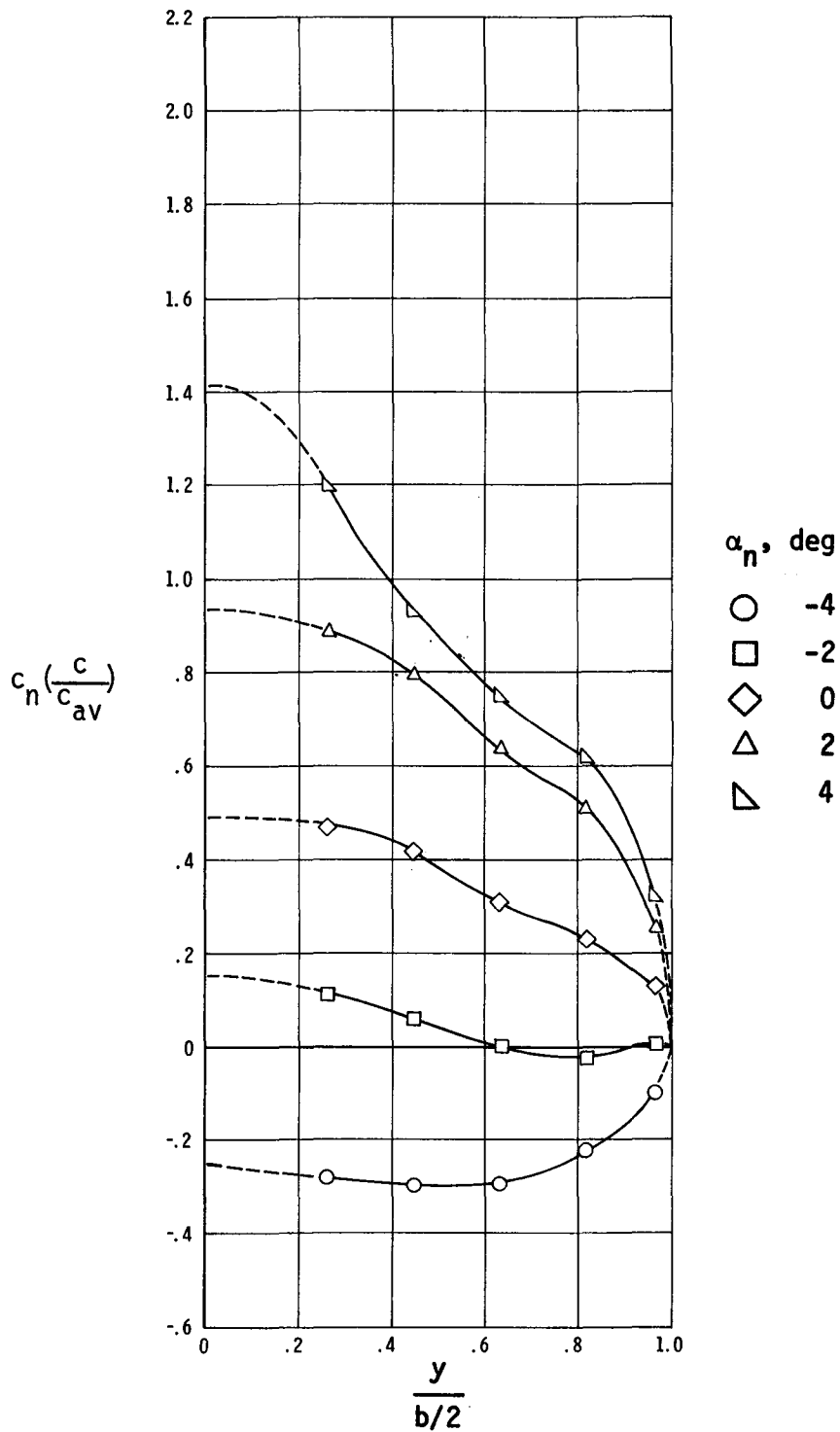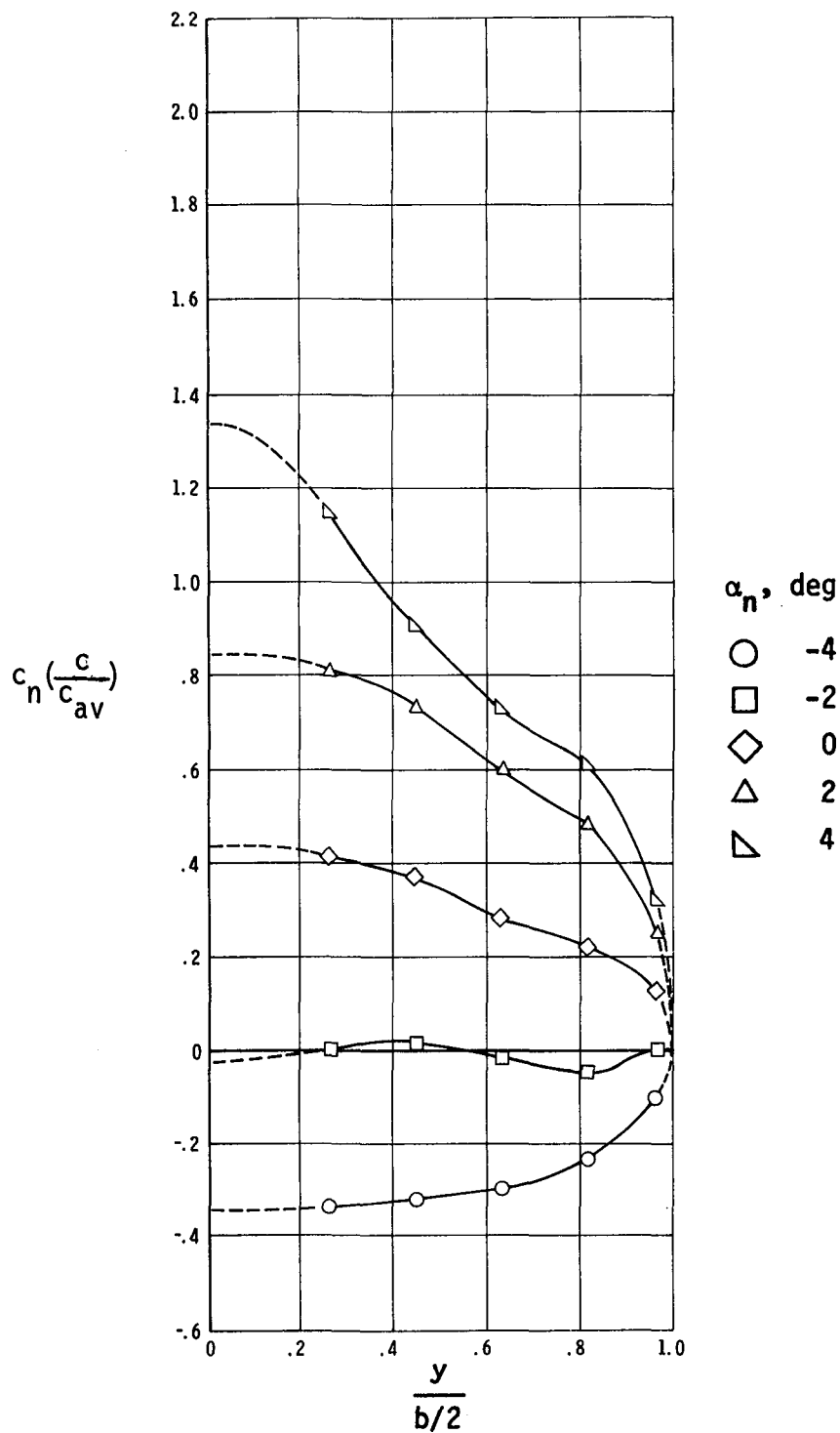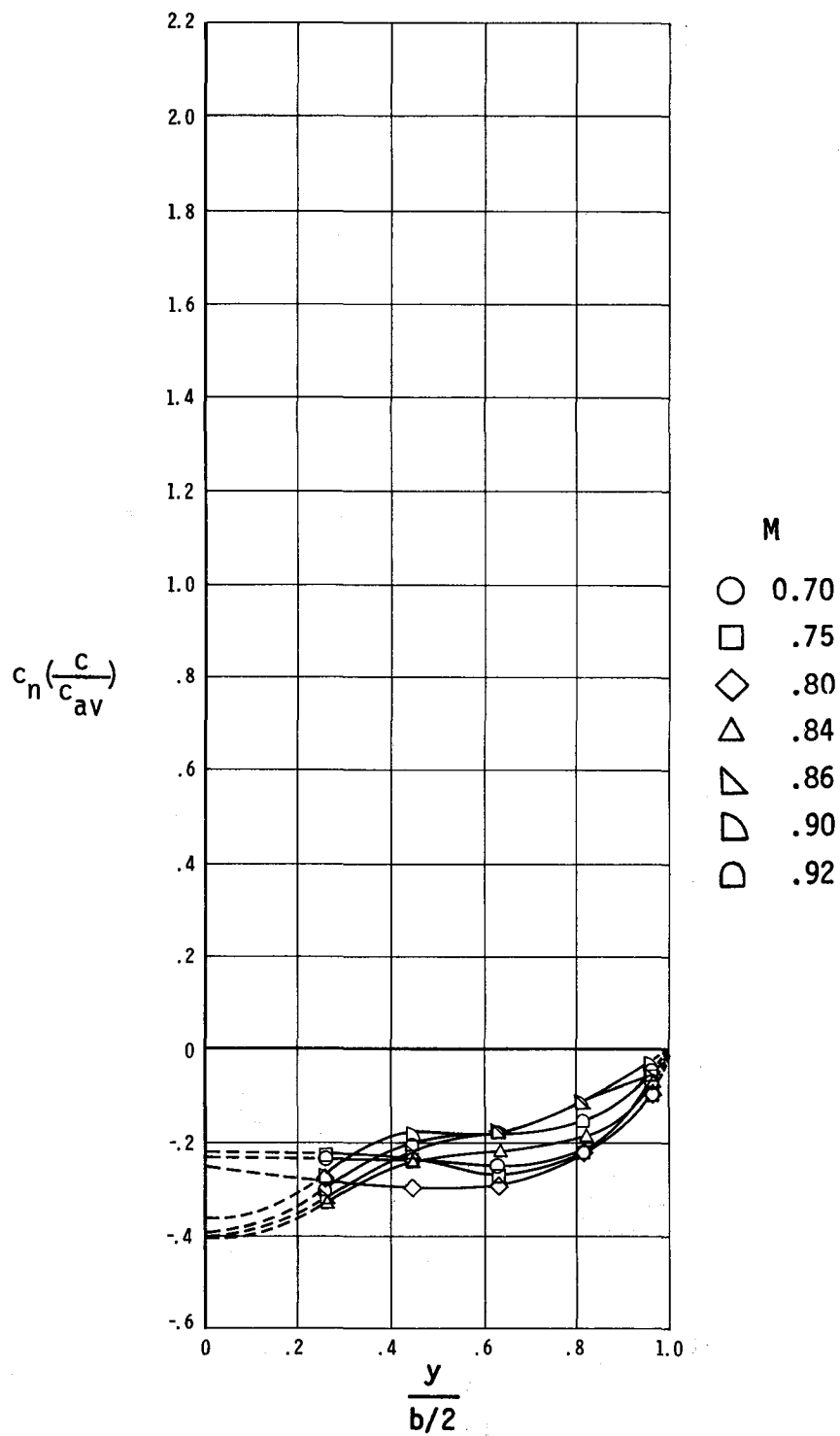
Model configuration A

(a) $\alpha_n = -4°$.

Figure 23.- Variation of wing-panel loading with Mach number.
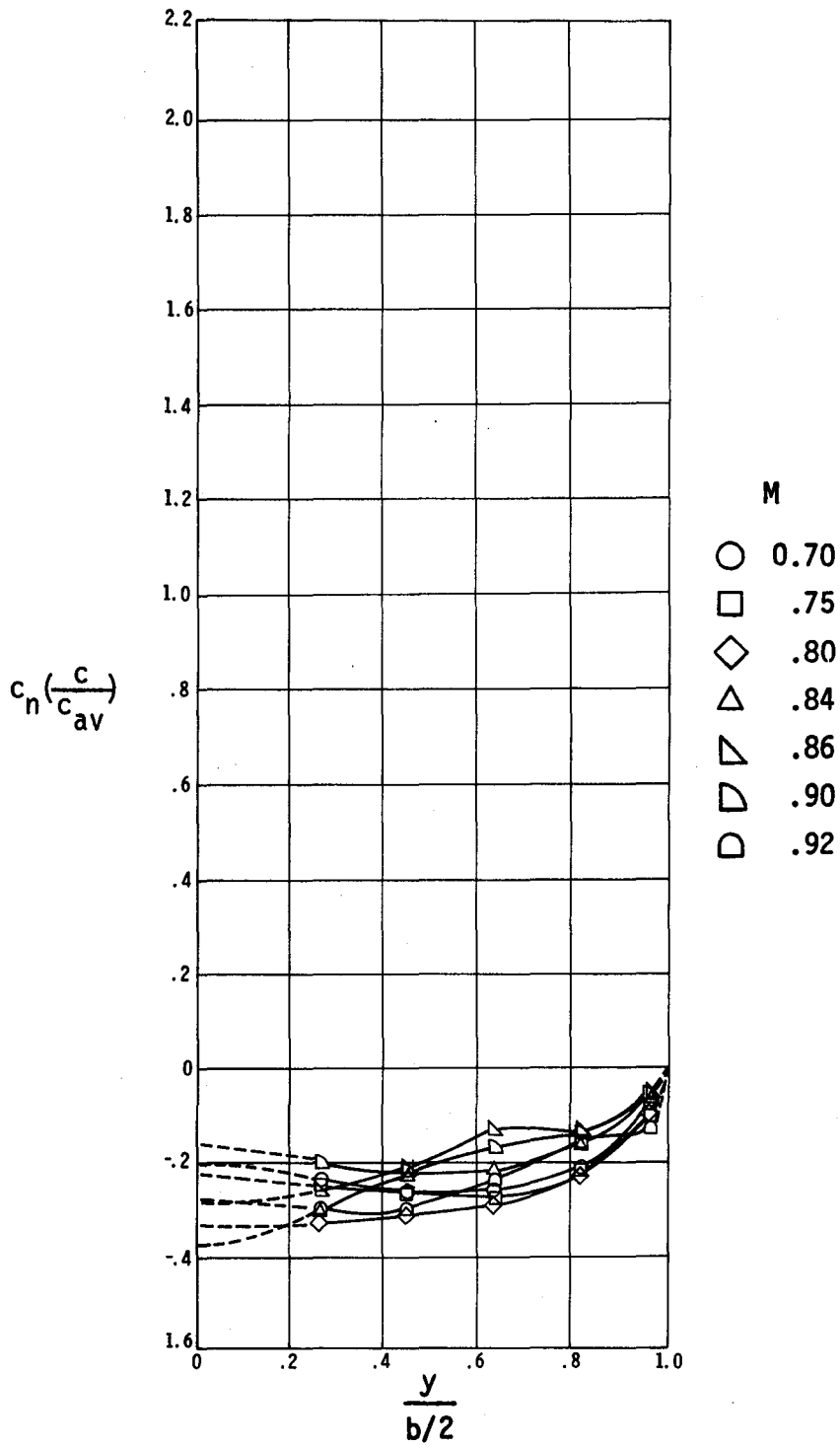
Model configuration B

(a) Concluded.

Figure 23.- Continued.
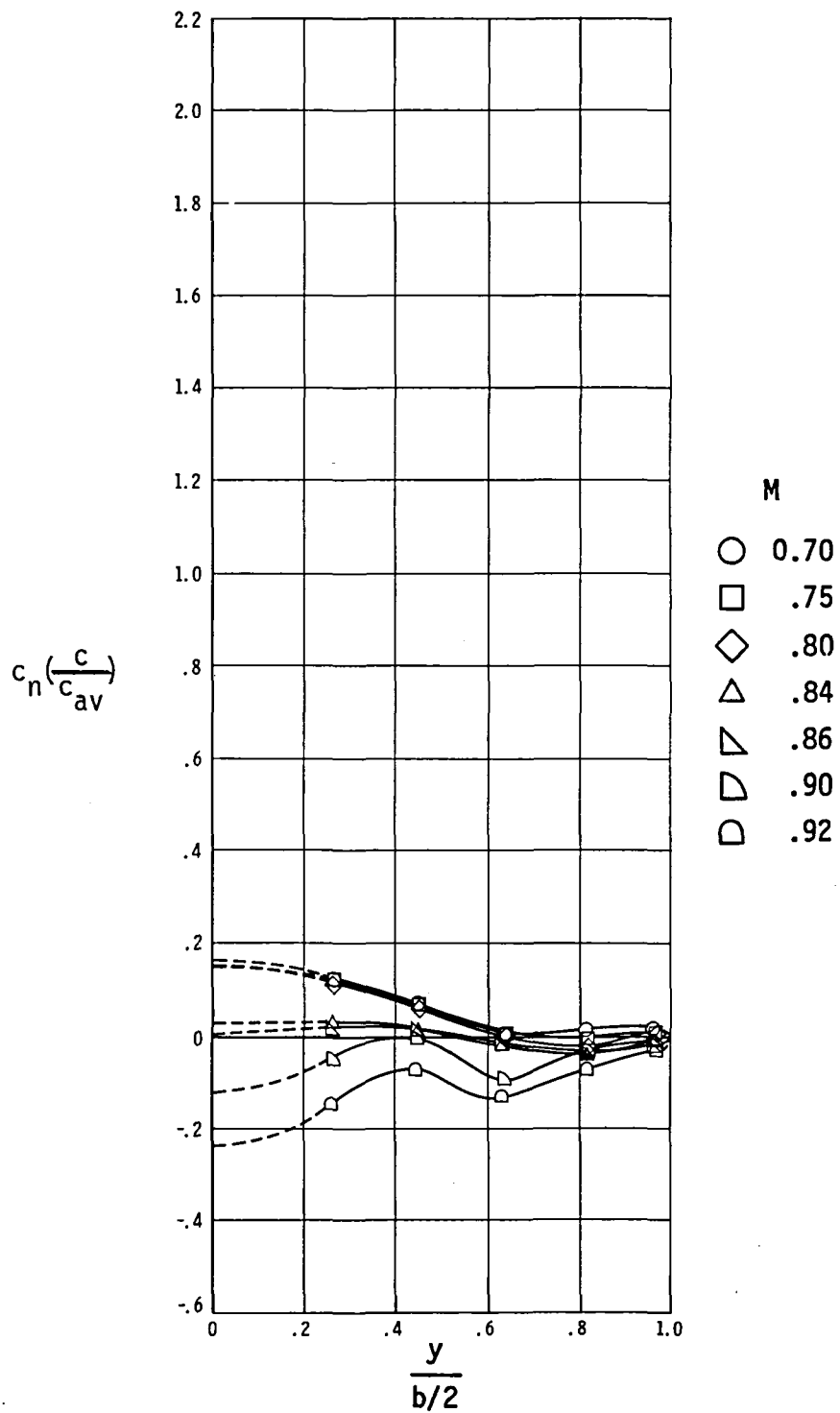
Model configuration A

(b) $\alpha_n = -2°$.

Figure 23.- Continued.
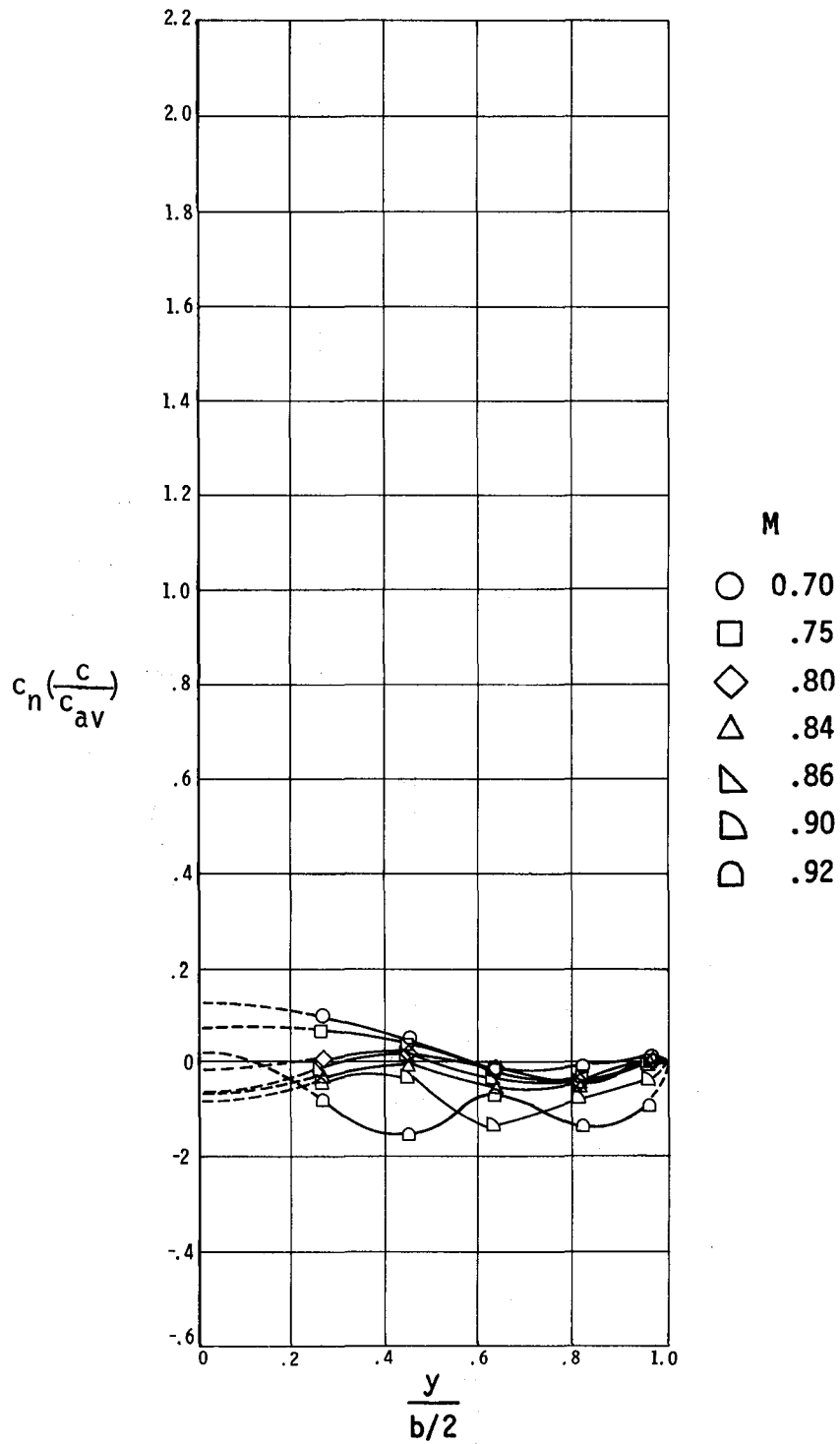
Model configuration B

(b) Concluded.

Figure 23.- Continued.
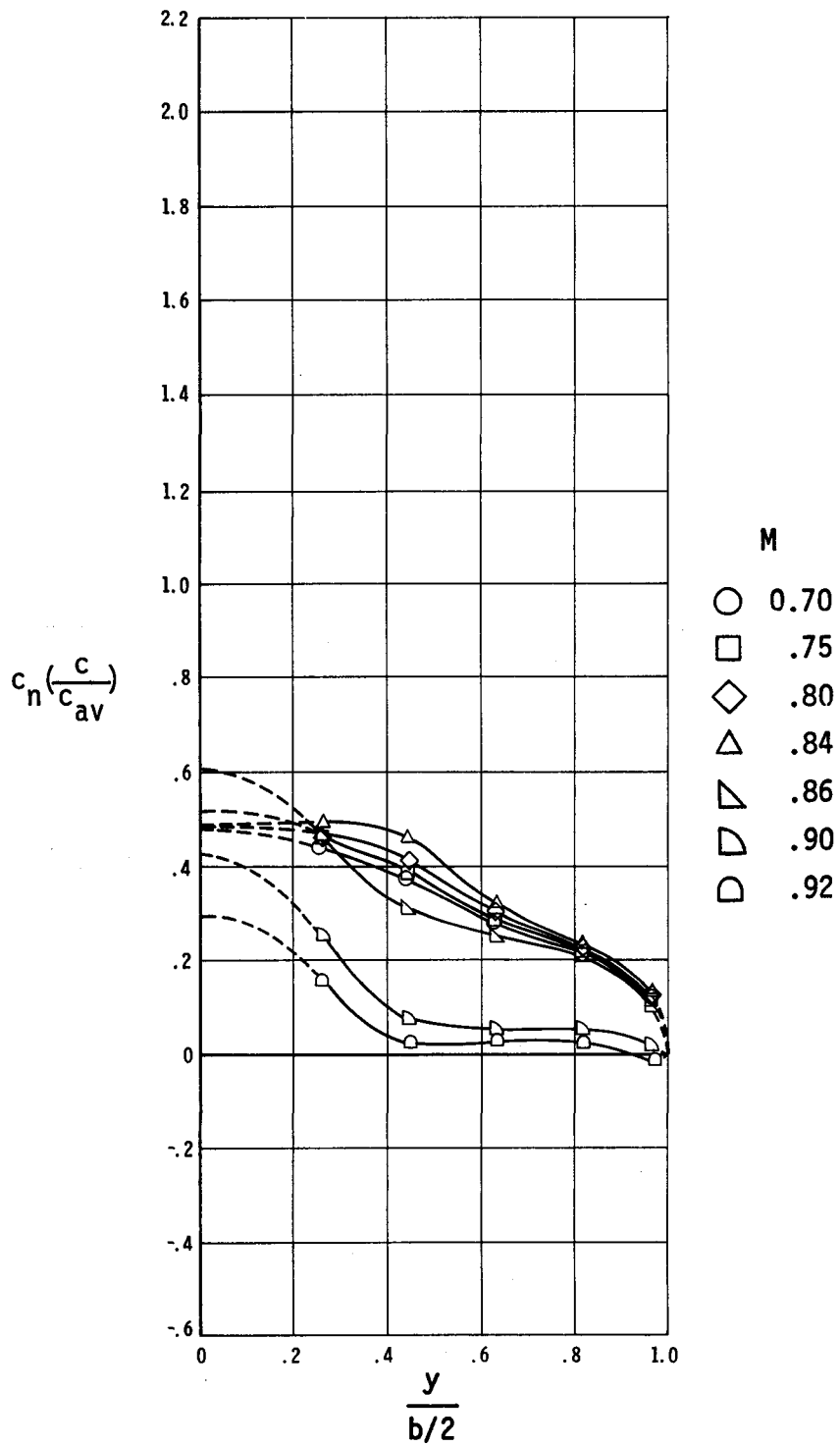
Model configuration A
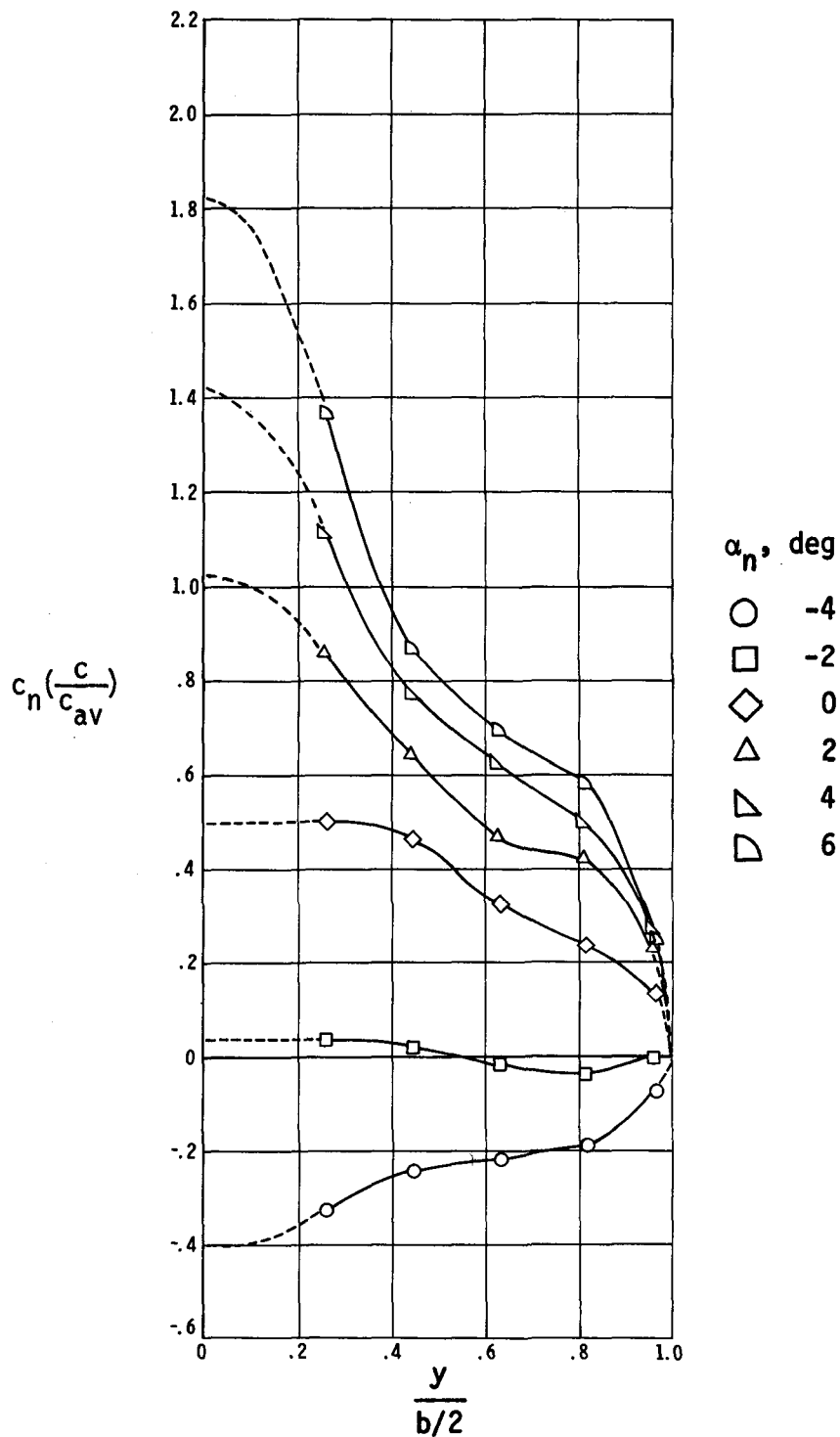
(c)  $\alpha_n = 0°$.

Figure 23.- Continued.
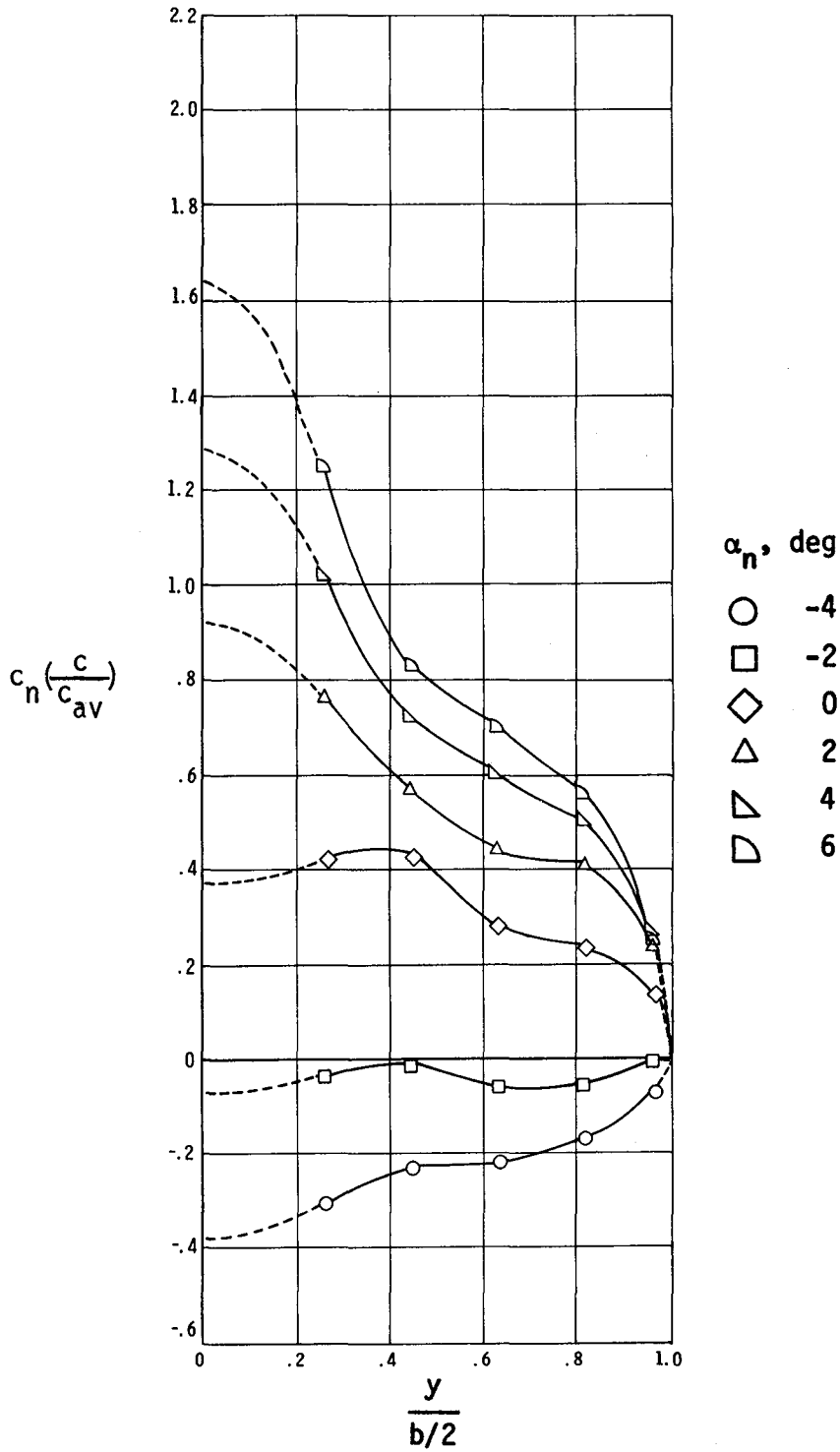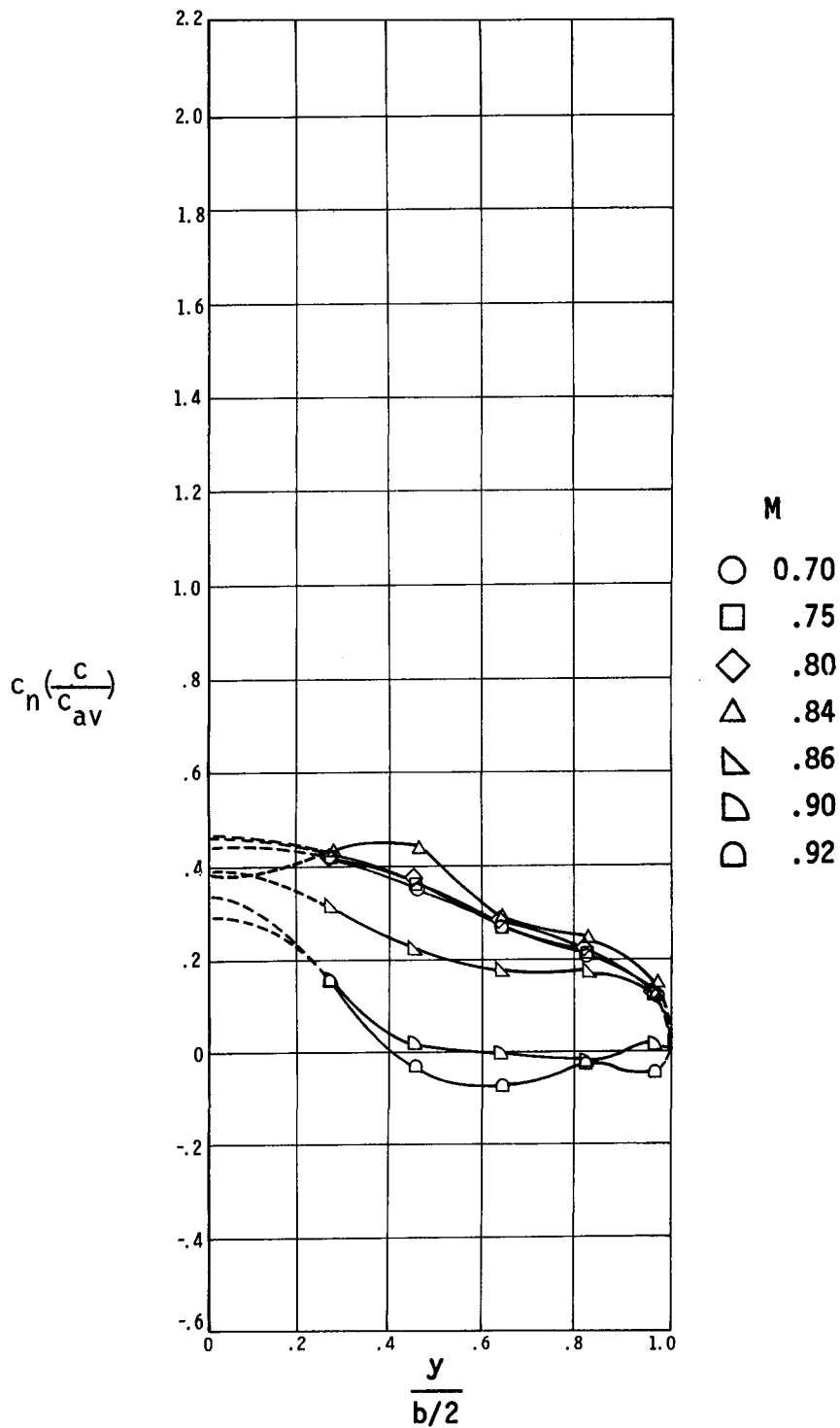
Model configuration B

(c) Concluded.

Figure 23.- Continued.
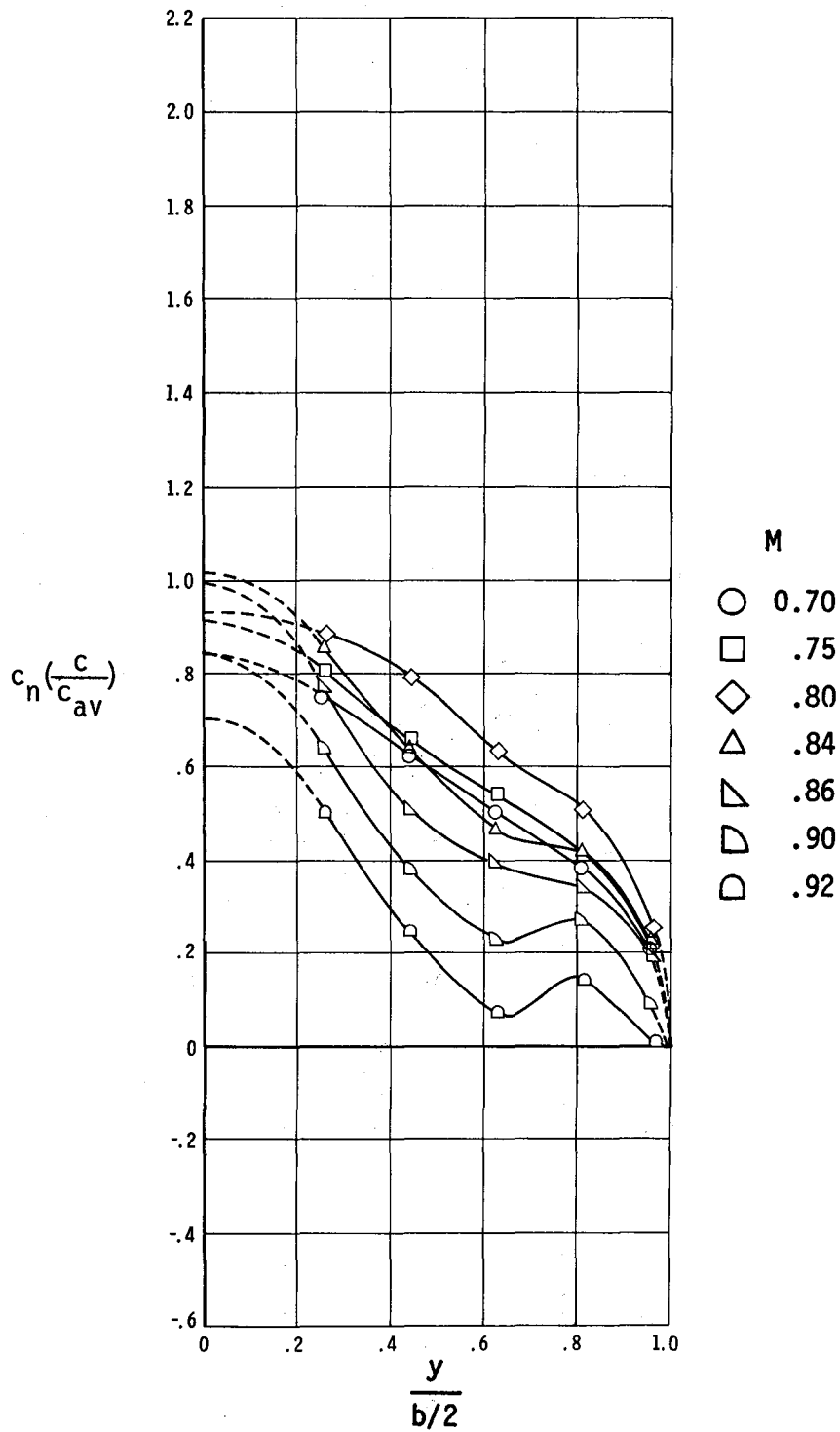
Model configuration A
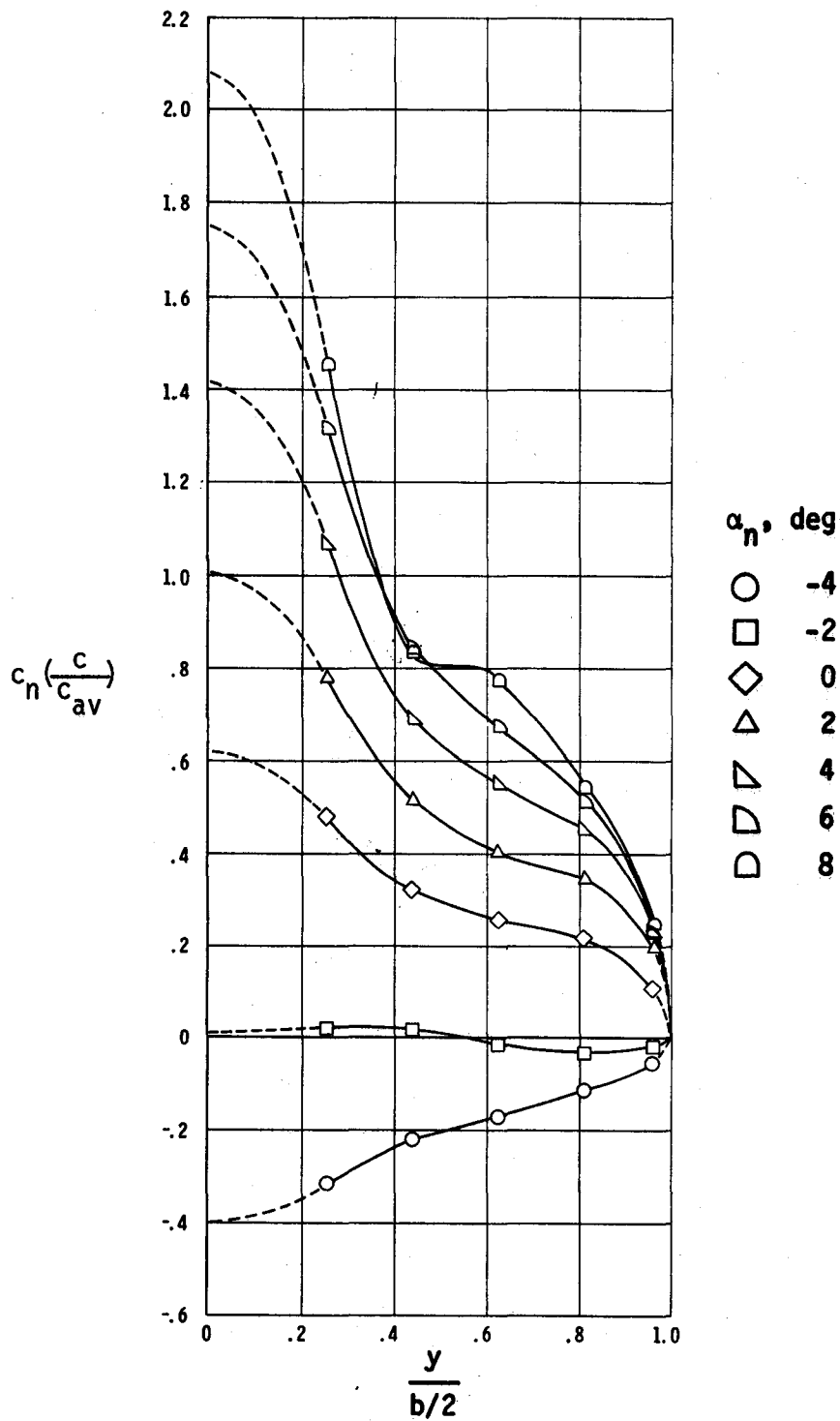
(d)  $\alpha_n = 2°$.

Figure 23.- Continued.
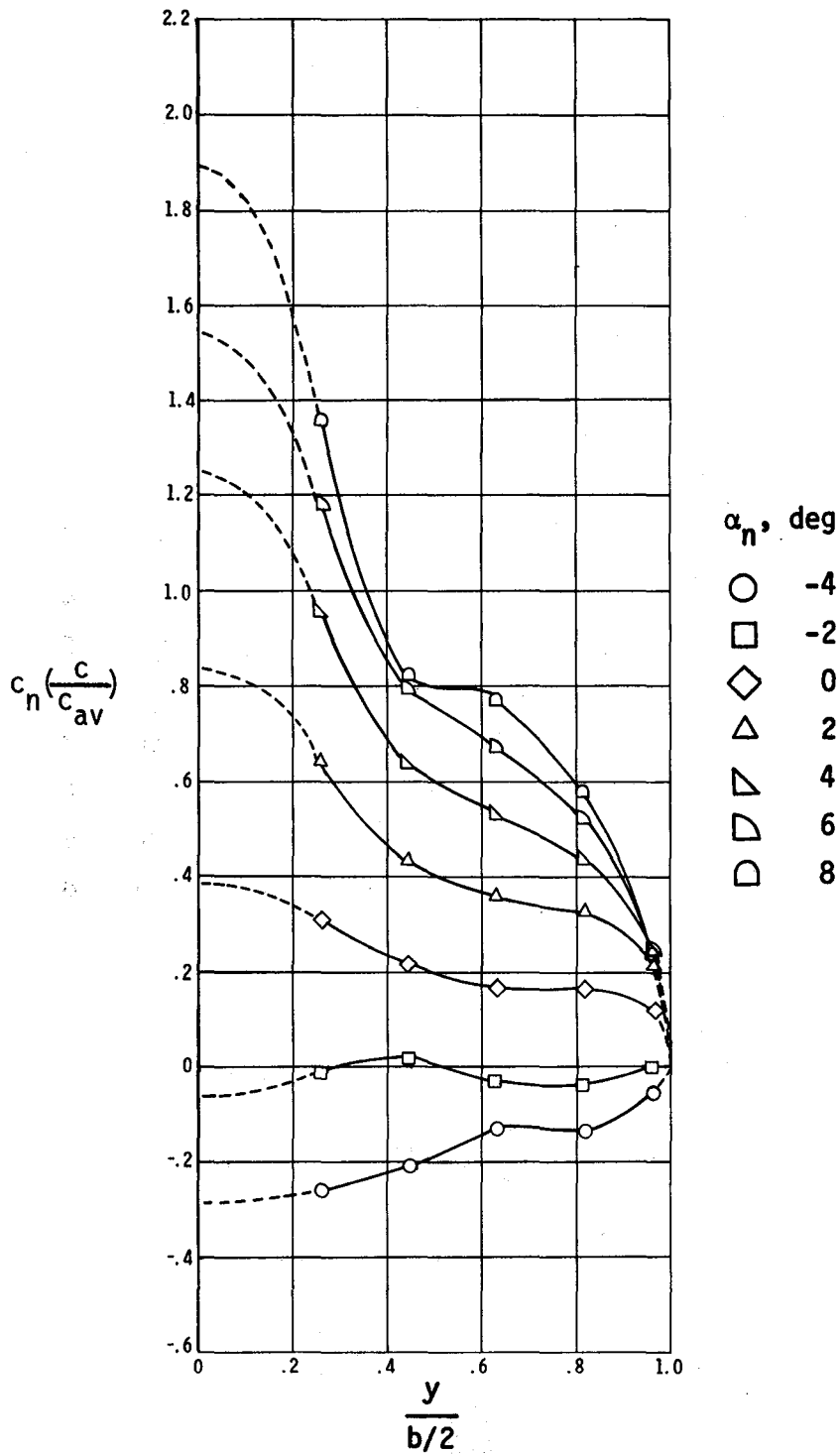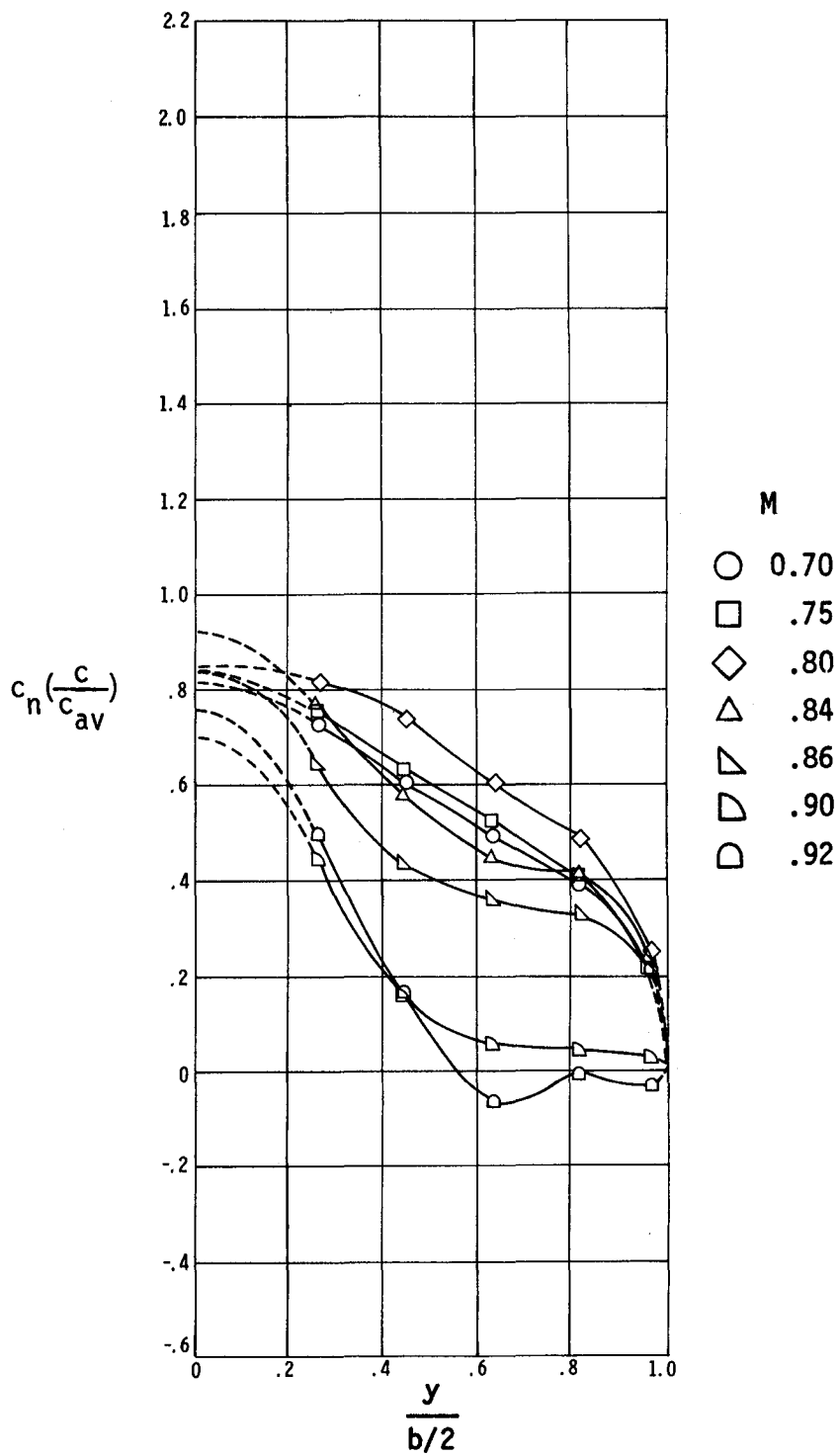
Model configuration B

(d) Concluded.
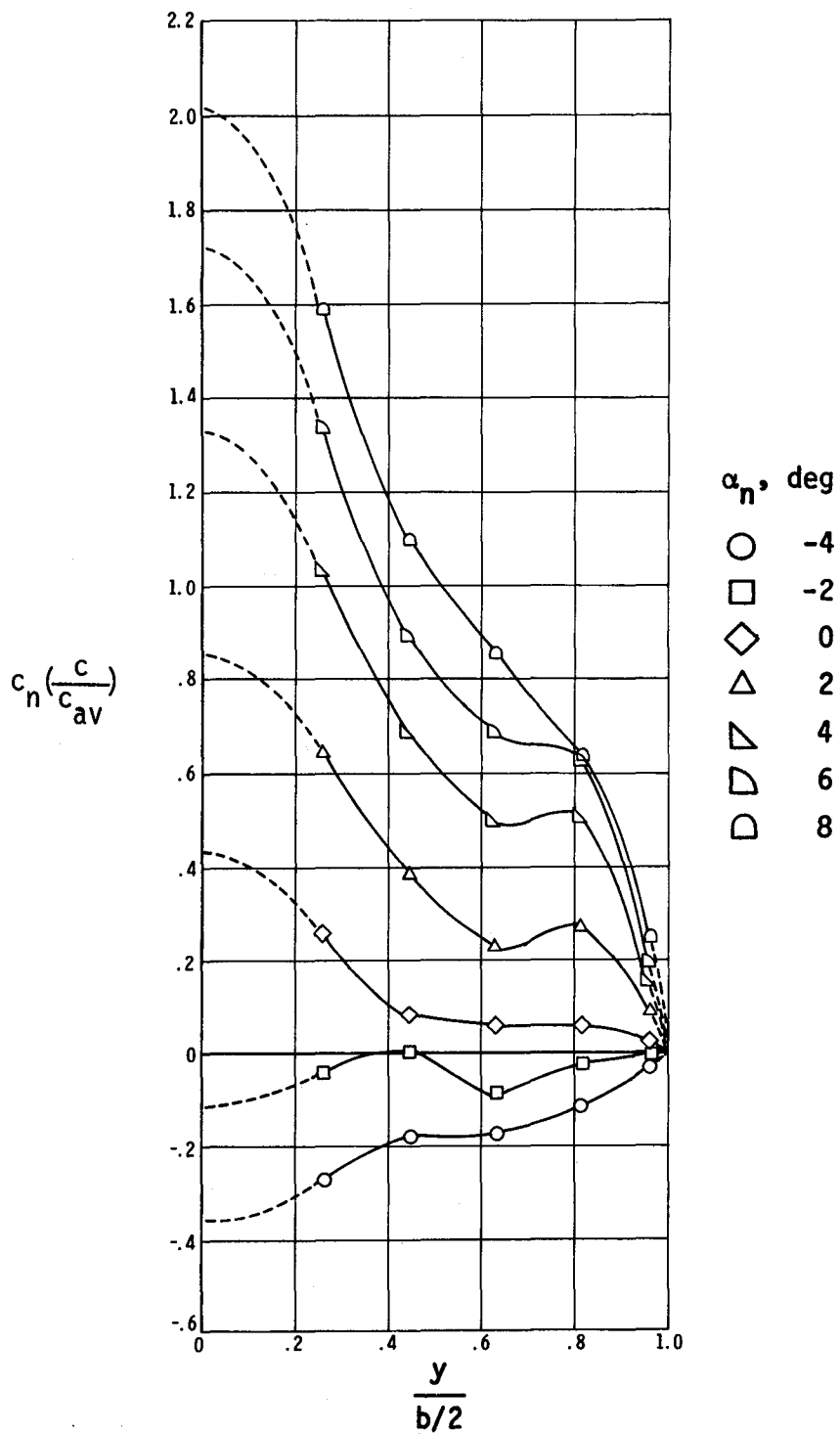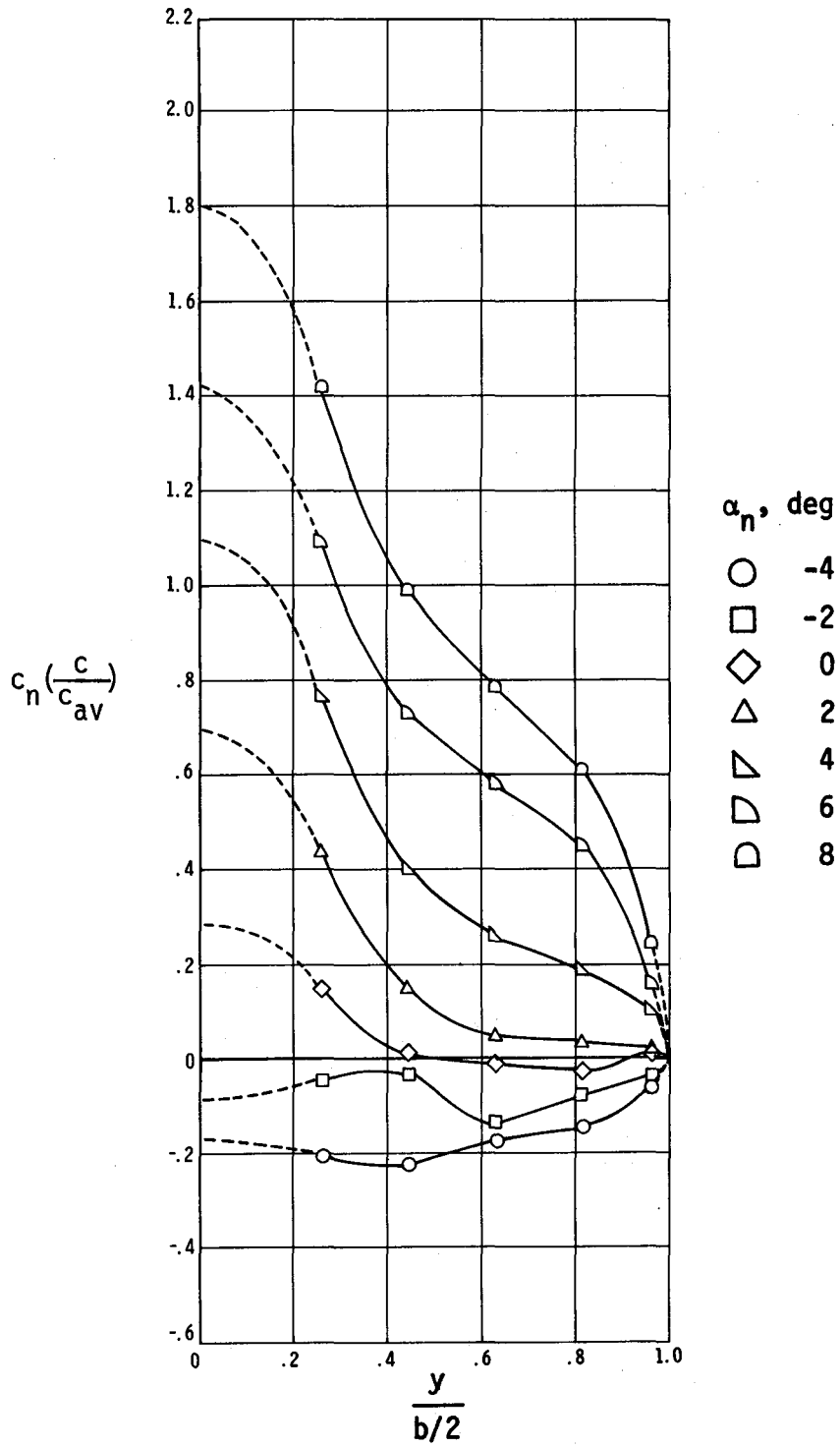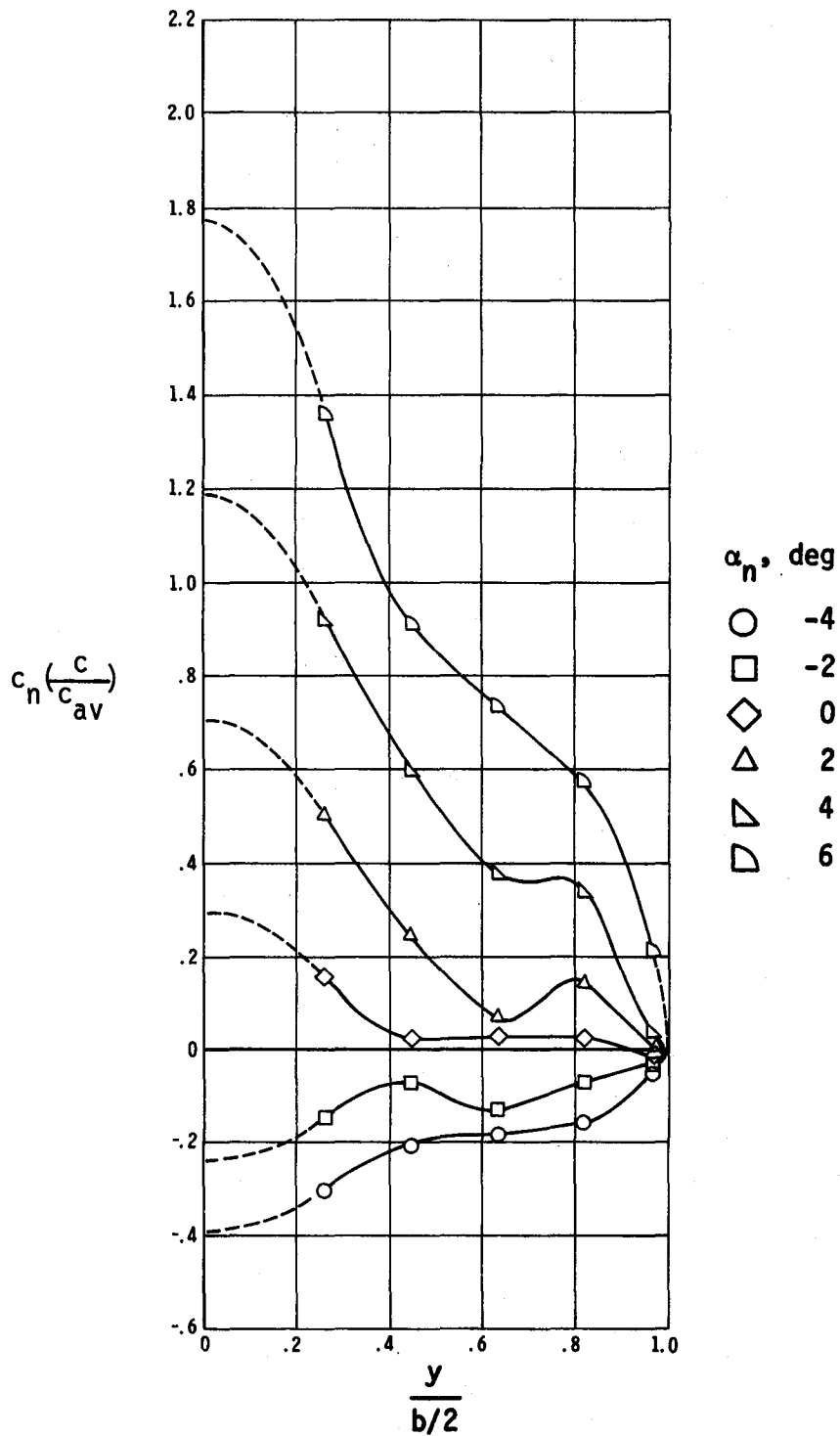
Figure 23.- Continued.
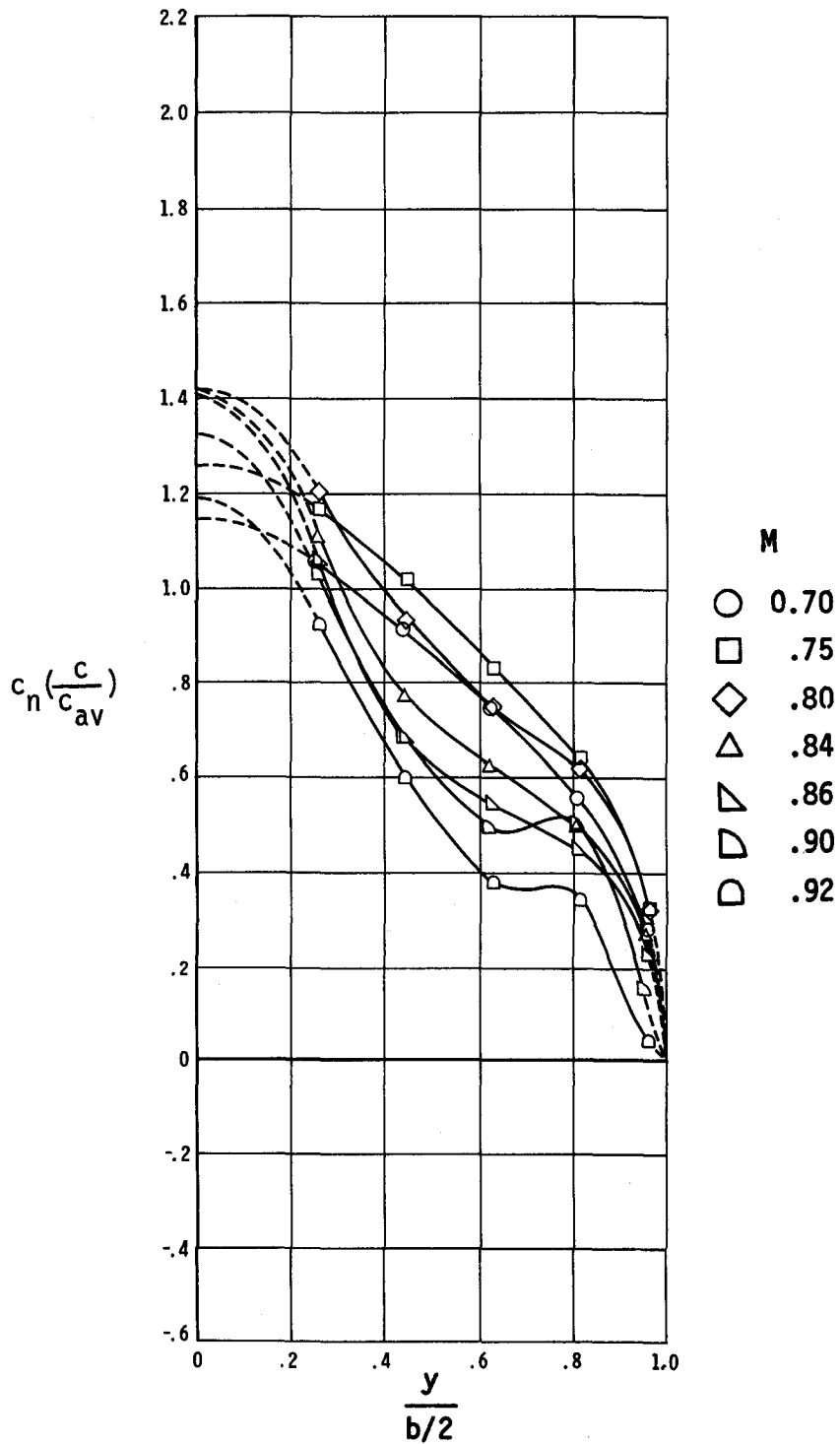
Model configuration A

(e) $\alpha_n = 4°$.

Figure 23.- Continued.

$c_n \left( \dfrac{c}{c_{av}} \right)$

M

○ 0.70

□ .75

◇ .80

△ .84

▷ .86

▷ .90

◠ .92

$\dfrac{y}{b/2}$
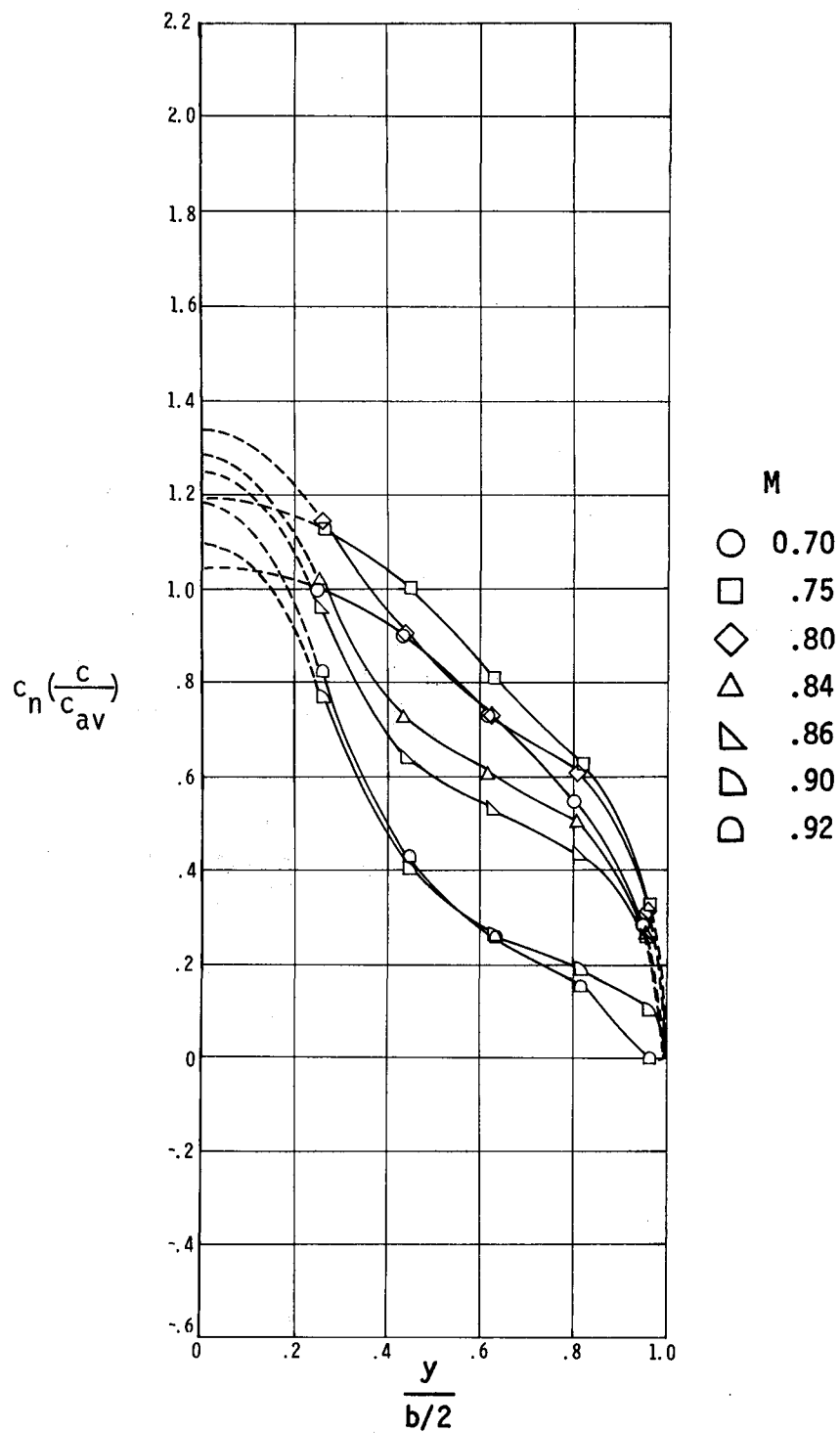
Model configuration B

(e) Concluded.

Figure 23.- Concluded.
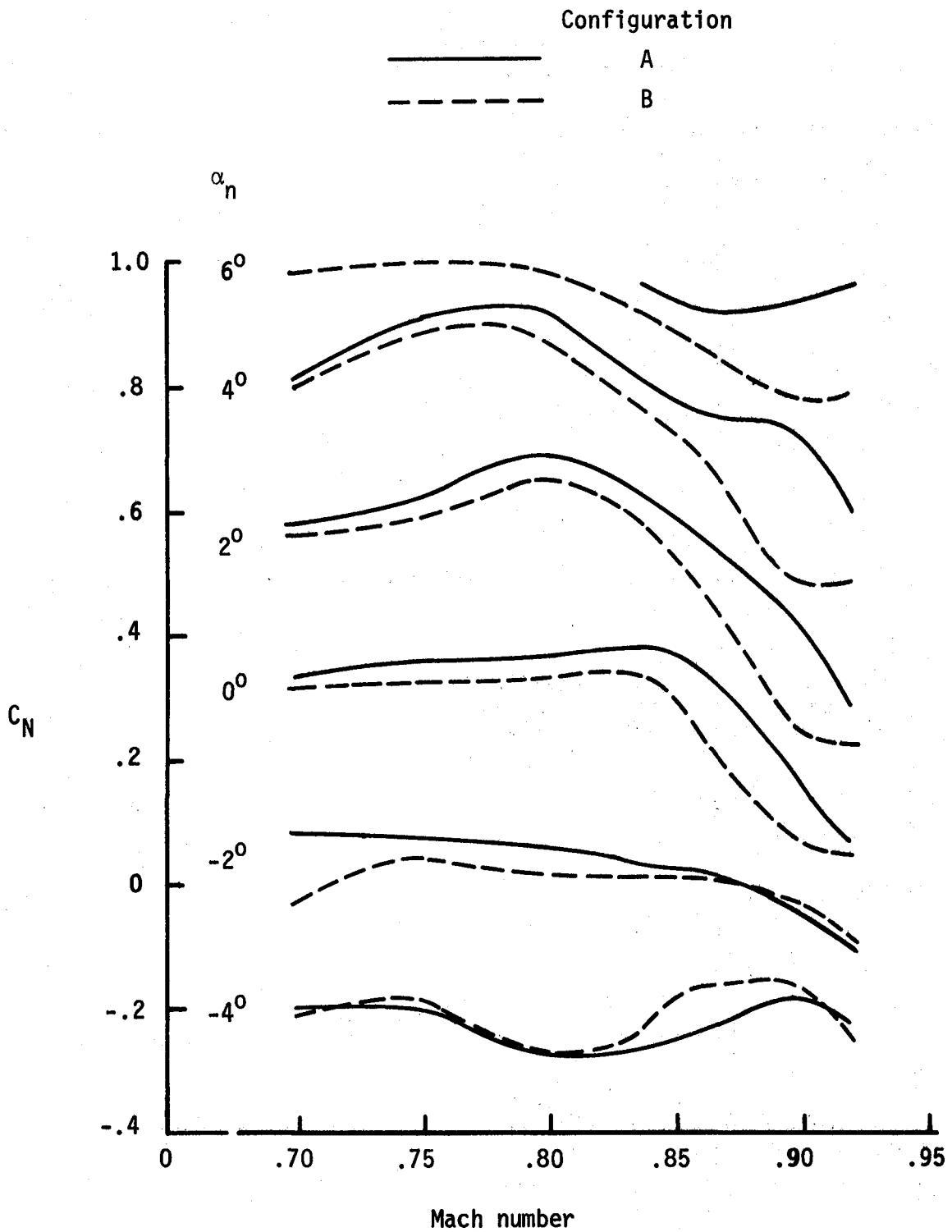
Figure 24.- Variation of panel normal-force coefficient with Mach number.
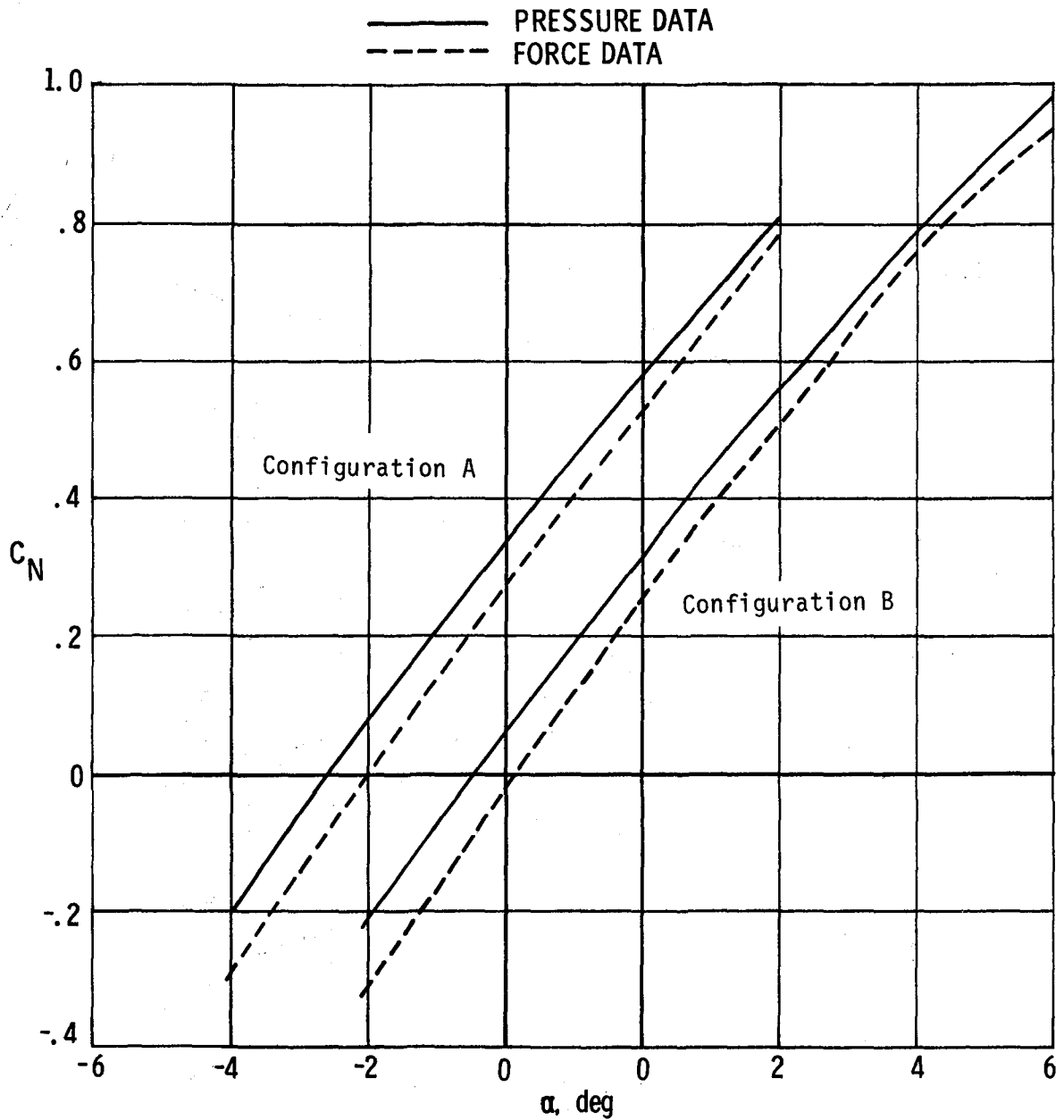
(a)  M = 0.70.

Figure 25.- Comparison of wing-panel normal-force coefficient and balance-measured normal-force coefficient for model configurations A and B.
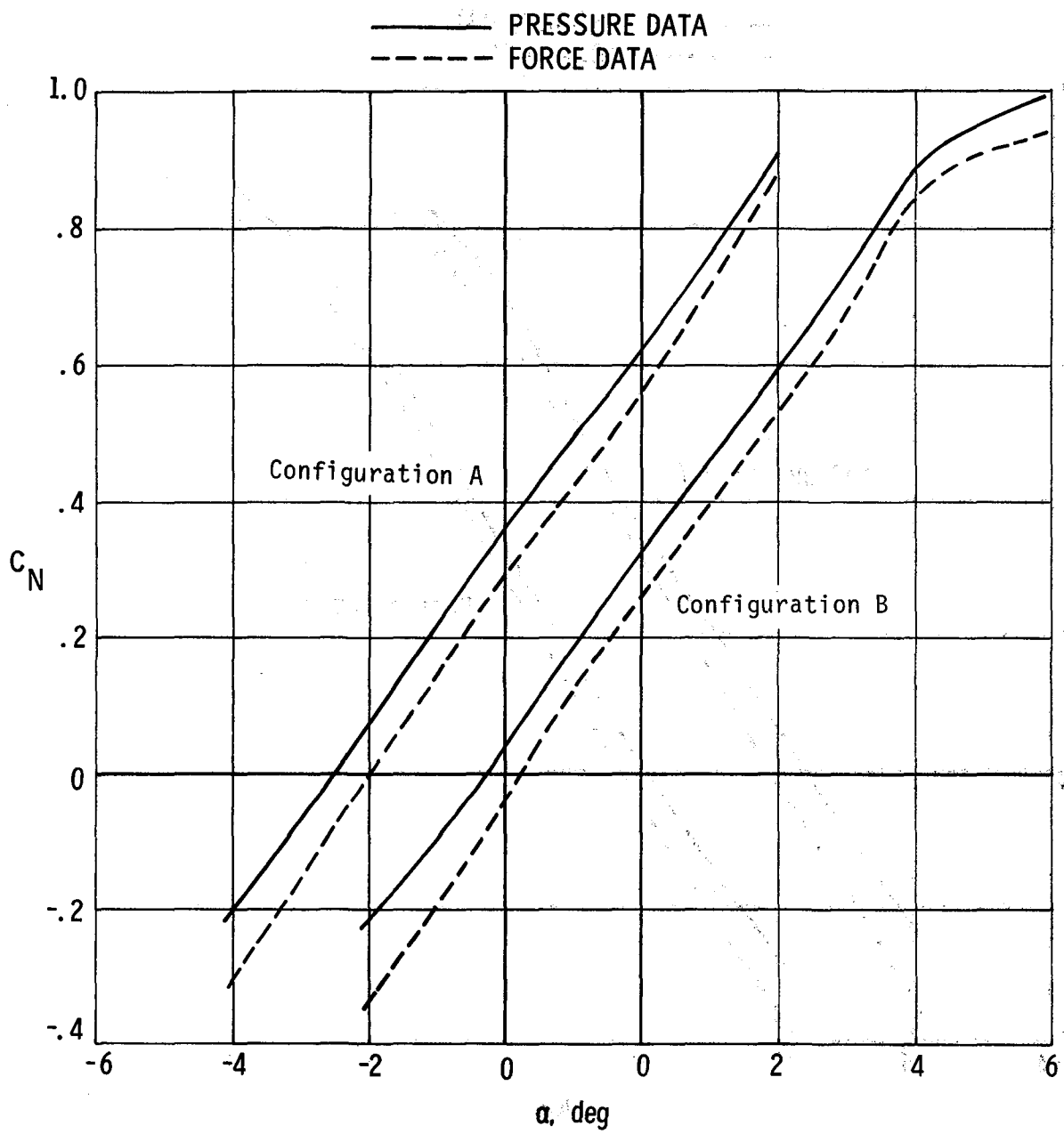
(b)   M = 0.75.

Figure 25.- Continued.
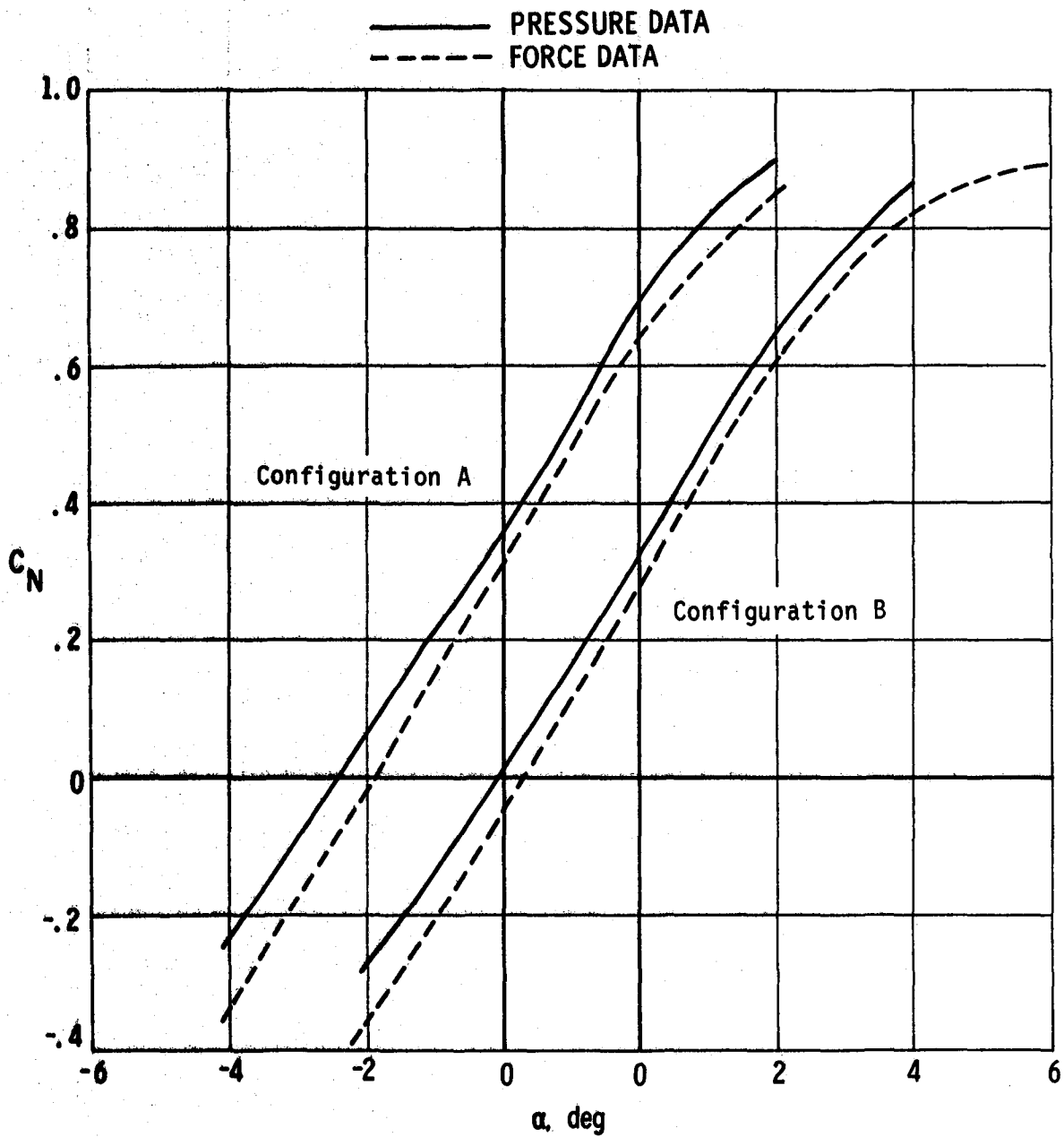
(c)  M = 0.80.

Figure 25.- Continued.
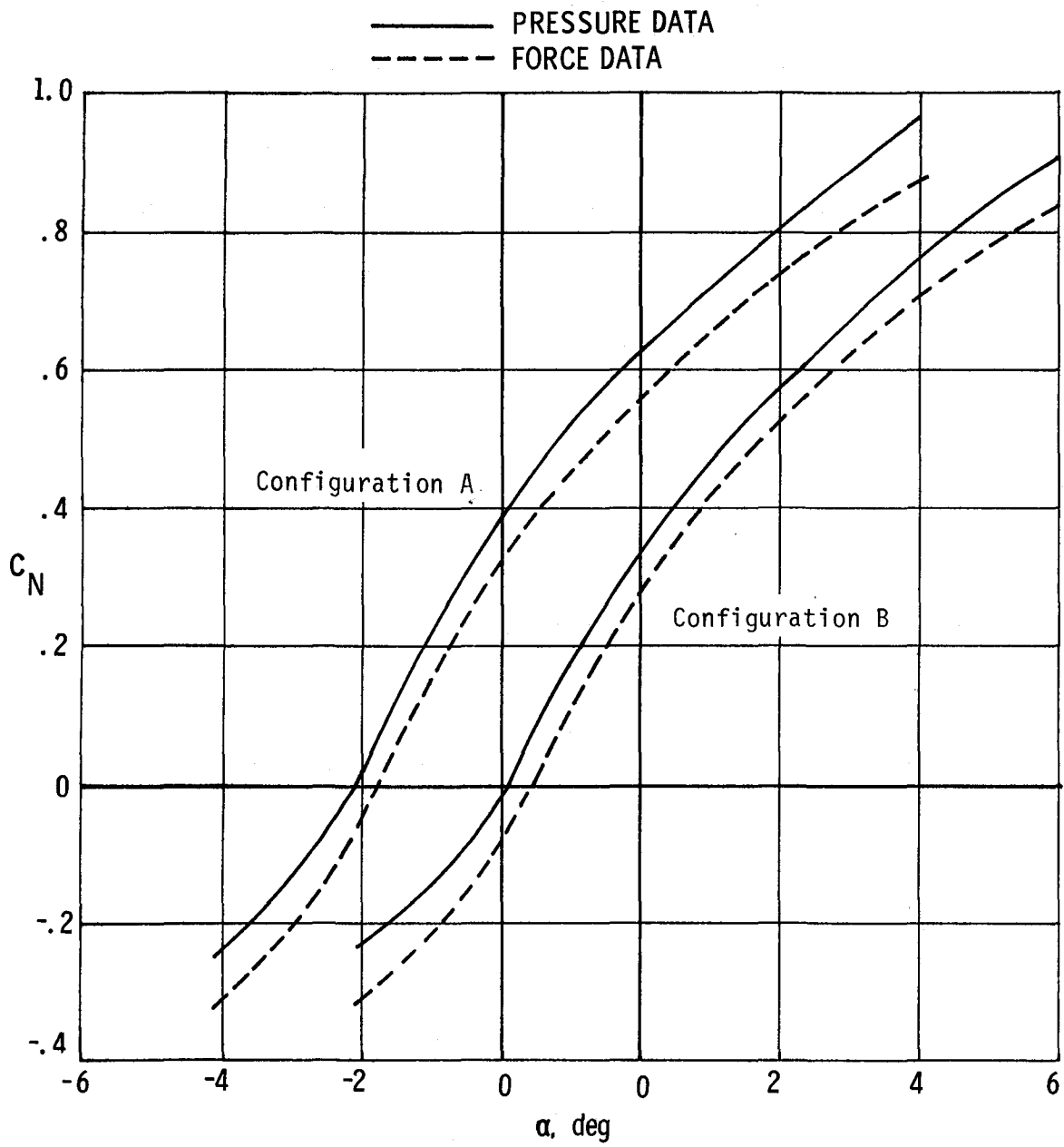
(d)   M = 0.84.

Figure 25.- Continued.
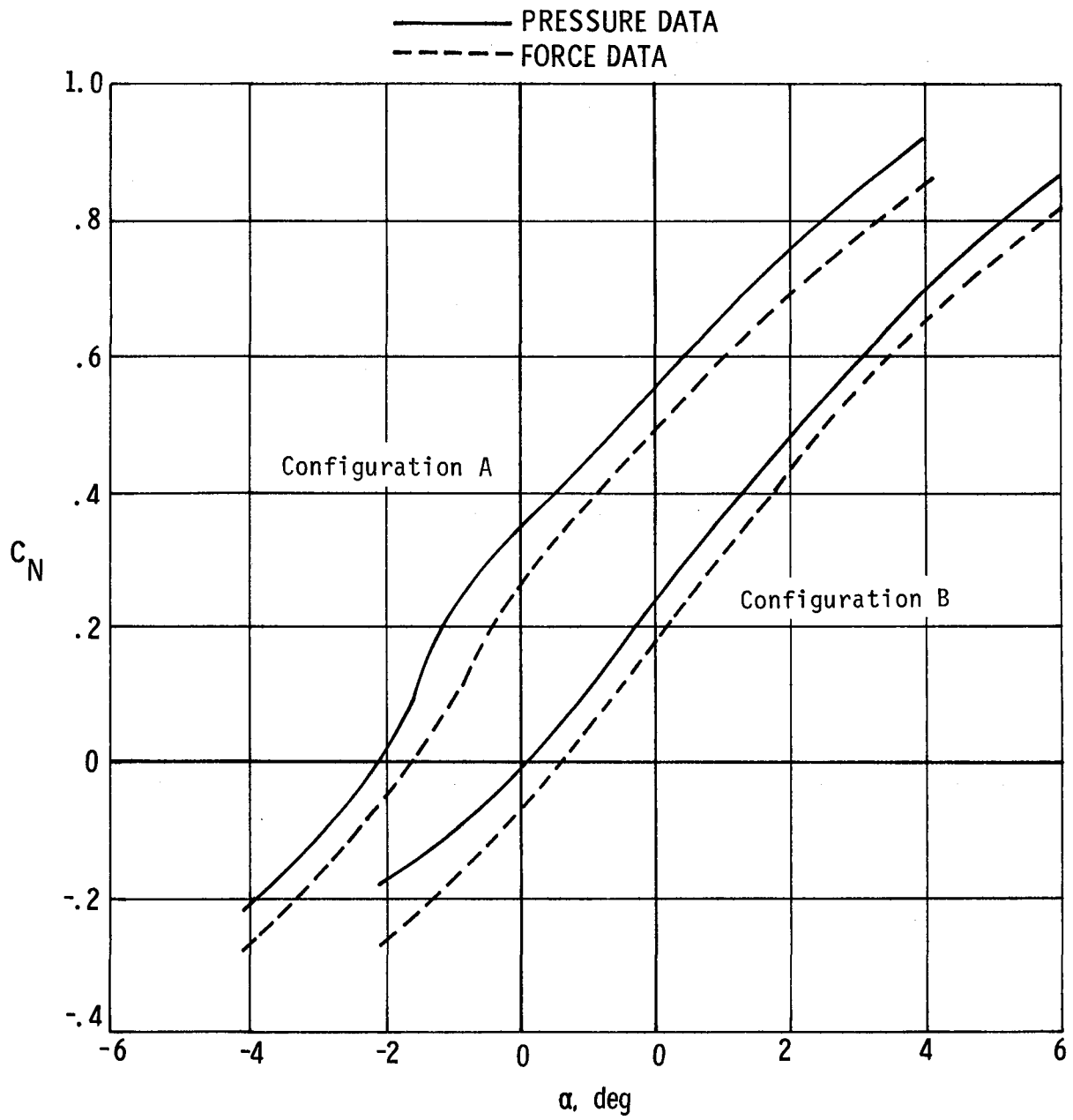
(e)  M = 0.86.

Figure 25.- Continued.
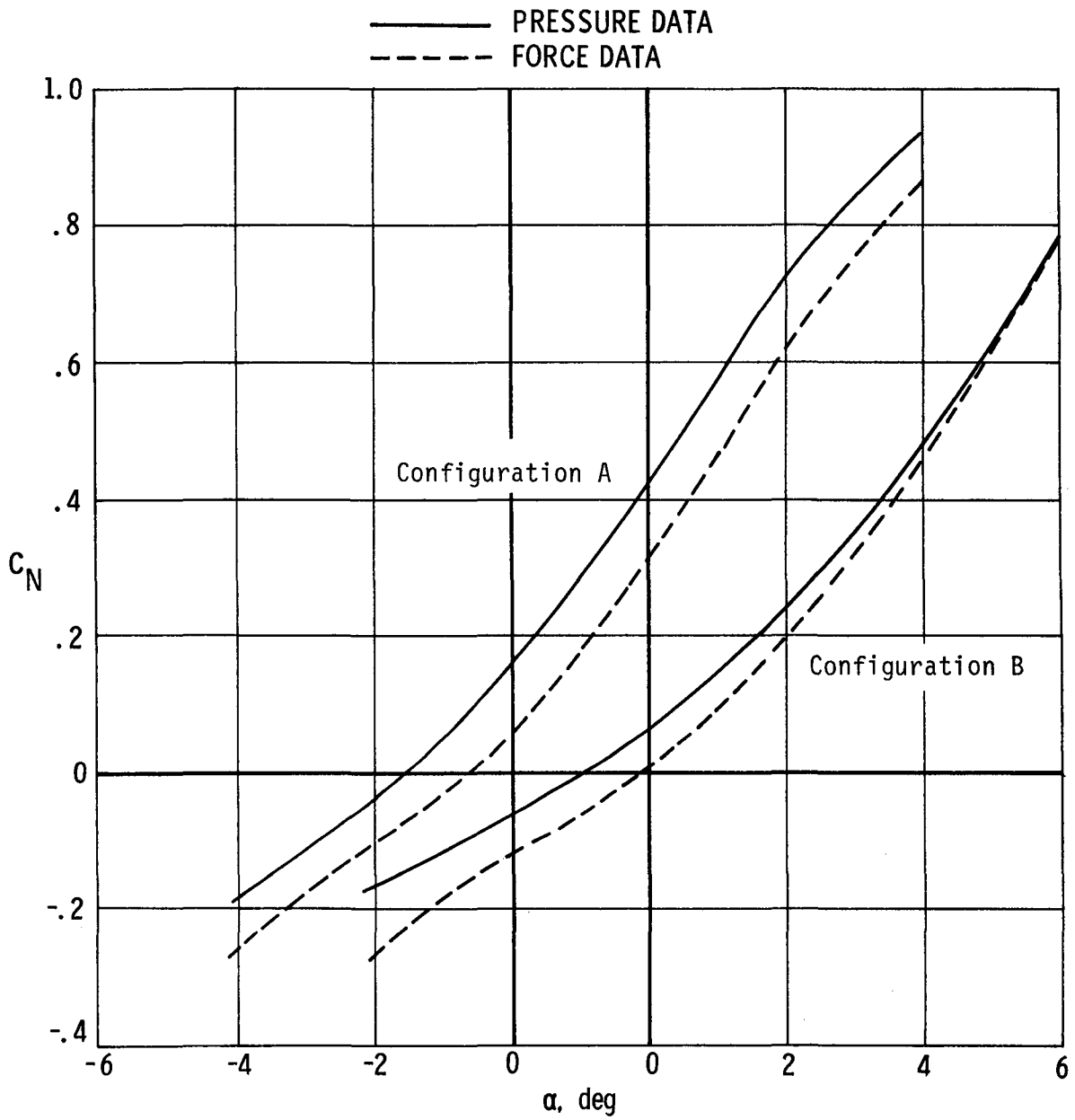
(f)  M = 0.90.

Figure 25.- Continued.
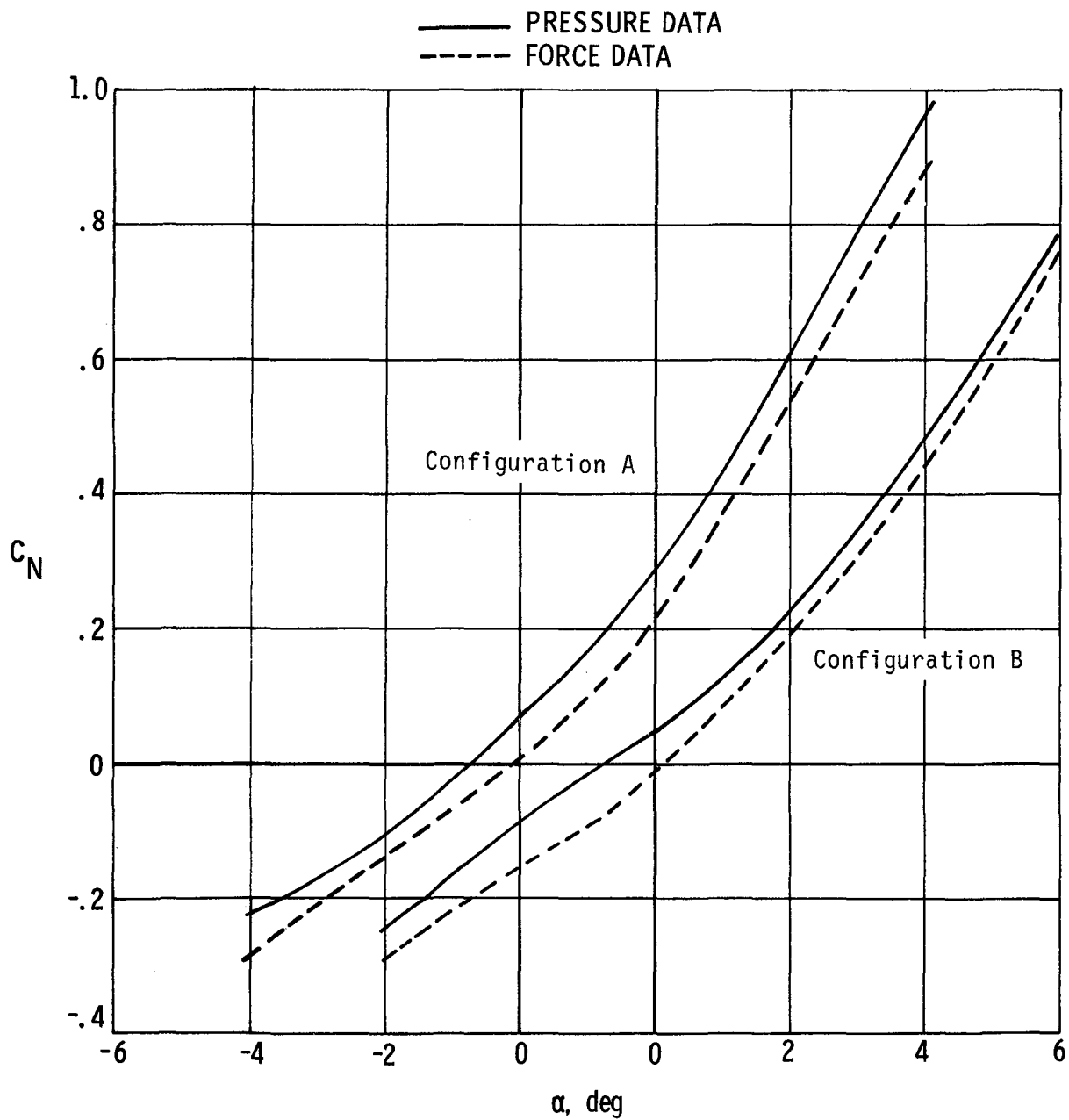
(g) M = 0.92.

Figure 25.- Concluded.

Cut here
- - - - - - - - - - - - - - - - - - - - - - - - - - - - - - - - - - - - - - - - - - - - - - - - - - - -

Date _____

Please forward "Supplement to NASA TM-84614" to

_____
Name of organization

_____
Street number

_____
City and state                                                    Zip code

Attention: _____
                Name

           _____
                Title
- - - - - - - - - - - - - - - - - - - - - - - - - - - - - - - - - - - - - - - - - - - - - - - - - - - -

| 1. Report No.<br>NASA TM-84614 | 2. Government Accession No. | 3. Recipient's Catalog No. |
|---|---|---|
| 4. Title and Subtitle<br>WIND-TUNNEL INVESTIGATION OF AERODYNAMIC LOADING ON A 0.237-SCALE MODEL OF A REMOTELY PILOTED RESEARCH VEHICLE WITH A THICK, HIGH-ASPECT-RATIO SUPERCRITICAL WING | | 5. Report Date<br>June 1983 |
| | | 6. Performing Organization Code<br>534-02-13-21 |
| 7. Author(s)<br>Thomas A. Byrdsong and Cuyler W. Brooks, Jr. | | 8. Performing Organization Report No.<br>L-15536 |
| | | 10. Work Unit No. |
| 9. Performing Organization Name and Address<br><br>NASA Langley Research Center<br>Hampton, VA 23665 | | 11. Contract or Grant No. |
| | | 13. Type of Report and Period Covered<br>Technical Memorandum |
| 12. Sponsoring Agency Name and Address<br>National Aeronautics and Space Administration<br>Washington, DC 20546 | | 14. Sponsoring Agency Code |

16. Abstract

Wind-tunnel measurements were made of the wing-surface static-pressure distributions on a 0.237-scale model of a remotely piloted research vehicle equipped with a thick, high-aspect-ratio supercritical wing. Data are presented for two model configurations (with and without a ventral pod) at Mach numbers from 0.70 to 0.92 at angles of attack from -4° to 8°. Large variations of wing-surface local pressure distributions were developed; however, the characteristic supercritical-wing pressure distribution occurred near the design condition of 0.80 Mach number and 2° angle of attack. The significant variations of the local pressure distributions indicated pronounced shock-wave movements that were highly sensitive to angle of attack and Mach number. The effect of the vertical pod varied with test conditions; however at the higher Mach numbers, the effects on wing flow characteristics were significant at semispan stations as far outboard as 0.815. There were large variations of the wing loading in the range of test conditions, both model configurations exhibited a well-defined peak value of normal-force coefficient at the cruise angle of attack (2°) and Mach number (0.80).

| 17. Key Words (Suggested by Author(s))<br>Supercritical wing<br>Pressure distribution<br>Aerodynamic loading | 18. Distribution Statement<br>Unclassified - Unlimited<br><br>Subject Category 02 |
|---|---|

| 19. Security Classif. (of this report)<br>Unclassified | 20. Security Classif. (of this page)<br>Unclassified | 21. No. of Pages<br>213 | 22. Price<br>A10 |
|---|---|---|---|

National Aeronautics and
Space Administration

Washington, D.C.
20546

SPECIAL FOURTH CLASS MAIL
BOOK

# NASA

POSTMASTER:    If Undeliverable (Section 158
Postal Manual) Do Not Return